Development of insulation materials for sustainable building performance

BIO-BASED MATERIALS, GEOPOLYMERS AND AEROGEL

Koh Chuen Hon

Bouwstenen 387

Development of insulation materials for sustainable building performance

bio-based materials, geopolymers and aerogel

Koh Chuen Hon

This project is done under the financial support of the MOOI project "Bright Renovatie Isolatie voor woningschil door (Advanced) Materialen en Methodes (BRIMM)", funded by the Netherlands Enterprise Agency (RVO)

CIP-DATA LIBRARY TECHNISCHE UNIVERSITEIT EINDHOVEN

Development of insulation materials for sustainable building performance / by Koh Chuen Hon
A catalogue record is available from the Eindhoven University of Technology Library
ISBN: 978-90-386-6118-6
Bouwstenen 387
NUR 955

Cover design: Koh Chuen Hon
Ph.D. thesis, Eindhoven University of Technology, the Netherlands

Development of insulation materials for sustainable building performance

bio-based materials, geopolymers and aerogel

PROEFSCHRIFT

ter verkrijging van de graad van doctor aan de Technische Universiteit Eindhoven,
op gezag van de rector magnificus, prof.dr. S.K. Lenaerts,
voor een commissie aangewezen door het College voor Promoties,
in het openbaar te verdedigen op dinsdag 10 september 2024 om 13:30 uur

door

Koh Chuen Hon

geboren te Kuantan, Maleisië

Dit proefschrift is goedgekeurd door de promotoren en de samenstelling van de promotiecommissie is als volgt:

Voorzitter:	prof. dr. ir. T.A.M. Salet
Promotor:	prof. dr. ir. H.J.H. Brouwers
Copromotor:	dr. Dipl.-Min. K. Schollbach
	dr. F. Gauvin
Promotiecommissieleden:	prof. dr. L.M. Ottosen (Danmarks Tekniske Universitet)
	prof. dr. S. Roels (Katholieke Universiteit Leuven)
	prof. dr. S. Amziane (Université Clermont Auvergne)
	prof. dr. ir. J.L.M. Hensen

Het onderzoek of ontwerp dat in dit proefschrift wordt beschreven is uitgevoerd in overeenstemming met de TU/e Gedragscode Wetenschapsbeoefening.

PREFACE

I have had the honour of embarking on this journey at the Eindhoven University of Technology, guided by the Building Material Group in the Department of the Built Environment. I am deeply grateful to the MOOI project "Bright Renovation Insulation for building envelope through (Advanced) Materials and Methods (BRIMM)", funded by the Netherlands Enterprise Agency (RVO), which has supported my research program. My research has been focused on the development of building insulation materials for sustainable building performance, a topic of immense relevance and importance in our current global context.

I owe a profound debt of gratitude to my promotor, prof.dr.ir. H.J.H. Brouwers, whose expertise and insights have been invaluable throughout this process. Your unwavering support and encouragement have been a constant source of motivation. I would also like to express my gratitude to my daily supervisors, dr. Dipl.-Min. K. Schollbach and dr. F. Gauvin, whose guidance and feedback have been instrumental in shaping this research. I extend my heartfelt thanks to prof.dr. L.M. Ottosen, prof.dr. S. Roels, prof.dr. S. Amziane, and prof.dr.ir. J.L.M. Hensen, who have agreed to be part of my PhD defence committee.

Finally, I would like to express my deepest gratitude to my family, friends, and colleagues. Your unwavering support and belief in my capabilities have been a constant source of strength throughout this journey.

This thesis is not just a reflection of my academic journey, but also a testament to the collaborative spirit of scientific inquiry. I hope that this work contributes to the ongoing discourse on sustainable building insulation materials and inspires further research in this field. As I close this chapter and look forward to the next, I carry with me not just a thesis, but a treasure trove of experiences, learnings, and memories.

Alex Koh
Eindhoven, June 2024

SUMMARY

This thesis explores the development of insulation materials aimed at enhancing sustainable building performance, focusing on reducing energy demand, carbon emissions, and material consumption in the construction sector. The key findings are as follows:

In-depth Analysis of Bio-Based Insulation Composites: Several bio-based materials, including straws, hemp, grass, cork, and mycelium, were investigated. Cork composite emerged as the most promising, with the lowest thermal conductivity, low sorption properties, and minimal risk of mould growth. In contrast, mycelium composite had the highest thermal conductivity and was prone to mould growth in humid environments. Barley straws demonstrated superior performance over wheat straws, with lower sorption capacity, lower thermal conductivity, and reduced mould growth. The application of an antifungal surface treatment with boric acid significantly enhanced the mould resistance of straw-based insulation. The study emphasizes the importance of selecting bio-based materials based on specific applications and climatic conditions to optimize their performance and durability.

Development and Evaluation of Insulation Composites from Bio-Based, Waste-Based, and By-Products: This thesis explores the development of insulation boards and lightweight aggregates. Fly ash-based geopolymer proved to be a viable alternative to Ordinary Portland Cement (OPC) in producing wood wool geopolymer boards (WWGB), meeting required strength benchmarks. The mechanical strength of these boards was primarily influenced by the Na_2O concentration, followed by the slag percentage and the modulus. However, substituting wood wool with straw in straw geopolymer boards (SGB) resulted in reduced overall performance. Both SGB and WWGB exhibited higher environmental impacts in more than half of the 19 assessed impact categories compared to conventional wood wool cement boards (WWCB), highlighting the need for a comprehensive evaluation of multiple environmental indicators, as material substitution can lead to trade-offs in sustainability. Additionally, waste stone wool was successfully repurposed to produce alkali-activated lightweight aggregates, aligning with high-grade recycling initiatives within the circular economy framework.

Energy Rehabilitation of Existing Building Stocks: Simulations of a typical Dutch building with a cavity wall, rehabilitated with an advanced aerogel composite, showed significant reductions in annual heating and cooling demand, along with improved thermal comfort for occupants. For crawl space rehabilitation, using lightweight aggregates as ground cover insulation led to a notable reduction in water content and an increase in floor surface temperature within the floor assembly.

Moisture-Dependent Thermal Conductivity: A two-phase model was proposed to predict moisture-dependent thermal conductivity in porous materials, providing a reliable fit to the experimental data.

This thesis highlights the potential of bio-based and waste-based insulation materials to contribute significantly to sustainable building practices, while also addressing the challenges in balancing performance, durability, and environmental impact.

Contents

1. INTRODUCTION

1.1. BACKGROUND AND MOTIVATION

The global building and construction sector significantly impacts energy consumption and carbon emissions, accounting for 34% of final energy demand and 37% of total global CO_2 emissions [1]. Moreover, the built environment demands approximately 23.5 billion tonnes of raw materials globally [2], making up 30% of the total material demand across various sectors in high-income countries. Despite a 15% expansion in building floor space since 2015, energy use per square meter has improved by a mere 6% during the same period [3]. This, coupled with a consistent annual increase of around 1% in overall energy demand and emissions [1], underscores the challenges at hand. Climate change further compounds these challenges, necessitating the retrofitting of existing buildings and the design of new ones to withstand climate extremes [1]. Given these complexities, it is crucial to explore all avenues for sustainable development within the building and construction sector, with the aim of reducing energy demand, carbon emissions, and material demand. To tackle these challenges, stakeholders have adopted three core strategies: energy retrofitting of existing building stocks [1, 3], decarbonization of construction materials [4], and the application of circular economy principles in the built environment [5, 6, 7], as illustrated in **Fig. 1.1**.

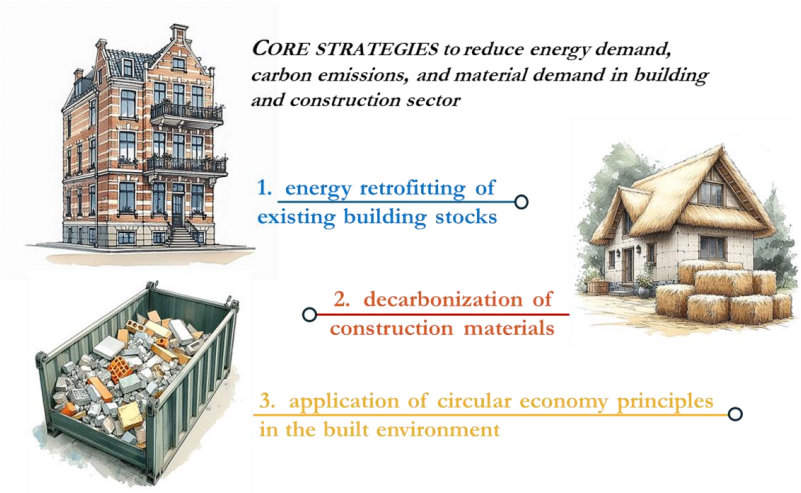

Fig. 1.1 Illustration of core strategies for sustainable building development.

In cold climate zones, energy retrofitting of existing building stocks is essential to reduce overall heating demand. Buildings with poor insulation, suboptimal design and insufficient ventilation can risk overheating during heat waves, amplifying health risks and escalating energy demand [1]. However, the average retrofitting rate of the building stock is less than 1% per year, resulting in a reduction of less than 15% in energy intensity [3]. To achieve a 50% reduction in carbon emissions by 2030, the retrofitting rate would need to increase to between 2.5 and 5% annually. This necessitates the rehabilitation of the building envelop, including glazing, to enhance insulation

performance in the majority of housing stocks, including those buildings with insufficient space for an additional insulation layer. Significant progress has been made in this area, such as the application of superinsulation materials like vacuum insulation panels and silica aerogel, which could be applied to these building stocks.

In the Netherlands, building-related energy consumption in the services and households sectors accounts for 37% of the total energy consumption, with the largest part being used for space heating [8]. Many residential properties built before the 1970s in the Netherlands feature empty cavity walls and crawl spaces that require retrofitting [9]. The Dutch government has implemented a wide variety of policies and actions for the rehabilitation effort, including providing financial subsidies for insulation installation for homeowners [10]. In 2020 alone, over a million energy-saving measures were taken in existing housing in the Netherlands, with cavity wall insulation being one of the most common [8]. More than 3 million m^2 of cavity filling was carried out by certified contractors [11]. Amid these positive trends, ongoing progress is being made in the research and development of advanced materials that can further improve insulation performance. In addition, the performance of post-rehabilitated buildings with these advanced insulation materials is attracting further investigation [12].

While energy retrofitting focuses on reducing the operational energy in a building's life cycle, it is necessary to lower the embodied carbon of the construction material to reduce the overall carbon footprint of the building. Policies on incorporating whole-life carbon have already gained traction in countries such as the Netherlands, Denmark and France where CO_2 limits are imposed on new buildings [13]. Three pathways are proposed for the decarbonization of building materials [4]: avoid the extraction and production of raw materials by galvanising a circular economy, shift to regenerative material practices such as low carbon earth- and bio-based building materials, and improve methods to radically decarbonize conventional materials such as concrete and fossil-based polymer materials.

Bio-based building materials, either wood-based or containing other natural fibres, are one of the solutions for producing low-carbon materials. They generally have a lower embodied energy than synthetic materials, can be sourced locally, and have diverse building applications to achieve the desired performance characteristics [14]. One proposal for wider usage is to create incentives to encourage the conversion of biomass into building materials, and policy support is needed to encourage the conversion of biomass feedstock to bio-based insulation [4]. For instance, a similar policy has been implemented in the Netherlands, where extra financial subsidies for insulation installation for homeowners when bio-based insulation materials are applied in building rehabilitation [10]. However, the intrinsic hygroscopic nature of bio-based materials and their tendency to absorb moisture [15], the associated durability concerns such as mould development [16], and the lack of standardized best practices within building types and climate zones [1], may hinder their widespread usage. Other factors such as competition with other users of biomass, for example, biomass energy power plants [2], and the lack of investment in this front [1], pose a challenge in this effort as well.

The most frequently used thermal insulation materials in Europe are inorganic mineral fibres, followed by fossil-based polymer materials, such as expanded and extruded polystyrene and polyurethane foam, whilst all other materials only cover the remaining 1% of the market, including

bio-based materials [17]. For instance, polymer-based insulation materials used in buildings are rarely recycled at their end-use [4]. In the Netherlands, overall insulation materials constitute a notable proportion of construction and demolition waste (CDW), with a significant amount being landfilled and incinerated, at approximately 8.8% and 8.6%, respectively [18]. One solution is to shift from these mineral-based and fossil-based materials to bio-based materials, for example, cellulose insulation and straw-based materials. Another direction is to implement the circular economy concept in the full life cycle of these insulation materials.

A circular building is defined as optimizing the use of resources while minimizing waste in its full life cycle [6]. However, challenges abound when implementing the concept of resource efficiency and the circular economy in buildings, for example, structural resistance versus easy to disassemble, longevity versus flexibility, simple versus composite products, renovation versus new build, etc. [5]. The European Commission has focused on three specific objectives to tackle these challenges, which are the durability of building and their elements, adaptability including ease of replacement and refurbishment, and reducing waste and facilitating high-quality waste management [5]. Specifically, for building material development, a circular concept drives alternative material use, reduces the consumption of resources, and localises the supply chain [7]. For this reason, utilizing raw materials based on waste or by-products from local sources is especially important to close the circular loop. Industrial by-products such as slags and fly ash, and agricultural by-products such as straws, and CDW, are among the examples of this. These secondary materials enable applications such as applying fly ash and slag as precursors for alkali-activated binder, straws as main fibrous sources for insulation, and repurposing CDW into other building materials.

The development of insulation materials for sustainable development is a multifaceted challenge that requires a concerted effort across various sectors. This thesis draws motivations from the overarching approaches dealing with the challenges facing the building and construction sector, which are the energy retrofitting of existing building stocks, decarbonization of construction materials, and circularity economy principles in the built environment.

1.2. RESEARCH METHODOLOGY AND FRAMEWORK

1.2.1. Hygrothermal material properties

The hygrothermal material properties of insulation materials have been identified as a critical research component in advancing sustainable building development. The presence of moisture within the insulation materials leads to a higher thermal conductivity and potential material degradation. Understanding these properties is essential whether selecting the appropriate insulation solution for energy retrofitting of existing building stock, utilizing non-conventional materials such as bio-based insulation to reduce the carbon footprint of building materials, or developing new insulation composites from waste or by-products in line with circular economy principles.

As a result, the hygrothermal material properties of insulation materials are the central focus of this thesis. Key physical, thermal, and hygric properties that significantly influence hygrothermal

performance will be experimentally measured to provide a comprehensive understanding of these materials.

This thesis focuses on two primary thermal parameters: effective thermal conductivity for heat transport and specific heat capacity for heat storage. To gain a deeper understanding of moisture's impact on thermal conductivity, moisture-dependent thermal conductivity is also measured and included in this research. However, temperature-dependent thermal conductivity is not investigated, as the insulation materials studied are not intended for use in extreme temperature environments. Similarly, two hygric parameters are examined: sorption isotherm for moisture storage and water vapour diffusion resistance factor for moisture transport. The primary moisture transport mechanisms in porous building materials include vapour diffusion, capillary conduction, and surface diffusion. Accurately measuring each of these mechanisms individually is challenging. Therefore, this research focuses on the vapour diffusion resistance factor, excluding the liquid transport coefficient for water capillary conduction. This decision is based on the fact that the insulation materials studied are highly porous and are typically protected from direct exposure to driving rain or other water sources by surrounding components such as bricks or cladding. Additionally, physical parameters such as bulk density and porosity are investigated, with porosity specifically referring to pores with vapour-permeable walls that are accessible to water vapour. For bio-based materials, additional mould growth tests will be conducted.

While certain factors (such as liquid conduction, temperature-dependent thermal conductivity, and temperature-dependent enthalpy) are not considered in this research framework, the majority of factors influencing hygrothermal characteristics are addressed.

1.2.2. Numerical simulations

This thesis employs two types of numerical simulations to predict the performance of insulation composites under varying conditions. The first simulation type is heat, air, and moisture (HAM) modelling, which focuses on the hygrothermal performance of building assemblies incorporating the investigated insulation materials. The results of this simulation provide insights into the hygrothermal behaviour of non-conventional insulation materials or newly developed composites under different environmental conditions and assembly designs. The second simulation type is building performance modelling, which examines the hygrothermal performance, energy demands, and occupant comfort of a building that includes the investigated insulation materials. This simulation is particularly valuable for exploring building rehabilitation options using various insulation solutions. In both simulations, the experimental results of the insulation materials will be integrated into the numerical models to ensure accurate and reliable predictions.

For the HAM simulations, one-dimensional, non-steady-state heat and moisture transport processes are modelled using coupled differential equations in WUFI Pro software [19]. The governing equations for heat and moisture transport are:

$$\frac{\partial H}{\partial T}\frac{\partial T}{\partial t} = \frac{\partial}{\partial x}\left[\lambda \frac{\partial T}{\partial x}\right] + h_v \frac{\partial}{\partial x}\left[\frac{\delta}{\mu}\frac{\partial p}{\partial x}\right] \tag{1-1}$$

and

$$\rho_w \frac{\partial w}{\partial \varphi} \cdot \frac{\partial \varphi}{\partial t} = \frac{\partial}{\partial x}\left[\rho_w D_w \frac{\partial w}{\partial \varphi}\frac{\partial \varphi}{\partial x}\right] + \frac{\partial}{\partial x}\left[\frac{\delta}{\mu}\frac{\partial p}{\partial x}\right] \quad (1\text{-}2)$$

respectively. Here, D_w ($m^2 \cdot s^{-1}$) is the liquid transport coefficient, H ($J \cdot m^{-3}$) the enthalpy, h_v ($J \cdot kg^{-1}$) is the evaporation enthalpy of water, p (Pa) is the water vapour partial pressure, w ($m^3 \cdot m^{-3}$) is the water content, δ ($kg \cdot m^{-1} \cdot s^{-1} \cdot Pa^{-1}$) is the water vapour diffusion coefficient in air, T (°C) the temperature, λ ($W \cdot m^{-1} \cdot K^{-1}$) is the thermal conductivity, μ (dimensionless) is the vapour diffusion resistance factor, ϱ_w ($kg \cdot m^{-3}$) is the density of water, and φ (dimensionless) is the relative humidity. The left-hand side of both equations comprises the storage terms, while the transport terms are on the right-hand side. In this model, the heat storage consists of the heat capacity of the material, the heat transport includes both moisture-dependent thermal conductivity and vapour enthalpy flow, the moisture storage is directly linked to the sorption isotherm, and the moisture transport contains both the liquid transport and vapour diffusion terms. Assuming the assembly is airtight, air convection and air leakages are excluded from the HAM simulation. Material properties for the main insulation materials under investigation are derived from experimental results, while standard material properties from the software's database are used for other materials. Specific cases of assembly design and boundary conditions (environmental conditions) are defined for each topic. For bio-based materials, the risk of mould growth under different climate conditions and design scenarios is further assessed using WUFI Bio software, which predicts germination and mould growth using germination isopleths [20].

The building performance, including indoor climate and comfort conditions within a reference building, is examined in detail using the WUFI Plus software. This examination involves calculating the balance of heat and moisture transfers within the room [21]. The heat balance and moisture balance are represented by the following equations:

$$\frac{\partial H}{\partial t} = \sum\nolimits_j Q_{comp,j} + Q_{sol} + Q_{in} + Q_{vent} + Q_{HVAC} \quad (1\text{-}3)$$

and

$$\frac{\partial C}{\partial t} = \sum\nolimits_j \dot{W}_{comp,j} + \dot{W}_{in} + \dot{W}_{vent} + \dot{W}_{HVAC} \quad (1\text{-}4)$$

respectively. Here, H (J) is the overall enthalpy of the air in the simulated zone, C (kg) is the overall moisture content of the air in the simulated zone, $Q_{comp,j}$ (W) is the transmission heat flow over component j, Q_{sol} (W) is the short-wave solar radiation leading directly to heating the inner air, Q_{in} (W) is the convective heat sources in the room, Q_{vent} (W) is the heat flow from ventilation, Q_{HVAC} (W) is the convective heat flow from building ventilation systems, $\dot{W}_{comp,j}$ ($kg \cdot s^{-1}$) is the moisture flow between inner wall surface j and room air, $\dot{W}_{in}$ ($kg \cdot s^{-1}$) is the moisture source in the room, $\dot{W}_{vent}$ ($kg \cdot s^{-1}$) is the moisture flow due to ventilation, and $\dot{W}_{HVAC}$ ($kg \cdot s^{-1}$) is the moisture flow due to building ventilation systems. Material properties for the primary insulation materials under investigation are derived from experimental results, while standard properties from the software's database are used for other materials. Specific cases of building design, assembly design, and

boundary conditions, including necessary simplifications and assumptions, are defined for each topic.

By combining experimental data and simulation approaches, this research framework aims to provide a comprehensive understanding of the hygrothermal performance of building insulation materials, particularly non-conventional materials, including bio-based, waste-based, and by-product-based insulation composites. In addition, this approach enables the study of building rehabilitation performance using different insulation solutions in the absence of full-scale testing.

1.2.3. Composite development and characterizations

Another key component of the research framework in this thesis is the development and characterization of insulation composites. The focus is on utilizing low-embodied energy raw materials, with a particular emphasis on bio-based materials, as primary components in the composite development. This approach is complemented by the incorporation of waste-based and by-product-based materials.

In addition to the hygrothermal properties discussed earlier, several other critical characteristics are investigated. These include the chemical composition and additional physical properties of the materials. Fourier transform infrared (FT-IR) spectroscopy and thermogravimetric analysis (TGA) are employed as the primary tools for chemical composition analysis. Where relevant to the intended application, mechanical strength and acoustic performance are also evaluated. Furthermore, a life cycle assessment (LCA) is conducted as part of the thesis to assess the environmental impact of the developed composites.

The choice of tests and methodologies for each research topic is tailored to the specific focus and objectives of the individual study.

1.3. SCOPE AND OBJECTIVE

This thesis aims to advance the development of insulation materials that contribute to sustainable building performance. Based on key strategies identified for sustainable construction and the established research methodology, the research is structured around four primary objectives:

1.3.1. In-depth analysis of bio-based insulation composites

This study investigates the durability and hygrothermal performance of bio-based insulation materials, addressing a critical need for broader application in construction. The research focuses on two categories of bio-based materials: commercially available insulation products (such as cork, hemp, mycelium, and grass-based composites) and agricultural by-products (specifically wheat and barley straws) used as standalone insulation materials. The analysis includes an evaluation of their hygrothermal properties, resistance to mould growth, and susceptibility to mould under various climatic conditions and construction details. Additionally, the potential of boric acid treatment to enhance the durability of straw-based insulation materials is explored.

This scope seeks to fill existing research gaps concerning the hygrothermal properties and performance of non-conventional bio-based insulation materials, particularly regarding mould growth risks and possible treatment methods under diverse environmental conditions.

1.3.2. Development and evaluation of insulation composites from bio-based, waste-based, and by-products

The research aims to bridge the gap between conventional insulation materials and those derived from bio-based, waste-based, and by-product sources. It investigates two insulation applications: rigid insulation boards and lightweight insulation aggregates. The first part of the study proposes replacing high-embodied carbon raw material, ordinary Portland cement (OPC), in wood wool cement boards (WWCB) with fly ash-based geopolymer to create wood wool geopolymer boards (WWGB). The second part explores the potential of substituting commercial wood wool with straw in the production of straw geopolymer boards (SGB). The third part examines the recycling of stone wool to produce alkali-activated lightweight aggregates. The research covers manufacturing methods, design parameters, insulation and mechanical performance, as well as the physical and chemical properties of these materials. A life cycle assessment (LCA) is also conducted, focusing particularly on material replacement, allocation methods, and design parameters in the development of SGB.

This scope aims to address research gaps in the development of sustainable porous insulation materials from low-embodied energy raw materials, providing new insights into their physical and environmental characteristics.

1.3.3. Energy rehabilitation of existing building stocks

This research examines the hygrothermal performance of rehabilitated cavity walls and crawl spaces with limited space, an area requiring further study. The investigation focuses on two rehabilitation strategies: the use of commercially available aerogel composites in cavity walls, and the application of alkali-activated lightweight aggregates made from recycled stone wool as ground cover insulation in crawl spaces. The research includes both the characterization of these composites and the simulation of building performance following rehabilitation.

This scope aims to fill research gaps related to the energy rehabilitation of existing buildings, specifically through the application of different insulation solutions to reduce energy demand and enhance occupant comfort.

1.3.4. Moisture-dependent thermal conductivity

The research proposes a simplified approach for determining the moisture-dependent thermal conductivity of porous insulation materials, which are prone to moisture absorption, leading to increased heat transfer. The proposed solution, which relies on commonly measured and readily available parameters, is derived from existing multiphase models for porous materials. This approach is intended to simplify the typically complex measurement setup and analysis required for determining moisture-dependent thermal conductivity.

This scope aims to address research gaps in the application of effective thermal conductivity for moist porous materials, offering a straightforward predictive model.

1.4. OUTLINE OF THE THESIS

Fig. 1.2 and **Fig. 1.3** provide a visual representation of this thesis's structure. In **CHAPTER 2,** the thermal and hygric properties of four bio-based insulation composites (mycelium, hemp, grass, and cork) are explored. Their hygrothermal performances, including mould growth potential, are simulated and analysed under various climate profiles and typical construction details. **CHAPTER 3** delves into the potential of wheat and barley straws as sustainable alternatives to conventional insulation materials. It also assesses the effectiveness of boric acid as an antifungal treatment for these straws. In **CHAPTER 4**, the focus shifts to the substitution of OPC with geopolymer in the production of wood wool geopolymer boards (WWGB). This chapter provides insights into manufacturing methods, design parameters, and performance characteristics. The composite formulation produced, involving fibre pre-treatment, adjustment of precursor components, and control of activator compositions, is also discussed. **CHAPTER 5** evaluates the environmental and performance implications of using industrial and agricultural by-products as substitutes for raw materials in wood wool cement boards (WWCB). Here, geopolymer replaces OPC, and straws substitute wood wool. The life cycle impacts of these by-products are assessed using both economic and no-allocation methods. **CHAPTER 6** examines the hygrothermal performance of rehabilitated cavity walls in the Netherlands, employing a state-of-the-art aerogel composite. **CHAPTER 7** investigates the high-grade recycling of stone wool from CDW into lightweight insulation aggregates, which are designed for ground cover insulation. It discusses the alkali-activation of various proportions of milled and as-is stone wools to produce these aggregates. **CHAPTER 8** aims to develop a generalized solution for moisture-dependent thermal conductivity in porous material. This solution utilizes readily available parameters and is based on existing multiphase models for porous materials. Finally, **CHAPTER 9** presents the conclusions of this thesis and proposes directions for future research and continuation.

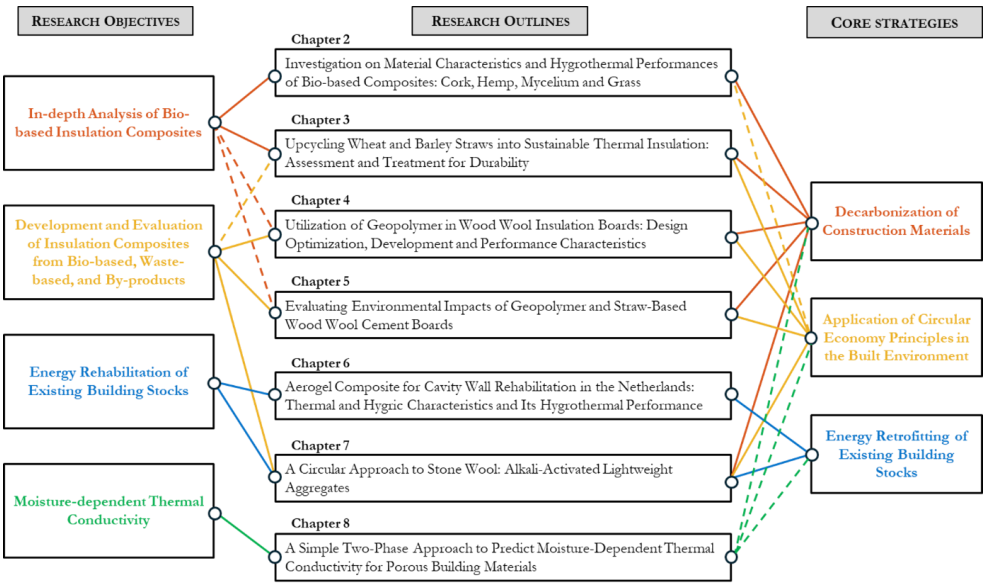

Fig. 1.2 Outline of the thesis.

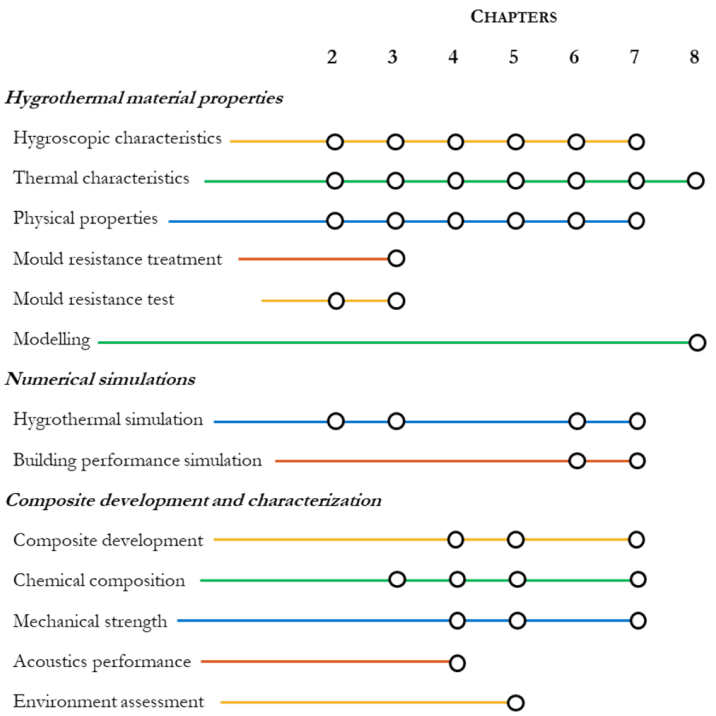

Fig. 1.3 Methodology used in this thesis.

2. INVESTIGATION ON MATERIAL CHARACTERISTICS AND HYGROTHERMAL PERFORMANCES OF BIO-BASED COMPOSITES: CORK, HEMP, MYCELIUM AND GRASS

ABSTRACT

This chapter investigates the thermal and hygric characteristics of four bio-based insulation composites: mycelium, hemp, grass, and cork. Their hygrothermal performances, including the potential for mould growth, are simulated and analysed under various climate profiles and typical construction details. Among the composites, cork exhibits the best hygrothermal performance and is found to be suitable for all investigated climates without any mould growth. This is attributed to its hydrophobic nature and low thermal conductivity. Conversely, the mycelium composite is highly susceptible to mould growth risk. A medium level of risk is observed for both the hemp and grass composites. These findings underscore the importance of selecting appropriate bio-based composites based on the assembly design and local climate conditions.

The results presented in this chapter are published in the following article:

C.H. Koh, F. Gauvin, K. Schollbach and H.J.H. Brouwers, "Investigation of material characteristics and hygrothermal performances of different bio-based insulation composites," Construction and Building Materials 346, 128440 (2022).

2.1. INTRODUCTION

In 2020, the building construction industry was responsible for 37% of global energy-related greenhouse gas (GHG) emissions, with 10% of these emissions resulting from the manufacturing of building construction materials [22]. To decarbonize the global buildings and construction sector, it is crucial to address the embodied energy in building materials and their manufacturing process, in addition to reducing energy demand and decarbonizing power supply [13]. Policies incorporating whole-life carbon have already gained momentum in countries like the Netherlands, Denmark, and France where CO_2 limits are imposed on new buildings. More countries are expected to implement similar policies to achieve overall carbon neutrality [13].

Bio-based building materials, whether wood-based or containing other natural fibres, offer a solution for producing low-carbon materials. These materials generally have lower embodied energy than synthetic materials, can be sourced locally, and have diverse building applications to achieve desired performance characteristics [14]. Plant-based materials such as hemp, expanded cork, straw, and grass are particularly well suited for providing satisfactory thermal insulation performance due to their porous structure and consequently low thermal conductivity, ranging between 0.037 and 0.080 $W \cdot m^{-1} \cdot K^{-1}$ [23]. However, the most frequently used thermal insulation materials in Europe are inorganic mineral fibres, such as glass wool and stone wool, followed by organic fossil fuel-derived foams, such as expanded and extruded polystyrene and polyurethane. All other materials, including plant-derived materials, cover only the remaining 1% of the market [17]. The usage of bio-based insulation materials can potentially result in significant savings on GHG emissions.

The limited usage of bio-based insulation materials can be attributed to their intrinsic hygroscopic nature, their tendency to absorb moisture from their surroundings [15], and associated durability concerns such as mould development under humid environments [16]. Building components containing organic matter are more susceptible to mould infestation than inorganic materials [24]. With the rise of energy-efficient buildings that rely on airtightness and highly insulated envelope design, these buildings tend to have higher indoor humidity, which consequently supports mould germination and growth [25]. Alarmingly, adverse health symptoms associated with exposure to indoor moulds, such as asthma, allergies, and infections, have been studied and established [25]. The use of bio-based materials has provided the optimal medium for fungal proliferation in the built environment. Therefore, it is essential to study the hygroscopic properties and mould growth potential of bio-based insulation materials, along with their hygrothermal performance under different environmental conditions, to overcome these concerns and provide factual guidelines for engineers and architects.

In this chapter, four bio-based insulation composites (cork, grass, hemp, and mycelium) are selected to examine their hygroscopic properties and hygrothermal performances under predefined built environments. These composites are selected based on their low thermal conductivity, low embodied energy, and commercial availability. They are preferrable composed of recycled or waste material. The declared thermal conductivity of these composites is around 0.040 $W \cdot m^{-1} \cdot K^{-1}$, [26, 27, 28, 29], which is in the same range as other conventional building insulation materials [30]. Their embodied energy is considered low since they are made of either agricultural residues or recycled materials and do not require an energy-intensive production process. An exception is made

for the mycelium composite, whose production methods, such as sterilization and inoculation [31], suggest a higher embodied energy than other bio-based materials. However, it is included for its novelty as a sustainable bio-based insulation material.

Several authors have investigated comparable insulation materials. A comprehensive hygrothermal characterization of expanded cork for building facades is provided by Simões et al. [32], where the studied cork boards are observed to have low thermal conductivity ranging from 0.037 to 0.041 $W \cdot m^{-1} \cdot K^{-1}$ with good resistance during long term durability testing. Relevant heat transfer modelling and hygrothermal simulations on the cork boards have also been carried out by the same research group [33, 34] and provide valuable insights into heat and moisture transport phenomena under the simulated built environment. An overview of grass-based composites is presented in [35], showing average thermal conductivities between 0.034 and 0.09 $W \cdot m^{-1} \cdot K^{-1}$, and also highlighting their good sorption desorption capability. For hemp-based composite, Latif et al. [36] and Collet et al. [37] have reported that hemp wools show higher sorption and similar vapour resistance factors as mineral wools. The thermal conductivities of hemp wool are reported between 0.038 and 0.06 $W \cdot m^{-1} \cdot K^{-1}$ [23]. Different mycelium-based composites have also been developed by various research groups, e.g. mycelium-miscanthus composites by Dias et al. [38] with reported thermal conductivities between 0.0882 and 0.104 $W \cdot m^{-1} \cdot K^{-1}$; mycelium-flax, mycelium-hemp and mycelium-straw by Elsacker et al. [31] at 0.0578, 0.0404, 0.0419 $W \cdot m^{-1} \cdot K^{-1}$ respectively; and mycelium bio-foam by Yang et al. [39] from 0.05 to 0.07 $W \cdot m^{-1} \cdot K^{-1}$.

Hygrothermal models are widely used to simulate the coupled heat and moisture transport process for one or multidimensional cases, either taking into account a single building component or a complete building envelope [40]. Material properties are first investigated in the lab and applied as inputs in the hygrothermal simulation tool, together with the other two main inputs, i.e. geometry of the enclosure and boundary conditions. By combining different boundary conditions (e.g. exterior and interior climate) and geometry (design of building components), the hygrothermal performance of different built environments can be simulated and predicted using validated software. In this chapter, European cities representing different climate zones as per Köppen climate classification are selected for the exterior boundary conditions, and the enclosure geometry is modelled one-dimensionally based on typical assembly wall designs found in cold climate zones.

The durability and hygrothermal performance of innovative bio-based insulation materials have not been widely investigated, and many open questions remain regarding efficiency and resistance to mould growth. This comparative study aimed to verify the performance of commercially available and state-of-the-art bio-based insulation material and to aid in the optimal selection and application of these materials under different conditions. The thermal and hygric characteristics of the selected materials are examined and used to simulate their hygrothermal performance under different construction details and various climates in Europe. Mould growth potential is further simulated and compared against laboratory results, to better assess the durability and fungal resistance of these bio-based insulation materials.

2.2. MATERIAL AND METHODOLOGY

2.2.1. Material

The selected bio-based insulation composites, as depicted in **Fig. 2.1**, include: (a) **Mycelium Composite:** this is composed of locally sourced agricultural biomass like straw, miscanthus and flax; the mycelium grows on these materials and acts as a binder; this composite is produced and supplied by Fairm [26]; (b) **Grass Composite:** this is made up of 72% fibres extracted from grass clippings, 20% jute fibres from recycled cocoa and coffee sacks, and 8% polyester binder fibres; these components are bound together through an airlaying and thermobonding process; this composite is produced and supplied by Gramitherm [27]; (c) **Hemp Composite:** this consists of 66% fibres from industrial hemp plants, 22% jute fibres from recycled cocoa and coffee sacks, 8% polymeric support fibres based on recycled polyethylene terephthalate (PET), and 4% soda; this composite is produced and supplied by HempFlax [28]; and (d) **Cork Composite:** this is made of expanded cork, which is created by autoclaving and steam-baking blond cork granules at 350°C; the proejct is formed and bound with its natural resin (suberin) during the heating process; this composite is produced by Amorim PT and supplied by Pro Suber [29].

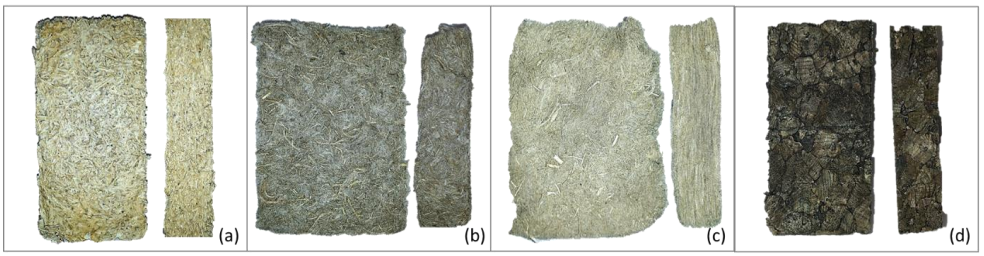

Fig. 2.1 (a) mycelium, (b) grass, (c) hemp, and (d) cork composites.

2.2.2. Characteristics assessment

The total porosity of the samples, which includes both open and closed pores, is calculated from their particle density $\varrho_{particle}$ (kg·m^{-3}) and bulk density ϱ_{bulk} (kg·m^{-3}) using the formula:

$$porosity = 1 - \frac{\rho_{bulk}}{\rho_{particle}} \quad (2\text{-}1)$$

A helium pycnometer (Micromeritics AccuPyc II 1340) is employed to measure their $\varrho_{particle}$.

The sorption isotherms of the insulation materials are obtained through conditioning under aqueous solutions [41]. Initially, the samples are dried in an oven at 50°C until a constant mass is achieved, yielding their dry weight (m_{dry}). These dry samples are then conditioned in desiccators containing various saturated salt solutions, each maintaining a constant relative humidity (RH). The salts used include magnesium chloride hexahydrate ($MgCl_2 \cdot 6H_20$) for 33% RH, potassium carbonate (K_2CO_3) for 43% RH, sodium bromide (NaBr) for 59% RH, sodium chloride (NaCl) for 75% RH, potassium chloride (KCl) for 85% RH, and potassium sulfate (K_2SO_4) for 98% RH. The desiccators are stored in a climatized room at a constant temperature of 20°C. Weighing is

performed at 24-hour intervals, and if five successive weighings show a mass loss change of less than 0.1%, it is assumed that a constant mass (m) has been achieved. For desorption, the same samples are transferred from a higher RH desiccator to a lower RH desiccator, and their equilibrium masses are measured using the same procedure. The equilibrium moisture contents (w in %kg·kg^{-1}) are plotted against RH (%) to obtain both sorption and desorption curves.

Free water saturation (w_{sat}) is approximated by conditioning the specimen at 100% RH, achieved by fully immersing the specimen in water for seven days at room temperature. The surface of the samples is then lightly blotted with a damped sponge to remove excess water, and their weight is measured.

The water vapour diffusion resistance factor (μ) is measured using both the wet cup (water) method and the dry cup (desiccant) method, as per the ASTM E96 standard [42]. The cups are filled with anhydrous calcium chloride ($CaCl_2$) for the dry cup method and distilled water for the wet cup method. Specimens with a thickness (d_μ in m) are attached to the cups with a specific exposed area (A_μ in m^2), and the edges are sealed to block vapour passage at the edge of the specimen. The test cups are kept in a climatized room at 60% RH and 20°C. The change of mass (Δm in kg) at successive times (Δt in s) is measured by weighing the cups to obtain the density of the water vapour transmission rate (g in kg·m^{-2}·s^{-1}) as:

$$g = \frac{1}{A_\mu}\frac{\Delta m}{\Delta t} \tag{2-2}$$

The measurement is considered complete once five successive values of g vary within ± 5%. The value of μ (dimensionless) is then calculated using:

$$\mu = \frac{\Delta p \cdot \delta_{air}}{g \cdot d_\mu} \tag{2-3}$$

where Δp (Pa) is the water vapour partial pressure difference and δ_{air} (kg·m^{-1}·s^{-1}·Pa^{-1}) is the water vapour permeability of air.

The transient line source method is utilized to measure the thermal conductivity (λ in W·m^{-1}·K^{-1}) using a thermal needle probe (AP Isomet model 2104), with a declared accuracy of 5% of the reading plus 0.001 W·m^{-1}·K^{-1}. Samples under three RH conditions (0%, 50% and 80%) are examined for their λ values. The samples are dried at 50°C in an oven (Memmert universal oven UF260) to reach near 0% RH and conditioned in a climate chamber (Memmert climate chamber ICH750) for 50% and 80% RH, all until a constant weight is achieved. The samples are protected using low vapour permeability plastic wrap before and during the λ measurements to maintain their moisture content. The λ measurements are taken at room temperature (20 ± 2°C).

For the specific heat capacity (C_p in J·kg^{-1}·°C^{-1}), differential scanning calorimetry DSC (TA Instruments DSC Q2000) is used at temperatures ranging from -20°C to 50°C at a heating and cooling ramp of 10°C·min^{-1} in a nitrogen atmosphere with a flow of 50 ml·min^{-1}. Three heat-cool cycles are run for each sample, and the C_p value at 20°C from the third heat cycle is taken for

subsequent hygrothermal study. Crushed samples weighing 5-10 mg are prepared for mycelium, hemp, and grass composites, and 3-5 mg for cork composite.

A thermogravimetric analyser (TA Instruments TGA Q500) is further used to investigate the thermal stability of samples from room temperature up to 650°C at a heating rate of 5°C·min^{-1} in a nitrogen atmosphere with a flow of 60 ml·min^{-1} by observing their mass change due to thermal degradation.

2.2.3. Hygrothermal performances assessment

Simulations of heat, air and moisture transport (HAM) are conducted on two distinct wall assemblies exposed to six different exterior climates while maintaining a consistent indoor climate. The annual moisture content of the insulation materials is scrutinized, with particular emphasis on the interfaced layer, that is, the insulation layers adjacent to the exterior and interior. The section in insulation material exhibiting the highest moisture content is further simulated for mould growth risk and compared with laboratory mould growth test results.

For the HAM simulations, one-dimensional non-steady heat and moisture transport processes are solved by coupled differential equations using WUFI Pro software [19]. The heat transport and moisture transport are represented by **Eqs. (1-1)** and **(1-2)**, respectively.

The assembly wall design in this study is based on two common exterior walls found in cold climate zones, namely, masonry wall [43] and timber frame wall [44], both with an air cavity as depicted in **Fig. 2.2**. For comparative study purposes, the insulation layer thicknesses are adjusted to achieve an overall R-value of 4.7 K·m^2·W^{-1} as per the Dutch requirement for an exterior wall in a residential building [45], equivalent to a U-value of 0.205 W·m^{-2}·K^{-1}. Cellulose insulation material is included in the HAM study as the reference material, due to its low embodied energy among other conventional building materials [30]. Material properties of Cellulose and other building components of a masonry wall and timber frame wall (Wood Fibre Board, Gypsum Board, Solid Brick) are listed in **Table A.1**, **Fig. A.1** and **Fig. A.2** (see **Appendix A**). For the masonry wall, 10 cm thick bricks are applied for both exterior and interior sides, with 1.3 cm thick wood-fibre board as an exterior sheathing board, and a 4 cm air cavity with an arbitrary air change rate of 10 h^{-1} (between the 5 and 20 h^{-1} used in [46]). For the timber frame wall, 2 cm spruce wood is applied as exterior cladding, similar to a 4cm fully ventilated air cavity as the brick cavity, with a 1.3 cm thick wood fibre and gypsum board as exterior and interior sheathing boards respectively. Building components outward from the ventilated air layer are set up for their shielding of rain and radiation, and are disregarded from the U-value calculation. The original wall design included a vapor retarder on the interior side. However, given the focus of this study on bio-based materials, it is beneficial to avoid using vapor retarders in such walls, as this allows the materials to naturally absorb and release moisture. The vapor retarder is therefore removed to more accurately study the moisture transport behaviour of the bio-based materials without the influence of a high vapour resistance layer on the interior side.

Six locations in Europe representing different climate zones have been selected for the hygrothermal analysis. **Table B.1** (see **Appendix B**) shows the annual weather summary in all six locations, while **Fig. B.1** (see **Appendix B**) displays the annual air temperature and RH profile

[47]. Climate Cfa is represented by Milan with a humid subtropical climate, Climate Cfb for Eindhoven with a temperate oceanic climate, Climate Cfc for Tórshav with a subpolar oceanic climate, Climate Dfa for Kherson with a hot-summer humid continental climate, Climate Dfb for Oslo with a warm-summer humid continental climate, and Climate Dfc for Sodankylä with subarctic climate. The wall is facing the main driving rain direction (**Table B.1**, see **Appendix B**) for the hygrothermal simulations in all cases. The interior climate is set as per ISO 13788 with humidity class 3 which represents a building with unknown occupancy [48], and a constant air temperature of 20°C. The simulation is run for ten years or until hygrothermal equilibrium is reached, and results from the final year are extracted for further analysis. The boundary and initial conditions are summarized in **Table B.2** (see **Appendix B**).

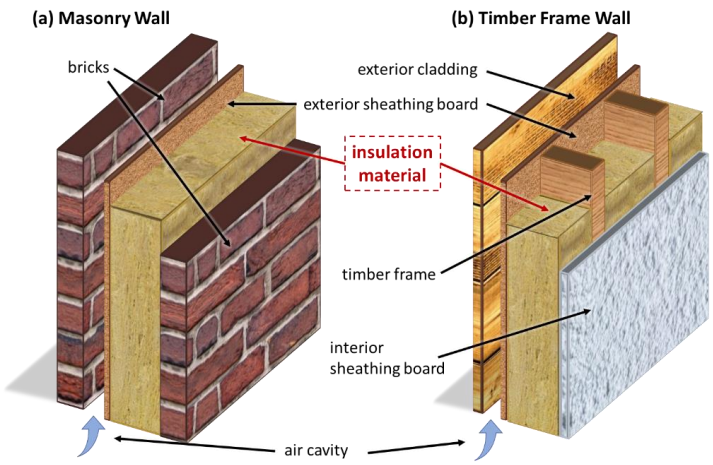

Fig. 2.2 Simulated wall assemblies (a) brick wall and (b) timber frame wall with air cavity.

The monthly transient U-value (U_M) is calculated using the simulated data as follows:

$$U_M = \frac{-Q_M}{\Delta T_M} \tag{2-4}$$

where Q_M is the monthly mean heat flux density through the interior surface on the entire assembly, and ΔT_M is the monthly mean temperature difference between the interior and exterior composite surfaces. The Q_M for each component ($Q_{i,M}$) is calculated as:

$$Q_{i,M} = \frac{1}{R_i}\Delta T_{i,M} \tag{2-5}$$

where R_i is thermal resistance of individual component, and $\Delta T_{i,M}$ is the monthly mean temperature difference between the surfaces of the component.

2.2.4. Mould growth assessment

Mould growth tests on specimens are conducted in accordance with the European Assessment Document EAD 040005-00-1201 Annex B [49]. Test samples are subjected to a high humidity environment (nearly 100% RH) for a duration of four weeks at a steady temperature of 20°C. This is achieved using a desiccator filled with water at the bottom. Following this period, the specimens undergo visual inspection for the presence of mould fungus, both with the naked eye and under a microscope (ZEISS Axio Imager 2), as per ISO 846 [50].

Further investigation of the wall assemblies is carried out to assess the risk of mould growth under selected climates. This is done using the WUFI Bio software, which is based on the bio-hygrothermal model developed by Sedbauer et al. [51]. The software utilizes a germination isopleth, which plots the times required for germination in a temperature-humidity diagram. By modelling the critical water content of potential mould spores, it can predict germination and mould growth if the water content in the model spore surpasses the critical level. All samples in this study are assumed to belong to substrate class I, i.e. bio-utilizable substrates.

However, this bio-hygrothermal model does not account for biogenic factors, pH value, surface quality, and several other influential factors that could hinder germination and growth [20]. As a result, the simulation results obtained tend to be conservative, indicating a higher risk of mould growth than in actual conditions. Therefore, these simulation results are evaluated in conjunction with the results from the aforementioned laboratory mould growth test.

2.3. RESULTS AND DISCUSSION

2.3.1. Characteristics assessment

As depicted in **Table 2.1**, all four insulation samples under study exhibit low bulk density and high porosity. The grass and hemp composites primarily comprise loosely interwoven cellulose fibres with open porosity, demonstrating similar porosity levels at 96.5% and 96.3% respectively. The mycelium composite, on the other hand, consists of fibres (a mix of straw, miscanthus and flax) enveloped by mycelium ligaments. This composite presents a denser and more homogenous surface coverage, with macroporous structures following the fibre packing remaining inside the block, resulting in a porosity of 94.4%. The cork composite, with the lowest porosity at 87.4%, contains both closed and open pores. The closed pore structures originated from their stacked hexagonal cells microstructure [52], while the macro open pores form during the expanded cork manufacturing process.

The hemp, grass, and mycelium composites exhibit hydrophilic behaviour and have similar adsorption-desorption curves as shown in **Fig. 2.3**. They can absorb up to eight or nine times their weight of water under the full water immersion test (**Table 2.1**). Conversely, the cork composite has lower adsorption despite its porous structures, attributed to the hydrophobic nature of the cork surface with low water wettability. It is noteworthy that the mycelium specimen (all three samples) under 98% RH reached maximum mass gain around the seventh day in the sorption test, after which it underwent mass loss and showed signs of mould growth on the surface. As a result,

maximum mass gain, instead of equilibrium mass, is used to calculate the equilibrium moisture content at 98% RH as shown in **Fig. 2.3**. The equilibrium moisture content under the desorption process is only slightly higher than the adsorption process, with no significant variation between both curves for all samples.

Table 2.1 Density, Porosity, Specific Heat Capacity, Water Vapour Resistance Factor and Free Water Saturation for mycelium, hemp, grass, and cork composites.

	Mycelium	**Hemp**	**Grass**	**Cork**
Bulk Density ϱ_{bulk}, dried (kg·m^{-3})	97.1	64.1	60.1	97.9
Particle Density $\varrho_{partocle}$ (kg·m^{-3})	1732.1	1747.3	1737.6	778.4
Porosity (%)	94.4	96.3	96.5	87.4
Specific Heat Capacity C_p (J·kg^{-1}·K^{-1})	1167	1140	1110	1160
Water Vapour Resistance Factor μ				
"Dry cup" condition (dimensionless)	3.4	3.0	2.9	9.7
"Wet cup" condition (dimensionless)	3.2	2.6	2.6	13.9
Free Water Saturation w_{sat} (%)	816%	889%	910%	117%

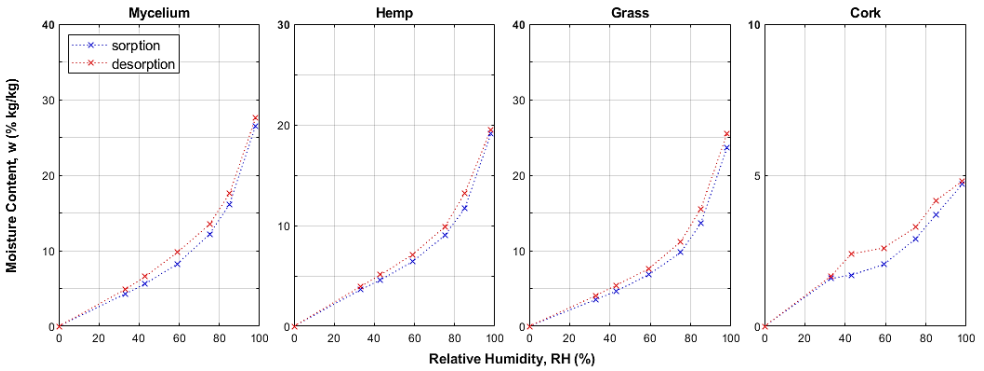

Fig. 2.3 Sorption-desorption curves with Moisture Content w plotted against RH for mycelium, hemp, grass, and cork composites. For Moisture Content at 100% RH, refer to wsat in **Table 2.1**.

The water permeability of the specimen is listed in **Table 2.1**. The hemp, grass, and mycelium composites have a similar μ-factor around 3 under both dry and wet cup methods, with lower permeability at 10 (dry cup) and 14 (wet cup) for the cork composite.

Typically, the water vapor diffusion resistance factor based on the dry-cup method is higher than that based on the wet-cup method. Under the wet-cup method, the higher RH induces surface diffusion [53] within the open pores of the specimen. A thin water film forms on the pore walls, flowing from regions of thicker film (higher RH) to thinner film (lower RH). In isothermal conditions, both vapor diffusion and surface diffusion occur in the same direction under the wet-cup method. When these phenomena are not separated, a lower apparent diffusion resistance is observed. This trend is evident in the measurement results for mycelium, hemp, and grass

composites, where the dry-cup value is higher than the wet-cup value. However, cork composite exhibits an opposite trend, showing a higher diffusion resistance under the wet-cup method. This behaviour could be attributed to the swelling and shrinking effects of the closed pore structure within expanded cork at different RH conditions. Under high RH, the swelling of the closed-cell structure reduces the open pores of the cork composite, thereby increasing the diffusion resistance. This swelling effect outweighs the surface diffusion phenomenon in expanded cork, resulting in a higher apparent diffusion resistance under the wet-cup method compared to the dry-cup method.

Fig. 2.4 summarizes the moisture-dependent thermal conductivity for all samples acclimatised to 0%, 50% and 80% RH, showing an increase in thermal conductivity with higher RH, except for the cork composite, which can be attributed to its hydrophobic surface. Although a generally linear relationship between thermal conductivity and moisture content of organic insulation materials is not typically observed, a simple linear fitting is nonetheless included in this study as input for subsequent hygrothermal simulation. In addition, uncertainties of 0.002 to 0.003 $W \cdot m^{-1} \cdot K^{-1}$ are presented in the measured thermal conductivities using the thermal needle probe. The grass composite has the lowest thermal conductivity, 0.045 ± 0.003 $W \cdot m^{-1} \cdot K^{-1}$ at 0% RH, and the cork composite exhibits an overall better thermal conductivity characteristic with a uniform 0.046 ± 0.003 $W \cdot m^{-1} \cdot K^{-1}$ under different RH. This is followed by the hemp and mycelium composite at 0.050 ± 0.004 and 0.051 ± 0.004 $W \cdot m^{-1} \cdot K^{-1}$ respectively. It should be noted that the declared thermal conductivity from the manufacturer of cork, grass and hemp composites is lower than the measurements in this study, i.e. 0.039, 0.040 and 0.040 $W \cdot m^{-1} \cdot K^{-1}$ respectively. The measured thermal conductivities are close to or within the range of other reported measurements, i.e. 0.037 to 0.041 $W \cdot m^{-1} \cdot K^{-1}$ for cork composite [32], 0.034 to 0.09 $W \cdot m^{-1} \cdot K^{-1}$ for grass composite [35], 0.038 and 0.06 $W \cdot m^{-1} \cdot K^{-1}$ for hemp composite [23], and 0.0404 to 0.0578 $W \cdot m^{-1} \cdot K^{-1}$ for mycelium composite [31].

The specific heat capacity (c_p) of all four samples falls within the range of 1100 to 1200 $J \cdot kg^{-1} \cdot °C^{-1}$ as listed in **Table 2.1** and **Fig. 2.5**.

Thermogravimetric analysis of the samples, as shown in **Fig. 2.6**, reveals that all four samples are thermally stable up to about 200°C, after which they start to decompose and reach their maximum rate of weight loss between 300 and 350°C. Therefore, it is necessary to protect these insulation composites from fire hazards with other fire and heat-resistant components, such as bricks and sheathing boards. The decomposition process of the samples follows a similar trend, corresponding to hemicelluloses being pyrolyzed in the range of 200 and 300°C, depolymerized cellulose in the range of 300 and 350°C, and lignin components pyrolyzed in the range of 225 and 450°C [54]. For the cork composite, depolymerization of suberin occurs between 400 and 500°C [55]. The second peak at 400°C is also observed on the grass composite, contributed by other recycled materials mixed in the composite. A similar small peak can be noticed for the hemp composite where recycled materials are also used. All composites end their volatile emissions at around 450°C with a remaining char residue of around 20 to 30% of the original dry weight.

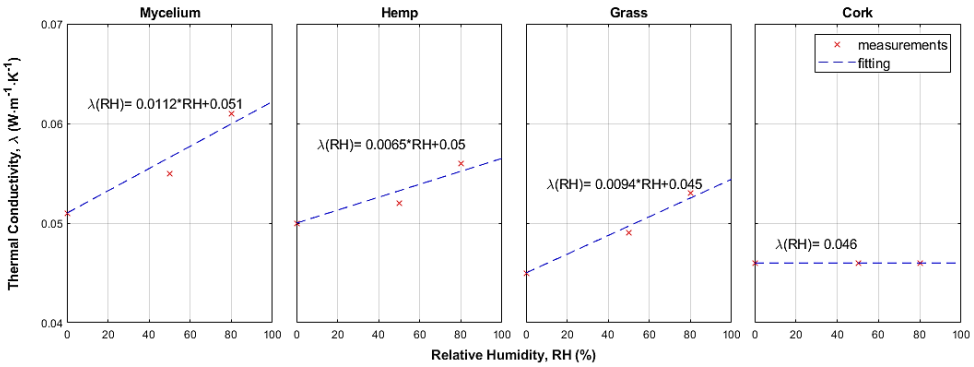

Fig. 2.4 Thermal Conductivity λ against RH for mycelium, hemp, grass, and cork composites.

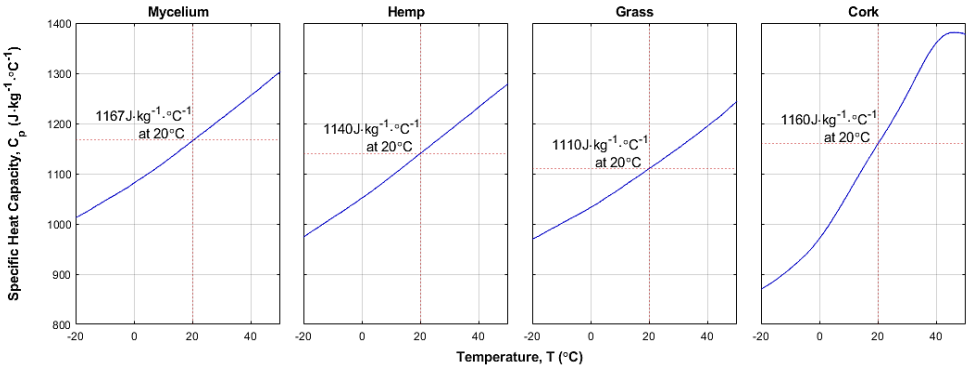

Fig. 2.5 Specific heat capacity C_p against Temperature T for mycelium, hemp, grass, and cork composites.

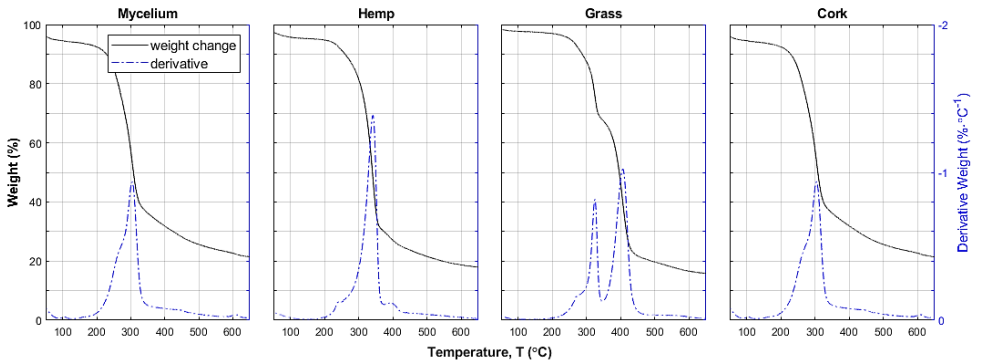

Fig. 2.6 Thermal stability against temperature T for mycelium, hemp, grass, and cork composites.

2.3.2. Hygrothermal performances assessment

The thermal conductivity findings in **Fig. 2.4** inform the insulation thickness for both wall types (**Fig. 2.2**) and all four studied insulation materials. These are designed to achieve an overall R-value

of 4.7 $K \cdot m^2 \cdot W^{-1}$, as per the Dutch requirement for an exterior wall in a residential building [45], equivalent to a U-value of 0.205 $W \cdot m^{-2} \cdot K^{-1}$. The required thicknesses are listed in **Table 2.2**. It is evident that all four materials necessitate a higher wall thickness compared to the reference Cellulose insulation material.

Table 2.2 Insulation thickness and total wall thickness (in bracket) for simulation.

	Mycelium	**Hemp**	**Grass**	**Cork**	**Cellulose (reference)**
Brick Wall (mm)	209.5 (463)	202.6 (456)	184.6 (438)	184.8 (438)	160.6 (414)
Timber Frame Wall (mm)	209.3 (295)	202.4 (288)	184.4 (270)	184.7 (271)	160.5 (247)

The transient thermal transmittance U-value of the investigated insulation materials, under two different wall types and six different climates, is explored and summarized in **Fig. 2.7**. Only transient U-values in the 'heating period' from October to March are included, as the U-value under warmer months would yield non-sensible results and is not of interest in this study.

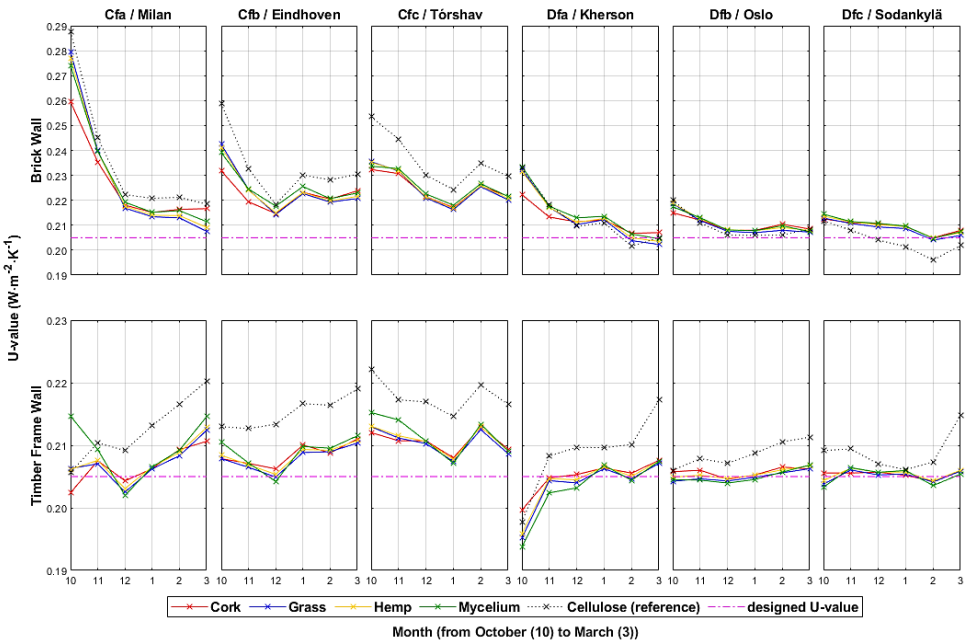

Fig. 2.7 Transient thermal transmittance (U-value) for mycelium, hemp, grass, and cork composites in the heating period (October to March) under different wall assembly types and climates/locations.

In general, all four insulation materials exhibit similar trends of transient U-value under the same climate and wall type. However, they diverge significantly when compared across different climates or wall types of the same material. Under continental climate Dfa (Kherson), Dfb (Oslo) and Dfc (Sodanskylä), the insulated walls provide uniform thermal insulation performance close to the designed U-value at 0.205 $W \cdot m^{-2} \cdot K^{-1}$ in the heating period. However, higher transient U-values are

observed on the walls under temperate climates Cfa (Milan), Cfb (Eindhoven) and Cfc (Tórshav), aligning with their milder and wetter climate profiles. Overall, the insulated timber frame walls outperform the brick walls, particularly under temperature climates, when a similar initial designed U-value is set for all cases. This is due to the thicker and denser brick layers (**Table A.1**, see **Appendix A**) which impede the moisture transport in the wall assemblies, leading to higher moisture accumulation in the insulation material. This pattern underscores the pivotal role of exterior climates and the type of building envelope design in evaluating building insulation performance, particularly when considering a similar category of insulation materials, in this case, the bio-based insulation materials.

Without considering durability aspects from potential deterioration due to mould growth under a humid environment, or disregarding overall wall thickness due to the thickness of the insulation layer required for the intended U-value, there is no specific material to recommend based on their transient U-value performance. However, when the wall thickness is a consideration, the cork composite, with its less demanding thickness requirement, is the preferred choice compared to other investigated bio-based materials, followed by the grass composites.

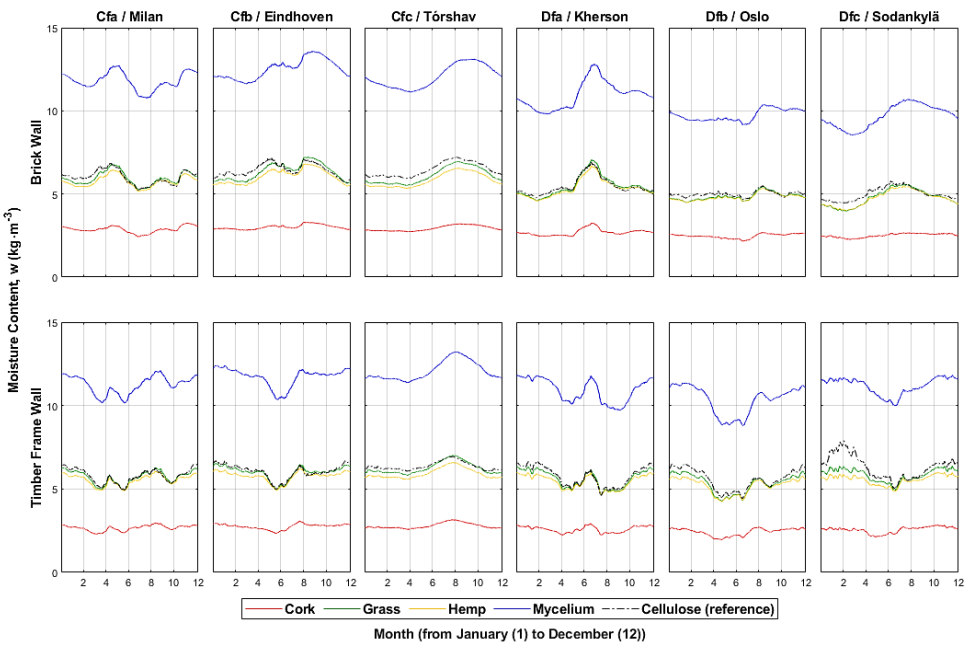

Fig. 2.8 Moisture Content w for mycelium, hemp, grass and cork composites under different wall assembly types, climates/locations, and months.

Fig. 2.8 shows the equilibrium moisture content in the investigated bio-based insulation composites under two different wall types and six different climates in a simulated year. The mycelium composite exhibits the highest moisture content under all climates and wall types, while the cork composite displays the lowest and most regulated moisture content throughout the year. Both grass and hemp composites show similar moisture content to the reference cellulose insulation material. These dynamic moisture content of the composites align with their sorption

isotherm, i.e. the higher sorption capacity of the mycelium composite and the opposite for the cork composite (**Fig. 2.3**).

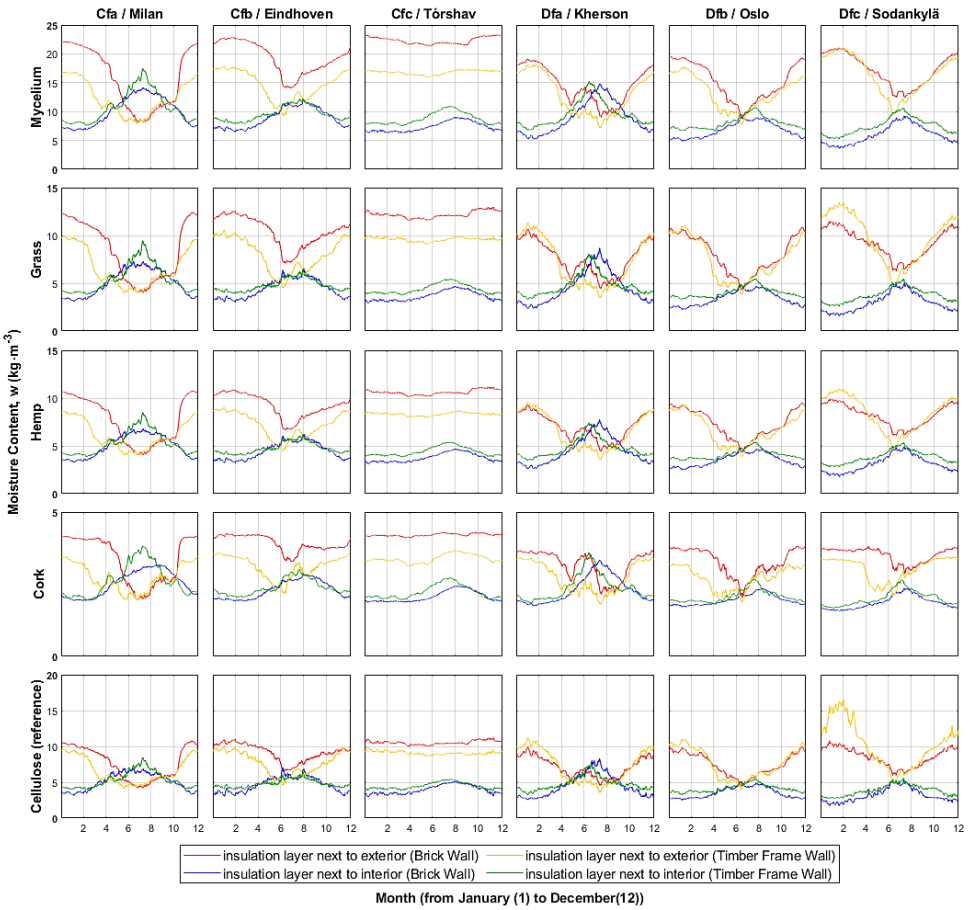

Fig. 2.9 Moisture Content w at insulation layer next to the exterior and next to the interior under different wall assembly types, climates/locations, and months.

Higher moisture content in an insulation layer is typically found at the near-interfaced layers. In the case of the selected wall type and climates, these are either at layers next to the exterior sheathing board or behind the interior sheathing board. The moisture content of both interfaced layers in a simulated year is extracted and presented in **Fig. 2.9**. A few observations can be generalized based on the climate types: for Cfa (Milan) and Dfa (Kherson), moisture tends to accumulate at the exterior interface during the winter period and interior interface during the summer period; for Cfb (Eindhoven), Dfb (Oslo) and Dfc (Sodanskylä), moisture accumulation is generally found on the exterior interface during the winter period, and while the moisture content is increasing on the interior interface during summertime, it is still not exceeding that of the exterior side; and for Cfc (Tórshav), the moisture content at the exterior interface is always higher than the interior interface. It can be established that the insulation layer at the exterior interface has the highest averaged

moisture content under all six climates, and consequently is most likely subjected to mould growth and degradation compared to other parts of insulation under different climate conditions.

In terms of wall type, insulation materials inside the timber frame walls generally have lower moisture content at the exterior interface than those inside brick walls across different climates except Dfc (Sodanskylä). The opposite trend is observed at the interior interface where the insulation layer in timber frame walls has higher moisture content compared to brick walls. It should be noted that no vapour retarder is included in the design of all simulated walls to retard the vapour diffusion process, and a ventilated air cavity is included in all cases to provide additional hygrothermal regulation to the overall wall assembly.

2.3.3. Mould growth assessment

After a four-week exposure to high humidity in a water-filled desiccator, the test specimen undergoes visual inspection for mould presence, both with the naked eye and under a microscope. **Fig. 2.10** presents photos of the specimen, both with and without high-humidity conditioning. The fungal growth on the test specimen is evaluated according to ISO 846 [50], and the intensity scales of mould growth are assigned as per **Table 2.3**.

Significant mould growth and degradation are found on the mycelium composite. It is worth noting that mould growth was already detected on the mycelium composite conditioned under 98% RH in the sorption test. Discolouring on the hemp composite is discernible to the naked eye, and fungi are easily identifiable under the microscope. For the grass composite, no evident mould growth or discolouring is observed with the naked eye; however, fibre deterioration is noticeable under the microscope. The cork composite shows no apparent deterioration, mould growth or discolouring. These results align with the literature: similar mould development can be distinguished with the naked eye on the mycelium-miscanthus test sample by Dias et al. [38]; fungi contamination can be observed under a microscope on hemp shiv composites by Viel et al. [56]; on the other hand, mould development on grass and cork composite is not presented in the literature.

The mould growth risk of the wall assemblies under the selected climates is further simulated, with the results shown in **Fig. 2.11**. The insulation layer, composed of any of the four composites under temperate climates Cfa, Cfb and Cfc in masonry walls, is predicted to have heavy mould growth with a mould index above 3. For timber frame walls, a high mould index is predicted for the mycelium, hemp, and grass composites only under Cfc climate, and medium mould growth potential for the grass composite under Cfb climate. Under continental climates Dfa, Dfb and Dfc, low mould growth potential is predicted for both wall designs and all four composites. Overall, a lower mould growth risk is predicted for timber frame walls compared to brick walls.

Fig. 2.10 Mould evaluation test (1) mycelium, (2) hemp, (3) grass and (4) cork composites. For the subset, (a) and (c) are samples without conditioning, (b) and (d) are samples conditioned under high RH.

Table 2.3 Assessment of mould growth.

Composites	Intensity	Evaluation
Mycelium	5	heavy growth, covering the entire test surface
Hemp	3	growth visible to the naked eye, covering up to 50% of the test surface
Grass	1	no growth is visible to the naked eye, but visible under the microscope
Cork	0	no growth is apparent under the microscope

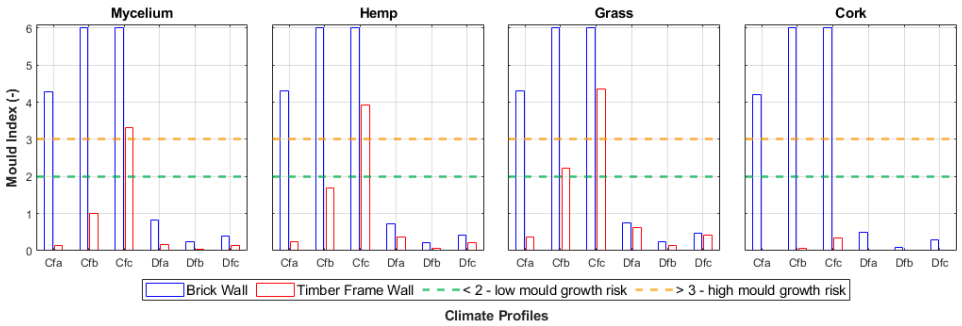

Fig. 2.11 Predicted Mould Index for mycelium, hemp, grass and cork composites under different wall assembly types and climates/locations.

2.4. CONCLUSIONS AND RECOMMENDATIONS

This chapter delves into the thermal and hygric attributes of selected bio-based composites, specifically mycelium, hemp, grass, and cork composites. It further simulates their hygrothermal performances in relation to two construction details across six distinct European climates.

Among the four composites under investigation, the cork composite stands out with the lowest thermal conductivity, minimal sorption properties, and no risk of mould growth. The hemp, grass, and mycelium composites exhibit similar hygric properties and show signs of deterioration under laboratory mould growth tests. The mycelium composite, in particular, demonstrated the least favourable characteristics and performance, possessing the highest thermal conductivity and a vulnerability to mould growth in humid environments. Compared to the reference material, cellulose, both the hemp and grass composites follow a similar pattern, while the cork composite outperforms them all in terms of thermal and hygric properties

In practical building applications, exterior climates and wall designs are pivotal in determining the hygrothermal performances of insulation material. The study finds that a simulated timber frame wall with a fully ventilated cavity is more suitable for low-density bio-based insulation materials compared to a fully ventilated brick wall. Moreover, the potential for mould growth in the studied insulation materials is higher under temperate climates (Cfa, Cfb and Cfc) when compared to continental climates (Dfa, Dfb and Dfc).

The findings of this chapter underscore the appropriateness of using different bio-based composites based on the assembly design and local climate conditions. They also provide a guideline for selecting the correct insulation material considering the geometry of the enclosure and boundary conditions.

By integrating the results of mould growth laboratory testing and hygrothermal simulations, the study offers the following recommendations for applying the studied bio-based composites as thermal insulation materials:

1. Mycelium composite is not recommended for use under temperate climates (Cfa, Cfb and Cfc). It is also unsuitable for any built environment with high humidity conditions (>80% RH) due to its susceptibility to rapid mould growth. Ensuring the airtightness of wall construction is crucial to prevent direct water exposure or high humidity conditions.
2. Hemp and grass composites are not advised for use under temperate climates (Cfa, Cfb and Cfc). Similar to mycelium composite, airtightness of wall construction is necessary to avoid direct water exposure or high humidity conditions.
3. Cork composite is suitable for use under the investigated temperate and continental climates, whether as exposed or covered components.
4. Timber frame walls are more compatible with low-density bio-based insulation material compared to brick walls.

3. UPCYCLING WHEAT AND BARLEY STRAWS INTO SUSTAINABLE THERMAL INSULATION: ASSESSMENT AND TREATMENT FOR DURABILITY

ABSTRACT

This chapter investigates the potential of wheat and barley straws as sustainable alternatives to conventional insulation materials. The focus is on evaluating the risk of mould growth in straw-filled wall assemblies across different climate types, while comparing the physical, thermal, hygroscopic, and durability properties of wheat and barley straws. Additionally, the effectiveness of boric acid as an antifungal treatment on straws is assessed. The findings reveal that both barley and wheat straws exhibit low thermal conductivity, ranging from 45 and 65 $mW \cdot m^{-1} \cdot K^{-1}$ for bulk density of 60 to 100 $kg \cdot m^{-3}$. Notably, barley straws demonstrate lower sorption capacity, higher vapour diffusion, lower thermal conductivity, and reduced mould growth intensity, rendering them more suitable as insulation material. The application of boric acid treatment effectively enhances the mould resistance of straws without adversely affecting their hygric and thermal properties. Consequently, boric acid treatment is recommended for wheat straw under unfavourable climatic conditions.

The results presented in this chapter are published in the following article:

C.H. Koh, F. Gauvin, K. Schollbach and H.J.H. Brouwers, "Upcycling wheat and barley straws into sustainable thermal insulation: Assessment and treatment for durability," Resources, Conservation and Recycling 198, 107161 (2023).

3.1. INTRODUCTION

Straws, the leftover stalks of cereal plants, are a by-product of crop production. They have been upcycled as building materials, used as bedding for livestock, utilized as biomass for energy generation and animal feed, as well as burned or ploughed back into soils [57, 58]. Of all crops grown in the world, wheat and barley are ranked third and twelfth by production volume; the annual production in 2019 is estimated at 764 and 159 million tonnes respectively [59]. As a by-product, approximately 1.5 tonnes of straws can be obtained for every ton of cereal production [57].

Straws are an abundant, sustainable, and cost-effective source of low-embodied carbon raw materials. Utilizing straws as a building material presents a viable low-carbon alternative to high embodied energy materials currently available in the market. By and large, straws are used for thermal insulation purposes [58], and can be incorporated as a load-bearing strawbale wall or as infill in post-and-beam structures in buildings [60, 61, 62]. To optimize their use as insulation material, it is essential to assess the hygrothermal and durability performance of various straw types in different climates and develop strategies to enhance their resource efficiency.

Wheat and barley are under the same *Poaceae* family but in different genera: *Triticum* for wheat and *Hordeum* for barley, hence physical differences between wheat [63, 64] and barley straws [64, 65, 66] are presented. These physical variances could impact their thermal and hygric behaviours and influence their suitability as insulation material. For instance, different sorption isotherms have been measured between wheat [63, 64, 67, 68] and barley straws [64, 66, 69], where their microstructure could play a determinative role in this regard. On the other hand, no notable deviation of thermal conductivity between different types of straws is established, with measurements between 40 and 80 $mW \cdot m^{-1} \cdot K^{-1}$ under bulk density between 60 to 120 $kg \cdot m^{-3}$ reported in different studies [58].

Straws, like other natural bio-based materials [70], are prone to mould growth when exposed to humid environments, leading to deterioration. The well-established negative health effects of indoor moulds [71, 72, 73] necessitate the prevention of straw becoming a source of fungal proliferation. Freshly harvested wheat and barley straws are naturally contaminated with several fungi species such as *Aspergillus* and *Penicillium spp.* from soil [74], and generally, straws are dried and applied directly, without treatment as building materials. A prior hygrothermal study on strawbale buildings reveals that there is a potential risk of mould growth on straws under unfavourable construction designs and local climates [75]. Conversely, mould growth on straws used for insulation is seldom reported [58]. A few observations however are described on fresh straw samples: mould is detected on a wheat straw sample [76], at the inner cell wall of a barley straw sample [64], and on a rice straw sample [77]. These findings highlight the need to address the mould growth risk on straws and emphasize the necessity of knowledge to ensure safe application. Several strategies can be employed, such as selecting a suitable straw type with higher mould resistance or applying a non-toxic antifungal treatment on straws to minimize the risk.

In terms of composition, wheat and barley straws are similar, but the average ratio of lignin to cellulose-hemicelluloses is lower in wheat straw than in barley straw, at 0.20 and 0.23, respectively [78]. The higher content of lignin in barley straw protects the cellulose and hemicellulose more

effectively from glycoside hydrolases from fungi, thus delaying their degradation into simple sugars that could enhance mould growth [79]. In addition, barley straw has a higher percentage of wax [78] , which provides a protective surface layer [80] and acts as the first barrier against any fungal attack. Both factors, i.e., higher ratios of lignin and wax against cellulose-hemicellulose, suggest that barley straw is more resistant to mould growth than wheat straw. However, limited information is available in the literature, and a comparative study between wheat and barley straws is necessary to determine which is more effective as an insulation material.

Irrespective of the straw type, antifungal treatment is a feasible approach to enhance the durability of straws. Boric acid and its sodium borate salts, which are relatively inexpensive and non-toxic, can be utilized to impede fungal growth by obstructing their reproductive process [81, 82]. Wood preservation is a common application of boric acid against wood-decaying fungi [83, 84], with higher effectiveness against brown rot fungi than white rot fungi [84]. Positive results have also been demonstrated using boric acid or borate compounds on other bio-based building materials, for example, on corn pith composites [85], wood composites [86] and cellulose insulation [87]. However, the effectiveness of boric acid on wheat and barley straws against fungi is yet to be established.

This chapter aims to address research gaps concerning the use of two commonly available straw types, namely wheat and barley straws, as thermal insulation materials. The straw types are selected based on their status as the top two grain crops produced in the Netherlands and their frequent utilization as building materials compared to other crops. The study seeks to investigate their hygrothermal properties, mould growth resistance, mould growth risk in different climates, and the effectiveness of applying boric acid treatment to enhance their durability. The findings of this chapter will provide insights into the most suitable straw type for thermal insulation and assess the feasibility of using boric acid as an antifungal treatment to improve the durability of straws.

3.2. MATERIAL AND METHODOLOGY

The material properties and hygrothermal performance of wheat and barley straws are assessed following the methodology illustrated in **Fig. 3.1**. The mould growth risk of a wall assembly with straw infill under different climate types is modelled using computer simulation. In addition, laboratory experiments are conducted to evaluate material properties, anti-fungal treatment efficacy, and mould resistance.

3.2.1. Simulation setup

This study conducts Heat, Air, and Moisture Transport (HAM) simulations for a wall assembly that includes straws as insulation material and is exposed to twenty-two different exterior climates (**Fig. 3.1a**). The analysis focuses on the annual moisture content of the insulation material, with a special emphasis on the interfaced straw layers next to the exterior and interior sides. The interfaced layers are then simulated further for mould growth risk.

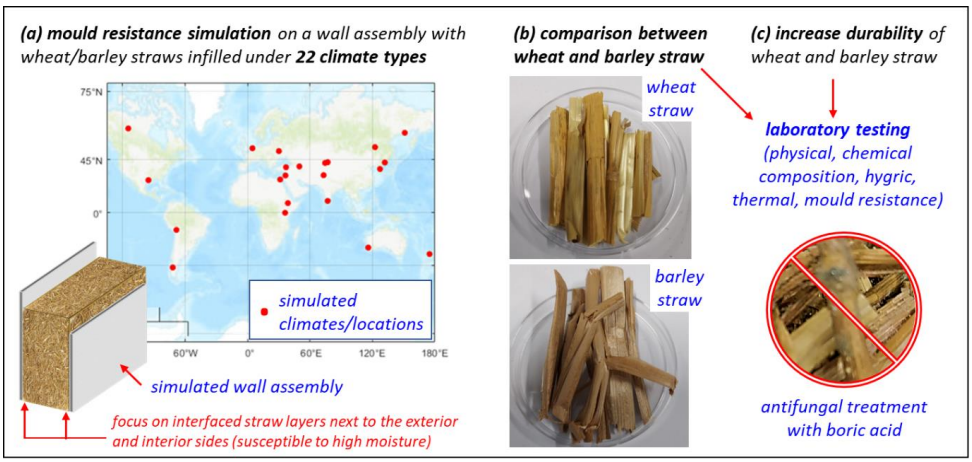

Fig. 3.1 Methodology.

Non-steady heat and moisture transport processes are solved by coupled differential equations using the software WUFI Pro 6.6 [19], i.e. heat transport and moisture transport by **Eqs. (1-1)** and **(1-2)**, respectively.

The mould growth risk is examined using the software WUFI Bio 4.0, which employs the bio-hygrothermal model developed by Sedbauer et al. [51]. By plotting the germination times in a temperature-humidity diagram and modelling the critical water content of mould spores, the germination and mould growth can be predicted if the water content in the model spore exceeds the critical water content. The substrate class I, i.e. bio-utilizable substrates, is assumed for all samples in this research.

For the hygrothermal analysis, this study has carefully selected twenty-two locations that represent distinct climate zones based on the Köppen climate classification. These locations encompass a wide range of transient boundary conditions, effectively capturing the major climate variations. Furthermore, only cities situated in countries that locally produce wheat and barley crops have been included in the analysis. **Table B.3** (see **Appendix B**) summarizes the annual weather conditions [47] and the annual wheat and barley crop yields in their respective countries [59] for all twenty-two locations.

The assembly wall design [88, 60] consists of a 50 cm thick straw layer that is covered with 3 cm lime plasters on both the exterior and interior sides, with material properties listed in **Table A.2** and **Fig. A.3** (see **Appendix A**). The wall faces the main driving rain direction in all cases. The interior climate is set according to ISO 13788, with humidity class 3, which represents a building with unknown occupancy [48], and a constant air temperature of 20°C. The simulation runs for ten years or until hygrothermal equilibrium is achieved, and the results from the final year are extracted for further analysis. The boundary and initial conditions are summarized in **Table B.4** (see **Appendix B**).

3.2.2. Material

The wheat and barley straws used in the study were obtained from local sources in the Netherlands, provided by Strobouwer, Haaren. To prepare the samples, the straws were chopped into smaller pieces measuring 6 ± 4 cm in length, as shown in **Fig. 3.1b**. While the barley straw consists solely of stalks, the wheat straw contains about 10% spikes and leaves. However, for comparative analysis, the leaves and spikes were removed from the wheat straw samples used in this study.

An aqueous solution of boric acid, $B(OH)_3$, at a concentration of 4 %w/w (referred to as BA) is used as an antifungal agent, which is within the concentration limit of 5.5 %w/w set by the European regulation [89]. For antifungal treatment, the outer surface of the straws is sprayed with the BA solution and manually mixed to create an almost uniform surface coating. The amount of BA present in each specimen is 9 ± 1% by weight of the dry straw.

Samples with five different bulk densities, denoted by ϱ_{bulk} (60, 70, 80, 90, 100 $kg \cdot m^{-3}$), are prepared for measuring thermal conductivity and vapour diffusion resistance. The bulk densities are controlled by adjusting the weight of the straws (± 0.1 g) in fixed-volume containers.

3.2.3. Characteristics assessment

For microstructure observation, the surface and cross-section of the straws are visually inspected with an optical microscope (ZEISS Axio Imager 2) and a scanning electron microscope SEM (Phenom ProX).

The particle density $\varrho_{particle}$ ($kg \cdot m^{-3}$) of the straws is measured using a helium pycnometer (Micromeritics AccuPyc II 1340) with a 10 cm^3 cup. The porosity φ (%) of the specimen is calculated from their $\varrho_{particle}$ and ϱ_{bulk} ($kg \cdot m^{-3}$) following **Eq. (2.1)**. The pycnometer has an accuracy of 0.03% in reading plus 0.03% of sample capacity.

The water contact angle (°) of the surface of the straws is measured using a contact angle system (Dataphysics OCA30) for its hydrophobicity. The apparatus has an accuracy of 0.1° reading.

Fourier transform-infrared FT-IR spectroscopy aligned with attenuated total reflection ATR attachment (PerkinElmer Frontier FT-IR) is utilized to analyse the chemical composition of the straws. The major components in both wheat and barley straws [90, 91] are polysaccharides (cellulose, hemicellulose, lignin) which cannot be easily distinguished using individual IR bands. It is, however, possible to use certain bands that can be assigned to specific components for identification and use the relative intensity of each band as an approximation proportion of those components in a sample [92]. The selected components and bands are listed in **Table 3.1**.

The sorption isotherms of the straws are measured using the gravimetric sorption technique through dynamic vapour sorption (DVS) (Surface Measurement Systems DVS Resolution). The specimen is conditioned in the relative humidity RH environment between 0% and 95% RH. The weight of the specimen is measured at a 10% RH increment step for the sorption curve, and at a 10% decrement step for the desorption curve, all under a constant temperature of 20°C. The specimen is considered to reach its constant mass once the rate of mass change dw/dt

(%kg·kg^{-1}·min^{-1}) is equal to or less than 0.01. The DVS apparatus has a declared accuracy of 0.5% RH reading and a balance noise of less than 0.3 μg.

Table 3.1 The selected ATR FT-IR bands for the chemical composition in straws.

To represent	With selected bands	Ref	Representative ratios
Cellulose	C-C ring breathing band at 1155 cm^{-1}	[92]	As denominator
	C-O-C glycosidic ether band at 1105 cm^{-1}		
Lignin	C=C in-plane aromatic vibrations at 1505 cm^{-1}	[92]	I_{1505}/I_{1155}, I_{1505}/I_{1105}
	C=C in-plane aromatic vibrations at 1595 cm^{-1}		I_{1595}/I_{1155}, I_{1595}/I_{1105}
Wax	C=O ester band at 1735 cm^{-1}	[91, 93]	I_{1735}/I_{1155}, I_{1735}/I_{1105}
	CH_2 asymmetric stretching at 2918 cm^{-1}	[94, 95]	I_{2918}/I_{1155}, I_{2918}/I_{1105}

The vapour diffusion coefficient (D, in cm^2·s^{-1}) of the straws is measured in parallel with the sorption measurement using the DVS apparatus. The diffusion coefficient can be calculated using the following equation [96]:

$$\frac{M_t}{M_\infty} = \frac{4}{d}\sqrt{\frac{Dt}{\pi}} \tag{3-1}$$

where M_t represents the amount of vapour absorbed at time t, M_∞ is the amount of vapour absorbed at thermodynamic equilibrium, and d is the thickness of the sample. This equation is applicable when $M_t/M_\infty < 0.4$, and the diffusion coefficient D can be determined by plotting M_t/M_∞ against $t^{1/2}/d$ using data obtained from the DVS measurements.

The free water saturation w_{sat} is approximated by fully immersing the straws in water for 7 days, an approximation method based on ASTM C1498-01 note 3 [41]. The surface of the samples is then lightly blotted with a damp sponge to remove excess water and their weight is measured.

The water vapour diffusion resistance factor μ is measured using the wet cup and the dry cup methods according to standard ISO 12572 [97]. The cups are filled with anhydrous calcium chloride $CaCl_2$ for the dry cup method and water for the wet cup method. Specimen with a thickness d_μ (m) are attached to the cups with a specific exposed area A_μ (m^2) and the edges are sealed with aluminium tapes to block vapour passage at the edge of the specimen. The change of mass Δm (kg) at successive times Δt (s) is measured by weighing the cups to obtain the density of water vapour transmission rate g (kg·m^{-2}·s^{-1}) following **Eq. (2-2)**. The measurement is considered complete once five successive values of g only vary within ± 5%. The value of μ (dimensionless) is then calculated using **Eq. (2-3)**.

The measurement of thermal conductivity λ (W·m^{-1}·K^{-1}) is done using the transient line source method with a thermal needle probe (AP Isomet model 2104). The probe has a declared accuracy of 5% of the reading plus 0.001 W·m^{-1}·K^{-1}. Five different bulk densities (60, 70, 80, 90, and 100 kg·m^{-3}) are prepared for measurements under dry conditions. To conduct measurements under dry

conditions, the samples are first dried at 40°C in an oven and then transferred to a desiccator filled with silica gel to reach a near 0% RH condition. For moisture-dependent thermal conductivity measurements, only samples with a bulk density of 80 kg·m^{-3} are selected for analysis. The study includes five RH conditions, namely near 0%, 33%, 43%, 59%, and 85% RH. All measurements are taken at room temperature (20 ± 2°C). The sample is placed inside a fixed 500 ml container, with the straws randomly distributed to average the effect of fibre orientation. The weight of the straws is carefully adjusted (± 0.1 g) to achieve the predetermined bulk densities.

To determine the growth rate and presence of mould on the straws, a mould growth test was conducted following European Assessment Document EAD 040005-00-1201 Annex B [49]. The test involved placing the straws in a desiccator filled with water for two months, during which time they were exposed to high relative humidity. At the end of each month, the specimens were visually examined for the presence of mould using both the naked eye and a microscope, following ISO 846 [50].

3.3. RESULTS AND DISCUSSION

3.3.1. Simulated performance

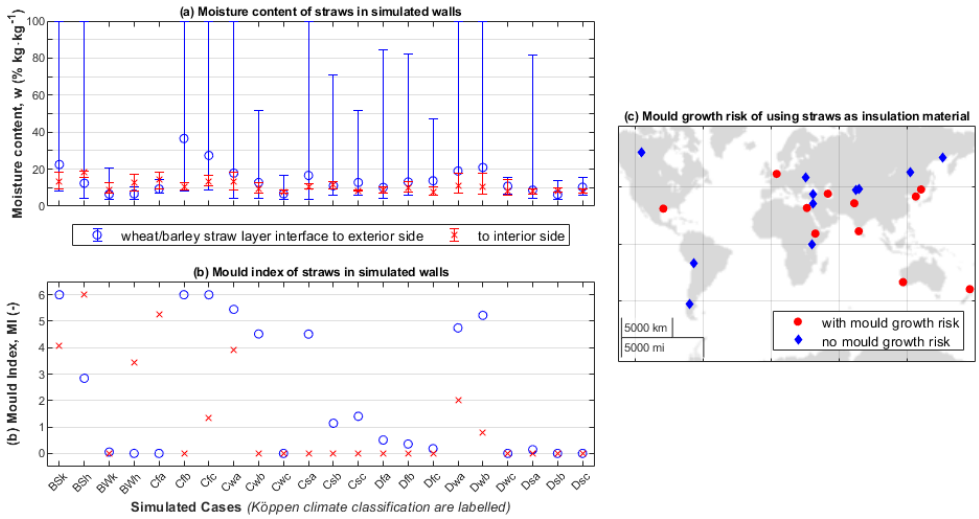

Fig. 3.2 Simulated results (a) moisture content of straws in simulated walls, (b) mould index of straws in simulated walls, (c) mould growth risk of using straws as insulation material.

In the selected wall type and climates, the areas with higher moisture content in the insulation layer are typically at the layers adjacent to the exterior lime plaster or behind the interior lime plaster. **Fig. 3.2a** presents the moisture content of these interfaced layers over a simulated year. The mould growth risk of these straw layers is then computed and shown in **Fig. 3.2b**, with a summary of the results in **Fig. 3.2c**. The results demonstrate no substantial distinction in mould growth risk

between using wheat or barley straws as insulation material in the simulated wall assembly. Consequently, both types of straws are combined in the same figure.

Out of the twenty-two cases that represent different climate types, half of them have a significant risk of mould growth within the straw layers. Among these cases, eight (BSk, BSh, Cfb, Cfc, Cwa, Cwb, Csa, Dwa, Dwb) have a higher mould growth risk at their exterior interfaced layer, while six cases (BSk, BSh, BWh, Cfa, Cwa, Dwa) have a higher risk at their interior interfaced layer. These findings suggest that it is essential to select a straw type with greater resistance to mould growth or apply an anti-fungal treatment on the straws when using them as insulation material in these unfavourable climates.

3.3.2. Physical properties and chemical composition

The straws used in this study have different stalk structures (**Fig. 3.3**). The stalk of the barley straw is wider and fuller on average than the wheat straw. It has a light-brown colour compared to the yellowish colour of the wheat straw. It contains a combination of macropores (~100-500 μm) and mesopores (~10-50 μm) and thicker stalk wall layers, while the wheat straw contains only mesopores. This gives barley straws a less dense structure compared to wheat straws. On average, the barley straw has a particle density of 872 $kg \cdot m^{-3}$, compared to 1013 $kg \cdot m^{-3}$ for the wheat straw (**Table 3.2**). This lower particle density of barley straw makes them more vapour diffusible per individual stalk; with a diffusion coefficient of 3.4 x 10^{-7} $cm^2 \cdot s^{-1}$ compared to the wheat straw at 0.8 x 10^{-7} $cm^2 \cdot s^{-1}$. In bulk, a material made of barley straws has a lower porosity compared to those made of wheat straws; a typical 80 $kg \cdot m^{-3}$ bulk material made of barley straws has an open porosity of 91%, compared to 92% for wheat straws.

After the antifungal surface treatment using BA, the particle density of the barley and wheat straws decreases by around 5%, which suggests that a more porous stalk structure is created. However, no significant cracks or wall collapse is observed under the microscope which can be directly attributed to the BA treatment. Nevertheless, the increasing vapour diffusion coefficient on both the treated straws likewise indicates that the straws are becoming more permeable due to the collapse in some of their wall structures.

Both the wheat and barley straws show overall similar intensities in their FT-IR spectrum compared to their untreated counterparts, suggesting that there is no significant change in the chemical composition of the surface of the straw after being treated with BA (**Fig. 3.4**). The relative ratios of lignin and wax to cellulose in the treated straws are largely lower than their corresponding untreated straws (**Table 3.2**). The relative ratios also show both wax and lignin contents in the wheat straw are closer to the barley straw after treatment. This could imply that the impact of BA on the wheat straw is stronger than the barley straw, with more wax and lignin now exposed on the surface during the measurements.

On the other hand, the water contact angle measurement on the treated straws shows an increase in their hydrophobicity, implying that additional waxes or other nonpolar compounds may have been released onto the surface after the straws are treated with BA (**Table 3.2**). The water contact angle of the wheat straw increased to 100° while the barley straw to 99°.

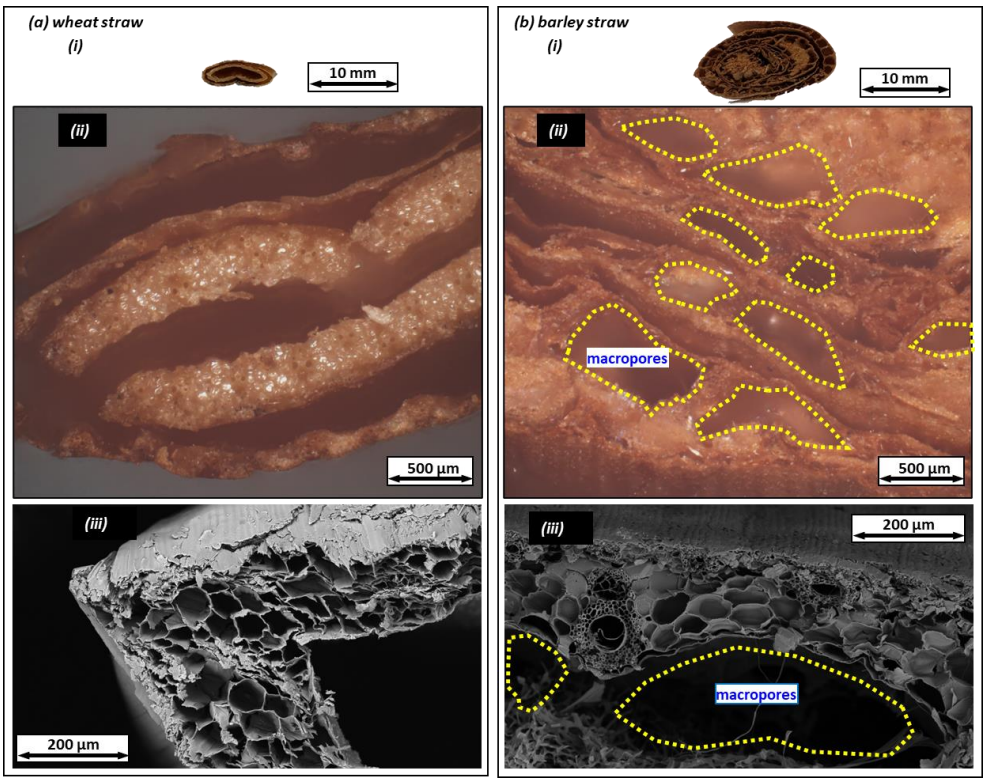

Fig. 3.3 Cross-section of (a) the wheat straw and (b) the barley straw; photos taken using an optical microscope (ii) and SEM (iii).

Table 3.2 Material properties and chemical composition of the wheat and barley straws for bulk density at 80 kg·m^{-3} (untreated and treated).

	Wheat straws		**Barley straws**	
	Untreated	**Treated BA**	**Untreated**	**Treated BA**
Stalk wall thickness (µm)	270 ± 80	-	540 ± 100	-
Particle density $\varrho_{partocle}$ (kg·m^{-3})	1013 ± 18	961 ± 13	872 ± 24	830 ± 23
Open porosity φ (%)	92.1 ± 1.8	91.7 ± 1.4	90.8 ± 2.8	90.4 ± 2.8
Vapour diffusion coefficient (x 10^{-7} cm^2·s^{-1})	0.8 ± 0.2	1.1 ± 0.4	3.4 ± 0.7	4.0 ± 1.2
Water contact angle (°)	76.7 ± 2.6	100.4 ± 9.0	81.3 ± 2.1	99.2 ± 16.1
Ratio lignin to cellulose				
I_{1595} / I_{1155}	0.87 ± 0.10	0.70 ± 0.14	0.94 ± 0.06	0.66 ± 0.06
I_{1595} / I_{1105}	0.78 ± 0.12	0.57 ± 0.15	0.86 ± 0.11	0.56 ± 0.11
I_{1505} / I_{1155}	0.85 ± 0.10	0.68 ± 0.14	0.87 ± 0.10	0.52 ± 0.05
I_{1505} / I_{1105}	0.77 ± 0.12	0.55 ± 0.15	0.79 ± 0.14	0.44 ± 0.10

	Wheat straws		Barley straws	
	Untreated	**Treated BA**	**Untreated**	**Treated BA**
Ratio wax to cellulose				
I_{2918} / I_{1155}	0.95 ± 0.13	1.00 ± 0.21	1.07 ± 0.17	1.40 ± 0.45
I_{2918} / I_{1105}	0.86 ± 0.16	0.81 ± 0.22	0.97 ± 0.23	1.00 ± 0.49
I_{1734} / I_{1155}	0.86 ± 0.09	0.72 ± 0.15	0.90 ± 0.10	0.69 ± 0.33
I_{1734} / I_{1105}	0.78 ± 0.11	0.58 ± 0.16	0.82 ± 0.15	0.58 ± 0.37

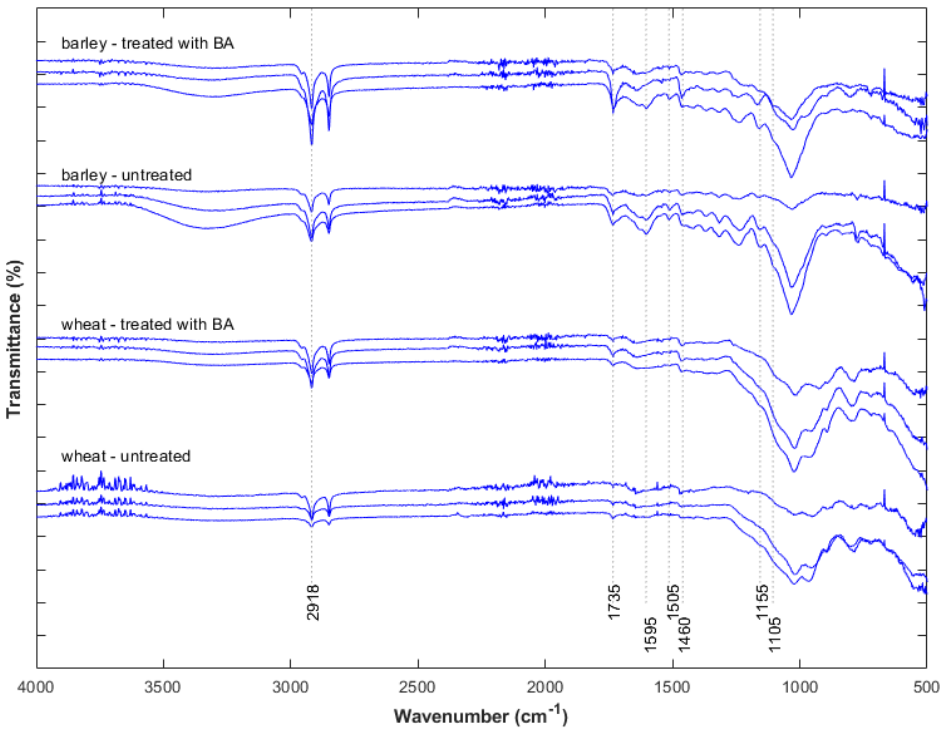

Fig. 3.4 ATR FT-IR Spectroscopy of the wheat and barley straws (treated and untreated); three samples per category are shown.

3.3.3. Hygroscopic and thermal properties

The measured moisture content of the straws is plotted against the predetermined RH conditions, as shown in **Fig. 3.5a**. The average moisture that can be adsorbed by the wheat and barley straws is in the range of 12 to 13% at 80% RH, which is aligned with those found in other studies [58]. During the desorption process, their moisture contents are in the range of 14% to 17% at 80% RH.

The wheat straw has a higher sorption capacity and kinetics than the barley straw. The results are aligned with the microstructure observed in the straws, where the wheat straw has only mesopores compared to the barley straw with a combination of mesopores and macropores. The smaller pores (mesopores) are quicker to be filled with water vapour and reach a saturated state, while the larger pores (macropores) take a longer time to be filled under the same pore volume. In addition, the capillary rise is inversely proportional to the radius of the pore, i.e. the smaller the pore is, the greater the rise or fall of the moisture in the pore [98], and the higher the sorption kinetics.

The second observation is that the treated straws have a higher sorption capacity than the untreated straws. The higher sorption capacity suggests that additional microcracks are introduced in the straw structure that allow more vapour to be filled. This explanation is parallel to the vapour diffusion coefficient of a treated straw, where it becomes more permeable due to the collapse of some of its wall structures.

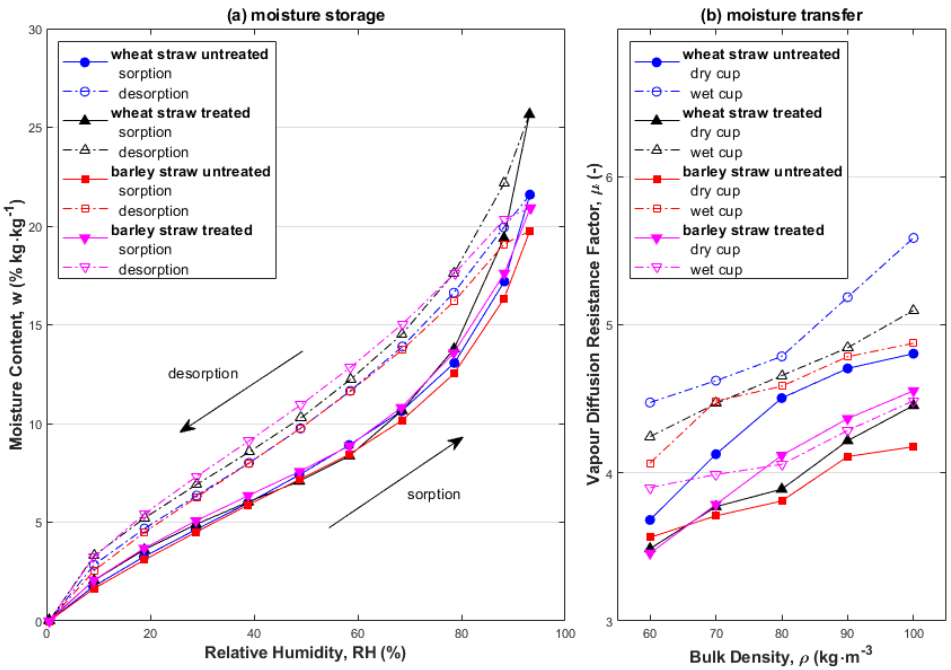

Fig. 3.5 (a) Sorption isotherms and (b) vapour diffusion resistance factor for the wheat and barley straws (treated and untreated).

From the full immersion test, the free water saturation w_{sat} for the wheat straw is around 600% of their dry weight, and 500% for the barley straw. These results are higher than the 400% estimation typically used in the sorption models for straws [99, 67, 63]. No significant difference in w_{sat} is found between the treated and untreated straws. The higher w_{sat} of the wheat straw is mainly contributed by their higher open porosity in bulk compared to the barley straw, which can be filled with more water under full immersion.

The vapour diffusion resistance factor μ is used to describe the vapour permeability of bulk material (**Fig. 3.5b**). The barley straw shows a slightly lower factor than the wheat straw, however, both are in the range of 4 and 5 under the investigated bulk densities, similar to those reported in [77, 100, 101, 102]. No substantial change is found between the treated and the untreated straws. There is a slight increment of the factor with increasing density, aligned to the finding in [103].

Overall, the water vapor diffusion resistance factor based on the wet-cup method is higher than that based on the dry-cup method for both wheat and barley straws discussed in this chapter. This observation is contrary to the typical trend, where the resistance factor based on the dry-cup method is higher due to the additional surface diffusion under high RH, resulting in a lower apparent resistance factor in the wet-cup method. Similar to the observation of expanded cork composite in **Chapter 2**, the closed pore structure within individual straws swells under high RH, thereby reducing the open pores within the test specimen. This reduction in open pores leads to a higher apparent diffusion resistance under the wet-cup method, as observed in this chapter.

The effective thermal conductivity λ of both treated and untreated wheat and barley straws are plotted against their bulk densities in **Fig. 3.6a**. The thermal conductivities fall within the range of 45 and 65 $mW \cdot m^{-1} \cdot K^{-1}$ for bulk density ranging from 60 to 100 $kg \cdot m^{-3}$, which aligns with values reported in previous studies [58]. In general, a lower bulk density or higher porosity results in a lower thermal conductivity of the straws. This is because the air in the pores has a lower thermal conductivity than the solid part of the straws, which is consistent with the findings of other studies [104, 105]. The treated straws have a lower porosity compared to the untreated straw at the same bulk density, resulting in higher thermal conductivities.

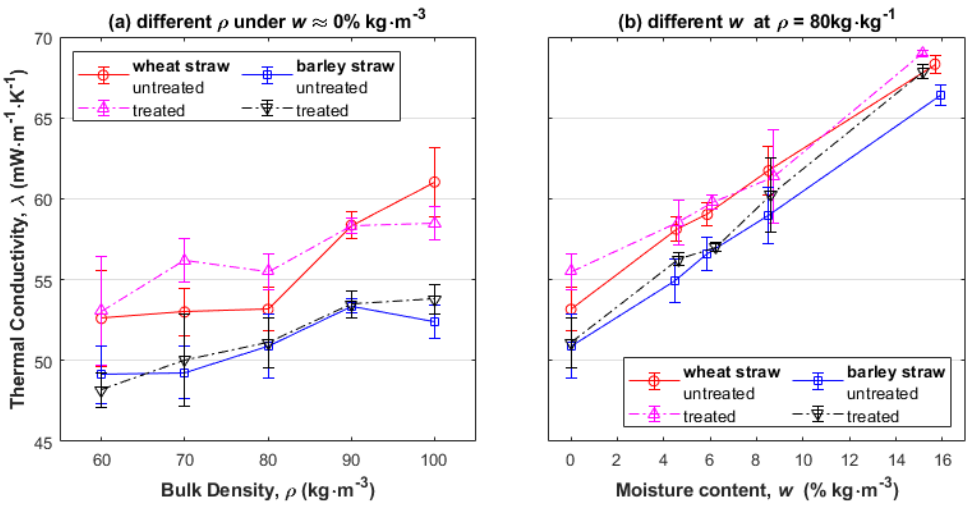

Fig. 3.6 Thermal conductivity plotted against (a) different bulk densities and (b) different moisture content of the wheat and barley straws (treated and untreated).

The thermal conductivity of barley straw is only slightly lower than that of wheat straw. At a bulk density of 80 $kg \cdot m^{-3}$, the mean dry thermal conductivity (λ_{dry}) of barley straw is 51 $mW \cdot m^{-1} \cdot K^{-1}$,

while that of wheat straw is 53 $mW \cdot m^{-1} \cdot K^{-1}$. As the bulk density increases from 60 to 100 $kg \cdot m^{-3}$, the mean thermal conductivity of barley straw increases from 49 to 53 $mW \cdot m^{-1} \cdot K^{-1}$, while that of wheat straw increases from 53 to 61 $mW \cdot m^{-1} \cdot K^{-1}$. The wheat and barley straws have different microstructures, with barley straw having larger pores and thicker wall structures, which could affect their effective thermal conductivity.

There is no noticeable difference in thermal conductivity between the treated and untreated straws. The use of an antifungal treatment with boric acid (BA) has no significant impact on the thermal conductivity of the straws.

Straw samples with a bulk density of 80 $kg \cdot m^{-3}$ are selected for additional moisture-dependent λ analysis. **Fig. 3.6b** illustrates the linear relationship between the thermal conductivity and moisture content of both treated and untreated wheat and barley straws. The thermal conductivity of the straws increases with increasing moisture content in the pores because water has a higher thermal conductivity than air within a pore (598 $mW \cdot m^{-1} \cdot K^{-1}$ as opposed to 25 $mW \cdot m^{-1} \cdot K^{-1}$). Both straws demonstrate a comparable incremental trend in thermal conductivity with increasing moisture content, emphasizing the prominent role of moisture in determining the overall insulation performance. No significant difference in thermal conductivity between the treated and untreated straws is observed under different moisture contents.

3.3.4. Mould resistance

The test specimen is subjected to high humidity conditions in a desiccator filled with water for two months. At the end of the first and second months, the specimen is visually examined with the naked eye and a microscope to detect the presence of mould. The specimens before humidity conditioning and after the first and second months under high humidity conditioning are shown in **Fig. 3.7**. The intensity of fungal growth on the test specimen is evaluated according to the scales of mould growth specified in ISO 846 [50].

By the end of the first month, significant mould growth covering more than half of the test surface is observed on the untreated wheat straw, while only minor mould growth is present on the barley straw as observed with the naked eye. After an additional month of humidity conditioning, heavy mould growth is visible on the entire surface of the wheat straw, but no significant increase in mould growth is observed on the barley straw. These results support the hypothesis that the lower ratio of lignin to cellulose-hemicellulose and a lower percentage of wax in barley straw contribute to its higher resistance to mould growth compared to wheat straw. In addition, wheat straws have higher moisture content and are less permeable, i.e. with higher sorption isotherms compared to barley straws and a higher vapour resistance factor, which signifies more free water in wheat straws to sustain any mould growth.

Fig. 3.7 Mould resistance tests on the wheat and barley straws (treated and untreated). Photos are taken on Day 1, Day 28, and Day 56, with the intensity of mould growth (IG) included.

The use of BA as an antifungal treatment on both wheat and barley straws resulted in a significant improvement in retarding mould growth under the same humidity conditioning. Although visible mould growth covering up to 25% of the surface of the treated wheat straw can still be observed, no mould growth is visible on the treated barley straw to the naked eye or under the microscope by the end of the first month. By the end of the second month, significant mould growth covering up to 50% of the wheat straw is observed, while minor, visible mould growth started to show up on the barley straw. The effectiveness of BA as a fungicide on the straws is noticeable, with improved mould resistance on the treated straws.

Additionally, whitish spots observed on the treated wheat straw (**Fig. 3.7b**, Day 56) match the account of white rot fungi [106]. This aligns with the literature where BA has a higher efficacy against brown rot fungi compared to white rot fungi [84]. It should be noted that severe testing conditions were applied, i.e. continuous exposure under a high-humidity environment for a long period. Therefore, the results are conservative and show higher mould growth potential than what is expected in actual applications.

3.4. CONCLUSIONS

This chapter aims to explore the possibility of using renewable alternatives, namely wheat and barley straws, as substitutes for conventional insulation materials, leveraging their widespread availability as by-products of global crop production. The study investigates the risk of mould growth in wall assemblies with straw infill across twenty-two distinct climate types, while also comparing the physical, thermal, hygroscopic, and durability properties of wheat and barley straws. Furthermore, the study evaluates the effectiveness of using boric acid as an antifungal surface treatment on straws and assesses its impacts on straw properties.

In general, half of the twenty-two simulated cases, representing different climate types, demonstrate a considerable probability of mould growth within the straw layers. This finding highlights the importance of selecting straw types with higher resistance to mould growth or applying antifungal treatments when using straws as insulation material in such unfavourable climates.

When applied as thermal insulation material, barley straws exhibit better hygrothermal characteristics compared to wheat straws. Specifically, barley straws demonstrate a lower sorption capacity, lower moisture content at the same relative humidity level compared to wheat straws, and a lower thermal conductivity, albeit insignificant, at 51 ± 2 $mW \cdot m^{-1} \cdot K^{-1}$ compared to 53 ± 1 $mW \cdot m^{-1} \cdot K^{-1}$ under the dry condition and bulk density at 80 $kg \cdot m^{-3}$. In terms of durability, barley straws exhibit a lower intensity of mould growth compared to wheat straws, which can be attributed to the higher wax and lignin contents, lower sorption isotherms, and higher vapour diffusion due to the existence of macropores within stalk structures. Collectively, these factors suggest that barley straws are more suitable as thermal insulation material than wheat straws.

Boric acid, recognized for its low toxicity and affordability, has been utilized as a fungicide. The straightforward application of boric acid as an antifungal treatment involves simple spraying onto the surface of straws. This treatment can be applied to straw bales, loose-fill, or other bulk materials

composed of straws. In the case of straw bales, boric acid can be sprayed onto the bale surface, considering that higher moisture content in the insulation layer is typically concentrated at the layers adjacent to the next layer, where mould growth is prone to occur. Straw bales can be pre-treated and air-dried in the field prior to transportation to the construction site, minimizing the cost impact of pre-treatment. Similarly, for loose straw infill, the straws can be treated during the shredding process. As only surface treatment is necessary, excess moisture from pre-treatment can be eliminated through ambient air-drying or low-temperature accelerated drying.

The application of antifungal surface treatment using boric acid on both wheat and barley straws substantially improves their resistance to mould growth. Treated straws demonstrate a lower intensity of mould growth under identical testing conditions. Although the treated straws exhibit slightly higher sorption capacity compared to the untreated ones, no significant effect is observed on their thermal conductivity.

To conclude, both barley and wheat straws demonstrate significant potential as thermal insulation materials, characterized by low thermal conductivities and no risk of mould growth in favourable climate conditions. The research findings further indicate that barley straws are more suitable than wheat straws for thermal insulation, based on their thermal, hygric, and durability characteristics. Moreover, it is recommended to utilize boric acid as an antifungal treatment for straws in building materials, particularly for wheat straws in unfavourable climatic conditions. This treatment effectively enhances the mould resistance of both wheat and barley straws while having minimal adverse effects on their hygric and thermal properties. Future research should explore the viability of other straw types as insulation materials, assess the effectiveness of boric acid on a broader range of bio-based materials, and investigate the long-term durability of boric acid-treated insulation.

4. UTILIZATION OF GEOPOLYMER IN WOOD WOOL INSULATION BOARDS: DESIGN OPTIMIZATION, DEVELOPMENT AND PERFORMANCE CHARACTERISTICS

ABSTRACT

This chapter investigates the substitution of ordinary Portland cement (OPC) with geopolymer in the production of wood wool geopolymer boards (WWGB), offering insights into manufacturing methods, design parameters, and performance characteristics. The composite formulation involves fibre pre-treatment, adjustment of precursor components, and control of activator compositions. The optimized formulation results in a lightweight composite with a density of 392 $kg \cdot m^{-3}$ and porosity of 76%, meeting the prescribed minimum compressive (20 kPa) and bending strength (1700 kPa) requirements. The inclusion of natural fibres influences the optimal Na_2O concentration and modulus for strength, with treated fibres recommended for higher modulus applications and improved strengths. Furthermore, it exhibits low thermal conductivity at 77 $mW \cdot m^{-1} \cdot K^{-1}$, minimal moisture sorption, and low vapour resistance, offering a sustainable alternative in the field of insulation materials.

The results presented in this chapter are published in the following article:

C.H. Koh, Y. Luo, F. Gauvin, and K. Schollbach, "Utilization of geopolymer in wood wool insulation boards: Design optimization, development and performance characteristics," Resources, Conservation and Recycling 204, 107510 (2022).

4.1. INTRODUCTION

Wood wool cement board (WWCB), comprising wood wool fibres bonded with ordinary Portland cement (OPC), has gained widespread usage in construction due to its resistance to decay and insects, lightweight nature, and favourable acoustic and thermal insulation properties [107, 108]. However, OPC manufacturing has a high embodied carbon, resulting in approximately 600 to 850 kg of CO_2 emissions per tonne [109, 110]. Sustainable alternatives are sought, with geopolymers emerging as promising candidates that offer significant carbon footprint reduction [111] and potential performance advantages over OPC [112]. Exploration of wood wool geopolymer board (WWGB) could potentially address the environmental concerns; however, wood-cement compatibility, optimal binder formulation, fibre conditions, and manufacturing methods need clarification.

A key challenge in manufacturing wood-cement composites arises from the chemical incompatibility between wood and cement [113, 114]. Saccharides in natural fibres can inhibit cement setting and hardening when leached out [115, 116]. However, promising compatibility has been reported between geopolymer binders and wood fibres [117, 118, 119, 120], as well as other natural fibres [121, 122, 123, 124, 125, 126, 127, 128]. Substituting OPC with geopolymer holds promise in producing WWGB.

Tailoring the geopolymer binder is crucial in determining WWGB performance. Geopolymers, formed by activating industrial aluminosilicate waste materials like coal fly ash (FA) and ground granulated blast furnace slag (GGBFS) using alkali agents [112, 129], have been extensively studied. The geopolymerisation of ASTM Class F FA, offering a low-calcium alkali-activated system with the primary reaction product of sodium aluminosilicate hydrate gel (N-A-S-H), provides better thermal stability compared to OPC or other alkali-activated materials [112]. The formulation of alkali activators, with varying SiO_2-to-Na_2O ratios (modulus) and Na_2O concentrations, significantly influences geopolymer gel formation. Furthermore, the inclusion of GGBFS in the FA-based precursor can enhance reactivity, leading to quicker setting and early strength development [130]. Therefore, investigating geopolymer formulation for WWGB production is essential.

Effective adhesion of fibres to geopolymer gels and potential surface morphology enhancement through pre-treatment is vital. Alkaline treatment increases fibre hydrophobicity and roughness [131], potentially improving adhesion. Alkali-treated wood fibres have demonstrated improved mechanical performance within cementitious matrices [132], and efforts have been made to use alkali-treated fibres for geopolymer reinforcement [128, 133, 134]. Therefore, WWGB made from pre-treated fibres is expected to exhibit improved adhesion and structural interlocking between fibres and the geopolymer binder.

Maximizing fibre content is critical for achieving the desired insulation properties. However, most studies have focused on using fibres as reinforcing components in geopolymer composites [121, 122, 117, 123, 124, 125, 126, 127, 128, 135]. For instance, [121] examined the dry mixing-spraying process to produce geopolymer-bonded fibreboards with up to 50 wt% fibre content. Although the composite exhibited good bending strength, bulk densities exceeded 1000 $kg \cdot m^{-3}$ and no thermal conductivity measurements were reported. [122] investigated the production of wheat

straw geopolymer composites, and the resulting boards exhibited relatively low densities ranging from 235 to 894 $kg \cdot m^{-3}$ and thermal conductivities ranging from 92 to 186 $mW \cdot m^{-1} \cdot K^{-1}$. However, these values were less favourable compared to commercially available WWCB products, which have thermal conductivities of 80 to 90 $mW \cdot m^{-1} \cdot K^{-1}$ with densities of 390 to 420 $kg \cdot m^{-3}$ [136]. Therefore, manufacturing methods should be further explored to close the performance gaps.

This chapter aims to replace the high embodied carbon raw material (OPC) with geopolymer in the production of wood wool boards. Specifically, we will focus on the manufacturing method, the effect of spruce wood wool with and without alkali pre-treatment for binding with geopolymer, the inclusion of GGBFS into the FA-based precursor, and the modulus and Na_2O concentration of the alkali activator to optimize geopolymer gel formation for WWGB. By investigating the feasibility, characteristics and performances of a wood wool board based on geopolymer, this chapter aims to address the increasing demand for environmentally friendly alternatives in the field of insulation materials.

4.2. MATERIAL AND METHODOLOGY

4.2.1. Raw material

Locally sourced raw materials, namely spruce wood wool (WW), Class F fly ash (FA) and ground granulated blast furnace slag (GGBFS) obtained from the Netherlands, are utilized. The average particle size (d_{50}) of FA and GGBFS is 13.9 μm and 19.3 μm, respectively, as determined by a laser particle size analyzer (Mastersizer 2000). The WW, with dimensions of 1 mm width, 0.3 mm thickness, and 25 cm length, is stored at 50 ± 5% relative humidity and 20 ± 2°C. The chemical composition of FA and GGBFS is analysed using X-ray fluorescence spectrometry (XRF) (PANalytical Epsilon 3), and their loss on ignition (LOI) is determined between 105 to 1000°C, as presented in **Table 4.1**. For the alkali activator, sodium silicate solution (27.7% SiO_2, 8.4% Na_2O and 63.9% H_2O) and sodium hydroxide (NaOH) pellets are employed. Furthermore, 1 wt% sodium hydroxide solution is prepared for fibre pre-treatment.

4.2.2. Boards design and manufacturing

Life cycle assessments comparing the replacement of OPC with geopolymer [137, 138, 139, 140, 141] generally concur that geopolymer production yields a lower CO_2 footprint than OPC. However, the extent of reduction in global warming potential (GWP) varies based on assessment methods, assumptions, and data quality. Notably, alkali activators, namely sodium hydroxide with a GWP of 1.27 kg $CO_2 \cdot kg^{-1}$ [138] and sodium silicate solution with a GWP of 0.424 kg $CO_2 \cdot kg^{-1}$ [142] emerge as major contributors to GWP. Higher Na_2O concentration and SiO_2-to-Na_2O modulus result in increased raw material consumption and, consequently, higher GWP. Striking a balance between environmental impact and overall performance is crucial when determining alkali activator design parameters. Additionally, both precursor materials (FA and GGBFS) are by-products of industrial processes and are subjected to emission allocation between primary products and by-products [143]. Although studies suggest a potential higher GWP for GGBFS compared to

FA [144, 143, 137], the FA-to-GGBFS ratio is considered less critical for the overall environmental impact of the board.

In this study, four key parameters are investigated to achieve optimum performance of WWGB: (i) alkali pre-treatment of WW, (ii) Na_2O concentration, (iii) SiO_2-to-Na_2O modulus of the alkali activators, and (iv) percentage of GGBFS and FA in the precursor. A baseline geopolymer formulation is established with a blend weight ratio of 95% FA and 5% GGBFS for the precursor, along with an alkali activator with a modulus of 1.8 and Na_2O concentration of 8% determined as optimal based on previous research [145] and preliminary experiments.

From this baseline, the design parameters are varied, exploring different Na_2O concentrations ranging from 6% to 12%, modulus values spanning from 1.0 to 2.2, and different percentages of GGBFS ranging from 0% to 15%. Each geopolymer formulation is applied to both alkali pre-treated WW and untreated WW samples. The detailed compositions of the mixtures can be found in **Fig. 4.1a**.

To ensure optimal activation and workability during the mixing process with WW, the water-to-dry geopolymer (dry sodium silicate, sodium hydroxide, FA and GGBFS) ratio is set at 0.4. Furthermore, the weight percentage of WW in the total dry weight (WW and dry geopolymer) is set at 30%. This percentage strikes a balance between effective binding and preventing binder runoff during the board-forming process. The density of WW without geopolymer is maintained at 90 $kg \cdot m^{-3}$ by controlling the amount of WW added, ensuring consistency in the final volume. To ensure a homogenous coating of geopolymer pastes onto the WW within the designated fabrication timeframe, WW is pre-wetted by spraying with water and the water-to-fibres ratio is set at 0.4.

Energy expended in board fabrication, especially during the curing and heating process, is optimized. Preliminarily investigations consider both ambient and heat curing [130, 146, 147], with a decision in favour of heat curing at 60°C for 24 hours to achieve the required early strength.

Table 4.1 Chemical composition of FA and GGBFS.

Oxides (wt%)	**FA**	**GGBFS**
SiO_2	54.57	29.41
Al_2O_3	21.60	13.21
Fe_2O_3	9.04	0.37
CaO	6.12	41.67
K_2O	2.85	0.42
MgO	1.17	8.57
SO_3	0.41	2.64
Other	2.13	1.07
LOI (1000°C)	2.11	1.15
Specific density ($kg \cdot m^{-3}$)	2225	2760

(a) Mixed details of WWGB sample

geopolymer formulation		wood wool treatment	
variables	fixed	without	with
% Na_2O		Group A specimens	Group D specimens
6%		A1	D1
8%	1.8 Modulus	A2	D2
10%	5% GGBFS	A3	D3
12%		A4	D4
Modulus		Group B specimens	Group E specimens
1.0		B1	E1
1.4	8% Na_2O	B2	E2
1.8	5% GGBFS	B3	E3
2.2		B4	E4
% GGBFS		Group C specimens	Group F specimens
0%		C1	F1
5%	1.8 Modulus	C2	F2
10%	8% Na_2O	C3	F3
15%		C4	F4

(b) WWGB sample production procedure

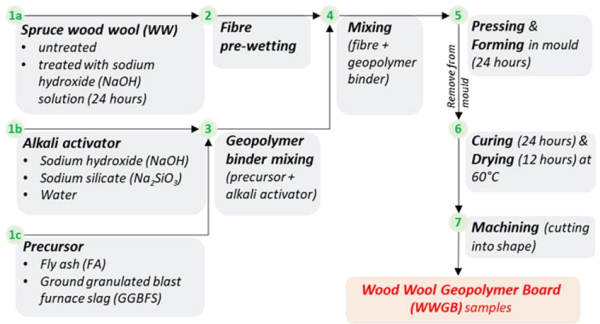

(c) Example of fabricated WWGB sample (E4)

Fig. 4.1 (a) Mixed details for WWGB production, (b) WWGB sample production procedure, and (c) example of fabricated WWGB sample (E4).

The production procedure is illustrated in **Fig. 4.1b**. WW is divided into two batches: one undergoing pre-treatment and the other remaining untreated. For the treated WW batch, immersion in a 1 wt% sodium hydroxide solution is conducted for 24 hours [148]. Subsequently, the treated WW is rinsed with water to eliminate alkali residue and impurities and left to dry under ambient conditions. The alkali activators are synthesized beforehand by blending sodium silicate solution, sodium hydroxide pellets, and additional water based on predetermined formulations.

During the main production process, WW is pre-wetted by spraying with water, using a water-to-fibre ratio of 0.4. The precursor materials (FA and GGBFS) and alkali activator solution are then added to a mixer and blended until a homogeneous paste is achieved. This geopolymer mixture is poured onto the WW and thoroughly mixed to ensure optimal coating of the binder onto the WW surfaces. The resulting mixture is transferred into a fixed-volume mould (350x250x15 mm^3) and compressed overnight. Throughout the forming process, the coated fibres are randomly laid and deagglomerated to ensure a consistent and homogeneous mixture.

After 24 hours, the compressed board is removed from the mould, wrapped in plastic foil, and cured overnight in an oven at 60°C for 24 hours. Following curing, the plastic is removed, and the board is further dried in an oven at 60°C for another 12 hours. Subsequently, the board is taken out of the oven, representing the final WWGB, and trimmed to its final dimensions (300x200x15 mm^3). A total of 24 WWGB samples are fabricated in this study, encompassing 20 distinct recipes (**Fig. 4.1c**).

4.2.3. Characteristics assessment

The mechanical properties of the samples are evaluated using a mechanical testing system (Instron 5967) equipped with a 5 kN load cell. The evaluation is based on the minimum criteria outlined in the European Standard EN 13168 [149], which serves as the benchmark for this testing. EN 13168 establishes the requirements for factory-manufactured wood wool products, presented in the form of boards or slabs, designed for application in the thermal insulation of buildings.

For the measurement of bending strength, the testing method specified in EN 12089 [150] is employed. Two test specimens per sample type are cut into dimensions of 150x125x15 mm^3. The test machine is set to a constant speed of 10 $mm \cdot min^{-1}$. The maximum force exerted during the bending test is used to calculate the bending strength (σ_b). The minimum required σ_b value of 1700 kPa [149] is used as a reference.

To determine the compressive strength at 10% deformation (σ_{10}), the testing procedure outlined in EN 826 [151] is followed. Two test specimens per sample type with dimensions of 50x50x15 mm^3 are cut. The specimens are compressed at a constant displacement rate of 1.5 $mm \cdot min^{-1}$. The compression stress at a strain of 10% (σ_{10}) is recorded. The minimum required σ_{10} at 20 kPa [149] is used as a reference.

The measurement of thermal conductivity (λ) is carried out using the transient line source method with a thermal needle probe (AP Isomet model 2104). The thermal needle probe, known for its accuracy of 5% of the reading plus 0.001 $W \cdot m^{-1} \cdot K^{-1}$ is employed. All samples are conditioned at a relative humidity of 50 ± 5%, and the measurements are conducted at 20 ± 2°C. Three measurements are taken at different locations on each board.

The hygroscopic sorption properties of the samples are determined following standard ISO 12571 [152]. The moisture contents (w) of all samples are measured after conditioning them at 80% relative humidity in a climate chamber (Memmert ICH750). However, for the sorption isotherms measurement from 0% to 85% relative humidity, only samples A2 and D2, which represent WWGB made of untreated and treated WW, are included. To monitor the moisture uptake, the samples are weighed at 24-hour intervals using a digital balance. Constant mass is considered reached when three successive weighings show a mass loss change of less than 0.1%.

The water vapour diffusion resistance factor (μ) is measured using the cup methods as outlined in standard ISO 12572 [97]. Samples A2 and D2 are used to investigate the water vapour transmission properties. The measurement is considered complete when five successive readings of the water vapour transmission rate density vary within ± 5%.

The measurement of sound absorption coefficient (α) and sound transmission loss (TL) is conducted using two impedance tubes: BSWA SW422 and SW477. These impedance tubes cover different frequency ranges, with SW422 covering the range of 63-1600 Hz and SW477 covering the range of 800-6300 Hz. The SW422 requires samples with a diameter of 100 mm, while the SW422 requires samples with a diameter of 30 mm. Only samples A2 and D2 are included. The sound absorption coefficient is measured following ISO 10534-2 [153], while the sound transmission loss is based on the transfer function method.

Visual inspection is conducted using a scanning electron microscope (SEM) (Phenom ProX). Additionally, the cross-section of the samples is analysed using micro-computed tomography (micro-CT) analyses (Scanco μCT 100).

To determine the particle density ($\varrho_{particle}$), a helium pycnometer (Micromeritics AccuPyc II 1340) with a 10 cm^3 cup is used. From the measured particle density, the porosity φ (%) of the specimen is calculated using **Eq. (2-1)**. The pycnometer has an accuracy of 0.06%.

The chemical composition of the samples is analysed using Fourier transform-infrared (FT-IR) spectroscopy in conjunction with an attenuated total reflection (ATR) attachment (PerkinElmer Frontier FT-IR). The FT-IR spectra are collected over a wavenumber range of 4000 to 400 cm^{-1}, with a resolution of 1 cm^{-1}.

Thermogravimetric analysis (TGA) is performed using a thermogravimetric analyser (TA Instruments TGA Q500). The heating process starts from room temperature and continues up to 900°C, with a heating rate of 10°C·min^{-1}. The samples are analysed under a controlled nitrogen atmosphere with a constant flow rate of 60 ml·min^{-1}.

4.3. RESULTS AND DISCUSSION

4.3.1. Mechanical strength

Fig. 4.2a illustrates the relationship between the bending strength of WWGB and various design parameters. Notably, the most significant increase in bending strength is observed with higher Na_2O concentration, followed by an increase in modulus and GGBFS percentage. However, when considering the minimum bending strength requirement specified in EN 13168 for a 15mm thickness board (1700 kPa) [149], WWGB samples made with a minimum of 8 wt% Na_2O concentration, a modulus of 1.8 or higher, and a GGBFS ratio above 5% meet the minimum strength requirement.

All samples meet the minimum requirement specified in EN 13168 [149], which mandates a minimum compressive stress at 10% strain (σ_{10}) of 20 kPa (CS(10/Y)10) for handling purposes. Notably, samples with higher Na_2O concentrations (samples A4 and E4) exhibit the highest compressive strengths. This observation indicates an increased formation of aluminosilicate products under higher Na_2O concentrations, resulting in a stronger binding mechanism. Moreover, it is evident that the compressive strength of WWGB samples reaches a plateau within the range of 1.4 and 2.2 modulus and with a GGBFS range of 10% and 15%.

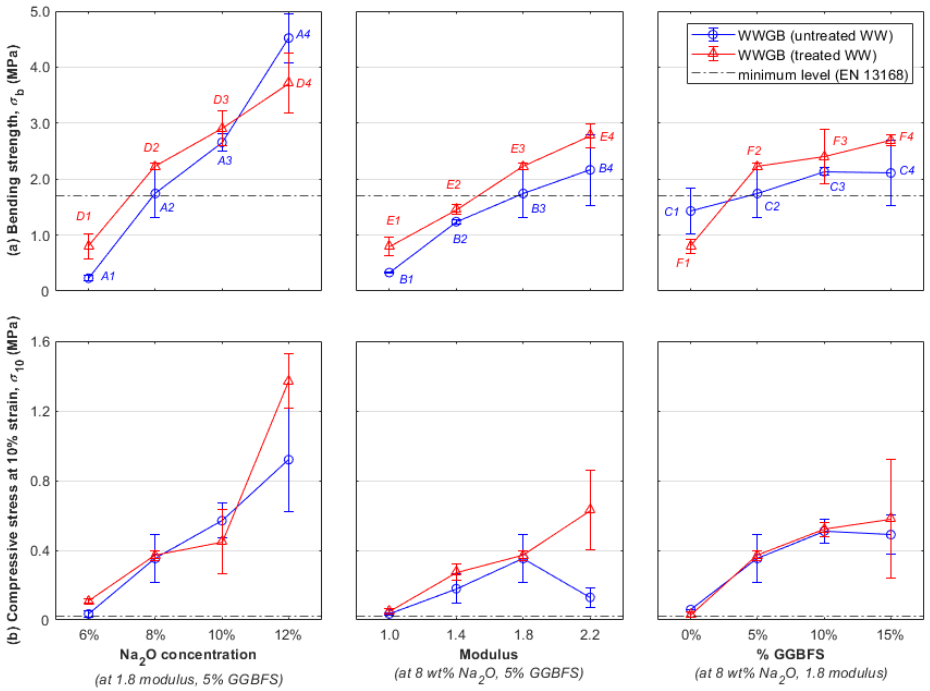

Fig. 4.2 (a) Bending and (b) compressive strengths of WWGB samples as a function of Na2O concentration, Modulus, and %GGBFS.

From previous research [154], the optimal Na_2O concentration is found to be between 5.5 to 10 wt% for a standalone geopolymer paste. Excessive Na_2O concentrations further hinder the subsequent formation of geopolymer gel [155]. However, a higher Na_2O concentration at 12 wt% is found to further increase the compressive strength in samples A4 and E4. This suggests that part of the excess hydroxide from the activator reacts with the hydroxyl groups present in the WW fibres [148], instead of inducing early gel precipitation [154]. The presence of natural fibres significantly influences the optimal value of Na_2O concentration of an activator.

Compressive strength continues to increase up to a modulus of 1.8 for samples with untreated WW and 2.2 with treated WW in this study, under a fixed 8 wt% Na_2O concentration. Notably, the compressive strength of sample B4 drops significantly; however, no reduction in its bending strength is observed. This implies a disruption in the forming of geopolymer binder, while the WW cellulose structure remains largely intact. A two-fold cause is suggested. First, hydroxide dissolves hemicellulose from untreated WW and releases carboxylic acid, weakening the alkali medium [156] of the alkali activator. Second, the optimal value of the modulus correlates with its Na_2O concentrations, achieving an equilibrium between alkaline hydrolysis and the absorption rate of soluble Si [154]. Excess SiO_2 may induce polymerized SiO_4 that suppresses the subsequent geopolymerisation process [154].

Generally, increasing GGBFS content in an FA-based geopolymer tends to improve its overall compressive strength [130]. However, in this study, the inclusion of 10% or more GGBFS results in a paste with low workability and a shortened setting time. The adhesion between the geopolymer binder and WW fibres is subsequently compromised, especially in samples with untreated WW (sample C4).

Further discussions on the formation of aluminosilicate products will be provided through subsequent FTIR and TG analyses.

The disparity in bending strength between WWGB samples made with treated and untreated WW is more pronounced compared to the differences in their compressive strengths. Generally, WWGB samples incorporating treated WW demonstrate higher bending strengths. This improvement can be attributed to the removal of non-cellulose components, such as wax, and the presence of mercerised cellulose structures in treated WW, which enhance adhesion with the geopolymer gels [157, 131]. It is worth noting that WWGB samples incorporating treated fibres only exhibit slightly better compressive strength compared to untreated samples. This indicates that the geopolymer binder, rather than the fibres, primarily determines the compressive strength, as the formation of aluminosilicate products plays a crucial role in providing interconnecting strength within the composites.

No reduction in bending strength is observed in this study, with alkali activators up to 12 wt% Na_2O concentration. The structural cellulose largely remains unaffected because alkaline hydrolysis is limited to the surface layer (waxes, oils) and hemicelluloses, either during the fibre pre-treatment or geopolymerisation process. This is aligned with the previous study [158], which suggested that alkalinity is not the main degradation mechanism of natural fibre but other mechanisms such as fibre mineralisation are a bigger influence. It is expected that the long-term performance of the WW will not be significantly compromised by the alkaline pore solution in the geopolymer; however, further study is warranted.

4.3.2. Insulation properties

The primary objective of WWGB is to enhance thermal insulation in building envelopes. The thermal conductivities of all samples are presented in **Fig. 4.3a**. Generally, heat transfer primarily occurs through the interconnected gel network within WWGB. Samples with higher porosity exhibit lower thermal conductivities due to their porous structure, where the internal air voids, including mesopores and macropores, serve as the main insulating component. The results indicate an increase in thermal conductivities with higher Na_2O concentration, modulus and GGBFS content, suggesting a denser gel structure within the samples, which correlates with their mechanical strength. Interestingly, WWGB made of untreated WW demonstrates lower thermal conductivities compared to the treated counterpart. This reveals a trade-off associated with fibre pre-treatment; while it improves mechanical strength, it sacrifices thermal insulation performance due to the denser structure within treated fibres. The median thermal conductivities for all groups range between 70 and 85 $mW \cdot m^{-1} \cdot K^{-1}$. These values are comparable to commercially available WWCB products, such as 80 and 90 $mW \cdot m^{-1} \cdot K^{-1}$ for WWCB with densities of 390 and 420 $kg \cdot m^{-3}$, respectively [136]. Notably, sample A1 exhibits an even lower thermal conductivity below 70 $mW \cdot m^{-1} \cdot K^{-1}$; however, its porous structure sacrifices its mechanical strength.

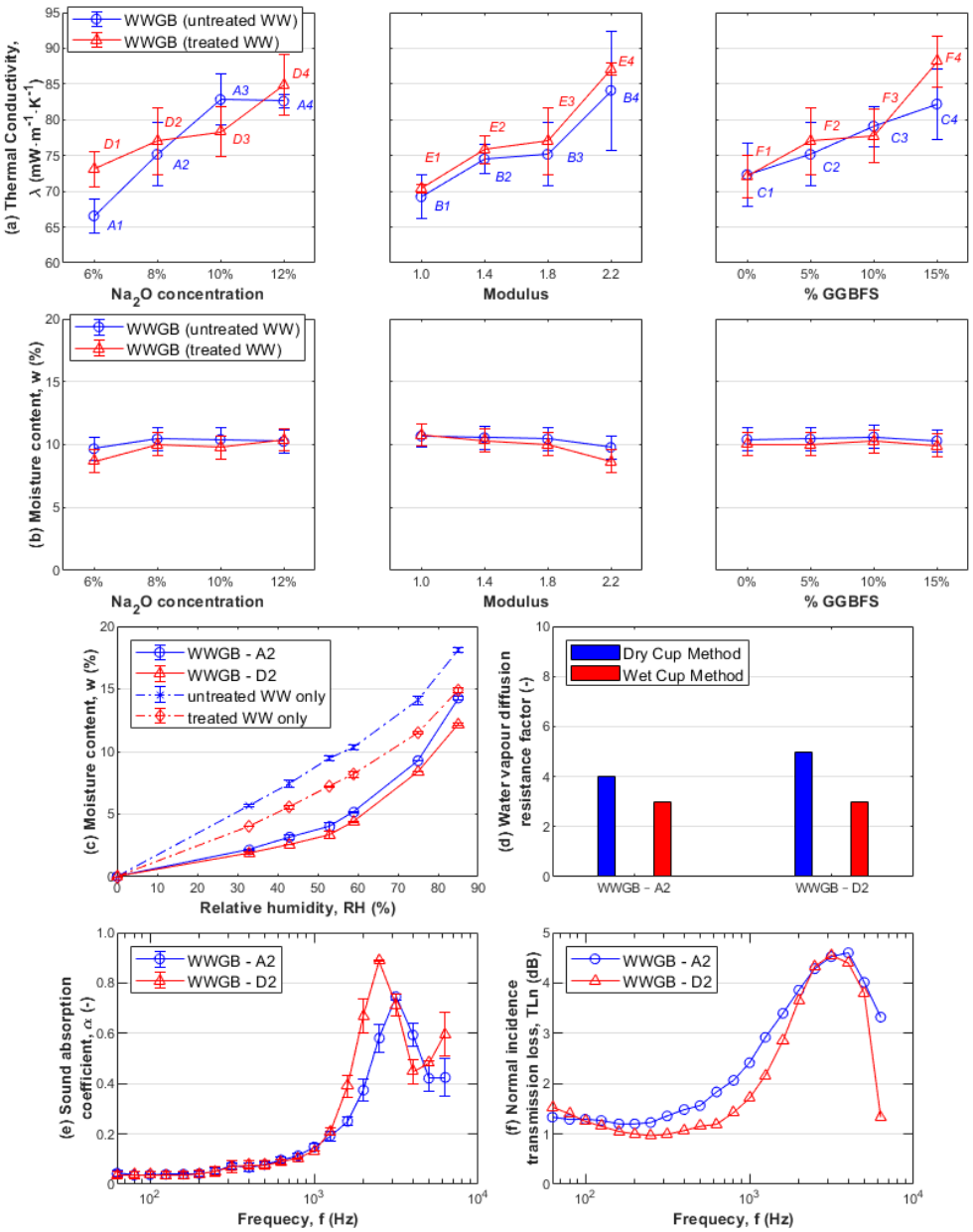

Fig. 4.3 (a) Thermal conductivities and (b) moisture content at 80% relative humidity of WWGB samples as a function of Na_2O concentration, Modulus, and %GGBFS. (c) Sorption isotherm, (d) water vapour diffusion resistance factor, (e) sound absorption coefficient, and (f) normal incidence of transmission loss of WWGB samples A2 and D2.

Fig. 4.3b shows the moisture contents of all WWGB samples conditioned at 80% relative humidity. Overall, the moisture sorption of the WWGB can be considered low compared to typical

WWCB, which has a moisture content of 12% at 80% relative humidity [136], slightly higher than the average of 10% measured in this study.

From **Fig. 4.3c**, the sorption capacities of WWGB are reduced compared to the original WW component under lower relative humidity, with smaller differences at higher relative humidity. Mesopores can be found in WW [159], and when they are not covered by geopolymer, water initially fills up these mesopores at lower relative humidity. In contrast, in the geopolymer paste, there is a combination of macropores and mesopores [160], along with the macropore structure in the WWGB, where moisture only fills up in these larger pores at higher relative humidity. Under different geopolymer compositions, a slight increase in moisture content can be observed with higher Na_2O concentration or lower modulus of the alkali activator, while no notable trend is discerned with different GGBFS percentages in the precursor. This may indicate the creation of a denser network of mesopore structures with higher Na_2O concentration or lower modulus [161].

It can also be observed that the WW treated with NaOH solution exhibits lower sorption isotherms compared to the untreated WW. The alkali treatment degraded the cell wall material and reduced the number of hydroxyl groups accessible to water, resulting in increased hydrophobicity [131, 148]. Accordingly, the WWGB made from untreated WW (sample A2) has slightly higher sorption isotherms compared to the WWGB with treated WW (sample D2). These consistent trends suggest that the moisture sorption in WWGB is primarily influenced by the fibre component. This observation is further supported by the moisture contents of all WWGB samples conditioned at 80% relative humidity, where the WWGB with treated WW has lower moisture contents compared to their counterparts.

The water vapour diffusion resistance factors for the samples are found to be between 3 and 5 using the wet cup and dry cup method (**Fig. 4.3d**). The low resistance factors indicate that the WWGB has a high moisture diffusivity property. This value is similar to that of typical WWCB, which has a factor of 3 (at a density of 420 $kg \cdot m^{-3}$) [136].

Fig. 4.3e shows the normal incidence sound absorption coefficient of Samples A2 and D2. Both samples exhibited a similar trend in sound absorption within the tested frequency range, with the WWGB made from treated WW showing higher absorption coefficients at higher frequencies. Sample D2 shows an absorption peak at 2500 Hz, while sample A2 exhibits a peak at 3150 Hz. These sound absorption patterns are comparable to previous findings on WWCB [162]. However, due to the small sample size used in this measurement, the effect of WW treatment is not conclusive. Both samples have a similar sound absorption rating of Class E, with a weighted sound absorption coefficient α_w of 0.15 according to ISO 11654, indicating poor sound absorption (low absorption capability). In comparison, commercial WWCB available in the market achieves an α_w of 0.35 (Class D) when employing a 25 mm thick WWCB attached to a concrete layer [163]. This suggests that the sound absorption capability of the WWGB samples is relatively close to that of a commercial WWCB.

Both samples, A2 and D2, demonstrate low normal incidence transmission losses below 5 dB, particularly at lower frequencies (**Fig. 4.3f**). These suboptimal transmission losses can be attributed to the uneven circumference of the samples caused by their porous structure, leading to flanking

transmission during testing. Additionally, the developed WWGB are thin and lightweight, which is not ideal for effective standalone sound insulation [164].

4.3.3. Physical properties

The alkali treatment of WW fibres leads to significant changes in surface morphology, as illustrated in **Fig. 4.4b**, compared to untreated WW fibres (**Fig. 4.4a**). The treated fibres display signs of fibrillation. The reaction between NaOH and the hydroxyl groups present in the wood fibres results in the removal of a portion of lignin, hemicellulose, and wax from the fibres [148]. This mercerised cellulose structure enhances interfacial bonding between the fibres and geopolymer gels [157, 165] in WWGB. **Fig. 4.4c** shows the geopolymer gel on the surface and between the fibres provides the primary binding strength in the WWGB. Unreacted and partially reacted FA particles can also be observed on the WWGB, indicating an incomplete reaction of the FA particles during the geopolymerisation process, similar to previous reports [166, 167].

The micro-CT scan of the cross-section of WWGB sample A2 (**Fig. 4.4d**) reveals three main components: geopolymer gel (shown in solid grey), pores and voids (shown in solid black) and WW (shown in grey dotted with black). The geopolymer gels, with varying thicknesses, including some exceeding 1 mm, can be observed wrapping around the WW, forming an interconnected network throughout the structure of the WWGB. The original mesopore structure within the WW fibres remains distinguishable. Additionally, new macropores are formed between the coated WW fibres, and mesopores can be observed within the geopolymer gel. Overall, the internal structure exhibits a high level of inhomogeneity. This inhomogeneity highlights the challenges associated with maintaining consistency in the final product at a smaller laboratory scale. However, these challenges could potentially be resolved by scaling up production to the larger scale typically used for WWCB production [108].

In general, the samples exhibit similar ranges of bulk densities, ranging between 350 and 450 $kg \cdot m^{-3}$, depending on the specific design parameters (**Fig. 4.4e**). The bulk densities show the greatest increase with an increment in Na_2O concentration, followed by an increase in silica modulus, and were least affected by the percentage of GGBFS in the precursor. These findings align with the general trend observed in mechanical strength and insulation performance; samples characterized by denser structures exhibit both higher thermal conductivity (**Fig. 4.3a**) and mechanical strength (**Fig. 4.2**).

The open porosities of the fabricated WWGB range from 70% to 80% (**Fig. 4.4f**). In most cases, samples made with either untreated or treated WW exhibit similar porosity under the same designed parameters. The open porosity shows a clear decreasing trend with an increase in Na_2O concentration owing to the promoted activation; however, no clear trend can be observed when changing the modulus of alkali activators or the percentage of GGBFS in precursors.

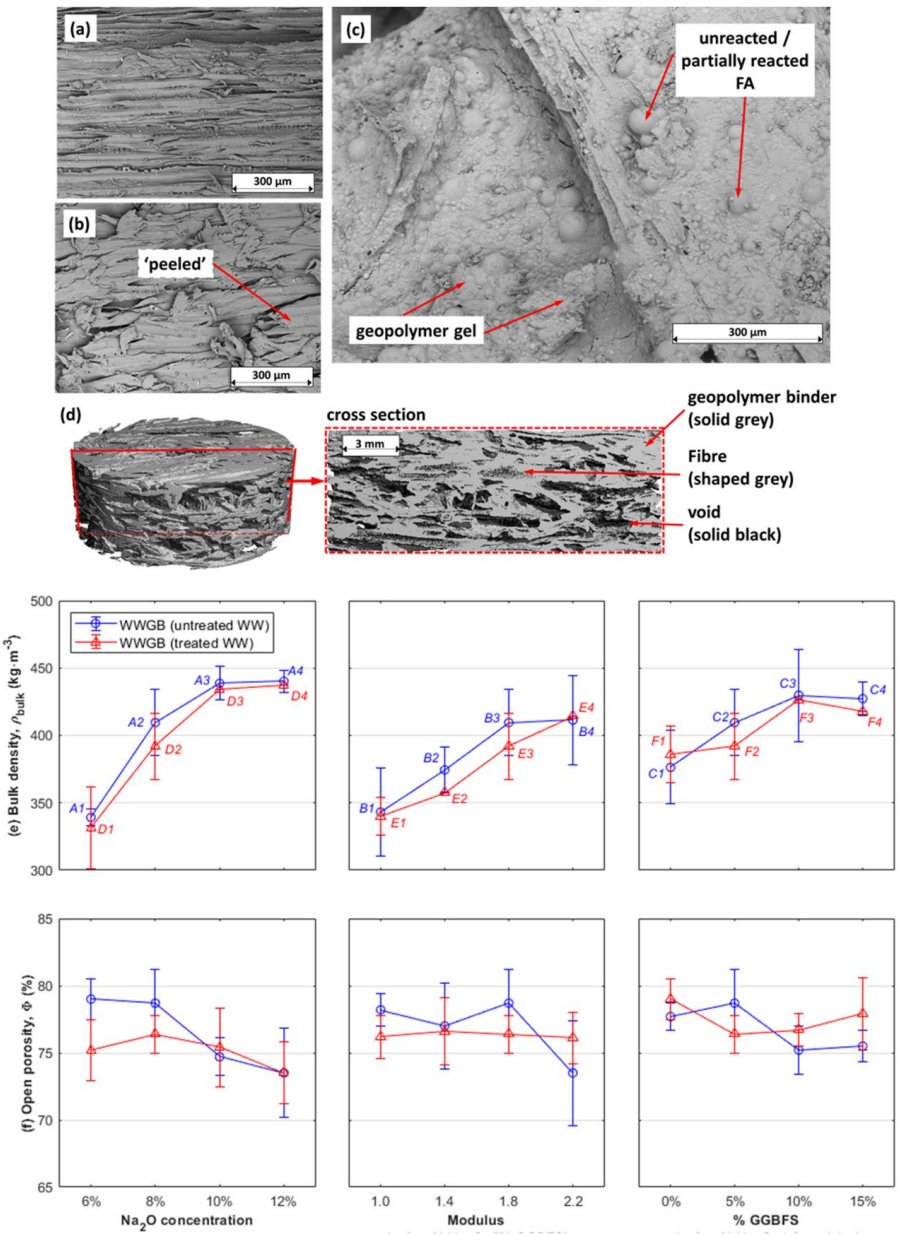

Fig. 4.4 SEM images of (a) untreated wood wool, (b) treated wood wool, and (c) WWGB. (d) WWGB cross-section from micro-CT scan. (e) Bulk densities and (f) open porosities of WWGB samples as a function of Na_2O concentration, Modulus, and %GGBFS.

4.3.4. Chemical compositions

The alkali treatment of WW fibres leads to delignification, resulting in the disappearance of characteristic peaks associated with lignin vibrations at 1250 cm^{-1} and 1025 cm^{-1}, which represent the C-O ester vibrations [168](**Fig. 4.5a**). Additionally, the peak at 1510 cm^{-1} attributed to aromatic skeletal vibration [169] is no longer observed. These observations align with the fibrillation observed in the treated WW (**Fig. 4.4b**). The treated fibres also exhibit a reduced intensity of the band at 3300cm^{-1}, which is associated with the OH group [170]. This reduction suggests the disruption of intermolecular hydrogen bonding in cellulose or a decrease in free water content within the treated fibres.

Fig. 4.5b displays the main peaks at broad bands 1030 cm^{-1} and 900 cm^{-1} for FA and GGBFS respectively. These peaks correspond to the asymmetric stretching vibration modes of Si-O-T bonds (T = tetrahedral Si or Al), exhibiting different glassy networks for FA and GGBFS [171, 172]. Upon alkali activation, the bands for all samples in this study are centred at or around 1000 cm^{-1}, which is typical for an FA-based geopolymer [173]. This suggests the formation of a highly polymerized aluminosilicate network as the primary reaction product.

In a blended FA and GGBFS system, the shifting of the main Si-O-T band primarily reflects changes in the polymerization degree of Si-O-T crosslinking. In this study, an increase in the GGBFS ratio in the precursor causes the main Si-O-T band to shift from 1000 cm^{-1} to a lower wavenumber at 980 cm^{-1} (**Fig. 4.5c/iii**), indicating a lower polymerization degree due to the presence of a calcium source from GGBFS [174]. Varying Ca concentrations also impact the formation of geopolymer gel composition, and can lead to the formation of N-A-S-H, C-A-S-H, or intermediate gel (N-C-A-S-H and C-N-A-S-H) [155]. However, the exact nature of the gels formed is still disputed [172, 175, 166]. C-N-A-S-H type gel is assumed to be predominantly formed in samples with 5% or higher percentage of GGBFS in the precursor.

Furthermore, the choice of Na_2O percentage also influences the final gel structure. The alkalinity in the environment controls the dissolution of silicate and aluminate from FA and the availability of calcium from GGBFS [166]. This effect is demonstrated in **Fig. 4.5c/i**, where samples with 10 wt% and 12 wt% Na_2O concentration exhibit a broader and higher wavenumber shift in the Si-O-T band, indicating variations in the composition/structure of the hybrid C-N-A-S-H gel [155]. Moreover, a higher modulus increases the availability of silica and raises the pH of the activator, which, in turn, influences the dissolution of precursors and alters the polymerization process of the geopolymer gel [176]. This behaviour is evident in **Fig. 4.5c/ii**, where the Si-O-T band shifts to a broader and higher wavenumber with a larger modulus, implying a higher polymerization of the final aluminosilicate gel.

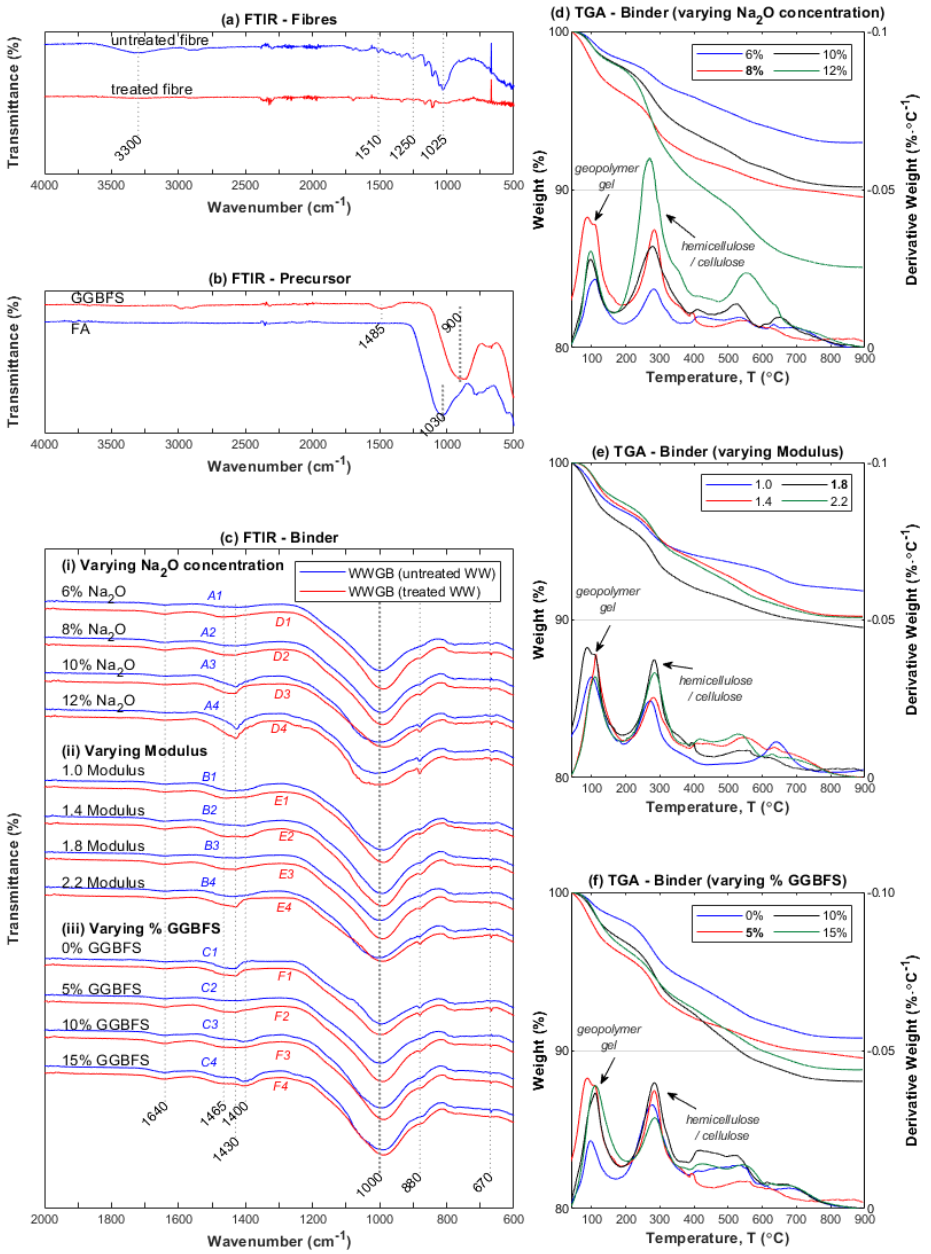

Fig. 4.5 FTIR results of (a) wood wool fibres, (b) precursors, and (c) binder gel as a function of Na_2O concentrations, modulus, and %GGBFS; TGA and DTG results of WWGB samples (primarily composed of the binder) as a function of (d) Na_2O concentration, (e) Modulus, and (f) %GGBFS.

The observed shifts in wavenumber correlate with trends in compressive strength (**Fig. 4.2b**), illustrating a broader and higher shift associated with the increase in Na_2O concentration compared to variations in modulus and GGBFS content. Additionally, sample B4 manifests a higher peak near 1030 cm^{-1}, indicating the present of unreacted FA, correlating with the observed low compressive strength.

All recipes display a similar small peak at 1640 cm^{-1} (and 3350 cm^{-1}, not presented in **Fig. 4.5c**), which can be attributed to the OH groups [171] originating from chemically bound water in the gels.

Carbonation products are detected in both the raw materials and reaction products. For GGBFS, the peak at 1480 cm^{-1} corresponds to the asymmetric stretching mode of the O-C-O bonds, indicating that carbonation had already occurred [177]. The reaction products exhibit peaks at 1465 cm^{-1}, 1430 cm^{-1} and 880 cm^{-1}, corresponding to vibrations of O-C-O in carbonates, revealing that carbonation took place during the forming and curing process [171, 177]. However, in samples with higher GGBFS ratios (10% and 15% GGBFS), an additional band at 1400 cm^{-1} is observed, corresponding to O-C-O vibrations from the additional GGBFS content [166].

Fig. 4.5d-f illustrates the thermogravimetric analysis results of the extracted geopolymer binder powder obtained from WWGB after the thorough removal of fibres. The initial derivative thermogravimetry (DTG) peak is observed in the temperature range of 40 to 200°C, indicating the release of physically and chemically bound water present in the geopolymer gel structure [166]. The second peak, spanning from 200 to 400°C, corresponds to the decomposition of hemicellulose and cellulose derived from the spruce WW [178] that is mixed within the extracted powder. Additionally, several DTG peaks are observed between 500 and 700°C, suggesting the presence of carbonates [176]. It is worth noting that the variations in mass loss, corresponding to gel decomposition, are more pronounced in the WWGB samples with different Na_2O concentrations compared to adjustments in the silica modulus and GGBFS ratio in the precursor. This observation suggests that the Na_2O concentration plays a more influential role in the formation of the aluminosilicate product, consistent with the observation that the most significant increase in mechanical strength is observed with higher Na_2O concentration.

4.4. CONCLUSIONS

This chapter demonstrates the substitution of OPC with geopolymer in the production of wood wool geopolymer boards (WWGB). Here are the key findings and characteristics of WWGB:

1. WWGB samples with at least 8% Na_2O concentration, a modulus of 1.8 or higher, and a GGBFS ratio above 5% meet both the prescribed minimum compressive strength (20 kPa) and bending strength (1700 kPa) requirements. Mechanical strength is primarily influenced by the Na_2O concentration, followed by the GGBFS percentage and the modulus, as supported by FTIR and TG analyses indicating an increased reaction degree.
2. The present of natural fibres impacts the optimal value of Na_2O concentration and modulus for compressive strength. Treated fibres are recommended when applying a

higher modulus to avoid hindrance in the geopolymerisation process. Furthermore, WWGB made from treated wood wool exhibits higher bending strengths.

3. Median thermal conductivities of WWGB fall within the range between 70 and 85 $mW \cdot m^{-1} \cdot K^{-1}$. WWGB made from treated wood wool demonstrates slightly higher thermal conductivities compared to the untreated counterpart, revealing a trade-off associated with fibre pre-treatment.
4. Moisture sorption in WWGB is primarily influenced by the fibre component, with untreated WWGB exhibiting slightly higher sorption isotherms. WWGB show low moisture sorption and water vapour diffusion resistance.
5. Bulk densities of WWGB range from 350 to 450 $kg \cdot m^{-3}$, and open porosities range from 70% to 80%. These properties are primarily influenced by the Na_2O concentration and silica modulus, while the GGBFS percentage has minimal impact.

In conclusion, this chapter underscores geopolymer as a viable alternative to OPC in WWGB production, providing insights into manufacturing methods, design parameters and performances. Opportunities for improvements include enhancing acoustic performance. Further investigations should assess fire resistance and durability, explore alternative natural fibre materials, conduct a comprehensive life cycle assessment, and optimize curing, drying, and alkali activators for lower embodied carbon.

5. EVALUATING ENVIRONMENTAL IMPACTS OF GEOPOLYMER AND STRAW-BASED WOOD WOOL CEMENT BOARDS

ABSTRACT

This chapter assesses the environmental and performance implications of utilizing industrial and agricultural by-products as alternative raw materials in the manufacturing of wood wool cement boards (WWCB). In this context, geopolymer replaces OPC, and straws replace spruce wood wool. Both economic and no allocation methods are applied to these by-products to assess their life cycle impacts according to EN 15804+A2. The findings highlight the environmental benefits of replacing OPC with geopolymer in terms of global warming potential, although the impact on other environmental indicators is less certain. However, substituting straws for wood wool in the production of straw geopolymer boards (SGB) results in poor environmental and performance outcomes, diminishing its viability as a solution. Notably, the treatment of straws does not substantially enhance overall performance and leads to a higher environmental burden. Furthermore, the study recommends adopting a consistent by-product allocation method to ensure accurate reporting of environmental impacts across different industries.

The results presented in this chapter are included in the following manuscript:

C.H. Koh, F. Gauvin, K. Schollbach and H.J.H. Brouwers, "Evaluating environmental impact of geopolymer and straw-based wood wool cement boards," under peer review.

5.1. INTRODUCTION

Wood wool cement boards (WWCB), composed of wood wool fibres bonded with ordinary Portland cement (OPC), are widely used for acoustic and thermal insulation in buildings [107, 108]. To reduce the high embodied carbon associated with OPC manufacturing, geopolymers have emerged as alternative binders, enabling the production of wood wool geopolymer boards (WWGB). **CHAPTER 4** [179] has demonstrated the feasibility of using geopolymers as a viable alternative to OPC in WWGB production, providing insights into manufacturing methods, design parameters, and performance. Additionally, straws, by-products of crop production, have been identified as potential non-wood fibres for creating straw-geopolymer composites [157, 180, 117, 165, 122], suggesting the feasibility of replacing commercially produced wood wool in the production of straw geopolymer boards (SGB).

However, there is a research gap in the actual quantification of the environmental benefit and a comprehensive life cycle assessment (LCA) on these alternative raw material substitutions. To validate the environmental advantages of alternative raw materials, LCA systematically assesses various potential environmental impacts. Previous LCA studies on geopolymers [181, 182, 141] indicate that alkali activators and heat curing are dominant factors affecting environmental impacts. Additionally, the allocation method for industrial and agricultural by-products, including fly ash (FA), ground granulated blast furnace slag (GGBFS), and straws, requires detailed consideration.

FA and GGBFS could be categorized as waste or by-products of industrial processes. According to the European Waste Framework Directive [183], both FA and GGBFS are defined as by-products rather than end-of-waste. This classification is reinforced in the Netherlands, where both FA and steel slags are deemed by-products, as outlined in legal opinions [184, 185] and case law [186]. Despite these clarifications, technical issues such as allocation methods remain undefined, and industry actions further introduce complexity. CEMBUREAU (European Cement Association) considers both GGBFS and FA as by-products of steel and electricity production, respectively, applying economic allocation, as reflected in their official environmental product declaration (EPD) for CEM II and CEM III [187, 188]. Conversely, GCCA (Global Cement and Concrete Association) and PCA (Portland Cement Association) recommend no allocation when utilizing GGBFS and FA in cement production, considering them as waste from previous life cycles [189, 190]. Meanwhile, the World Steel Association [191] advocates the system expansion method for GGBFS, or an alternative physical partitioning method proposed by Eurofer (European Steel Association) [192], both resulting in higher greenhouse gas (GHG) emissions for BFS compared to economic and no allocation methods [192].

LCA studies [182, 143] reveal similar concerns, where different allocation scenarios significantly impact the overall life cycle performance of FA or GGBFS-based geopolymer composite. Applying mass allocation to FA or GGBFS may result in more than double the global warming potential (GWP) in geopolymer compared to OPC, while economic allocation could yield a similar GWP to OPC [182], potentially disincentivizing the replacement of OPC with conventional industrial by-product. Conversely, applying no allocation methods could lead to under-reporting the overall environmental footprint of the products.

Wood wools are commercially produced from wood logs harvested from forest plantations, typically spruce woods. While wood is considered a renewable biomass resource, the environmental impacts from its harvesting must be accounted for, which are closely related to forest management and supply chain practices [193, 194, 195]. On the other hand, straws are abundant, sustainable, and cost-effective sources of low-embodied carbon raw materials [57]. Agricultural by-products such as straws are excluded from the European Waste Framework [183]. This exclusion aligns with the European Renewable Energy Directive [196], which classifies straw as agricultural waste and residue, primarily promoting renewable biofuels. Proposals for fair allocation between the agriculture sector and other industries utilizing agricultural by-products as raw material are available, based on mass, energy, or economic values [197].

To quantify the raw material and manufacturing requirements for LCA, WWGB production from **CHAPTER 4** is referenced, while SGB are manufactured following the same WWGB fabrication procedure. Two commonly available straw types, wheat and barley straws, are selected for SGB production based on their status as the top two grain crops produced in the Netherlands. Both straws possess distinct physical properties and chemical compositions, with barley straw having a wider and fuller stalk than wheat straw, along with higher wax and lignin contents [198]. However, unprocessed straws may require additional treatment, such as alkali treatment, to improve adhesion between fibres and binders by decreasing fibre hydrophobicity and roughness [131]. In contrast, wood wools are specifically produced into thin flat strains for optimized production of WWCB, where additional treatment is not necessary. The influence of fibre selection and treatment, both physically and environmentally, requires investigation.

This chapter aims to investigate the environmental performance of insulation boards using alternative raw materials. Straws as alternative fibres for wood wool, and geopolymer as an alternative for OPC, are explored as substitutes in WWCB production. To ensure the feasibility of these substitutions, SGBs are fabricated, and their physical characteristics are compared against WWGB and WWCB. The life cycle assessment from the perspective of material replacement, allocation method, and design parameters are investigated and discussed.

5.2. MATERIAL AND METHODOLOGY

5.2.1. Material and fabrication

Wheat and barley straws, obtained locally from Strobouwer, the Netherlands, in bale form, are used in this study without further processing. Class F fly ash (FA) and ground granulated blast furnace slag (GGBFS) from the Netherlands are also employed. The average particle sizes (d_{50}) of FA and GGBFS are determined to be 13.9 μm and 19.3 μm, respectively, using a laser particle size analyzer (Mastersizer 2000). Chemical composition analysis of FA and GGBFS is performed via X-ray fluorescence spectrometry (XRF) (PANalytical Epsilon 3), with their loss on ignition (LOI) determined between 105 to 1000°C, as detailed in **Table 4.1** from **CHAPTER 4**.

The alkali activator used in this study comprises sodium silicate solution (27.7% SiO_2, 8.4% Na_2O and 63.9% H_2O) and sodium hydroxide (NaOH) pellets. Sodium hydroxide solutions of 0.5M and 1.0M are prepared for fibre treatment.

5.2.2. Design parameters and manufacturing methods

This study refers to the optimized parameters from **CHAPTER 4**, which include a blend weight ratio of 95% FA and 5% GGBFS for the precursor, an alkali activator with a modulus of 1.8 and Na_2O concentration of 8%, a water-to-dry components ratio of 0.4, and a weight percentage of fibres set at 30% of the total dry weight (fibres and dry geopolymer).

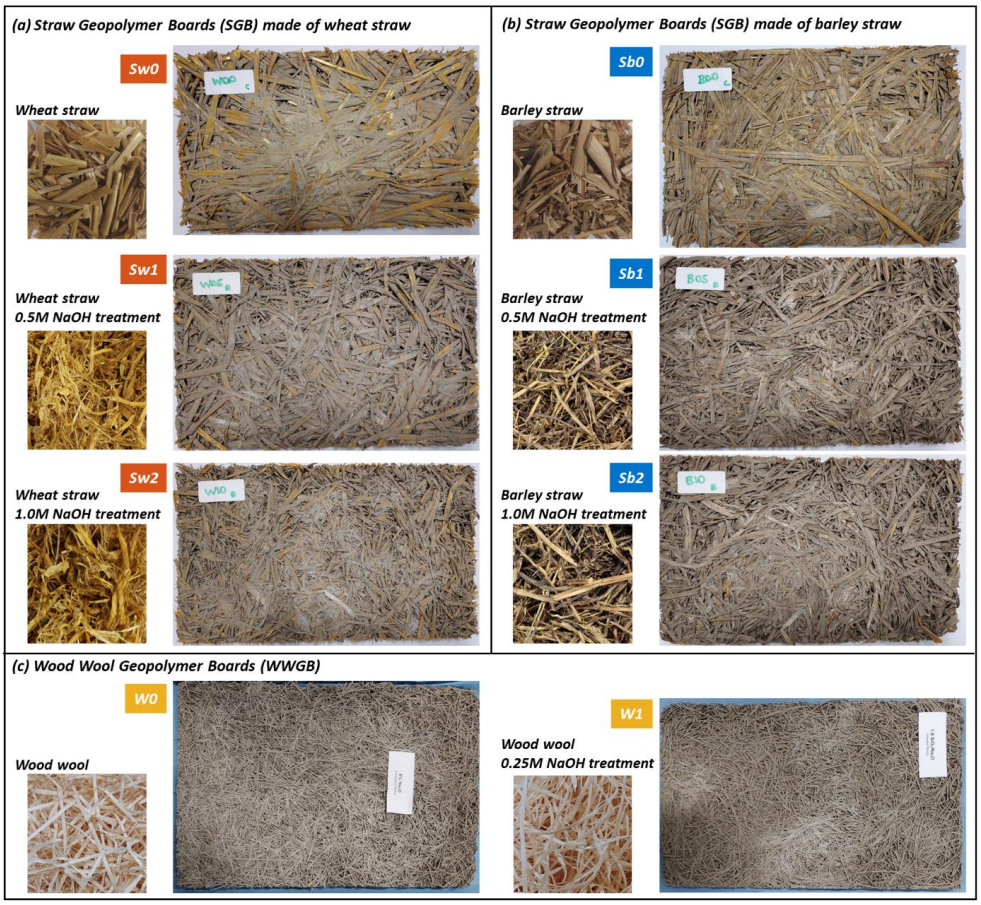

Fig. 5.1 SGB and WWGB samples (with their fibre components) manufactured for this study.

The fibre treatment process involves a 24-hour immersion in a sodium hydroxide solution, followed by a rinse with water to remove any residual alkali and impurities. The fibres are then dried under ambient conditions. Alkali activators are synthesized in advance by blending a sodium silicate solution, sodium hydroxide pellets, and additional water to achieve the desired composition.

During the main production process, the fibres are pre-wetted by spraying with water at a ratio of 0.4 water-to-fibre. The precursor materials and alkali activator solution are then mixed until a homogeneous paste is achieved. This geopolymer mixture is applied to the fibres and thoroughly mixed to ensure optimal binder coating on the surfaces. The resulting mixture is transferred into a mould and compressed overnight. After 24 hours, the compressed board is removed from the mould, wrapped in plastic foil, and cured overnight in an oven at 60°C for 24 hours. Following the curing process, the plastic is removed, and the board is further dried in an oven at 60°C for another 12 hours. The board is then removed from the oven, representing the final SGB, and trimmed to its final dimensions (300x200x15 mm^3).

This study includes two different Wood Wool Geopolymer Boards (WWGB), one with fibre treatment (0.25M NaOH treatment) and one without. For the Straw Geopolymer Boards (SGB), six different samples are fabricated, involving two design parameters: straw types (barley and wheat straws) and NaOH concentration for fibre treatment (0M, 0.5M, and 1.0M). **Fig. 5.1** shows the SGB and WWGB samples manufactured for this study.

5.2.3. Environmental assessment

In this study, the life cycle assessment (LCA) method conforms to EN 15804+A2 [199], which provides standardized product category rules for construction products. Notable amendments compared to the previous version, EN 15804+A1 [200], include an expansion of core environmental impact indicators from 7 to 13, with further subdivisions such as global warming potential and eutrophication. Additionally, it is now obligatory to encompass life cycle stages beyond cradle to gate (modules A1-A3), extending to end of life (modules C1-C4) and benefits and loads beyond the system boundary (module D) for all construction products, with no exemption granted to products containing biogenic carbon. However, in this study, the focus is on comparative analysis, assuming similar life cycle profiles for modules C and D for WWCB, WWGB and SGB. This includes incineration of discarded boards at the end-of-life cycle and similar benefits from energy production through incineration for all. Alternatively, both geopolymer and OPC-based boards are assumed to be crushed and utilized for different applications at their end-of-life stages (C1-4) [201]. Therefore, modules C and D are excluded, with only modules A1-A3 considered. **Fig. 5.2** illustrates the applied system boundary applied for the LCA, encompassing raw material supply (A1), transportation (A2), and manufacturing (A3).

Thirteen core environmental impact indicators and six additional indicators as per EN 15804+A2 [199] are included in the analysis. Additionally, a single weighted scope (SWS) on these characterized indicators is incorporated, calculated following guidelines from [202]

$$SWS = \sum_{i=1}^{n} \frac{characterized\ indicators_i}{NF_i} x\ WF_i \tag{5-1}$$

where the normalized factors (NF) are based on Environmental Footprint (EF) 3.1 [203], and weighting factors (WF) are based on [204].

Two life cycle inventory databases are utilized: Ecoinvent 3.8 (Nov 2021) and Agri-footprint version 6 (June 2022). Additionally, environmental product declaration (EPD) for FA and GGBFS

are referenced. **Table 5.1** details the inputs and their corresponding data sources, with LCA software SimaPro 9.4 employed for the calculation.

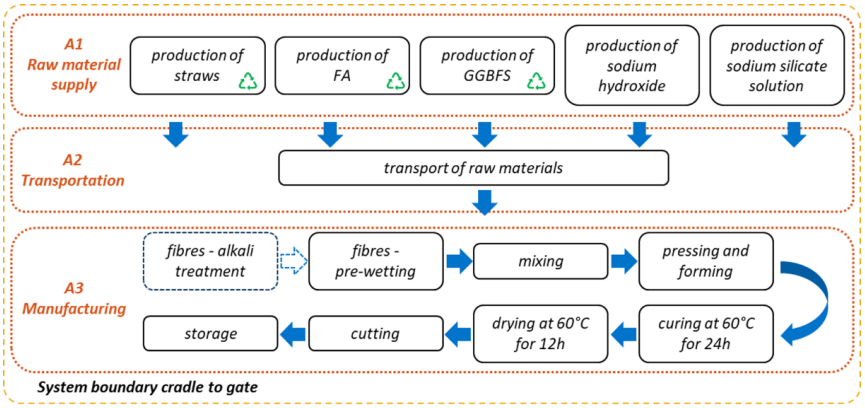

Fig. 5.2 LCA system boundary applied for the life cycle assessment for modules A1-A3.

Table 5.1 Input to life cycle assessment for modules A1-A3.

Input	Data sources	Data unit and descriptions
Barley straw	Agri-footprint 6	1 kg Barley straw at farm {NL} Economic.
Wheat straw	Agri-footprint 6	1 kg Wheat straw at farm {NL} Economic.
Straw handling	Ecoinvent 3.8	1 p Baling {RoW}processing
Straw handling	Ecoinvent 3.8	1 p Bale loading {RoW}processing
Wood wool	Ecoinvent 3.8	1 kg Wood wool {RER}
Sodium hydroxide	Ecoinvent 3.8	1 kg Sodium hydroxide, without water, in 50% solution state {RER}
Sodium silicate	Ecoinvent 3.8	1 kg Sodium silicate, without water, in 37% solution state {RER}
FA	EPD	1 ton fly ash [205]
(allocation)	Ecoinvent 3.8	1 kWh Electricity high voltage {NL}electricity production. hard coal
GGBFS	EPD	1 ton ground granulated blast furnace slag [206]
(allocation)	Ecoinvent 3.8	1 kg Pig iron {RER} pig iron production
OPC	Ecoinvent 3.8	1 kg Cement Portland {Europe without Switzerland}
Water	Ecoinvent 3.8	1 kg Tap water {RER}
Transport	Ecoinvent 3.8	1 tkm Transport freight lorry 16-32 metric ton euro6 {RER}
Energy	Ecoinvent 3.8	1 kWh Electricity low voltage {NL}

[Geographies classification in databases: NL-Netherlands; RER-Europe; RoW-World;]

To investigate the impact of the allocation method on life cycle analysis, three allocation scenarios are included in the study. Scenario 1 aligns with the European Waste Framework Directive [183], considering FA and GGBFS as by-products while treating straws as waste. Scenario 2 considers all

FA, GGBFS and straws as by-products, taking part of the environmental burden from their main productions, i.e. coal power production to FA, pig iron production to GGBFS, and crops harvesting to straws. Scenario 3 considers FA, GGBFS and straws as waste rather than by-products, taking no burden from their main productions.

Module A1 – Raw Material Supply:

The FA utilized in this study was originally supplied by Vliegasunie B.V., Culemborg, now handled by BauMineral GmbH. The EPD for FA from BauMineral GmbH is referenced [205, 207], where the system boundary commences after the electrostatic precipitator in the coal power plant, without allocation from the main coal power generation. GGBFS is originally sourced from ENCI, IJmuiden. In the absence of an EPD from ENCI, the EPD from a similar local supplier, Ecocem, Moerdijk, is referenced [206]. The EPD's system boundary starts from the quenching process and the subsequent drying and milling processes, without taking allocation from the blast furnace operation for steel production. Assumptions are made to establish the economic allocation scenarios for FA and GGBFS. Based on [143], 1 kg of pig iron production is associated with 0.24 kg of slag as a by-product and 1 kWh of electricity power generation is associated with 0.367 kg of coal as a fuel source and 0.052 kg of FA as a by-product. The economic allocation of FA and GGBFS is based on [141], with 2.59% from pig iron production and 1% from coal power production allocated to slags and FA production.

Economic allocation for barley and wheat straws is available in the Agri-footprint database, with no allocation scenario estimated by calculating the straw handling process. Notably, the Agri-footprint database does not consider biogenic carbon storage; therefore, the uptake of biogenic carbon is approximated using standard EN 16449 [208].

Module A2 – Transportation:

Wheat and barley are cultivated extensively in regions including North Brabant, with 7% and 11% of land use per region per crop type [209] respectively. Tree farming and sawmills are also present in North Brabant [210, 209]. All fibres (wheat straw, barley straw, and wood wool) are assumed to be locally sourced within this region, with an estimated distance of 50 km from the source to the production site (Eindhoven). Two coal power plants are operational in the Netherlands, namely Maasvlakte and Eemshaven power stations [211]. The FA used is obtained from Vliegasunie, Culemborg and processed at their Maasvlakte plant, with minimal additional processing [212]. There is only one active blast furnace steel plant in the Netherlands [213], where the raw material blast furnace slag (BFS) is obtained. The GGBFS is supplied by HeidelbergCement ENCI, Ijmuiden, and the BFS is further processed (dying and milling) into GGBFS. Both materials are transported approximately 150 km from their sources. Freight transport category Euro 6 is applied [214] in this study.

Module A3 – Manufacturing:

Energy consumption (E) required for curing and drying processes is approximated using [182]

$$E = P_{oven} \cdot t + m \cdot C_p \cdot (T - T_{amb}) \tag{5-2}$$

where P_{oven} is the power of the oven, t is the curing or drying time, m is the mass of specimens, C_p is the specific heat capacity of specimens, T is the curing or drying temperature, and T_{amb} is the ambient temperature. The first term describes energy used to maintain temperature, and the second term describes energy used to heat materials. The first term can be further generalized by assuming a steady rate of heat transfer between the oven and the ambient environment:

$$P_{oven} = S_{oven} \cdot \lambda_{oven} \cdot (T - T_{amb}), \quad (5\text{-}3)$$

where S_{oven} is the conduction shape factor of the oven, and λ_{oven} is the effective thermal conductivity of the oven wall [215]. The estimation of energy consumption is based on the lab equipment utilized in this study.

5.2.4. Physical characteristics

To ascertain the viability of substituting raw materials in WWCB, specifically with SGB, an investigation into the physical characteristics of SGB is conducted and subsequently compared with those of WWGB.

The mechanical properties, including compressive and bending strengths, are evaluated using a mechanical testing system (Instron 5967) equipped with a 5 kN load cell. Compressive strength at 10% deformation (σ_{10}) is determined following the procedure outlined in EN 826 [151]. Test specimens measuring 50x50x15 mm^3 are prepared from the samples. The compression stress at a strain of 10% (σ_{10}) is recorded, with the minimum required σ_{10} at 20 kPa [149] serving as the reference for compressive strength evaluation. For the measurement of bending strength, the testing method specified in EN 12089 [150] is applied. Samples are cut into dimensions of 150x125x15 mm^3. The maximum force exerted during the bending test is recorded to calculate the bending strength (σ_b), with the minimum required σ_b value of 1700 kPa [149] considered as the reference for bending strength assessment.

Thermal conductivity (λ) is determined using the transient line source method with a thermal needle probe (AP Isomet model 2104). The probe, known for its accuracy of 5% of the reading plus 0.001 $W \cdot m^{-1} \cdot K^{-1}$, is employed under standardized conditions, with all samples conditioned at a relative humidity of 50 ± 5%. Measurements are conducted at room temperature (20 ± 2°C), with three readings taken at different locations on each board to account for potential variation within the sample.

The hygroscopic sorption properties of the samples are determined following standard ISO 12571 [152]. Sorption isotherms are measured by the saturated salt solutions method, covering specific relative humidity levels ranging from 0% to 85%. Moisture uptake is monitored by weighing the samples at 24-hour intervals using a digital balance until a constant mass is reached, defined as three successive weighings showing a mass loss change of less than 0.1%.

Microstructure analysis is conducted through an optical microscope (ZEISS Axio Imager 2).

Particle density is determined using a helium pycnometer (Micromeritics AccuPyc II 1340) with a 10 cm^3 cup is used. The pycnometer has a reading accuracy of 0.03% and an additional 0.03%

uncertainty related to the sample capacity. From the measured particle density, the porosity φ (%) of the specimen is calculated using **Eq. (2-1)**.

Chemical composition analysis is performed using Fourier transform-infrared (FT-IR) spectroscopy in conjunction with an attenuated total reflection (ATR) attachment (PerkinElmer Frontier FT-IR). This technique facilitates the identification and characterization of functional groups present in the samples, with spectra collected over a wavenumber range of 4000 to 400 cm^{-1} at a resolution of 1 cm^{-1}.

Thermogravimetric analysis (TGA) is employed to assess mass loss or decomposition events to temperature, utilizing a thermogravimetric analyser (TA Instruments TGA Q500). The heating process, starting from room temperature and continuing up to 1000°C at a rate of 10°C·min^{-1}, is conducted under a controlled nitrogen atmosphere with a constant flow rate of 60 ml·min^{-1}.

5.3. RESULTS AND DISCUSSION

5.3.1. Physical characteristics

The primary interconnecting structures within the composites are formed by the aluminosilicate hydration products of the geopolymer. Compared to WWGB samples, the geopolymer gels do not adhere as effectively to the surface of the straws in SGB samples. SGB samples made with untreated straws, both Sw0 and Sb0, display the weakest binder-to-straw adhesion, with partially coated straws detaching from the board during handling. For treated straws, the geopolymer binder exhibits improved coverage, but small areas of exposed straws can still be observed on all SGB samples, as depicted in **Fig. 5.3** for Sw1 and Sb1.

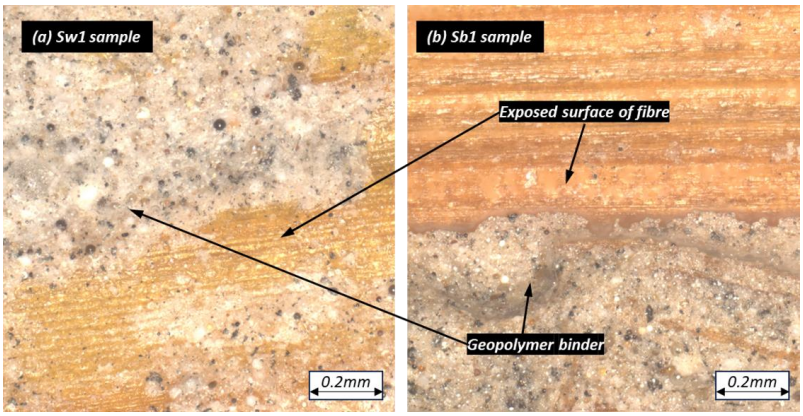

Fig. 5.3 Geopolymer binder and exposed surface of straw fibres for sample Sw1 and Sb1.

Fig. 5.4a illustrates the bending strength of the samples. It is evident that all SGB samples, irrespective of fibre treatment, exhibit lower strength than WWGB and do not meet the minimum bending strength requirement specified in EN 13168 for a 15mm thick board (1.7 MPa) [149]. Overall, wheat-based SGB demonstrates better bending strength compared to barley-based SGB.

SGB samples incorporating treated straws demonstrate higher bending strengths due to the removal of non-cellulose components and the presence of mercerised cellulose structures, which enhance adhesion with the geopolymer gels [157, 131]. However, the bending strength for Sw2 is lower than Sw1, indicating the dissolution of core cellulose structure within wheat straws under higher NaOH concentrations. Additionally, the structural cellulose of treated straws may undergo further alkaline hydrolysis during the geopolymerisation process, further weakening the cellulose structure. Conversely, the bending strength for Sb2 is slightly higher than Sb1, suggesting that barley straws remain more intact. This observation aligns with the higher lignin and wax-to-cellulose ratio for barley straws [198]. Higher alkali concentration is therefore necessary to significantly affect the structural cellulose.

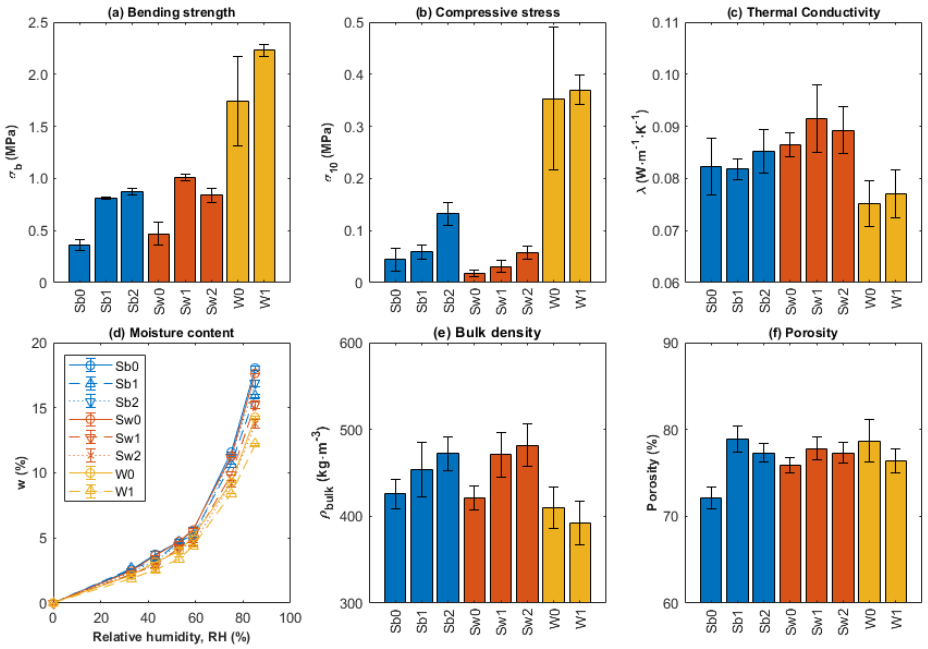

Fig. 5.4 (a) bending strength, (b) compressive strength, (c) thermal conductivity, (d) sorption isotherms, (e) bulk density, and (f) porosity of SGB and WWGB samples.

The compressive strength is mainly derived from the formation of aluminosilicate hydration products providing interconnecting strength within the composites, as discussed in **CHAPTER 4** [179]. SGB exhibits lower compressive stresses at 10% strain (σ_{10}) than WWGB, as shown in **Fig. 5.4b**. However, all samples meet the minimum requirement specified in EN 13168 (0.02 MPa) [149] for handling purposes. Sb2 exhibits better compressive strength compared to Sw2, indicating a higher degree of fibrillation on treated barley straw compared to wheat straw, providing additional interfacial bonding between the fibres and geopolymer gels. However, this high degree of fibrillation compromises bending strength.

Fig. 5.4c shows the thermal conductivity of the samples. Overall, barley-based SGB has slightly lower thermal conductivities than wheat-based SGB, attributed to the different microstructures of

their fibres. Barley straw has larger pores and thicker wall structures [198], which could lower the overall thermal conductivity of their composite. An increasing trend is observed when treated fibres are utilized, indicating a denser structure encouraging heat transfer. SGB has slightly higher thermal conductivity than WWGB, possibly due to thicker geopolymer binder forming in cluster areas on straws compared to a more homogeneous layer on wood wool.

Fig. 5.4d shows the sorption isotherms of SGB and WWGB samples. Overall, sorption for both SGB and WWGB decreases when treated fibres are utilized, attributed to the alkali treatment degrading the cell wall material and reducing the number of hydroxyl groups accessible to water, resulting in increased hydrophobicity [131, 148]. Barley-based SGB exhibits a higher sorption capacity, followed by wheat-based SGB and then WWGB, correlated with the existence of macropores in barley straw [198] compared to wheat straws and wood wool.

The bulk density and porosity of SGB and WWGB are shown in **Fig. 5.4e** and **5.4f**. Generally, SGB made with treated straws have higher bulk densities than those made of untreated straws, confirming a higher amount of geopolymer binder bonded to the treated fibres. Wheat-based SGB has slightly higher densities than barley-based SGB but lower compressive strength, indicating uneven distribution and adherence of aluminosilicate products to wheat-based SGB, agglomerating in the composite. It can be seen that Sb2 has a higher bulk density but lower porosity than Sb1, similarly between Sw2 and Sw1, indicating that at a more widely distributed gel formation on the straws treated with 1.0M NaOH compared to 0.5M NaOH. Conversely, WWGB has lower bulk densities than SGB but significantly higher compressive strength, indicating a lower gel-to-fibre ratio, with a thin layer but interconnected gel network formed in the composite, providing necessary strength at lower bulk density.

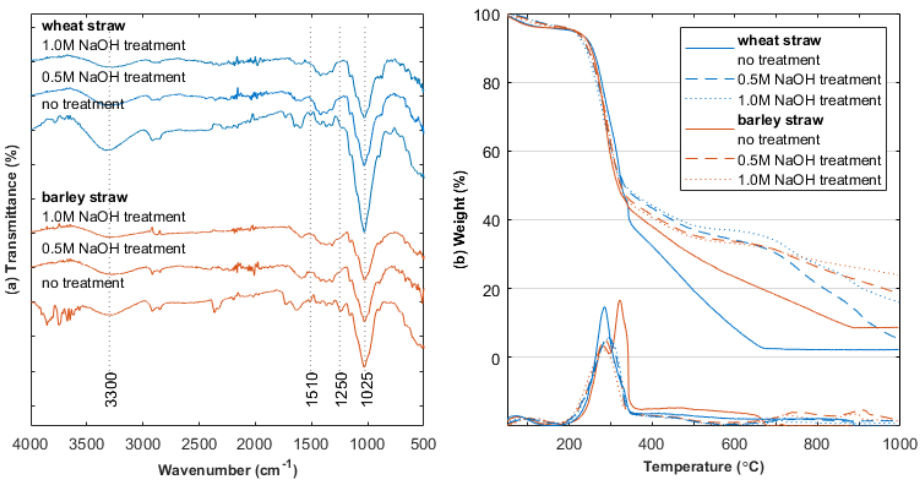

Fig. 5.5 (a) FTIR and (b) TGA of barley and wheat straw samples used in this study.

The effect of alkali treatment on straws is further verified using FTIR and TGA, presented in **Fig. 5.5**. Similar to the previous study on wood wool alkali treatment [179], both 0.5M and 1.0M NaOH treatment of straws leads to delignification, resulting in the reduction of characteristic peaks

associated with lignin vibrations at 1250 cm^{-1}, C-O ester vibrations peak at 1025 cm^{-1} [168], and aromatic skeletal vibration at 1510 cm^{-1} [169]. Additionally, a significant reduction in peak intensity at 3300cm^{-1} associated with the OH group [170] suggests disruption of intermolecular hydrogen bonding in cellulose or a decrease in free water content within the treated fibres. The thermogravimetric analysis confirms the delignification of the straws, with untreated straws exhibiting the highest mass loss followed by treated straws, indicating a higher degree of delignification with higher NaOH concentration. The main peak, spanning from 200 to 400°C, corresponds to the decomposition of hemicellulose and cellulose [178], and the lignin components pyrolyzed in the range of 225 and 450°C [54].

Overall, SGB performs poorly compared to WWGB, even when alkali-treated straws are utilized to improve adhesion with the geopolymer gels. Therefore, utilizing alternative non-wood fibres such as straws, as a substitute for wood wool, reveals disadvantages in overall performance, making it a less attractive solution.

5.3.2. Environmental assessment

Fig. 5.6 presents the cradle-to-gate environmental impact indicators, as per EN 15804+A2, for straw geopolymer board (SGB) and wood wool geopolymer board (WWGB), in comparison to wood wool cement board (WWCB). Both wheat-based SGB and barley-based SGB exhibit similar impact profiles, with only wheat-based SGB (Sw0, Sw1, and Sw2) shown for clarity. Under allocation scenario 3, which considers straws, FA, and GGBFS as waste rather than by-products, the lowest impacts are generally observed. Conversely, allocation scenario 2, where FA, GGBFS and straws are treated as by-products, has the highest impact due to taking on part of the environmental burden from their main productions. Surprisingly, under all allocation scenarios, both SGB and WWGB demonstrate higher environmental impacts across more than half of the 19 impact categories compared to WWCB. Under a no-allocation scenario, 10 and 12 impact indicators are higher for Sw0 and W0, respectively, increasing to 14 under a full-allocation scenario. Using the single weighted score based on the Environmental Footprint (EF-SWS) method, only Sw0 under a no-allocation scenario demonstrates a lower score than WWCB. Sw2 under a full-allocation scenario emerges as the worst case, with 16 out of 19 indicators showing higher impacts than WWCB, with EF-SWS as high as 181% compared to WWCB under a full-allocation scenario, strongly suggesting overall adverse environmental impacts from fibre alkali treatment.

Fig. 5.7 details the percentage contribution from different components (fibres, binders, treatment, transport, manufacturing, allocation). Generally, binders, both OPC and geopolymer, dominate most indicators, followed by the manufacturing process, primarily heat curing and drying in the oven. This emphasizes that while substituting OPC with geopolymer can reduce embodied carbon in module A1 (raw material), the need for heat curing in FA-based geopolymer increases impacts in module A3 (manufacturing). Alkali treatment on fibre is another major contributor, commonly used to modify fibre properties, especially when employing agricultural waste or by-products as alternative raw materials for building materials. Transportation is minimal in general as all materials are assumed to be locally sourced in the Netherlands, but it could become a dominant factor if raw materials are not locally produced.

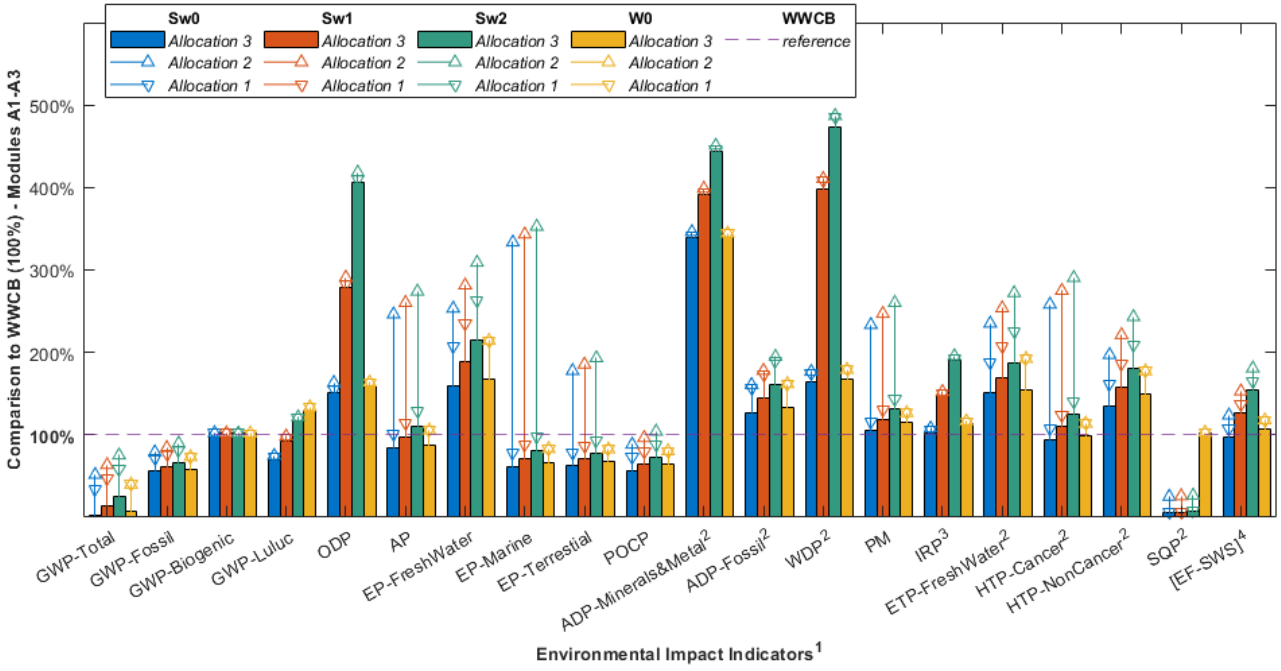

Fig. 5.6 Core and optional environmental impact indicators of SGB and WWGB relative to WWCB, modules A1-A3, under different allocation scenarios (1-marker-∇, 2-marker-Δ, 3-bar).

[1. global warming potential (GWP); land use and land use change (luluc); depletion potential of the stratospheric ozone layer (ODP); Acidification potential (AP); eutrophication potential (EP); formation potential of tropospheric ozone (POCP); abiotic depletion potential (ADP); water deprivation potential (WDP); particulate matter emissions (PM); ionizing radiation potential (IRP); eco-toxicity (ETP); human toxicity potential (HTP); soil quality potential (SQP)

2. The results of these environmental impact indicators should be used with care as there is limited experience with the indicators and the uncertainty is high.

3. This impact category deals mainly with the eventual impact of low-dose ionizing radiation on the human health of the nuclear fuel cycle. It does not consider effects due to possible nuclear accidents, occupational exposure or radioactive waste disposal in underground facilities. Potential ionizing radiation from the soil, radon and some construction materials is also not measured by this indicator.

4. Additional single weighted score (SWS) based on the Environmental footprint (EF) method. GWP-biogenic is excluded from the calculation.]

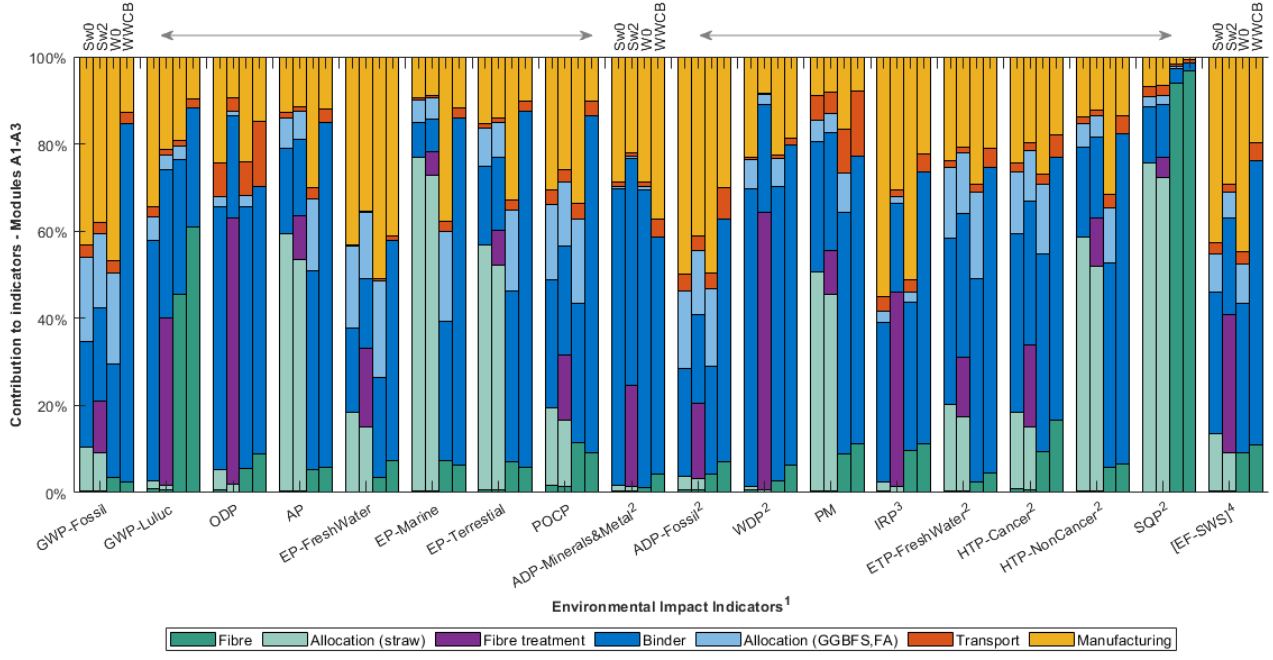

Fig. 5.7 Percentage contribution to different environmental impact indicators for SGB, WWGB and WWCB, based on component groupings under the Allocation 2 scenario. Global warming potential total (GWP-total) and biogenic (GWP-biogenic) are excluded from the chart for clarity.

*[1, 2, 3, 4. Similar notes as per **Fig. 5.6**]*

Table 5.2 Environmental impact of wheat straw, barley straw, FA and GGBFS for different impact indicators, per kg of raw material, based on no allocation and economic allocation.

Impact Indicator[1]	Unit	Wheat straw		Barley straw		FA		GGBFS	
		No allocation	Economic allocation	No allocation	Economic allocation	No allocation	Economic allocation	No allocation	Economic allocation
GWP-Total	kg CO_2 eq.	-1.7E+00	-1.4E+00	-1.7E+00	-1.4E+00	3.5E-02	2.3E-01	3.2E-02	2.1E-01
GWP-Fossil	kg CO_2 eq.	1.1E-02	2.5E-01	1.1E-02	2.8E-01	3.5E-02	2.3E-01	3.2E-02	2.1E-01
GWP-Biogenic	kg CO_2 eq.	-1.7E+00	-1.7E+00	-1.7E+00	-1.7E+00	-1.3E-04	-6.1E-04	2.9E-05	-5.4E-04
GWP-luluc	kg CO_2 eq.	9.4E-06	2.8E-05	9.4E-06	3.2E-05	4.2E-06	2.8E-05	9.8E-06	6.1E-05
ODP	kg CFC11 eq.	1.1E-09	1.0E-08	1.1E-09	1.1E-08	8.5E-10	2.6E-09	4.7E-09	1.2E-08
AP	mol H+ eq.	7.4E-05	1.0E-02	7.4E-05	1.2E-02	1.0E-04	6.3E-04	1.3E-04	8.0E-04
EP-FreshWater	kg P eq.	2.0E-06	2.2E-04	2.0E-06	2.9E-04	1.6E-05	1.2E-04	9.6E-07	7.3E-05
EP-Marine	kg N eq.	2.5E-05	4.9E-03	2.5E-05	4.8E-03	2.6E-05	1.6E-04	3.6E-05	1.9E-04
EP-Terrestial	mol N eq.	2.7E-04	2.1E-02	2.7E-04	2.4E-02	2.6E-04	1.6E-03	4.1E-04	2.1E-03
POCP	kg NMVOC eq.	8.2E-05	9.7E-04	8.2E-05	9.9E-04	6.7E-05	4.1E-04	1.1E-04	1.0E-03
ADP-Mineral&Metal[2]	kg Sb eq.	9.5E-08	4.1E-07	9.5E-08	4.6E-07	7.8E-08	1.4E-07	6.7E-08	2.0E-07
ADP-Fossil[2]	MJ	2.0E-01	1.0E+00	2.0E-01	1.0E+00	3.8E-01	2.5E+00	4.8E-01	2.3E+00
WDP[2]	m^3 depriv..	3.3E-03	7.0E-03	3.3E-03	7.7E-03	5.3E-04	1.4E-02	1.7E-03	1.1E-02
PM	disease inc.	4.0E-10	5.0E-08	4.0E-10	5.8E-08	4.4E-10	2.0E-09	7.9E-10	1.3E-08
IRP[3]	kBq U-235 eq.	6.4E-04	4.0E-03	6.4E-04	4.7E-03	4.4E-04	2.2E-03	6.2E-04	3.9E-03
ETP-FreshWater[2]	CTUe	1.6E-01	1.0E+01	1.6E-01	1.3E+01	6.0E-01	4.1E+00	1.8E-01	5.6E+00
HTP-Cancer[2]	CTUh	9.6E-12	2.2E-10	9.6E-12	2.6E-10	5.8E-12	3.1E-11	1.4E-11	9.9E-10
HTP-NonCancer[2]	CTUh	1.8E-10	3.5E-08	1.8E-10	4.1E-08	3.4E-10	1.6E-09	2.1E-10	4.0E-09
SQP[2]	Pt	5.3E-02	2.3E+01	5.3E-02	2.9E+01	7.7E-02	3.6E-01	6.9E-02	4.3E-01
EF-SWS[4]	Pt	2.0E-04	6.1E-03 (Δ 30-fold)	2.0E-04	7.0E-03 (Δ 35-fold)	3.2E-04	2.0E-03 (Δ 6-fold)	3.2E-04	2.5E-03 (Δ 8-fold)

*[1, 2, 3, 4. Similar notes as per **Fig. 5.6**]*

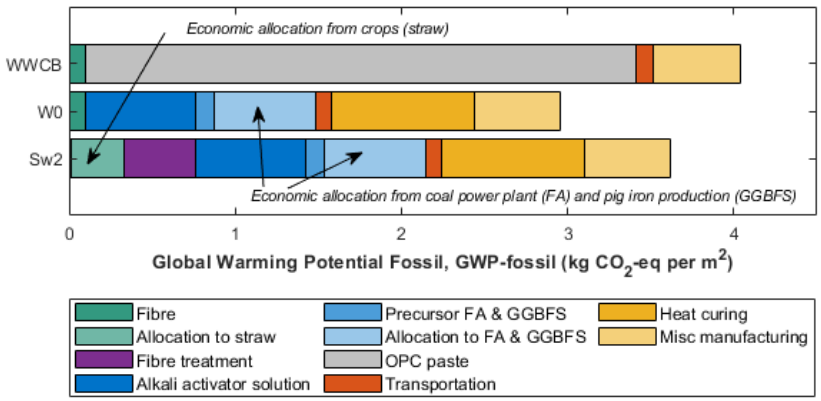

Fig. 5.8 Global warming potential fossil fuel (GWP-fossil) and global warming potential total (GWP-total) for Sw2, W0 and WWCB under allocation 2 scenario, showing contributions from different materials and processes.

Specifically, substituting OPC with geopolymer as a binder significantly reduces GWP from fossil fuel (GWP-fossil) by avoiding the energy-intensive production of OPC. Replacing wood wool with straws reduces GWP from land use (GWP-luluc) and water use (SQP) by avoiding timber harvesting for wood wool production.

Treating FA and GGBFS as by-products leads to significantly increased impact categories such as climate change, eutrophication, and human toxicity. Similarly, higher impact indicators can also be seen when straws are treated as by-products. The influence of treating these materials as waste or by-products is summarized in **Table 5.2**, aligning with calculations from [141]. Based on EF-SWS, there is a 6-fold increase in FA, and an 8-fold increase in GGBFS for the weighted average of all impact categories, when environmental burdens from coal power and pig iron productions are allocated. Similarly, a substantial 30-fold and 35-fold increase in wheat and barley straws occurs respectively when the burden from crop production is allocated to them.

Fig. 5.8 further details the contribution of different components to indicator GWP-fossil. Geopolymer binder reduces overall emissions under all allocation scenarios, but the need for heat curing on FA-based geopolymer diminishes this reduction. Under allocation scenario 2 (all economic allocation), there is a total reduction of 27% in GWP-fossil from WWCB to W0 and a reduction of 21% from WWCB to Sw0. If following the current practice where FA and GGBFS are considered as by-products but straws as waste (allocation scenario 1), a total reduction of 29% in GWP-fossil for Sw0 is accounted for. Allocation scenario 3, considering FA, GGBFS, and straws as waste, results in a total reduction of 42% for W0 and 44% for Sw0 from WWCB. However, in the context of the Netherlands, where FA and GGBFS are treated as by-products, allocation scenario 3 may under-account. Notably, GGBFS allocation based on physical and chemical partitioning by the steel industry is higher than the allocation by economic value applied in this study [192]. Since the same fibre mass is used in the design of SGB and WWGB, no significant difference is expected in the biogenic carbon stored in these boards, which will be released into the

atmosphere at the end of their life cycle, accounting for module C1-C4 which are not included in this study.

Fig. 5.9 shows the percentage change in GWP-fossil under different parameters, using sample Sw2 under allocation scenario 1 as the benchmark. Overall, for every 1% increase in Na_2O concentration and 0.1 increase in SiO_2-to-Na_2O modulus of the alkali activator, an increase of 2.5% and 0.7% occurs respectively. Conversely, increasing the percentage of GGBFS in FA-based geopolymer precursor does not significantly affect GWP. However, the local availability of FA and GGBFS plays a significant role in transportation emissions. An increase of 1 tkm between the raw material supplier and end production facility leads to a 0.5% increase in GWP. With the phasing out of blast furnace facilities and coal power plants, the local availability of FA and GGBFS may diminish, rendering their use as precursors impractical and resulting in higher GWP. Similarly, the local availability of fibre sources is crucial. While both straws and wood wool are assumed to be equidistant in this study, local availability should be a primary consideration when seeking substitutions. Additionally, treatments such as alkali treatment applied to straws in this study significantly reduce the environmental benefits of using agricultural waste as alternative fibres. An increase of up to 1.3% is expected for every additional 0.1M NaOH concentration. However, the recovery and recycling of waste alkali solutions after fibre treatment, which may reduce their environmental impacts, are not considered in this study. Curing temperature and duration significantly influence GWP, with each increment of 1°C and 1 hour resulting in a 1.0% and 1.3% increment in GWP, respectively. Therefore, optimal curing temperature and time, including drying requirements, should be carefully considered with both technical and environmental factors in mind.

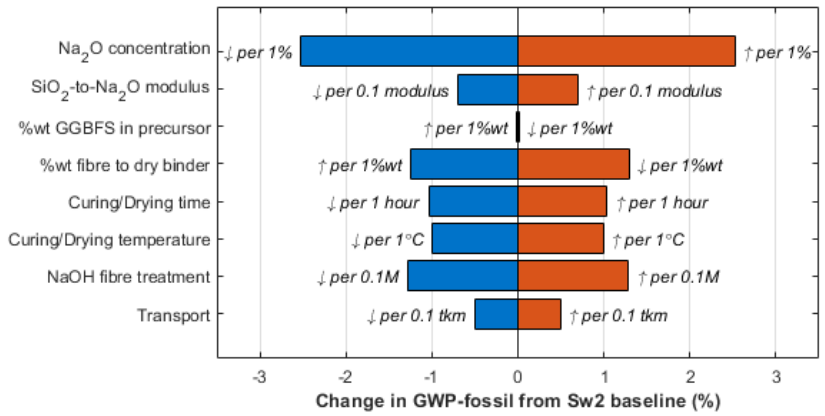

Fig. 5.9 Change in GWP-fossil against change in design parameters used in this study, based on sample Sw2 under allocation scenario 1.

5.4. CONCLUSIONS

This chapter explores the use of industrial and agricultural by-products as alternative raw materials in the production of insulation boards, specifically straw geopolymer boards (SGB). Here, straws serve as alternative fibres for wood wool, and geopolymer functions as a substitute for OPC.

The environmental impact indicators, as per EN 15804+A2, are assessed for SGB and compared to wood wool geopolymer board (WWGB) and wood wool cement board (WWCB). The focus of the investigation is on the implications of allocation methods for the raw materials, namely FA, GGBFS, and straws. These materials are either treated as by-products, sharing part of the environmental burden from their main productions, or as waste, thus not accounting for any burden from their main productions. Treating FA and GGBFS as by-products results in significantly increased impact categories such as climate change, eutrophication, and human toxicity. A similar increase in impact indicators is observed when straws are treated as by-products.

Both SGB and WWGB exhibit higher environmental impacts across more than half of the 19 impact categories compared to WWCB. Binders (precursor and alkali activator) dominate most indicators, followed by heat curing and drying in the oven. This highlights the trade-off between embodied carbon reduction in module A1 (raw material) and heat curing in FA-based geopolymer in module A3 (manufacturing). Alkali treatment on fibre is another major contributor, especially when characteristic improvement is required for fibre substitution. Transportation plays a minimal role; however, it could become a dominant factor if raw materials are not locally produced.

When considering only global warming potential (GWP), substituting OPC with geopolymer binder reduces overall emissions under all allocation scenarios. However, substituting wood wool with straws does not provide additional environmental benefits, especially when fibre treatment and economic allocation scenarios are applied.

In terms of physical performance, SGB performs poorly overall compared to WWGB. Lower mechanical strengths are observed even when alkali-treated straws are utilized. Exposed straws are visible on SGB samples, indicating uneven distribution and adherence of aluminosilicate products to the straws. While alkali treatment of straws leads to delignification and improved adhesion with the geopolymer gels, the strength improvement is not sufficient before high NaOH concentration destroys the core cellulose structure of the straws, subsequently impacting its bending strength.

This chapter indicates the environmental benefits of substituting OPC with geopolymer in terms of global warming potential. However, it is less obvious when considering other impact indicators. Utilizing straws as a substitute for wood wool reveals disadvantages in overall performance, making it less attractive as a solution. The substitution of wood with other alternative non-wood fibres is challenging and does not guarantee better sustainability. For life cycle assessment, a consistent allocation method for by-products is strongly recommended to avoid over or under-reporting environmental impacts across different industries.

6. AEROGEL COMPOSITE FOR CAVITY WALL REHABILITATION IN THE NETHERLANDS: THERMAL AND HYGRIC CHARACTERISTICS AND ITS HYGROTHERMAL PERFORMANCE

ABSTRACT

Energy retrofitting of existing building stocks is essential to reduce building-related energy consumption. Cavity wall insulations are commonly applied, however, their hygrothermal performance is not well established. This chapter focuses on the hygrothermal performance of rehabilitated cavity walls in the Netherlands. A state-of-the-art aerogel composite developed for cavity wall retrofitting using the blown-in method is presented. The aerogel composite has a dry thermal conductivity of 22.5 $mW \cdot m^{-1} \cdot K^{-1}$ and low sorption isotherms. A retrofitted masonry wall with a 6 cm cavity using the aerogel composite can achieve thermal transmittance (U-value) of 0.32 $W \cdot m^{-2} \cdot K^{-1}$, well below the 0.71 $W \cdot m^{-2} \cdot K^{-1}$ required in the Netherlands. It can reduce the annual heating and cooling demand by up to 72% in a simulated building, and also provides better thermal comfort to the occupants, lowering the percentage of thermally dissatisfied occupants from 51% to 18%. The tested aerogel composite outperforms conventional insulation materials in the market, without sacrificing the thermal comfort of its occupants.

The results presented in this chapter are published in the following article:

C.H. Koh, K. Schollbach, F. Gauvin, and H.J.H. Brouwers, "Aerogel composite for cavity wall rehabilitation in the Netherlands: Material characterization and thermal comfort assessment," Building and Environment 224, 109535 (2022).

6.1. INTRODUCTION

In 2020, energy consumption related to buildings in the services and households sectors accounted for 37% of the total energy consumption in the Netherlands, with the majority being used for space heating [8]. To curb greenhouse gas (GHG) emissions, the Dutch government has pledged to bring CO_2 emissions in the building sector down to net zero by 2050 [216]. Achieving this goal necessitates the energy retrofitting of existing building stocks.

Prior to the 1920s, Dutch residential buildings were predominantly constructed with single brick walls, which often necessitate an expensive rehabilitation strategy [9]. However, from the mid-1920s onwards, houses built with cavity walls started to emerge in the Netherlands. By the late 1970s, thermal insulation requirements were introduced for new buildings, leading to wider cavity walls filled with better insulation material instead of air. Buildings with cavity walls, constructed between the 1920s and 1970s, can be insulated without requiring extensive renovation. These buildings account for approximately 40% of the total housing stock, equivalent to more than 3 million homes in the Netherlands, and offer a significant potential for attainable CO_2 emission reduction. In 2020 alone, over a million energy-saving measures were implemented in existing housings in the Netherlands, with cavity wall insulation being one of the most common [8], and more than 3 million m^2 of cavity filling was carried out by certified contractors [11].

A typical cavity-filling procedure involves drilling holes in the outside façade and blowing the insulation material into the cavity through these holes. The holes are then grouted at the end of the filling [217]. In the Netherlands, the most commonly used blown-in insulation materials for cavity walls are glass wool, stone wool, and expanded polystyrene (EPS) beads, followed by polyurethane (PU) foam, urea-formaldehyde (UF) foam, and silicone-treated perlite. A brick wall with a 6 cm air cavity without any insulation material has a thermal transmittance (U-value) of around 2.50 $W \cdot m^{-2} \cdot K^{-1}$, which can be reduced to 0.59 $W \cdot m^{-2} \cdot K^{-1}$ once new insulation material is filled in [217]. This improved U-value meets the maximum U-value of 0.71 $W \cdot m^{-2} \cdot K^{-1}$ prescribed for wall renovation in an existing building [218].

To further enhance the U-value of retrofitted cavity walls using the blown-in insulation method, for instance, to reach the 0.21 $W \cdot m^{-2} \cdot K^{-1}$ required for a new building [219], an innovative, high-performance insulation product is crucial. Superinsulation materials, with thermal conductivity values below 20 $mW \cdot m^{-1} \cdot K^{-1}$, are often employed, particularly silica aerogel composites due to their low thermal conductivity, which can reach 12 $mW \cdot m^{-1} \cdot K^{-1}$ in their monolithic form, 15 $mW \cdot m^{-1} \cdot K^{-1}$ for an aerogel blanket, and 18 $mW \cdot m^{-1} \cdot K^{-1}$ in the granulate form [220].

Currently, aerogel particles in the granulate form are commercialized as insulating cavity wall infill. An example of retrofitting is a detached house in Biel, Switzerland, where aerogel granulate was blown into the cavity walls with a 90 mm air gap, improving their U-value from 1.10 to 0.18 $W \cdot m^{-2} \cdot K^{-1}$ [12]. Other forms of blown-in aerogel insulation are under investigation. An aerogel product 'Spacefill' was tested during the EFFESUS project [221], which is based on polyester fibre impregnated with aerogel, similar to an aerogel blanket. The composite was cut into 5 mm cubes and achieved thermal conductivity in the range of 18 to 25 $mW \cdot m^{-1} \cdot K^{-1}$ under both laboratory and mock-up testing [222, 223]. Another state-of-the-art aerogel composite 'Airofill' has been developed for cavity wall retrofitting using the blown-in method. This product contains silica

aerogel granulates, which are bound together with a propriety binder in a slurry form. Once the composite is blown into the cavity wall, it solidifies, dries up, and forms a continuous foam block inside. Other sprayable aerogel composites that can be used for cavity wall retrofitting offer thermal conductivity in the range of 20 to 27 $mW \cdot m^{-1} \cdot K^{-1}$ [224, 225].

The original air gap in a cavity wall is designed to regulate moisture transport and drain water in the cavity through air ventilation. Therefore, there is a concern that a filled cavity may lead to inferior hygrothermal performance, subsequently impacting the thermal comfort of its occupants. To address this concern, it is crucial to study the performance of blown-in insulation in a cavity wall under different environmental conditions. However, there is a gap in the literature related to hygrothermal performance after cavity wall rehabilitation, either using conventional blown-in insulation material or aerogel composite. The thermal conductivity of loose-fill blown-in stone wool, glass wool, and cellulose can be compromised under humid conditions [226]; but there are some indications that aerogel composites (blanket [227, 228, 229, 230, 231] and render [232]) work well to protect the wall and alleviate moisture risk owing to the hydrophobic nature of its main component, silica aerogel. Case studies using aerogel composites (in the form of blankets and boards) for refurbishments for heritage buildings suggest an improvement in comfort level inside the buildings [12]. Studies also found that applying aerogel-based render on exterior walls can prevent condensation risk in existing buildings [233, 234], however, the hygrothermal risk is predicted to increase in colder climates [234].

The hygrothermal performance of rehabilitated cavity walls has not been widely studied, and more investigations are required to examine the efficiency and their impacts on occupant thermal comfort conditions under a retrofitted building. This comparative study aimed to verify the performance of commercially available and state-of-the-art aerogel composite using the blown-in installation method. The thermal and hygric characteristics of the aerogel composite are examined and used to simulate the hygrothermal performance under a cavity wall construction and a typical Dutch climate, and conventional insulation materials are included for comparison purposes. Occupant thermal comfort conditions are further included to study the ergonomics of the thermal environment of a reference building using a simulation tool.

6.2. MATERIAL AND METHODOLOGY

6.2.1. Material

The Airofill, henceforth referred to as the 'aerogel composite,' is the chosen material for blown-in insulation in cavity wall retrofitting. The aerogel composite was made by and supplied by Takkenkamp, Zelhem. The sample in foam block form is shown in **Fig. 6.1a**, which is mainly made up of hydrophobic silica aerogel granulates which are bound together with a proprietary organic binder and other additives for rheology modification and durability improvement. The composite is pre-mixed and kept in a slurry form in a tank prior to site operation. By using a blowing machine, the composite is blown into the cavity wall via an injection nozzle, and subsequently solidifies and dries up within the wall under an ambient environment to form a continuous brittle foam block inside. It is important to note that the binder plays a crucial role in binding the aerogel granulates

during and after the retrofitting process. This is to prevent the aerogel granulates from dispersing into the surroundings (via leakage), which could potentially pose a health hazard to the occupants.

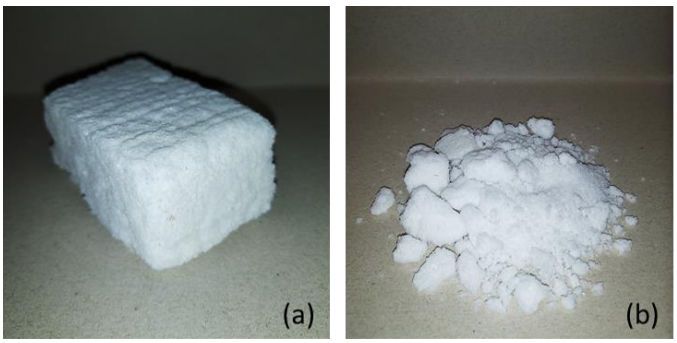

Fig. 6.1 Sample of the aerogel composite in (a) block form and (b) fragments.

6.2.2. Characteristics assessment

The sorption isotherm of the aerogel composite is determined using the gravimetric sorption technique through dynamic vapour sorption (DSV) (Surface Measurement Systems DVS Resolution). The DVS apparatus has a declared accuracy of 0.5% (relative humidity reading) and a balance noise of less than 0.3 μg. Three sets of fragmented samples, each weighing 12-15 mg, are prepared. Initially, the samples are dried in an oven at 70°C until a constant mass is achieved to determine their dry weight (m_{dry}). The moisture content (w) of the specimen is then measured using the DVS apparatus, ranging from 0% to 95% relative humidity RH for the sorption curve, and from 95% back to 0% RH for the desorption curve, all at a constant temperature of 20°C. The specimen is deemed to have reached its constant mass once the rate of mass change (dw/dt in $\%kg \cdot kg^{-1} \cdot min^{-1}$) is equal to or less than 0.01. The equilibrium moisture content (w in $\%kg \cdot kg^{-1}$) is plotted against RH (%) for both sorption and desorption curves, with the median result being considered.

Free water saturation (w_{sat}) is approximated by conditioning the specimen at 100% RH. This is achieved by fully immersing the specimen in water for 7 days at room temperature, an approximation method based on ASTM C1498-01 note 3 [41]. The surface of the samples is then lightly blotted with a damp sponge to remove excess water, and their weight is measured. Three sets of samples, each measuring 40x40x35 mm^3, are prepared, and the median result is taken to remove any outliers.

The water vapour diffusion resistance factor (μ) is measured using both the wet cup (distilled water) method and the dry cup (desiccant) method, as per the ASTM E96 standard [42]. The cups are filled with anhydrous calcium chloride ($CaCl_2$) for the dry cup method and distilled water for the wet cup method. Specimens with a thickness (d_μ in m) are attached to the cups with a specific exposed area (A_μ in m^2) and the edges are sealed with aluminium tapes to prevent vapour passage at the edge of the specimen. The test cups are kept in a climatized room at 60% RH and 20°C. The change of mass (Δm in kg) over successive time intervals (Δt in s) is determined by weighing the

cups to obtain the density of water vapour transmission rate (g in $kg \cdot m^{-2} \cdot s^{-1}$) using **Eq. (2-2)**. The measurement is deemed complete when five successive values of g vary within ± 5%. The dimensionless value of μ is then calculated using **Eq. (2-3)**. For each cup, a set of 40x40x35 mm^3 samples is prepared.

The total porosity of the specimen, encompassing both open and closed pores, is calculated from their particle density ($\varrho_{particle}$ in $kg \cdot m^{-3}$) and bulk density (ϱ_{bulk} in $kg \cdot m^{-3}$) using **Eq. (2-1)**. A helium pycnometer (Micromeritics AccuPyc II 1340) with a 10 cm^3 cup is employed to measure their $\varrho_{particle}$.

The steady-state thermal transmission test method is used to measure the thermal conductivity (λ in $W \cdot m^{-1} \cdot K^{-1}$) using a heat flow meter (Thermtest HFM-25), which has a declared accuracy of 3% of the reading. The specimen is placed between a pair of heating-cooling isothermal plate assemblies, with an upper-temperature setpoint at 30°C and a lower setpoint at 10°C, reaching an equilibrium mean temperature of 20°C for the specimen. The steady-state heat flux generated due to the temperature difference between the heating-cooling plates is used to measure the thermal resistance and calculate the thermal conductivity. Three sets of 40x40x20 mm^3 samples are prepared and conditioned separately under three RH (0%, 58% and 75%) for their λ values. The samples are dried at 70°C in an oven (Memmert universal oven UF260) to reach near 0% RH and conditioned in a desiccator under aqueous solutions [41] for 58% RH (sodium bromide NaBr) and 75% RH (sodium chloride NaCl), all until a constant mass is achieved. The samples are protected using low vapour permeability plastic wrap before and during the λ measurements to maintain their moisture content. The average measurement time for each specimen is around one hour, potentially causing redistribution of the moisture in the sample, and resulting in an additional error in the measurement results. This limitation, however, is disregarded here, and the moisture content is assumed to be constant throughout the specimen. In this study, the temperature dependence of the thermal conductivity is omitted and assumed to be constant within the simulated temperature range.

For specific heat capacity (C_p in $J \cdot kg^{-1} \cdot °C^{-1}$), differential scanning calorimetry (TA Instruments DSC Q2000) is used at temperatures ranging from -20°C to 50°C at a heating/cooling ramp of 10 $°C \cdot min^{-1}$ in a nitrogen atmosphere with a flow of 50 $ml \cdot min^{-1}$. Three heat-cool cycles are run for the sample, and the C_p value at 20°C from the third heat cycle is taken for the subsequent hygrothermal study. A 3 mg sample of crushed material is prepared.

A thermogravimetric analyzer (Netzsch Instruments STA F1 Jupiter Analyzer) is further used to investigate the thermal stability of samples from 40°C up to 800°C at a heating rate of 10 $°C \cdot min^{-1}$ in a nitrogen atmosphere with a flow of 20 $ml \cdot min^{-1}$ by observing their mass change due to thermal degradation.

6.2.3. Hygrothermal performances assessment

Simulations of heat, air and moisture transport (HAM) are conducted on masonry wall assemblies with a cavity thickness of 6 cm, exposed to identical climates. The annual moisture content of the insulation materials is analysed. A building featuring masonry cavity walls is further modelled to simulate the indoor climate, evaluating occupant comfort.

The HAM simulations involve solving one-dimensional non-steady heat and moisture transport processes using coupled differential equations. This is achieved using WUFI Pro software [19]. The heat transport and moisture transport are represented by **Eqs. (1-1)** and **(1-2)**, respectively.

The assembly wall design in this study is based on the common exterior wall found in older buildings in the Netherlands, specifically, a masonry wall with a 6 cm thick air cavity, as depicted in **Fig. 6.2a-b**. Glass wool, stone wool and PU foam are included in the HAM study as reference materials. For the masonry wall, solid bricks of 10 cm thickness are applied on both exterior and interior sides. The properties of the referenced insulation materials and the masonry are listed in **Table A.3** and **Fig. A.4** (see **Appendix A**). The original cavity wall, without insulation, is modelled with an arbitrary air change rate of 10 h^{-1} (between the 5 and 20 h^{-1} used in [46]) in its cavity.

Eindhoven in the Netherlands is chosen as the location for the hygrothermal analysis. **Table B.5** (see **Appendix B**) presents the annual weather summary, while **Fig. B.2** (see **Appendix B**) displays the annual air temperature and relative humidity profile [235]. The Netherlands experiences a temperate oceanic climate, classified as Cfb type according to the Köppen climate classification. For all hygrothermal simulations, the wall faces the main driving rain direction (southwestern). The interior climate is set as per EN 13788 to humidity class 3, which represents a building with unknown occupancy [48], and a constant air temperature of 20°C. The simulation is run for ten years or until a hygrothermal equilibrium is achieved. The boundary and initial conditions are summarized in **Table B.6** (see **Appendix B**).

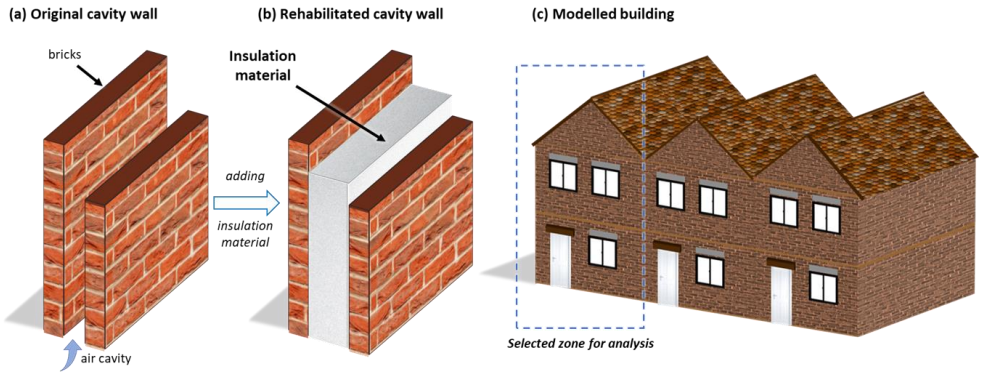

Fig. 6.2 (a) Simulated masonry cavity wall without and (b) with insulation material, and (c) building model for simulation.

6.2.4. Indoor climate and occupant comfort assessment

The indoor climate and comfort conditions within a reference building, characterized by masonry cavity walls, are examined in detail using the WUFI Plus software. This examination involves calculating the balance of heat and moisture transfers within the room [21]. The heat balance and moisture balance are represented by **Eqs. (1-3)** and **(1-4)**, respectively.

A model of terraced housing, a common architectural style in the Netherlands [236], is constructed for this study. For simplicity, the model comprises only three small housing units (as shown in **Fig. 6.2c**), with the simulation results from the corner unit selected for analysis. Each housing unit in the model measures 5 m x 8 m x 2.8 m (W x D x H) per floor, with a heated floor area of 80 m^2 and an unheated attic. The simulation includes five different cases of masonry walls with a 6 cm cavity, i.e. four different insulation materials (aerogel composite, glass wool, stone wool, PU foam) and the original construction without insulation material. Other significant building components modelled include a ground floor assembly with a U-value of 0.0956 $W \cdot m^{-2} \cdot K^{-1}$, a roof assembly with a U-value of 0.0867 $W \cdot m^{-2} \cdot K^{-1}$, and glazing with a U-value of 0.8 $W \cdot m^{-2} \cdot K^{-1}$.

The indoor environment parameters are set according to standard EN 16798-1 [237] to achieve a medium level of indoor environmental quality category II (IEQ_{II}), which corresponds to a normal level of expectations for occupants. The model includes a heating and cooling system to maintain an indoor temperature between 20°C and 26°C, and a constant air volume mechanical ventilation system to provide a steady airflow of 7 $l \cdot s^{-1}$ per person. The indoor heat and moisture loads are based on the software's predefined four-person family household occupancy. No mechanical humidification and dehumidification are included to limit the indoor RH level in this study. For simplicity, natural ventilation is not considered as a factor regulating the indoor environment. The simulation is run for ten years, and the indoor temperature and RH are extracted for analysis. Two thermal comfort indices, as defined by ISO 7730 [238], are assessed: the predicted mean vote (PMV) index, which is based on a seven-point thermal sensation scale of an occupant, ranging from cold (-3) and hot (+3); and the predicted percentage dissatisfied (PPD) index, which predicts the percentage of thermally dissatisfied occupants, with values ranging from 0% (thermally satisfied) to 100% (dissatisfied). The boundary and initial conditions are summarized in **Table B.7** (see **Appendix B**).

6.3. RESULTS AND DISCUSSION

6.3.1. Characteristics assessment

The aerogel composite has a bulk density of 88.6 $kg \cdot m^{-3}$ and a porosity of 93.4% (**Table 6.1**) in dry conditions. The specimen maintains its form under room temperature, however, is brittle and can easily be broken into pieces by hand (**Fig. 6.1b**). Despite this, its mechanical strength is not a concern as it is safeguarded within the cavity walls in its actual application.

The aerogel composite demonstrates low water vapour sorption properties, up to 95% RH. **Fig. 6.3** depicts the sorption isotherm of the aerogel composite and the duration for the specimen to reach mass equilibrium ($dw/dt=0.01\% kg \cdot kg^{-1} \cdot min^{-1}$) under the targeted RH. The equilibrium moisture content during the desorption process is marginally higher than the adsorption process, with no significant variation observed between the two curves. In a full immersion test, the aerogel composite can absorb more than four times its weight of water (**Table 6.1**). The presence of binders and other additives renders the aerogel composite less hydrophobic compared to pure silica aerogel. However, this water absorption is not problematic as the composite is shielded within the

cavity wall on both sides, thereby avoiding direct water exposure. The specimen exhibits a low water vapour resistance factor of 3 under both wet and dry cup methods (**Table 6.1**).

Table 6.1 Density, Porosity, Water Vapour Resistance Factor μ and Free Water Saturation for the aerogel composite.

	Aerogel Composite
Bulk density ϱ_{bulk}, dried (kg·m^{-3})	88.6
Particle density $\varrho_{partocle}$ (kg·m^{-3})	1340.7
Porosity (%)	93.4
Water vapour resistance factor μ	
- "Dry cup" condition (-)	3.4
- "Wet cup" condition (-)	3.4
Free water saturation w_{sat} (%)	428

The aerogel composite possesses a specific heat capacity (c_p) of 1273 J·kg^{-1}·°C^{-1} as illustrated in **Fig. 6.4**. This elevated heat capacity is primarily attributed to its organic binder component. The specimen exhibits a dry thermal conductivity of 22.5 ± 0.7 mW·m^{-1}·K^{-1} (**Fig. 6.5**) at room temperature, which is 7% higher than its primary silica aerogel granulates component at 21.1 ± 0.6 mW·m^{-1}·K^{-1}. At higher RH levels, the thermal conductivities rise to 22.9 ± 0.7 mW·m^{-1}·K^{-1} at 59% RH and 23.1 ± 0.7 mW·m^{-1}·K^{-1} at 75% RH. **Fig. 6.5** summarizes the moisture-dependent thermal conductivity, indicating a minor increase in thermal conductivity with higher RH. However, this trend is insignificant and falls within the measurement uncertainties. It is worth noting that only three data points were measured, yet a simple linear fitting is included in this study as input for subsequent hygrothermal simulation.

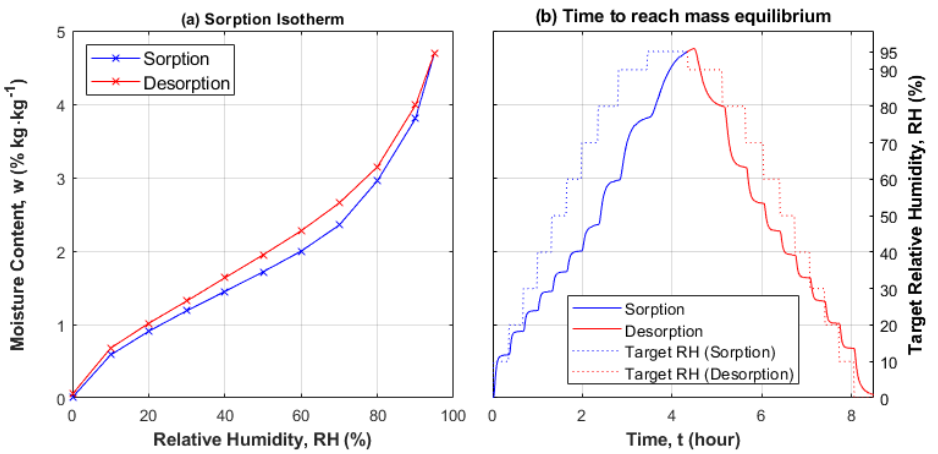

Fig. 6.3 (a) Sorption-desorption curves with moisture content plotted against RH and (b) time to reach mass equilibrium under dw/dt=0.01 for the aerogel composite.

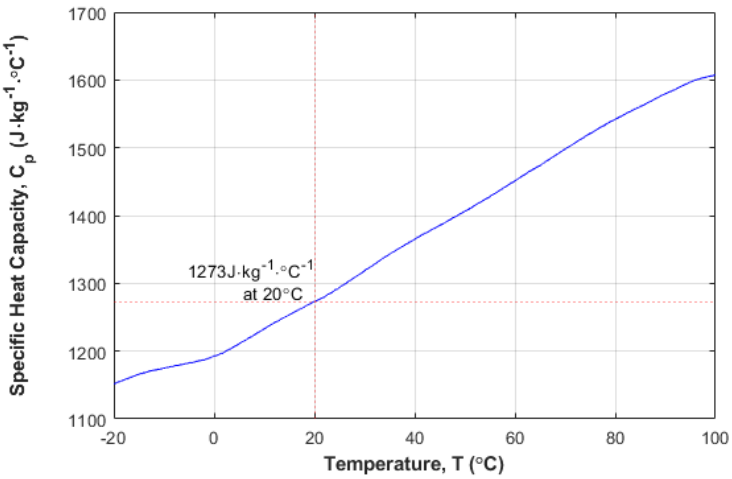

Fig. 6.4 Specific heat capacity against temperature for the aerogel composite. C_p value at 20°C is taken for subsequent hygrothermal study.

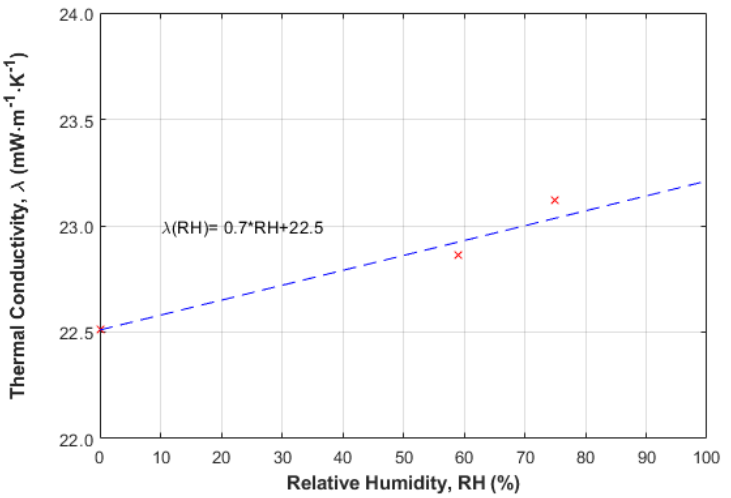

Fig. 6.5 Thermal conductivity λ against RH for the aerogel composite.

The thermogravimetric analysis of the sample is shown in **Fig. 6.6**. The composite begins to decompose at approximately 110°C, reaches its maximum rate of weight loss at 320°C, and is followed by another peak at 500°C. The composite concludes its volatile emissions at 650°C, retaining around 76% of the original dry weight.

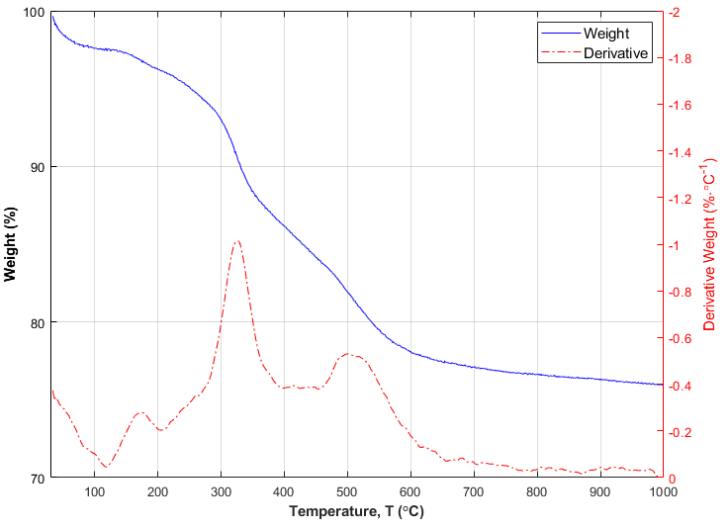

Fig. 6.6 Thermal stability against temperature for the aerogel composite.

6.3.2. Hygrothermal performance assessment

The reference masonry wall, designed with a 6 cm air cavity, has a U-value of 1.53 $W \cdot m^{-2} \cdot K^{-1}$. However, the application of the aerogel composite as a blown-in insulation material significantly improves this U-value, reducing it to 0.32 $W \cdot m^{-2} \cdot K^{-1}$. This performance surpasses the Dutch requirement for wall renovation, which stipulates a limit of 0.71 $W \cdot m^{-2} \cdot K^{-1}$, demonstrating the effectiveness of the rehabilitated wall using the aerogel composite.

When compared to conventional insulation materials (as shown in **Fig. 6.7**), the closed-cell PU foam achieves the second-lowest U-value after the aerogel composite, followed by glass wool and stone wool. All these reference materials meet the minimum U-value required for a retrofitted wall, assuming a cavity thickness of 6 cm. Notably, the aerogel composite stands out as the only insulation material capable of offering a new-build equivalent thermal insulation performance for cavity wall retrofitting, provided the cavity is sufficiently thick enough (e.g. 10 cm) for adequate insulation filling.

Fig. 6.7 summarizes the transient U-values of the retrofitted wall with the aerogel composite and reference materials, calculated using **Eqs. (2-4)** and **(2-5)**. A consistent trend of transient U-values is exhibited by the retrofitted wall, contrasting with the original wall without any insulation, irrespective of the type of insulation material inside the cavity. The insulating performance of the non-insulated wall is solely reliant on its brick component. The thermal conductivity of this component deteriorated under higher RH, shifting from 0.6 $W \cdot m^{-1} \cdot K^{-1}$ in dry conditions to 1.7 $W \cdot m^{-1} \cdot K^{-1}$ with a moisture content of 12.6%$kg \cdot kg^{-1}$ [239]. This shift results in highly fluctuating transient U-values.

Fig. 6.8 presents the equilibrium moisture content in the aerogel composite and reference materials over a simulated year. The aerogel composite exhibits the highest moisture content in all simulations, reflecting the reduced hydrophobic properties of the composite due to the inclusion of binder and additives, compared to standalone silica aerogel. Despite this, its average moisture content remains comparable to the PU foam and stone wool, albeit higher than the glass wool. The moisture content of the aerogel composite and the glass wool fluctuates more throughout the year compared to the PU foam and stone wool, which exhibit a narrower range.

Upon examining the moisture content at the interfaced layers adjacent to the exterior bricks and behind the interior bricks, it is evident that a higher moisture content accumulates at the exterior interfaced layer. For the aerogel composite and glass wool, significantly higher moisture contents are observed during the winter months, attributable to their enhanced moisture sorption properties under higher RH conditions during this period. All four insulation materials maintain a steady moisture content level at the interior interfaced layer.

Fig. 6.9 summarizes the surface condensation risk at different interfaced zones. The interface between the exterior bricks and insulation material for all rehabilitated walls exhibits a higher condensation potential compared to the original construction. However, no significant condensation risk is observed on the other interface layers, i.e. exterior bricks to outdoor climate, interior bricks to insulation material, and interior bricks to indoor climate. This observation aligns with the findings of Maia et al. [234], who predicted a higher condensation potential for a rehabilitated wall under a colder climate, or when there are larger differences in thermal conductivities between different layers (existing bricks and new insulation materials) [240].

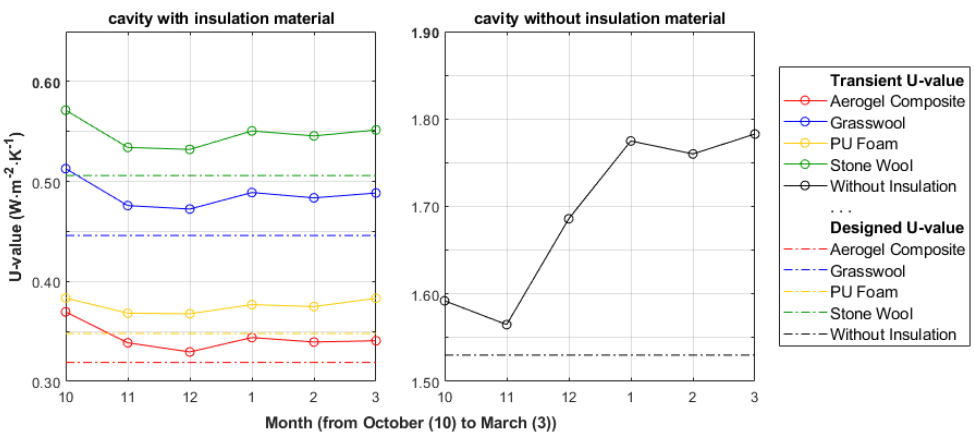

Fig. 6.7 Transient thermal transmittance (U-Value) for the masonry wall with aerogel composite, reference materials and original construction in the heating period (October to March).

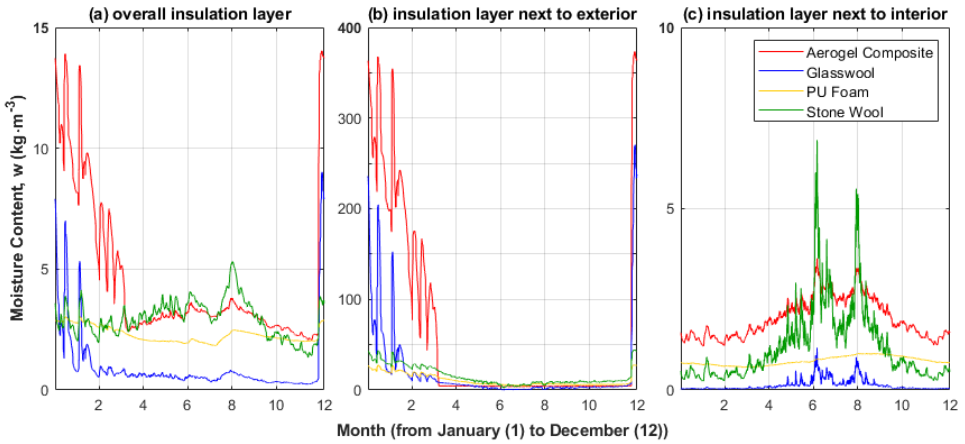

Fig. 6.8 Moisture content for the aerogel composite and reference materials in a masonry wall with 6 cm cavity thickness, showing (a) the overall insulation layer, (b) at insulation layer next to the exterior and (c) next to the interior.

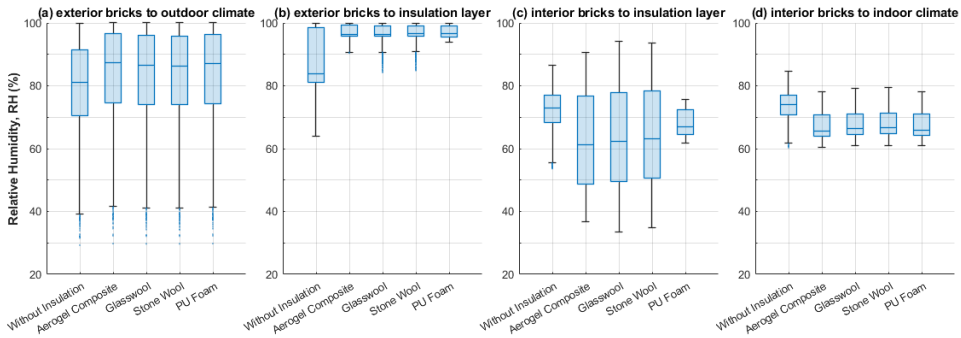

Fig. 6.9 Relative humidity of the (a) exterior bricks interface to outdoor climate, (b) exterior bricks interface to the insulation layer, (c) interior bricks interface to the insulation layer, and (d) interior bricks interface to indoor climate.

6.3.3. Indoor climate and occupant comfort assessment

Fig. 6.10 illustrates the simulated indoor air temperature, RH, and vapour pressure for five different cases of masonry walls with a 6 mm cavity. When this cavity is filled with insulation materials, the indoor RH of the reference building decreases, correlated to the changes in temperature. Specifically, it drops from an average of 60% RH for the original air cavity wall to 56%, 56%, 55% and 54% RH when filled with glass wool, stone wool, PU foam and aerogel composite, respectively.

In comparison to the IEQ_{II} limits (at 25% and 60% RH, respectively), 87% of the simulated hours in the reference building using aerogel composite fall within these limits. This is followed by PU

foam at 84%, glass wool at 82%, stone wool at 80%, and a mere 49% of the simulated hours in the original construction without insulated cavity walls.

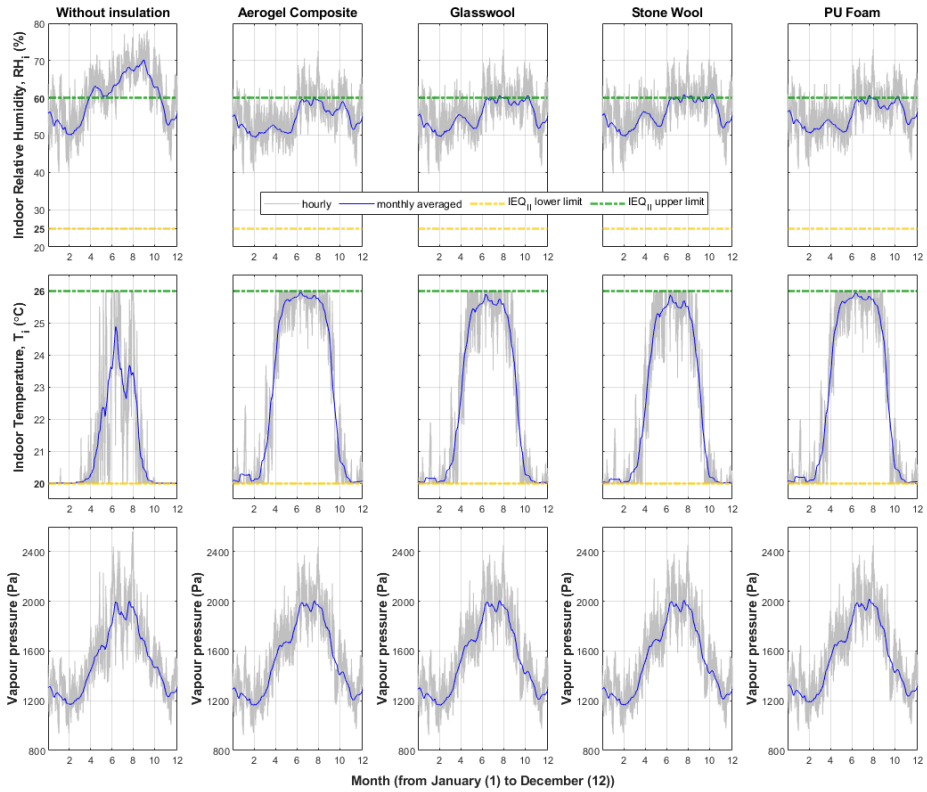

Fig. 6.10 Indoor relative humidity and temperature for the simulated building with masonry walls using aerogel composite, reference materials and original construction.

The indoor average room temperature experiences an increase from the original construction at 21°C to 22°C for rehabilitated construction using either glass wool or stone wool. It further increases to 23°C if using either PU foam or aerogel composite. This rise in mean temperature is directly associated with the annual heating and cooling demand of the reference building (**Table 6.2**). The annual heating demand is significantly reduced, with up to 84% reduction in the case of aerogel composite, followed by PU foam at 81%, stone wool at 76% and glass wool at 72% compared to the original construction. Conversely, the annual cooling demand increases two to threefold. However, the overall annual energy demand related to heating and cooling is still notably lower, with up to 72% reduction for the rehabilitated construction using aerogel composite. It is important to note that this model does not include natural ventilation (through openings) to regulate the indoor environment, which could potentially substitute for the cooling demand of the rehabilitated building during the summer period.

Fig. 6.11 displays the predicted mean vote (PMV) index and the predicted percentage dissatisfied (PPD) index of the reference buildings, with IEQ_{II}, IEQ_{III} and IEQ_{IV} representing medium, moderate, and low expectations, respectively, for the indoor environmental quality from occupants. The median PMV improves from -1.5 (cool) of the original construction to -0.8 (slight cool) of rehabilitated walls with aerogel composite, corresponding to the mean PPD of 51% and 18% of thermally dissatisfied occupants, respectively. While none of the rehabilitated buildings can reach a median PPD under either IEQ_{II} or IEQ_{III} due to the limited cavity thickness for applying insulation material inside, the rehabilitated buildings in all cases provide better thermal comfort than the original construction, with median PPD falling within the IEQ_{IV} limit. It is important to note that a lower PPD does not equate to an increase in health risk but merely a decrease in comfort level. The simulation results align with Ganobjak et al. [12], where case studies using different aerogel composites for building rehabilitation demonstrate an improvement in occupant thermal comfort.

Table 6.2 Annual heating and cooling demand per heated area for the reference building.

Masonry wall with 6 cm cavity	**Annual heating/cooling demand** (kWh·m^{-2})
Without insulation	260 / 8
With aerogel composite	43 / 33
With glass wool	72 / 22
With stone wool	63 / 25
With PU foam	49 / 29

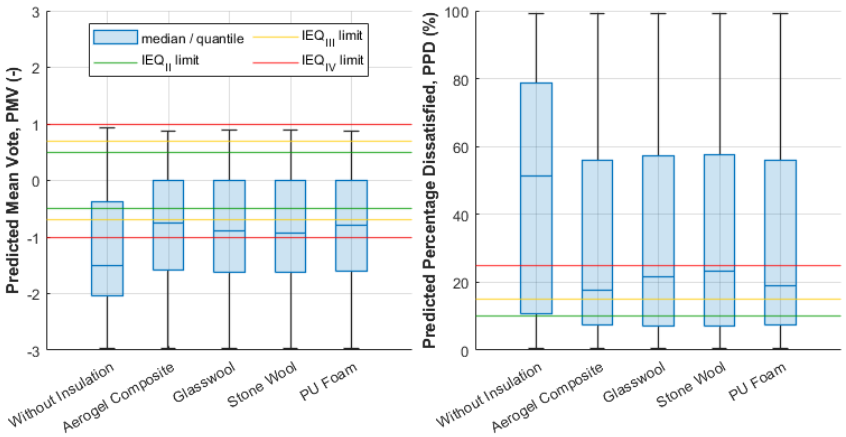

Fig. 6.11 Predicted mean vote PMV and predicted percentage dissatisfied PPD for the simulated building with masonry walls using aerogel composite, reference materials and original construction.

6.4. CONCLUSIONS

This chapter investigates the thermal and hygric properties of an advanced aerogel composite designed for cavity wall retrofitting. It simulates the hygrothermal performance of this composite in typical Dutch buildings that feature a cavity wall suitable for insulation material. The research also considers the thermal comfort level of occupants to evaluate the ergonomics of the thermal environment in the retrofitted reference building. For comparative analysis, three conventional insulation materials, i.e. closed-cell PU foam, stone wool, and glass wool, are included in the hygrothermal and thermal comfort assessment.

The aerogel composite demonstrates a remarkably low dry thermal conductivity of 22.5 $mW \cdot m^{-1} \cdot K^{-1}$ at 20°C, which is only 7% higher than that of pure silica aerogel granulates. It also exhibits a slight increase in thermal conductivity with higher RH. The composite maintains thermal stability up to 110°C before it begins to decompose. Additionally, it displays low water vapour sorption properties, a characteristic attributed to the hydrophobic nature of its primary silica aerogel component. The composite has a low density of 88.6 $kg \cdot m^{-3}$ and a porosity of 93.4%, along with a low water vapour resistance factor of 3.

The U-value designed for a retrofitted masonry wall with a 6 cm cavity using the aerogel composite is 0.32 $W \cdot m^{-2} \cdot K^{-1}$. This value is significantly lower than the 0.71 $W \cdot m^{-2} \cdot K^{-1}$ limit set for renovated walls under Dutch regulations. However, the aerogel composite exhibits a higher fluctuation of moisture content during the winter months at its interface layer adjacent to the exterior bricklayer. This is due to its enhanced moisture sorption properties under high RH conditions prevalent during the Netherlands' winter period.

When the cavity in masonry walls is filled with the aerogel composite, the indoor RH of the reference building decreases from an average of 60% RH for the original air cavity wall to 54% RH. This results in 87% of the simulated hours falling within the IEQ_{II} limits for a rehabilitated building using the aerogel composite, compared to only 49% in original construction without insulated cavity walls. The annual heating and cooling demands are significantly reduced, with up to a 72% reduction compared to the original construction.

The median PMV improves from -1.5 (cool) in the original construction to -0.8 (slightly cool) in rehabilitated walls with the aerogel composite. This corresponds to the mean PPD of 51% and 18% of thermally dissatisfied occupants, respectively. In all cases, rehabilitated buildings (using aerogel composite, glass wool, stone wool, or PU foam) provide better thermal comfort than the original construction, with median PPD falling within the IEQ_{IV} limit.

This chapter highlights the suitability of the tested aerogel composite for cavity wall retrofitting in the Netherlands' climate. It can outperform conventional insulation materials on the market without necessitating major renovation or compromising the thermal comfort of occupants. To validate the findings of this chapter, an in-field monitoring and survey campaign will be required. Additionally, a comprehensive life cycle assessment and cost analysis should be conducted to confirm the overall sustainability and economic viability of using aerogel composite in building rehabilitation.

7. A CIRCULAR APPROACH TO STONE WOOL: ALKALI-ACTIVATED LIGHTWEIGHT AGGREGATES

ABSTRACT

This chapter investigates the high-value recycling of stone wool from construction and demolition waste into alkali-activated lightweight insulation aggregates, designed for ground cover insulation. Various proportions of milled and as-is stone wools are alkali-activated to produce aggregates. The aggregates demonstrate loose bulk densities ranging from 720 to 850 $kg \cdot m^{-3}$ and dry thermal conductivity from 0.075 to 0.094 $W \cdot m^{-1} \cdot K^{-1}$, with moderate water sorption capacities. The fibre morphology of as-is stone wool influences rheology, introducing a greater number of pores or defects, which results in a decrease in mechanical strength. Hydrothermal simulations reveal that the floor assembly of the rehabilitated crawl space, partially filled with the fabricated aggregates, shows a reduction in water content and an increase in floor surface temperature. This observation suggests potential benefits for maintaining the structural integrity of buildings and enhancing occupant comfort.

The results presented in this chapter are published in the following article:

C.H. Koh, Y. Luo, K. Schollbach F. Gauvin, and H.J.H. Brouwers, "A Circular Approach to Stone Wool: Alkali-Activated Lightweight Aggregates," Developments in the Built Environment 19, 100506 (2024).

7.1. INTRODUCTION

In accordance with the European Waste Framework Directive [183], efforts to enhance the reuse, recycling and recovery of non-hazardous construction and demolition waste (CDW) have been mandated, with a target of achieving a minimum recycling rate of 70 % by weight. The Netherlands currently recycles approximately 88% of CDW [18]. However, despite these high recycling rates, the majority of recycled construction materials are downcycled or repurposed for backfilling. Specifically, recycled materials from CDW account for only about 8% of all construction materials used in new buildings, with the remainder primarily downcycled in infrastructural projects [18]. This practice does not align with the objectives of the National Circular Economy Programme established by the Dutch government to meet the growing demand for products and raw materials [241].

One of the key areas within the circularity action plans is the development of sustainable insulation materials. The goal is to adhere to circular design principles, thereby minimizing the incineration and landfilling of insulation materials at the end of their lifecycle. Insulation materials make up a significant proportion of CDW, with approximately 8.8% and 8.6% being landfilled and incinerated, respectively [18]. Among these materials, stone and glass wool collectively represent a significant share of the thermal insulation market in Europe, accounting for approximately 58% of the volume in 2014 [17]. Furthermore, the projected volumes of mineral wool waste in Europe exceed 2.5 million tonnes per year [242]. Therefore, high-value recycling of mineral wool is essential for achieving circularity targets.

Mineral wool waste exhibits homogenous physical and chemical properties compared to many other mineral wastes, making it a valuable source of consistent secondary raw materials [243]. The literature has explored various recycling approaches, including the use of mineral wool waste as reinforcement in cement mortar, thereby replacing conventional sand and aggregates [244, 245]. Additionally, lightweight aggregates produced from stone wool and glass wool through high-temperature sintering have shown potential [246]. Mineral wools are pozzolanic, making them potential precursors for producing alkali-activated materials [247, 248, 249]. However, the reutilization of mineral wool in alkali-activated lightweight aggregates is currently limited, and their performance as insulation material remains an area of ongoing research. This limitation could be attributed to the fibrous and light-density nature of mineral wool, which makes it challenging to process. Nevertheless, two studies on alkali-activating stone wool are worth mentioning. In one study, waste stone wool from fine processing and crushed final products were alkali-activated to create artificial aggregates used in geopolymer mortar [250]. Another study focused on alkali-activating stone wool waste from greenhouses to develop plant substrate materials [251]. Both studies demonstrate the potential for repurposing stone wool waste through alkali-activation and granulation.

This chapter investigates the potential fabrication and application of lightweight aggregates derived from stone wool for crawl space rehabilitation in the Netherlands. Many residential properties built before the 1970s in the Netherlands feature cavity walls and crawl spaces that require retrofitting [9]. Conventional methods, such as spraying polyurethane (PUR) foam beneath the floor, are commonly employed for crawl space rehabilitation [11]. However, these methods require sufficient crawl space height (above 35 cm) for access. For crawl spaces with limited accessibility (less than

35 cm), alternative strategies are necessary [252]. The lightweight aggregates developed in this chapter could potentially be applied in such retrofitting strategies, helping to mitigate ground moisture evaporation [253] and improve occupant comfort and health [254].

The primary objective of this chapter is to utilize stone wool as a precursor for producing alkali-activated lightweight aggregates. These aggregates are intended for use as ground cover insulation material in crawl space rehabilitation projects. Stone wool will be milled and alkali-activated to form aggregates, with unmilled stone wool included to provide porous structures. The characteristics and performance of the manufactured aggregates are investigated and utilized to simulate the hygrothermal performance of rehabilitated crawl spaces under typical Dutch climate conditions.

7.2. MATERIAL AND METHODOLOGY

7.2.1. Material and fabrication

In this study, commercially sourced stone wool, procured from Rockwool B.V. (Germany), is used as the primary material, simulating mineral wool waste free of significant impurities from other CDW. The chemical composition of the stone wool is analysed using X-ray fluorescence spectrometry (XRF) (PANalytical Epsilon 3) with a milled sample, and its loss on ignition (LOI) is determined within the temperature range of 105 to 1000°C, as presented in **Table 7.1**. The length of stone wool varies, with length-weighted-diameters ranging between 2.4 and 5.3 μm [255]. Sodium silicate solution (27.7% SiO_2, 8.4% Na_2O and 63.9% H_2O) and sodium hydroxide (NaOH) pellets are used as the alkali activator.

The overall production procedure and specimen composition are depicted in **Fig. 7.1**. Unmilled stone wool, characterized by a fibrous and voluminous structure, exhibits low workability and strength when used in its original form. The initially long stone wool fibres (**Fig. 7.1a**) undergo milling to produce a powder (**Fig. 7.1b**) using a ball mill (Planetary Mill Pulverisette 5). This milled stone wool serves as the solid precursor in the alkali-activated binder for this study. Additionally, as-is stone wool is incorporated into the mixture as a micro-fibre to enhance porosity and thermal insulation. Five distinct weight ratios of milled and as-is stone wool are prepared: 9.0, 6.1, 4.6, 3.5, and 2.8, denoted as M90, M86, M82, M78 and M74 respectively (refer to **Fig. 7.1c**). The workability of the paste deteriorates when the weight ratio decreases to 2.5 or lower. The alkali activator is synthesized in advance by blending sodium silicate solution, sodium hydroxide pellets, and additional water. The alkali activator formulation is established with a modulus of 1.8 and Na_2O concentration of 8%, based on the previous fly ash-based geopolymer formulation in **CHAPTER 4**. The water-to-dry components ratio (dry sodium silicate, sodium hydroxide, milled stone wool and as-is stone wool) is set at 0.4. The mass ratio of liquid (alkali activator solution and water) to precursor (milled stone wool) is fixed at 72%.

Table 7.1 Chemical composition of raw material.

Oxides (%)	Stone Wool
SiO_2	38.11
Al_2O_3	23.18
CaO	16.82
MgO	8.91
Fe_2O_3	7.43
TiO_2	1.56
K_2O	0.74
MnO	0.28
SO_3	0.07
Cr_2O_3	0.07
V_2O_5	0.05
Other	0.64
LOI (1000°C)	2.14
Specific density ($kg \cdot m^{-3}$)	2800 ± 2

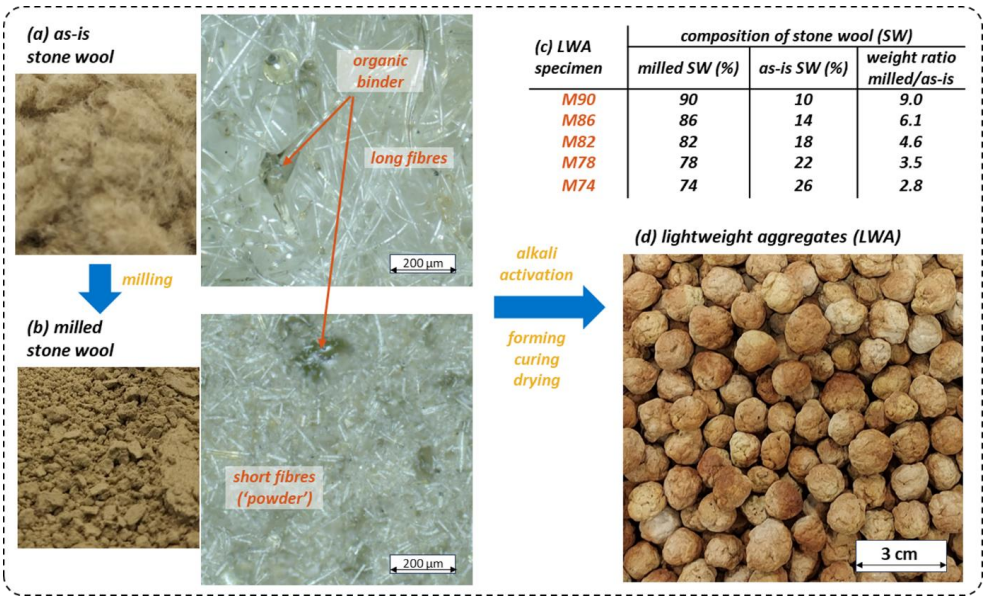

Fig. 7.1 (a) As-is stone wool, (b) milled stone wool, (c) specimen compositions, and (d) manufactured stone wool-based lightweight aggregates (LWA).

For the production process, milled stone wool and alkali activator solution are combined in a mixer and blended until a homogeneous paste is attained. Subsequently, as-is stone wool is added to the paste and thoroughly mixed until all fibres are coated. In this lab-scale manufacturing process, aggregates are shaped by placing the mixed material into spherical silicone moulds. For upscaling production, extrusion is suggested. The average diameter of the aggregates obtained is 2 ± 1 cm. The moulds containing aggregates are wrapped in plastic foil and cured in an oven at 60°C for 24 hours. Following curing, the aggregates are removed from the mould and subjected to further drying in an oven at 60°C for an additional 12 hours. Finally, the aggregates are retrieved from the oven for further characterization and assessment.

7.2.2. Characteristics assessment

Loose bulk density (ϱ_{bulk}) of the aggregates is determined in accordance with standard EN1097-3 [256]. Particle density ($\varrho_{particle}$) is assessed using a helium pycnometer (Micromeritics AccuPyc II 1340) with a 10 cm^3 cup is used. The pycnometer has a reading accuracy of 0.03% and an additional 0.03% uncertainty related to the sample capacity. Porosity of the specimen is calculated from particle density and bulk density using **Eq. (2-1)**. Open porosity is directly measured from the aggregates, while total porosity is determined from the powder obtained from crushed and milled aggregates.

Mechanical property is assessed using a mechanical testing system (Instron 5967) equipped with a 5 kN load cell. Single crushing strength (σ) is calculated using the formula proposed by [257]:

$$\sigma = \frac{2.8 * P}{\pi * d^2} \tag{7-1}$$

Where P represents the recorded failure load and d is the diameter of aggregate. An average value is computed from 10 aggregates per specimen group.

Thermal conductivity (λ) is determined utilizing the transient line source method with a thermal needle probe (AP Isomet model 2104). The probe has an accuracy of 5% of the reading plus 0.001 $W \cdot m^{-1} \cdot K^{-1}$. Measurements are taken at 20 ± 2°C, with three readings obtained per specimen group. To ensure consistency in measurements, samples are filled into the same cylindrical container utilized to determine bulk density.

Hygroscopic sorption properties are evaluated following standard ISO 12571 [152]. Sorption isotherms are measured by the saturated salt solutions (SSS) method, covering specific relative humidity levels from 0% to 98%. Moisture uptake is monitored by weighing the samples at 24-hour intervals using a digital balance until a constant mass is reached, defined as three successive weighings showing a mass loss change of less than 0.1%.

Water absorption is measured in accordance with standard EN1097-6 [258]. Samples are immersed in water in a pyknometer for 24 hours, and the mass of the saturated and surface-dried aggregates is recorded.

Microstructure analysis is performed through visual inspection using an optical microscope (ZEISS Axio Imager 2).

Thermogravimetric analysis (TGA) is conducted to assess mass loss or decomposition events with respect to temperature, utilizing a thermogravimetric analyser (TA Instruments TGA Q500). The heating process, starting from room temperature and continuing up to 1000°C at a rate of 10°C·min^{-1}, is carried out under a controlled nitrogen atmosphere with a constant flow rate of 60 ml·min^{-1}.

Chemical composition analysis is performed using Fourier transform-infrared (FT-IR) spectroscopy coupled with an attenuated total reflection (ATR) attachment (PerkinElmer Frontier FT-IR). Spectra are collected over a wavenumber range of 4000 to 400 cm^{-1} at a resolution of 1 cm^{-1}.

Mineralogical composition is further characterized by X-ray diffraction (XRD), utilizing a Bruker D2 (Co tube, Kα1 1.7890 [Å] Kα2 1.7929 [Å], step size 0.02 2Theta, range 10-90 2Theta).

7.2.3. Building performance simulation

Heat, air and moisture (HAM) transport simulations and indoor climate analyses are conducted on a terraced housing unit with a narrow crawl space and cavity walls, based on the model established in **CHAPTER 6** [259]. Specifically, the water content and temperature of the floor (wooden flooring and floor joist) above the crawl space are examined for the original unfilled crawl space and the crawl space filled with lightweight aggregates manufactured in this study. The software WUFI Plus is utilized to compute the heat and moisture balances within the room [21] using **Eqs. (1-3)** and **(1-4)**, respectively.

The building model encompasses dimensions of 5x8x2.8 m^3 per floor (width x depth x height) per housing unit, each featuring a floor area of 80 m^2 and an unheated attic, refer to **Fig. 7.2a**. An elevated wooden floor above sandy ground creates a narrow crawl space with a height of 30 cm (**Fig 7.2b**), exhibiting an arbitrary air change rate of 10 h^{-1} with the outdoor environments. Two-floor assembly designs are considered: one with the original unfilled crawl space and another filled with a 20 cm thick layer of manufactured aggregates on the sandy ground, leaving only 10 cm of airspace. The effective thermal transmittance (U-value) of the floor assembly with the unfilled crawl space is 0.332 W·m^{-2}·K^{-1}. Masonry walls with a 6 cm cavity filled with stone wool exhibit a U-value of 0.499 W·m^{-2}·K^{-1}. Additional building components include a ceiling assembly with a U-value of 0.087 W·m^{-2}·K^{-1} and glazing with a U-value of 0.8 W·m^{-2}·K^{-1}.

Boundary conditions are established based on the outdoor climate of Eindhoven in the Netherlands, characterized by a temperate oceanic climate (Cfb) according to the Köppen climate classification. The annual air temperature and relative humidity profile [260] are depicted in **Fig. 7.2c**. Two indoor scenarios are defined: one with a heating system maintaining an indoor temperature above 20°C, and another without any heating system. Cooling systems, mechanical humidification, and dehumidification systems are excluded, as they are not commonly utilized in residential housing in the Netherlands. A steady airflow of 7 l·s^{-1} per person is incorporated into the model. The indoor heat and moisture loads are based on the software's predefined four-person family household occupancy. The simulation is conducted for three years or until hygrothermal equilibrium within the building assemblies is reached. The main boundary and initial conditions are similar to **CHAPTER 6**, which are summarized in **Table B.7** (see **Appendix B**).

The simulated results are further compared against another commonly applied insulation aggregate, namely expanded perlite aggregates (EPA). The main properties of the reference material are: bulk density of 147 $kg \cdot m^{-3}$, porosity of 0.94, thermal conductivity of 0.04 and 0.05 $W \cdot m^{-1} \cdot K^{-1}$ under dry and 60% relative humidity (RH) conditions, respectively, and moisture content of 1 $\%kg \cdot kg^{-1}$ under 60% RH [261].

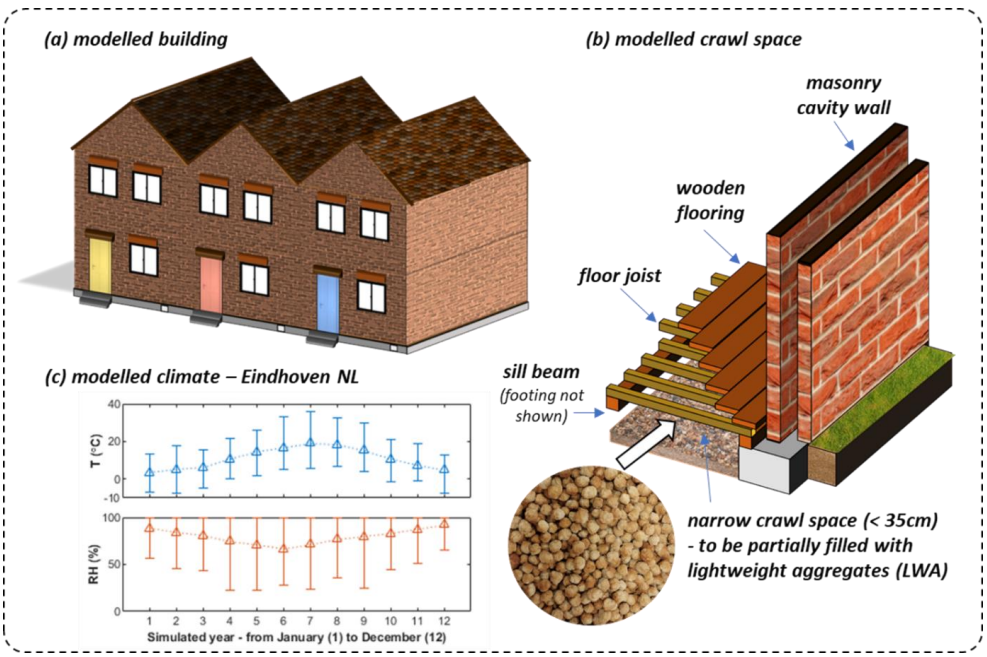

Fig. 7.2 (a) Building model, (b) crawl space design, and (c) exterior climates for simulation.

7.3. RESULTS AND DISCUSSION

7.3.1. Characteristics assessment

In this study, an increase in the content of as-is stone wool results in a more porous aggregate structure, as demonstrated by the elevated porosity and reduced bulk density (**Fig. 7.3a-b**). The internal porosity of the aggregates primarily comprises interconnected and open pores, with closed pores constituting less than 1% of the sample porosity. The bulk densities range from 720 (M74) to 850 $kg \cdot m^{-3}$ (M90), slightly lower than those reported for similar lightweight aggregates (LWA) derived from stone wool precursors, such as the 860 $kg \cdot m^{-3}$ reported by [246]. This reduction in weight primarily stems from the combination of as-is and milled stone wool used in this study. While the loose bulk density adheres to the 1200 $kg \cdot m^{-3}$ limit defined for LWA [262], these aggregates display notably higher densities than conventional expanded perlite aggregates (EPA), which typically range from 30 to 150 $kg \cdot m^{-3}$ [263]. This suggests a higher anticipated thermal conductivity; however, it also provides greater thermal mass than EPA.

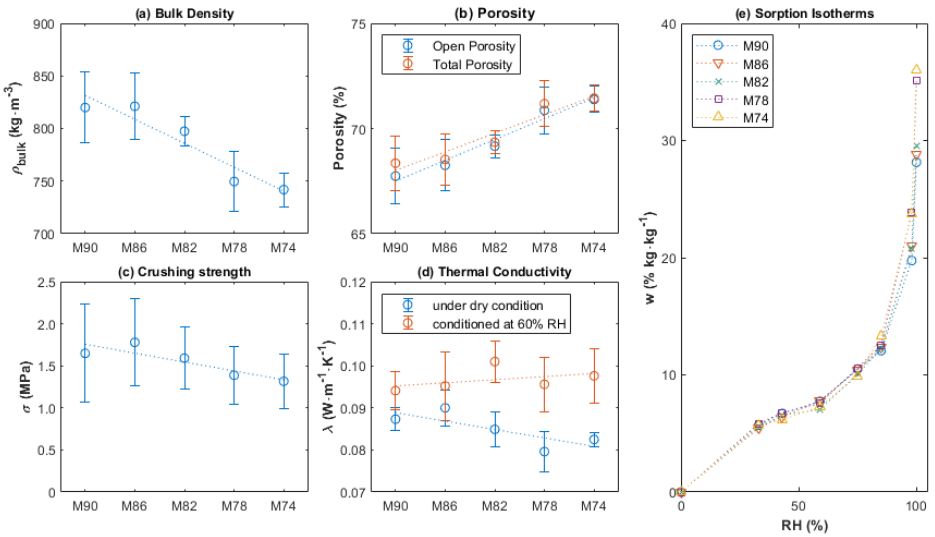

Fig. 7.3 (a) Bulk densities, (b) porosities, (c) crushing strength, (d) thermal conductivities, and (e) sorption isotherms of specimens.

The individual aggregate crushing resistance ranges between 1.0 and 2.3 MPa (**Fig. 7.3c**). The highest strength is observed in the M86 specimen. The results show that the strength decreases as a higher percentage of as-is stone wool is incorporated. The incorporation of as-is stone wool can impact rheology due to its fibre morphology, introducing more pores or defects. However, the overall strength is notably lower than that reported for other stone wool-based LWA, such as 8.8 MPa reported by [246] and 7.0 MPa by [250]. It is important to note that the higher strengths achieved in these studies are attributed to additional high-temperature sintering following the curing process. For loose-fill insulation applications in crawl spaces, crushing resistance is primarily necessary for the handling and installation of the material. Therefore, a comparable lower strength can be tolerated, and more importantly, lower energy manufacturing is achieved.

The dry thermal conductivity of the samples falls within the range of 0.075 and 0.094 $W \cdot m^{-1} \cdot K^{-1}$ (**Fig. 7.3d**). A decrease in thermal conductivity is observed with increasing as-is stone wool contents, aligning directly with the higher porosity evident in the aggregates. The greater volume of air voids within the aggregates results in reduced thermal conductivity. This range is consistent with other alkali-activated aggregates, as reported between 0.079 and 0.087 $W \cdot m^{-1} \cdot K^{-1}$ by [264]. However, the thermal conductivity is higher than that of typical EPA, which typically ranges from 0.04 to 0.05 $W \cdot m^{-1} \cdot K^{-1}$ [263], owing to their lower density. Under 60% relative humidity (RH) conditions, the thermal conductivity increases. Conversely, when compared against as-is stone wool contents, the thermal conductivity exhibits a slight increase with higher as-is stone wool contents. The heightened presence of open pores results in increased water content within the aggregate, subsequently elevating its effective thermal conductivity under high RH conditions. This suggests that further increases in as-is stone wool contents to achieve a more porous structure may compromise insulation performance in humid environments.

The moisture adsorption of the samples shows no significant difference up to 85% RH, with water contents measuring at 7 and 11 %kg·kg^{-1} under 60% and 80% RH respectively (**Fig. 7.3e**). The influence of as-is stone wool contents becomes more pronounced regarding water absorption capability. Water contents up to 36 %kg·kg^{-1} are measured in samples M74 and M78, while approximately 28 %kg·kg^{-1} is observed in samples M82, M86 and M90 under fully saturated conditions. This observation suggests the formation of larger pores when as-is stone wool content exceeds 22% in composition. It also implies that the thermal conductivity of aggregates with higher as-is stone wool contents will increase significantly under higher RH or when in contact with water, which is undesirable, especially when they are directly in contact with the ground. For comparison, water content for EPA is typically around 1 and 2 %kg·kg^{-1} under 60% and 80% RH respectively [263], although water absorption can reach as high as 71 %kg·kg^{-1} [265] due to the presence of large pores.

Pores are readily observable on the manufactured samples, as depicted in **Fig. 7.4** The as-is stone wool entraps air bubbles during the gel formation process, particularly in areas where wool is aggregated. This phenomenon leads to the formation of larger pores and defects within the matrix. Smaller pores are also discernible and randomly distributed within the binder gel. The internal structure exhibits a notable degree of inhomogeneity due to the random distribution of as-is stone wool and the lab-scale fabrication process.

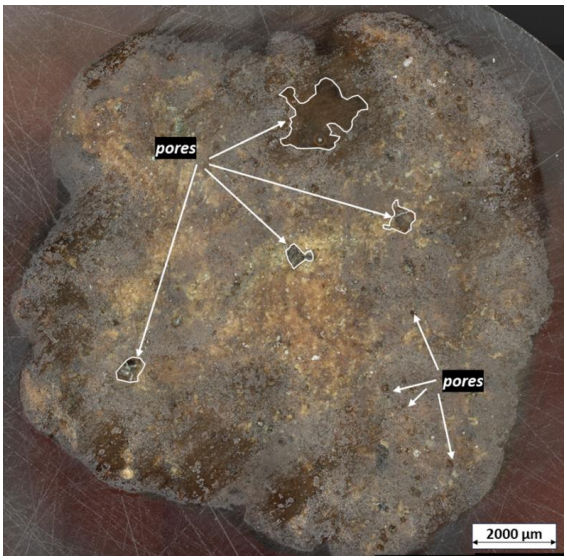

Fig. 7.4 Microscope images of samples M82 showing pores.

Fig.7.5a depicts the results of thermogravimetric (TG) analysis conducted on the crushed powder extracted from the aggregates. The initial derivative thermogravimetry (DTG) peak emerges within the temperature range of 100 to 300°C, signifying the release of physically and chemically bound water inherent in the aluminosilicate gel structure [266]. A subtle shift of the peak towards higher temperatures is observed with increased milled stone wool incorporation, transitioning from 179°C for M74/M78 to 185°C for M86/M90. This shift is attributed to the rapid dissolution rate of milled

stone wool compared to as-is stone wool, leading to an enhanced gel formation with more tightly bonded water, thus corroborating the observed trends in crushing strength. The original organic binder present in stone wool (**Fig. 7.1**) undergoes decomposition within the range of 300-500°C [267, 268]. Additionally, the DTG peak at 700 °C corresponds to the decomposition of carbonates [266]. However, within the same temperature range, an exothermic peak at 700°C is notable, particularly in raw stone wool, which may signify the devitrification of wool and subsequent formation of crystalline phases [269, 270]. A similar exothermic peak is also discernible in the aggregates, especially those with higher as-is stone wool content such as M74.

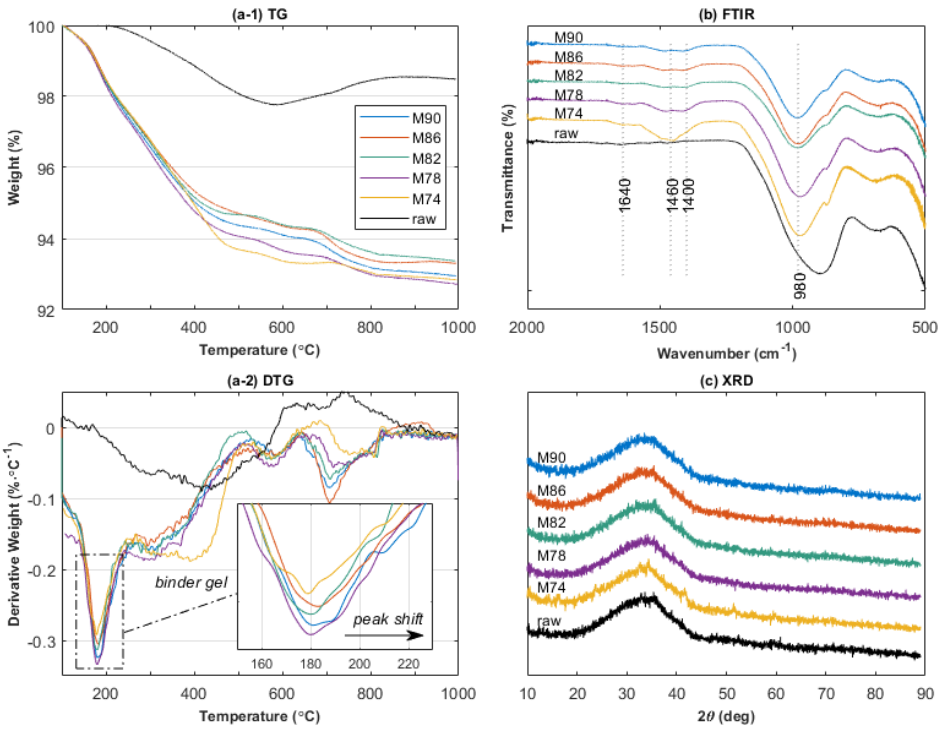

Fig. 7.5 (a) TG/DTG, (b) FTIR, and (c) XRD patterns of specimens and raw material.

Fig. 7.5b illustrates the Fourier transform-infrared (FT-IR) spectroscopy analysis on both the aggregates and raw stone wool. The primary peak at broad bands around 900 cm^{-1} on raw stone wool corresponds to the asymmetric stretching vibration modes of Si-O-T bonds (T = tetrahedral Si or Al) [248]. Upon alkali activation, the bands in the aggregates are shifted and centred at or around 980 cm^{-1}. This shift primarily reflects changes in the polymerization degree of Si-O-T crosslinking. In this investigation, an increase in milled stone wool leads to the shifting of the main Si-O-T band from 960 cm^{-1} to 980 cm^{-1}, indicating a higher polymerization degree with milled stone wool, consistent with the TG measurement. The humps at 1400 cm^{-1} and 1460 cm^{-1} are attributed to the presence of various carbonates [266]. Small peaks at 1640 cm^{-1}, attributed to OH groups [171], originating from chemically bound water in the gel, are also observed.

Raw stone wool primarily exhibits an amorphous structure, attributable to the rapid cooling during the manufacturing process [249, 267, 271], as confirmed by X-ray diffraction (XRD) analysis (**Fig. 7.5c**), wherein no discernible peaks are evident, but rather a broad halo around 30° 2θ. Similarly, the alkali-activated aggregates retain an amorphous nature without any crystalline phase formation, which is consistent with the findings reported by [248].

Based on the crushing strength results, specimen M86 is selected for further hygrothermal performance simulation as insulation aggregates for crawl space rehabilitation. The aggregates have a measured bulk density of 821 $kg \cdot m^{-3}$, open porosity of 68%, dry thermal conductivity of 0.090 $W \cdot m^{-1} \cdot K^{-1}$, heat capacity of 800 $J \cdot kg^{-1} \cdot K^{-1}$, and sorption isotherms as shown in **Fig. 7.3e**. The aggregates are assumed to be vapour-diffusive, with a water vapour diffusion resistance factor of 2. Additionally, the aggregates are assumed to exhibit the same liquid transport properties as sands to account for additional capillary liquid transport, shown in **Fig. A.5** (see **Appendix A**), during the hygrothermal simulation.

7.3.2. Building performance simulation

The water content profiles of the floor assembly, comprising the wooden flooring exposed to the indoor environment and the floor joist exposed to the crawl space, are depicted in **Fig. 7.6**. Both heated and unheated building scenarios are considered for comparison. In cold climates, building design typically incorporates a heating system to maintain an indoor temperature of approximately 20°C or higher, thereby preventing damage from ground frost, structural wetting, mould formation, and other moisture-related issues [272]. These distinct trends in water content within the floor assembly are discernible in the simulated profiles presented in **Fig. 7.6**.

In both heated and unheated scenarios, a reduction in water content is observed in the floor assembly of the rehabilitated crawl space partially filled with M86 aggregates, compared to the original construction with an empty crawl space. The reduction is more pronounced in the floor joist exposed to the crawl space, with reductions of up to 2.9% for heated buildings and up to 2.7% for unheated buildings (**Fig. 7.6b**). Conversely, for the flooring exposed to the indoor environment, reductions of approximately 1.2% and 0.5% are observed for heated and unheated buildings, respectively (**Fig. 7.6a**).

The moisture reduction profiles of M86 aggregates and conventional EPA used as filling aggregates for floor rehabilitation follow a similar trend. However, conventional EPA performs slightly better than M86 aggregates, providing up to an additional 0.2% moisture reduction in wooden flooring and an additional 0.4% moisture reduction in wooden floor joists. This difference is mainly due to the lower moisture sorption capacity of conventional EPA compared to the M86 aggregates manufactured in this chapter.

Despite being relatively small, these reductions in water content within the floor assembly offer potential benefits in mitigating structural damage, mould proliferation, or other health and safety hazards associated with undesirable levels of moisture content [254]. The simulated results in this study are consistent with previous research on measured and simulated moisture conditions in outdoor air-ventilated crawl spaces with ground cover, showing a reduction in relative humidity in the rehabilitated crawl space [273].

The effective thermal transmittance (U-value) of the rehabilitated floor assembly, filled with M86 aggregates, decreases from 0.332 $W \cdot m^{-2} \cdot K^{-1}$ to 0.191 $W \cdot m^{-2} \cdot K^{-1}$. For energy retrofitting of a ventilated crawl space, the most effective approach involves adding an insulation layer beneath the floor if sufficient crawl space height is available. Consequently, only a minor increase in floor temperature is observed when aggregates are placed on the ground in the crawl space, as illustrated in **Fig. 7.7**.

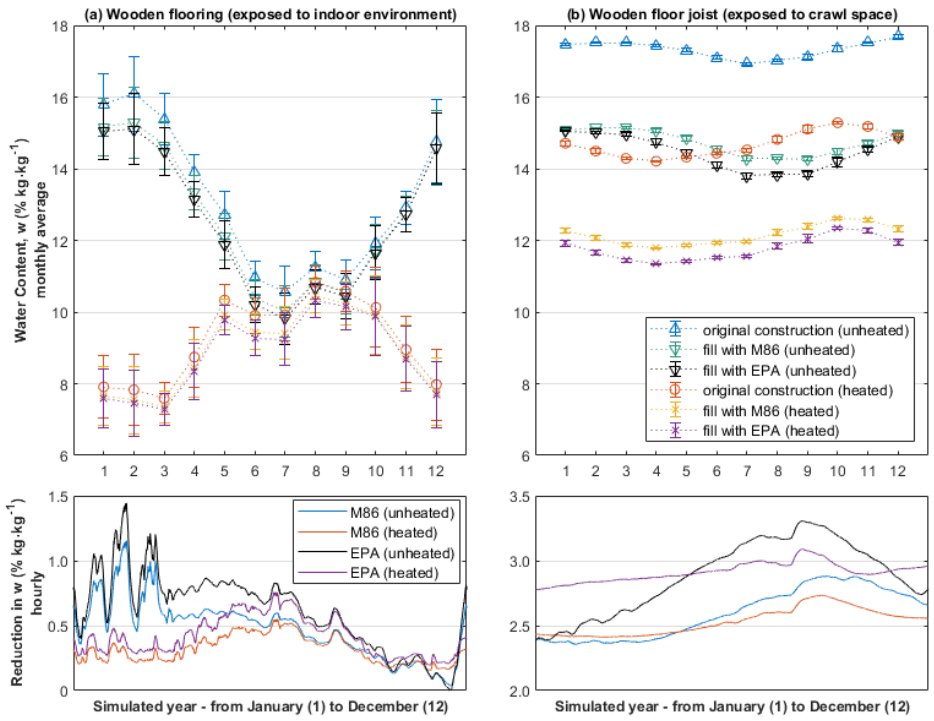

Fig. 7.6 Average water content in the floor assembly: (a) wooden flooring that is exposed to the indoor environment and (b) wooden floor joist that is exposed to crawl space.

During the winter period, temperature increments of up to 0.2°C and 0.4°C are noted for heated and unheated buildings, respectively, when applying M86 aggregates. Conversely, using conventional EPA as ground cover insulation offers an additional 0.1°C increment due to its lower thermal conductivity. For heated buildings, ground cover with M86 aggregates translates into an energy saving of 5.4% based on simulation results, reducing from 5992 to 5669 kWh after rehabilitation. This is slightly lower than the EPA case, which provides a 7.0% energy saving.

Interestingly, an undesirable decrease in temperature is observed in unheated buildings during the early winter period. This phenomenon is attributed to reduced access to ground heat, which could be more pronounced with materials of lower thermal conductivity or thermal mass, such as expanded perlite aggregates. However, it is important to note that this phenomenon is limited to unheated buildings.

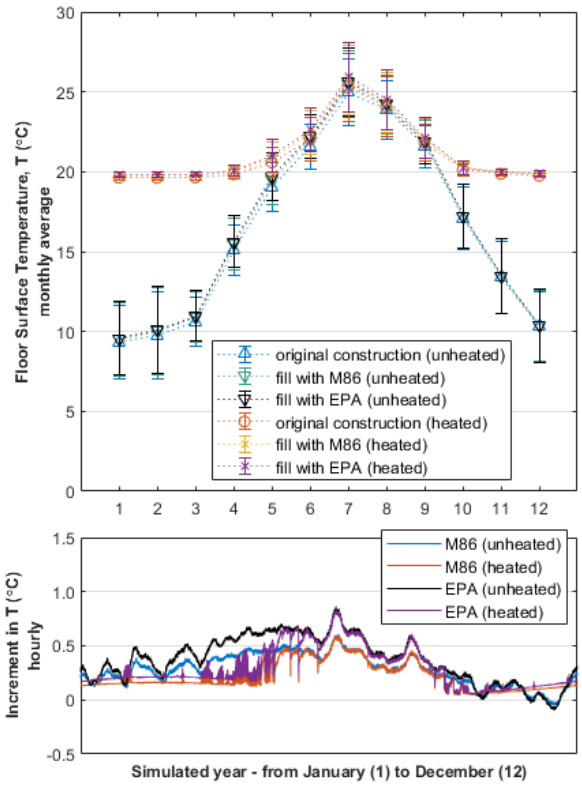

Fig. 7.7 Average floor surface temperature.

7.4. CONCLUSIONS

The properties of the fabricated stone wool-based aggregates are determined by the ratio of milled stone wool to as-is stone wool in their compositions. It has been observed that the fibre morphology of as-is stone wool influences rheology, introducing a greater number of pores or defects, which results in a decrease in mechanical strength. As the proportion of as-is stone wool increases from 10% to 26% in the stone wool mixture, there is a corresponding increase in the porosity of the specimens from 67% to 72%. These porous structures exhibit a thermal conductivity ranging from 0.075 to 0.094 $W \cdot m^{-1} \cdot K^{-1}$ under dry conditions. However, under humid conditions, aggregates with higher porosity demonstrate an increase in thermal conductivity, which can be attributed to their elevated moisture adsorption and water absorption capacity. When compared to conventional expanded perlite aggregates (EPA), the fabricated aggregates exhibit certain disadvantages such as higher density, thermal conductivity, and moisture adsorption capacity. However, they offer advantages such as lower water absorption and higher thermal mass.

In the hydrothermal simulation involving the use of stone wool-based aggregates for crawl space rehabilitation, a notable reduction in water content and an increase in floor surface temperature are

observed in the floor assembly of the rehabilitated crawl space partially filled with aggregates, compared to the original construction with an empty crawl space. This decrease in water content within the floor assembly offers potential advantages for maintaining the structural integrity of buildings and mitigating adverse impacts on occupant comfort and health. Furthermore, there is potential for a 5.4% reduction in heating energy consumption after rehabilitation.

The findings of this chapter suggest that stone wool-based aggregates provide a high-value recycling option suitable for crawl space retrofitting applications. These aggregates and their potential applications represent sustainable construction practices, contributing to the circular economy by repurposing insulation waste materials into valuable building insulation components. Future research focusing on durability, leaching behaviour, composition design, manufacturing optimization, and full life cycle assessment is essential for practical implementation.

8. A SIMPLE TWO-PHASE APPROACH TO PREDICT MOISTURE-DEPENDENT THERMAL CONDUCTIVITY OF POROUS MATERIALS

ABSTRACT

This chapter develops a generalized solution for moisture-dependent thermal conductivity (λ_{eff}) in porous media, utilizing readily available parameters. By introducing arbitrary dry and saturated phases, the tri-phase model (solid, gas, and water) is simplified into a two-phase model. Seven analytical solutions are adapted, including series-parallel, Maxwell-Eucken, Landauer's, exponential, and Somerton's relations. The proposed method requires only two parameters to predict λ_{eff} under different degrees of saturation (S_r): effective dry thermal conductivity (λ_{dry}, where $S_r = 0$) and effective saturated thermal conductivity (λ_{sat}, where $S_r = 1$). In the absence of direct λ_{sat} measurement, this λ_{sat} can be obtained using λ_{dry} and the parallel relation for highly porous media, and using Landauer's relation for medium-density materials. Validation results indicate that both Landauer's and exponential relations provide the upper bound and lower bounds, respectively, for λ_{eff}. For medium-density materials, the upper bound aligns with the parallel relation and the lower bound aligns with Landauer's relation.

.

The results presented in this chapter are published in the following article:

C.H. Koh and H.J.H. Brouwers, "A simple two-phase approach to predict moisture-dependent thermal conductivity of porous insulation materials," International Journal of Heat and Mass Transfer 234, 126138 (2024).

8.1. INTRODUCTION

Building thermal insulation materials, and many mineral-based construction materials, commonly feature a porous structure to leverage the low thermal conductivity of air or gas within their pores. However, these porous materials are highly susceptible to moisture adsorption, condensation, rain, and groundwater uptake. The presence of water within the insulation materials introduces an additional thermal conductor, leading to increased heat transfer through the material. This rise in water content compromises the thermal resistance of the insulation material, thereby diminishing its performance. Despite efforts to mitigate moisture adsorption and water infiltration, complete avoidance is often challenging. Therefore, understanding how changes in water content impact the effective thermal conductivity of porous materials is essential.

Several methods are available for measuring the effective thermal conductivity of wet porous building materials. These methods include the transient method (periodic method) proposed by ISO 16957 [274], and the steady-state method using a standardized guarded hot plate or heat flow meter as outlined in ISO 10051 [275]. However, measuring the thermal conductivity of moist porous materials presents challenges. In the steady-state method, the applied temperature gradient induces a non-uniform distribution of moisture within the material. While this issue could potentially be addressed using the periodic method outlined in ISO 16957, this approach entails a more complex measurement setup and analysis. Consequently, a simple analytical solution based on commonly measured parameters, such as thermal conductivity under dry conditions, would prove advantageous in this context.

Material-specific approximation through data fitting is the simplest method. For example, McFadden [276] proposed simple linear and exponential relations for moist insulation material based on measurements using different techniques. However, for a generalized model, a more complex approach is required.

Wang et al. [277] applied a tri-phase thermal conductivity model based on capillary structure using fractal theory. This model considers parameters such as porosity, pore size distribution, and fractal structure in determining the thermal conductivity under different moisture content. Similarly, Qin et al. [278] applied a fractal model for porous media under different degrees of saturation. Pei et al. [279] introduced a tortuosity correction in their tri-phase model to reflect the heat conduction path, alongside parameters such as porosity, water content, and thermal conductivity of the solid phase. Li et al. [280] proposed a multi-phase model for partially saturated cement-based porous composites, based on effective medium and mean-field theories, accounting for the pore shapes and orientations. Chu et al. [281] developed a fractal capillary bundle model at the pore scale for the effective thermal conductivity of porous geomaterials, considering structure parameters such as porosity, tortuosity, pore size distribution and its fractal dimension. For moist silica aerogel, Chen et al. [282] proposed a fractal-intersection sphere with an inhomogeneous water film structural model. Theoretical frameworks are also available on other porous mediums, such as soils and rocks. Ghanbarian and Daigle [283] proposed a model to predict thermal conductivity in these moist porous media based on percolation theory and effective medium theory.

While these generalized models provide analytical solutions for approximating the thermal conductivity of moist material, they often involve parameters that are challenging to obtain, such

as the thermal conductivity for the solid phase and pore size distribution. Therefore, a generalized model based on commonly measured parameters would be more practical for implementation.

This study aims to derive a generalized moisture-dependent thermal conductivity solution for porous insulation material, using only commonly measured and readily available parameters. Existing multiphase models for porous materials, as reviews by Carson et al. [284] and Smith et al. [285] are referenced when deriving solutions for moist porous materials. The derived solutions are further validated with experimental data from the literature.

8.2. MODELS AND METHODOLOGY

8.2.1. Two-phase models for effective thermal conductivity

The effective thermal conductivity (λ_{eff}) of air and water-filled porous materials can be approximated using a multiphase model approach. In a simplistic depiction, a dry porous material consists of a solid phase and a gas phase, while a fully saturated porous material comprises a solid phase and a water phase. This reduces the multiphase model to a two-phase model. Numerous analytical solutions exist for this model, each hinging on different assumptions regarding geometry and heat conduction pathways. Typically, these models involve three primary parameters: the thermal conductivity of the first phase (λ_1), typically assigned to the solid phase (λ_s); the thermal conductivity of the second phase (λ_2), typically assigned to the fluid phase in the pores, either gas (λ_g) or water (λ_w); and the contribution fraction of the second phase (x_2). Generally, x_2 is assumed to be equivalent to the physical volume fraction of the pore, also known as porosity (φ) [284, 285]. **Fig. 8.1** illustrates a porous material under both dry and fully saturated conditions, along with the primary components when applying a multiphase model to predict λ_{eff}.

Six solutions derived from multiphase models, as reviewed by Carson et al. [284] and Smith et al. [285], are included in this study, illustrated in **Fig. 8.2**.

Among the various two-phase models, the simplest approach to predict λ_{eff} involves treating the solid and fluid as thermal resistors either in series or in parallel with respect to the heat flow, as expressed in:

$$\lambda_{eff} = \frac{1}{(1 - x_2)/\lambda_1 + x_2/\lambda_2} \tag{8-1}$$

and

$$\lambda_{eff} = \lambda_1(1 - x_2) + \lambda_2 x_2 \tag{8-2}$$

respectively. Although these assumptions neglect physical interaction between phases, they provide lower and upper bounds for effective thermal conductivity (**Fig. 8.2**).

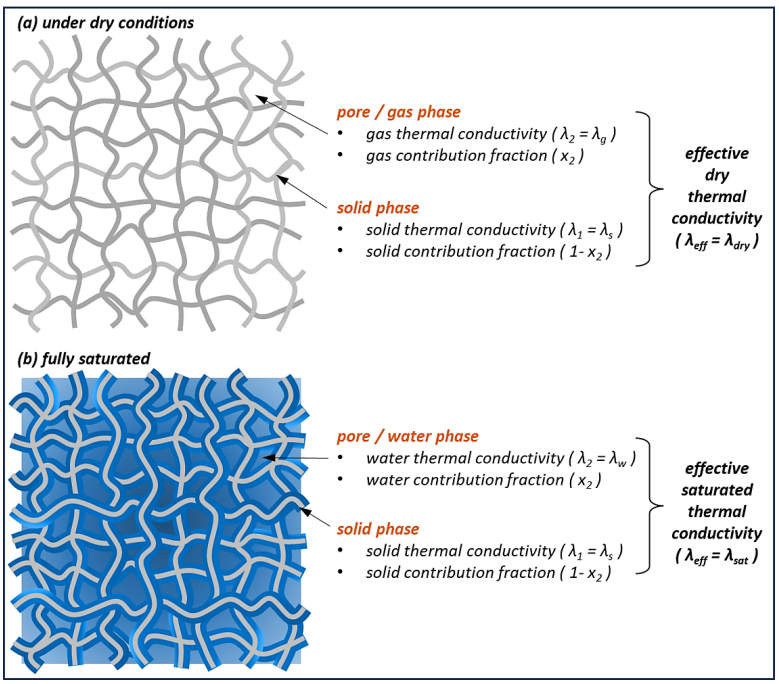

Fig. 8.1 Porous materials under both dry and fully saturated conditions, with the primary components when using a multiphase model approach. The depicted two-dimensional structure of the porous material is purely illustrative, and the actual structure could be fibrous, foam-like, or any other form of porous structure.

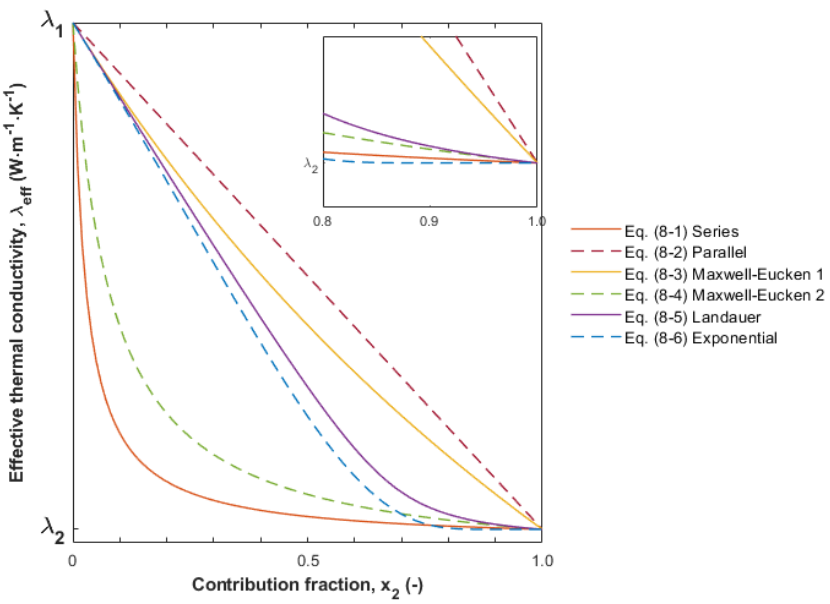

Fig. 8.2 Different two-phase model approaches for effective thermal conductivity.

Another well-established model is the Maxwell-Eucken relation [286], equivalent to the Hanshin-Shtrikman upper and lower bounds [287], and can be represented by:

$$\lambda_{eff} = \lambda_1 \frac{\lambda_2 + 2\lambda_1 - 2(\lambda_1 - \lambda_2)x_2}{\lambda_2 + 2\lambda_1 + (\lambda_1 - \lambda_2)x_2} \tag{8-3}$$

and

$$\lambda_{eff} = \lambda_2 \frac{\lambda_1 + 2\lambda_2 - 2(\lambda_2 - \lambda_1)(1 - x_2)}{\lambda_1 + 2\lambda_2 + (\lambda_2 - \lambda_1)(1 - x_2)} \tag{8-4}$$

respectively. This model delineates upper and lower limits for the effective thermal conductivity of macroscopically homogeneous and isotropic multiphase materials, in terms of phase volume fraction and phase conductions. The model assumes individual closed pores dispersed uniformly in the solid matrix and does not account for a continuous conduction pathway through pores. The Maxwell-Eucken bounds further refine the estimated range, falling within the bounds set by **Eqs. (8-1)** and **(8-2)**, as shown in **Fig. 8.2**.

Another approach, proposed by Landauer [288], is based on a random mixture assumption, treating each phase as if surrounded by a homogeneous medium with properties are the mixture. The model allows open porosity where the interconnected pore phase forms a continuous heat conduction pathway, leading to a stronger dependence of thermal conductivity on the pore phase. This solution, known also as the Effective Medium Theory (EMT), can be expressed either in its implicit form as follows:

$$(1 - x_2)\frac{\lambda_1 - \lambda_{eff}}{\lambda_1 + 2\lambda_{eff}} + x_2 \frac{\lambda_2 - \lambda_{eff}}{\lambda_2 + 2\lambda_{eff}} = 0 \tag{8-5}$$

alternatively, in its explicit form as follows:

$$\lambda_{eff} = \frac{1}{4}\left\{\lambda_2(3x_2 - 1) + \lambda_1(2 - 3x_2) + \sqrt{[\lambda_2(3x_2 - 1) + \lambda_2(2 - 3x_2)]^2 + 8\lambda_1\lambda_2}\right\} \tag{8-5a}$$

The solution sits within the bounds set by **Eqs. (8-3)** and **(8-4)**, however, do not universally fit all measurements examined in the original study.

A simple exponential relation, proposed by Tichá et al. [289], assumes a closed-pores microstructure with non-conducting pores, therefore eliminating the parameter λ_2. However, the proposed equation breaks down at a higher pore volume fraction and approaches zero. This breakdown can be mitigated by reconsidering the effect of the thermal conductivity of the second phase and is expressed by:

$$\lambda_{eff} = (\lambda_1 - \lambda_2) \cdot exp\left(\frac{-Bx_2}{1-x_2}\right) + \lambda_2 \quad (8\text{-}6)$$

where the parameter B relates to pore shape, with B = 3/2 assumed for spherical pores.

λ_s for inorganic minerals vary widely depending on mineral composition and crystal orientation, ranging from 1 to 5 $W \cdot m^{-1} \cdot K^{-1}$ [290], and up to 10 $W \cdot m^{-1} \cdot K^{-1}$ for quartz with crystal orientation parallel to the heat source [291]. Organic solid matter has lower λ_s values, ranging from 0.13 to 0.35 $W \cdot m^{-1} \cdot K^{-1}$ [292]. For insulation materials filled with air, λ_g is typically equivalent to the thermal conductivity of air (λ_a), around 0.026 $W \cdot m^{-1} \cdot K^{-1}$ at 20°C [293]. For a fully saturated porous material, λ_w is approximately 0.6 $W \cdot m^{-1} \cdot K^{-1}$ at 20°C [293].

8.2.2. Effective saturated thermal conductivity

8.2.2.1. Highly porous materials

For building insulation materials, the effective saturated thermal conductivity (λ_{sat}) is less commonly measured and investigated compared to the effective dry thermal conductivity (λ_{dry}), both commercially and in the literature. Theoretically, a fully saturated porous material can be simplified as a two-phase model by assuming all pores are filled with water in their saturated state. The same equations (**Eqs. (8-1)** to **(8-6)**) should provide a valid prediction for λ_{sat} based on the same contribution fraction x_2 used to predict λ_{dry}. To validate this assumption, **Eqs. (8-1)** and **(8-2)**, representing the lower and upper bounds for λ_{dry} (**Fig. 8.2**), are used to calculate λ_{sat} and compared against their measured λ_{sat}. Four porous insulation materials from the open-source MASEA database [294] are selected, and the parameters of these materials used in the calculations are listed in **Table 8.1**.

Table 8.1 Parameters of four porous insulation materials [294] for the calculation.

	Stone wool	Glass fibres	PU foam	Expanded cork
Measured values from [294]				
Dry thermal conductivity, λ_{dry} ($W \cdot m^{-1} \cdot K^{-1}$)	0.040	0.035	0.030	0.040
Saturated thermal conductivity, λ_{sat} ($W \cdot m^{-1} \cdot K^{-1}$)	0.60	0.61	0.60	0.61
Porosity, φ (-)	0.95	0.99	0.95	0.9
Density, ϱ ($kg \cdot m^{-3}$)	60	30	40	150
Estimated values				
Solid Thermal conductivity, λ_s ($W \cdot m^{-1} \cdot K^{-1}$)	3 [295]	1.4 [296]	0.21 [297]	0.4 [298]
Water Thermal conductivity, λ_w ($W \cdot m^{-1} \cdot K^{-1}$)	0.6 [293]			
Air Thermal conductivity, λ_a ($W \cdot m^{-1} \cdot K^{-1}$)	0.026 [293]			

When applying **Eqs. (8-1)** to **(8-6)** to predict λ_{dry}, x_2 is generally assumed to be equivalent to the physical porosity (φ). **Table 8.2** presents the calculated x_2 for the pore when applying **Eqs. (8-1)** and **(8-2)** based on measured λ_{dry}, and λ_s and λ_a obtained from the literature. The calculated x_2 from

Eqs. (8-1) and **(8-2)** form the lower and upper limits for the measured φ, and it appears that the prediction of x_2 following **Eq. (8-2)** is closer to φ.

Table 8.2 Calculated contribution fraction (x_2) using **Eqs. (8-1)** to **(8-2)** based on λ_{dry}, λ_s and λ_a from **Table 8.1**.

	Calculated x_2		Measured Porosity φ
Equations	**Series, Eq. (8-1)**	**Parallel, Eq. (8-2)**	
Stone wool	0.6469	0.9953	0.95
Glass fibres	0.7380	0.9934	0.99
PU foam	0.8478	0.9783	0.95
Expanded cork	0.6257	0.9626	0.90

λ_{sat} is further predicted based on x_2 calculated from **Table 8.2** and compared to λ_{sat} calculated from the measured φ. Here, the second phase is the water phase. Both sets are then compared against the measured λ_{sat}. The results are listed in **Table 8.3**. Among all four calculations, λ_{sat} calculated from x_2 using **Eq. (8-2)** is closer to the measured λ_{sat}, aligning with the lower boundary close to the second phase (λ_w at 0.6 $W \cdot m^{-1} \cdot K^{-1}$). In contrast, λ_{sat} calculated from the measured φ significantly deviates from the measured λ_{sat}. This deviation suggests the limitation of using porosity (φ) as x_2 in estimating λ_{eff}. It should also be noted that the physical pore volume accessible to water is not always the same as the total pore volume that can be filled by gas (air).

Table 8.3 Calculated saturated thermal conductivity (λ_{sat}) using **Eqs. (8-1)** and **(8-2)** based on x_2 and φ (**Table 8.2**).

	Calculated λ_{sat}				Measured λ_{sat}
Equations	**Series, Eq. (8-1)**	**Parallel, Eq. (8-2)**	**Series, Eq. (8-1)**	**Parallel, Eq. (8-2)**	
	$x_{2,eq1}$	$x_{2,eq2}$	φ	φ	-
Stone wool	0.8362	0.6113	0.6250	0.7200	0.60
Glass fibres	0.7056	0.6052	0.6034	0.6080	0.61
PU foam	0.4678	0.5915	0.5490	0.5805	0.60
Expanded cork	0.5054	0.5925	0.5714	0.5800	0.60

Despite the varying λ_s value (0.21 to 3 $W \cdot m^{-1} \cdot K^{-1}$), all samples exhibit a similar range in λ_{sat}. This similarity indicates that the influence of the solid phase's thermal conductivity has little effect on the thermal conductivity of saturated insulation material, aligning with findings from [299]. This is evident from the MASEA database [294], where the majority of porous materials have λ_{sat} values close to λ_w.

Based on these findings, in the absence of direct λ_{sat} measurement, λ_{sat} can be approximated using the parallel relation. The contribution fraction x_2 is first estimated using **Eq. (8-2)** with λ_{dry}, λ_s, and λ_a as inputs. Then, λ_{sat} is approximated using the same **Eq. (8-2)** with the calculated x_2, λ_s and λ_w as the inputs. It appears that λ_{sat} is often close to the boundary of the second phase (λ_w). Therefore, when λ_s is not known, it is reasonable to equate λ_{sat} to λ_w for highly porous materials.

8.2.2.2. Medium-density materials

The λ_{sat} approximation is further applied to four medium-density materials [300, 301, 302], typical examples are clay and sand, and cement-based construction materials such as mortar and concrete. The parameters of these materials used in the calculations are listed in **Table 8.4**.

Table 8.4 Parameters of four medium-density materials [294] for the calculation.

	Peat [300]	**Sand [300]**	**Concrete [301]**	**Clay-cement [302]**
Measured values				
Dry thermal conductivity, λ_{dry} ($W \cdot m^{-1} \cdot K^{-1}$)	0.10	0.15	0.42	0.43
Saturated thermal conductivity, λ_{sat} ($W \cdot m^{-1} \cdot K^{-1}$)	0.73	1.85	1.16	1.50
Porosity, φ (-)	0.77	0.55	0.20	0.48
Density, ϱ ($kg \cdot m^{-3}$)	600	1200	2142	1283
Estimated values				
Solid Thermal conductivity, λ_s ($W \cdot m^{-1} \cdot K^{-1}$)	1.06	7.5	1.65	3.2
Water Thermal conductivity, λ_w ($W \cdot m^{-1} \cdot K^{-1}$)	0.6 [303]			
Air Thermal conductivity, λ_a ($W \cdot m^{-1} \cdot K^{-1}$)	0.026 [303]			

The prediction of x_2 from **Eqs. (8-1)** and **(8-2)** significantly deviate from the measured φ (**Table 8.5**). However, it is observed that the measured φ falls between the calculated x_2 values from **Eqs. (8-1)** and **(8-2)**. To provide a more accurate approximation, Landauer's relation (**Eq. (8-5)**), also known as Effective Medium Theory, is included as well. The prediction of x_2 following **Eq. (8-5)** is shown to be closer to φ.

The calculated λ_{sat} based on the calculated x_2 (**Table 8.5**) and the measure φ are listed in **Table 8.4**. Similarly, λ_{sat} calculated from x_2 using **Eq. (8-5)** is closer to the measured λ_{sat}. Additionally, Eq. (8-5) forms the lower bound for the λ_{sat} estimation, while **Eq. (8-1)** remains the upper bound.

Based on these findings, in the absence of direct λ_{sat} measurement, λ_{sat} can be approximated using Landauer's relation for medium-density materials. However, its accuracy is lower than applying the parallel relation on highly porous materials.

Table 8.5 Calculated contribution fraction (x_2) using **Eqs. (8-1)**, **(8-2)** and **(8-5)** based on λ_{dry}, λ_s and λ_a from **Table 8.4**.

	Calculated x_2			**Measured Porosity φ**
Equations	**Series, Eq. (8-1)**	**Parallel, Eq. (8-2)**	**Landauer, Eq. (8-5)**	
Peat	0.2414	0.9284	0.6994	0.77
Sand	0.1676	0.9841	0.7113	0.55
Concrete	0.0469	0.7574	0.5206	0.20
Clay-cement	0.0528	0.8727	0.5994	0.48

Table 8.6 Calculated saturated thermal conductivity (λ_{sat}) using **Eqs. (8-1)**, **(8-2)** and **(8-5)** based on x_2 and φ (**Table 8.5**).

	Calculated λ_{sat}						Measured λ_{sat}
Equations	**Series, Eq. (8-1)**	**Parallel, Eq. (8-2)**	**Landauer, Eq. (8-5)**	**Series, Eq. (8-1)**	**Parallel, Eq. (8-2)**	**Landauer, Eq. (8-5)**	
	$x_{2,eq1}$	$x_{2,eq2}$	$x_{2,eq5}$	φ	φ	φ	-
Peat	0.8945	0.6329	0.7194	0.6654	0.7041	0.6886	0.73
Sand	2.5619	0.7168	1.4214	1.0287	3.7257	2.4550	1.85
Concrete	1.5249	0.8547	1.0169	1.2222	1.4400	1.3909	1.16
Clay-cement	2.6045	0.9309	1.3005	1.0390	1.9520	1.6204	1.50

8.2.3. Adaptation of solid-gas-water models to two-phase models

A partially saturated porous material consists of three distinct phases: solid, water and gas, as illustrated in **Fig. 8.3a**. Within the pores, both water vapour and condensed water are treated as a single water phase. Analytical solutions for these tri-phase systems can be derived from multiphase models. This study simplifies the tri-phase solutions into two-phase solutions by introducing two arbitrary phases: the 'solid-water' phase and the 'solid-gas' phase, corresponding to saturated and dry conditions, respectively, as shown in **Fig. 8.3b**.

The three-phase moist material is transformed into two separate two-phase components. The 'solid-water' phase is represented by the effective saturated thermal conductivity (λ_{sat}) and an arbitrary contribution fraction (x_2); the 'solid-gas' phase is represented by the effective dry thermal conductivity (λ_{dry}) and a corresponding arbitrary contribution fraction (1 - x_2). The arbitrary contribution fraction x_2 is assumed to be proportional to the physical degree of saturation (S_r) in the moist porous material. By assuming a similar volume fraction of the solid phase is allocated to the 'solid-water' phase, x_2 is equivalent to S_r. Similarly, the contribution fraction for the 'solid-gas' phase can be equated to ($1 - S_r$). The relationship between S_r and water content (w in kg water / kg dry material) can be described using:

$$S_r = \frac{w \cdot \rho_r}{\phi} \tag{8-7}$$

where ρ_r is the relative density of the dry porous material with respect to water (specific density of solid divided by water density), and φ is the amount of pore volume accessible to water. $\varphi = 1$ represents the maximum amount of water the material can absorb in its saturated state, where $S_r = 1$. φ is typically equivalent to open porosity but should include closed pores with vapour-permeable walls that are also accessible to water vapour.

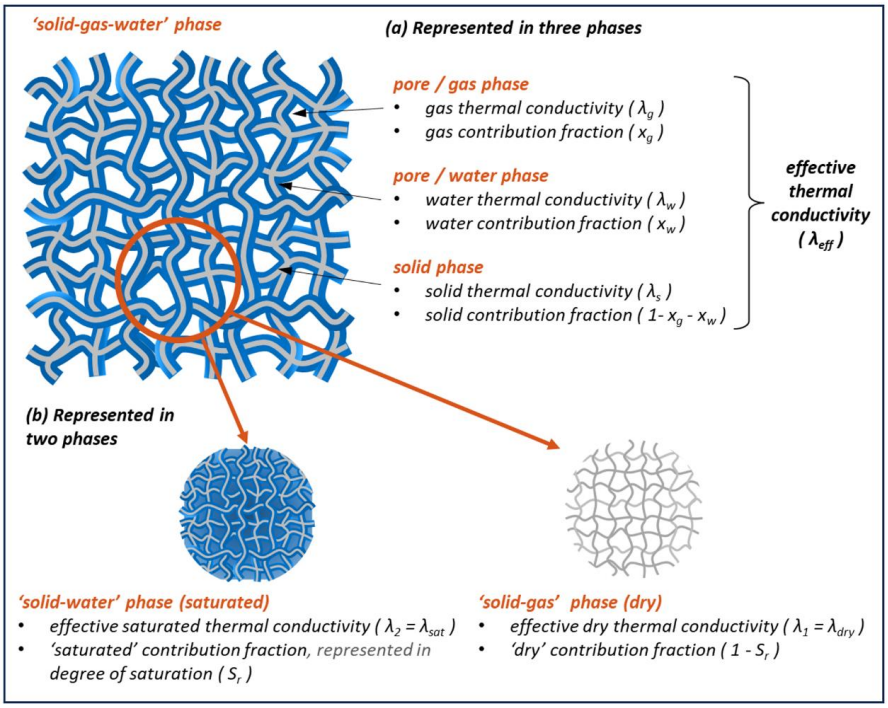

Fig. 8.3 Effective thermal conductivity for moist materials represented in (a) three phases, and (b) two phases.

This reduction transforms the tri-phase moist porous model into a two-phase model characterized by two parameters: effective dry thermal conductivity (λ_{dry}, where $S_r = 0$) and effective saturated thermal conductivity (λ_{sat}, where $S_r = 1$). λ_{dry} and λ_{sat} form the lower and upper boundary limits, respectively, of $\lambda_{eff}(S_r)$. This approach eliminates the need for the solid phase parameter (λ_s). Measuring λ_s for a continuous solid state without any pore spaces in a porous material is impractical [304]. Moreover, λ_s values based on the main constituents of a material provide only an approximation.

Based on these assumptions, the two-phase models are adapted for effective thermal conductivity, $\lambda_{eff}(S_r)$, as follows:

$$\lambda_{eff}(S_r) = \frac{1}{(1 - S_r)/\lambda_{dry} + S_r/\lambda_{sat}} \tag{8-8}$$

$$\lambda_{eff}(S_r) = \lambda_{dry}(1 - S_r) + \lambda_{sat} S_r \tag{8-9}$$

$$\lambda_{eff}(S_r) = \lambda_{dry}\frac{\lambda_{sat} + 2\lambda_{dry} - 2(\lambda_{dry} - \lambda_{sat})S_r}{\lambda_{sat} + 2\lambda_{dry} + (\lambda_{dry} - \lambda_{sat})S_r} \tag{8-10}$$

$$\lambda_{eff}(S_r) = \lambda_{sat}\frac{\lambda_{dry} + 2\lambda_{sat} - 2(\lambda_{sat} - \lambda_{dry})(1 - S_r)}{\lambda_{dry} + 2\lambda_{sat} + (\lambda_{sat} - \lambda_{dry})(1 - S_r)} \tag{8-11}$$

and

$$\lambda_{eff}(S_r) = \frac{1}{4}\left\{\lambda_{sat}(3S_r - 1) + \lambda_{dry}(2 - 3S_r) + \sqrt{\left[\lambda_{sat}(3S_r - 1) + \lambda_{dry}(2 - 3S_r)\right]^2 + 8\lambda_{dry}\lambda_{sat}}\right\} \tag{8-12}$$

Additionally, the exponential function in **Eq. (8-7)** is modified to:

$$\lambda_{eff}(S_r) = \lambda_{dry} \cdot exp(B'S_r) \tag{8-13}$$

with B' defined as:

$$B' = ln\left(\frac{\lambda_{sat}}{\lambda_{dry}}\right) \tag{8-14}$$

An empirical relation based on Somerton et al. [305, 306] is included for comparison, suggesting the following correlation:

$$\lambda_{eff}(S_r) = \lambda_{dry}(1 - \sqrt{S_r}) + \lambda_{sat}\sqrt{S_r} \tag{8-15}$$

This relation is derived from partially brine-saturated quartz sand. This model follows a similar parallel relation but assigns a higher contribution fraction to the saturation phase.

These models are illustrated in **Fig. 8.4**. Similar to the initial models, both series and parallel relations form the outermost lower and upper bounds, followed by the Maxwell-Eucken relations. Both Landauer's and exponential relations fall within the bounds of Maxwell-Eucken's relation. However, the Somerton relation is an outlier, suggesting a higher λ_{eff} than the parallel model.

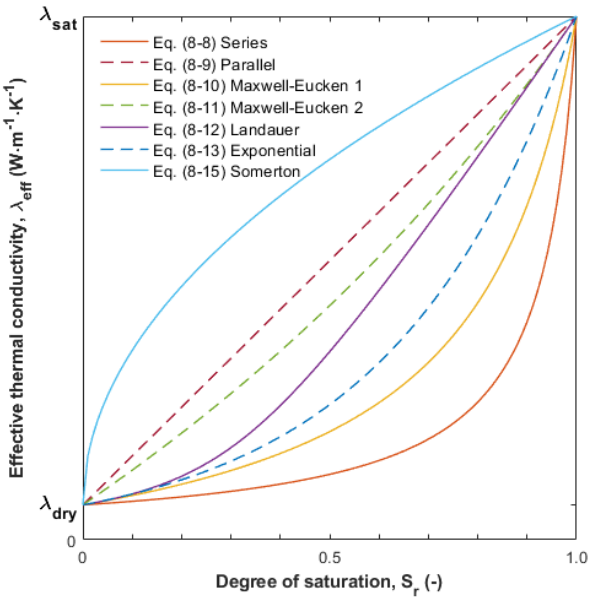

Fig. 8.4 Different two-phase model approaches for effective thermal conductivity under moist conditions.

The equations for $\lambda_{eff}(S_r)$ require only two parameters: λ_{dry} ($S_r = 0$) and λ_{sat} ($S_r = 1$). The λ_{dry} is a commonly measured property for insulation materials. As discussed in the previous section, for highly porous material, λ_{sat} can be approximated using parallel relation with λ_{dry}, λ_a and λ_s. The results, however, are close to λ_w. When λ_s is not known, it is therefore reasonable to equate λ_{sat} to λ_w for highly porous materials. By making this assumption, the estimation of $\lambda_{eff}(S_r)$ requires only one measured parameter, namely λ_{dry}.

Other critical environmental parameters, particularly temperature, are assumed to be independent and constant in this study. This assumption simplifies the model but could be revisited in future studies to account for the temperature dependence of thermal conductivity, especially for materials and conditions where temperature variations are significant

8.3. RESULTS AND DISCUSSION

8.3.1. Model validation to highly porous insulation materials

The validation of **Eqs. (8-8)** to **(8-15)** are conducted using materials featuring measured moisture-dependent thermal conductivity data. Two established sources are used for model validation: the open-source MASEA database [294] and a commercial database [307]. Only materials with measured moisture-dependent thermal conductivity are considered, leading to a selection of thirteen porous insulation materials. These materials include various types such as stone wools, expanded polystyrene (EPS) foam, urea-formaldehyde (UF) foam, cork, phenolic (PF) foam,

polyurethane (PU) foam, extruded polystyrene (XPS) foam and glass fibres. Materials with estimated properties are excluded from the analysis.

The measured moisture-dependent thermal conductivities are plotted against the corresponding degree of saturation (S_r), alongside the predicted values from **Eqs. (8-8)** to **(8-15)**, as depicted in **Fig. 8.5**. The S_r is converted from water content (w) using **Eq. (8-7)** based on the measured porosity (φ) and bulk density (ϱ).

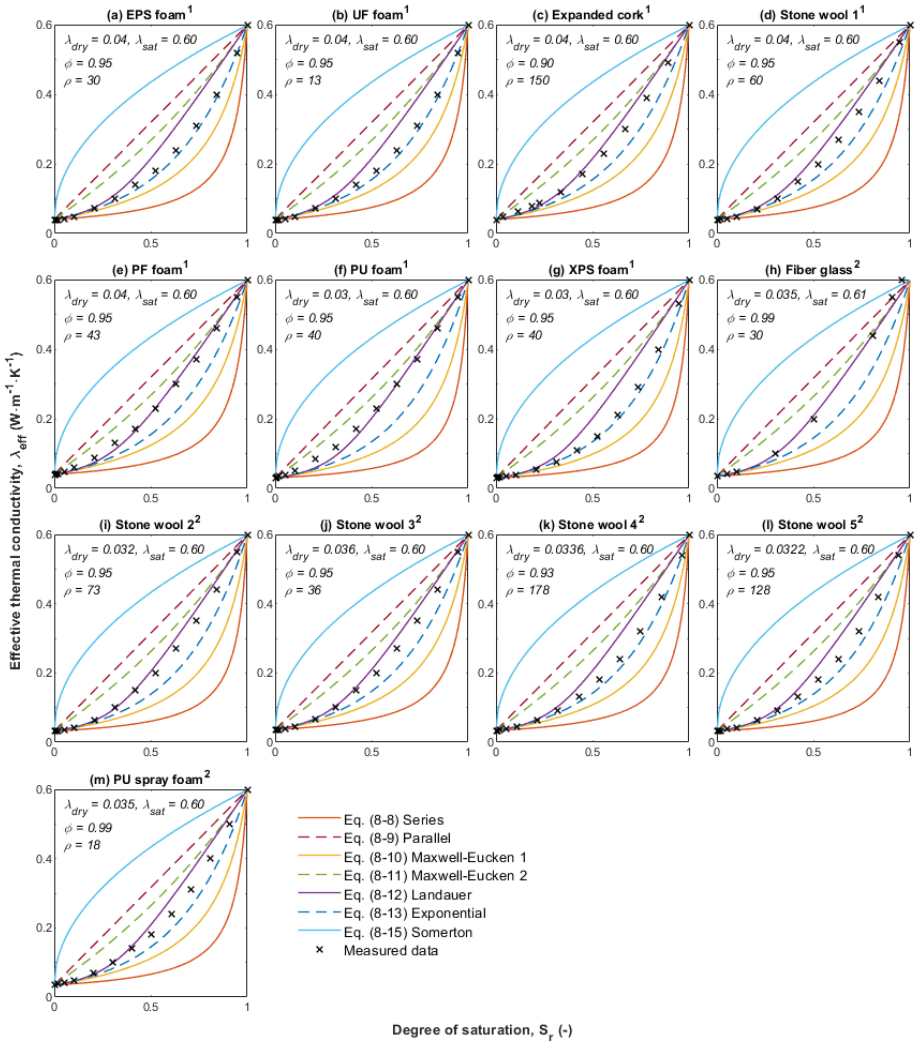

Fig. 8.5 Analytical solutions to approximate moisture-dependent thermal conductivities using **Eqs. (8-8)** to **(8-15)**, in comparison to measurement data of different porous insulation materials from the MASEA database from Fraunhofer-IBP (denoted 1) and material database from WUFI (denoted 2).

Overall, the measurement data generally falls within the upper and lower bounds set by both the series-parallel relations and Maxwell-Eucken's relations. The fittings also indicate the validity of equating contribution fraction x_2 to S_r in estimating λ_{eff} when applying **Eqs. (8-8)** to **(8-15)**.

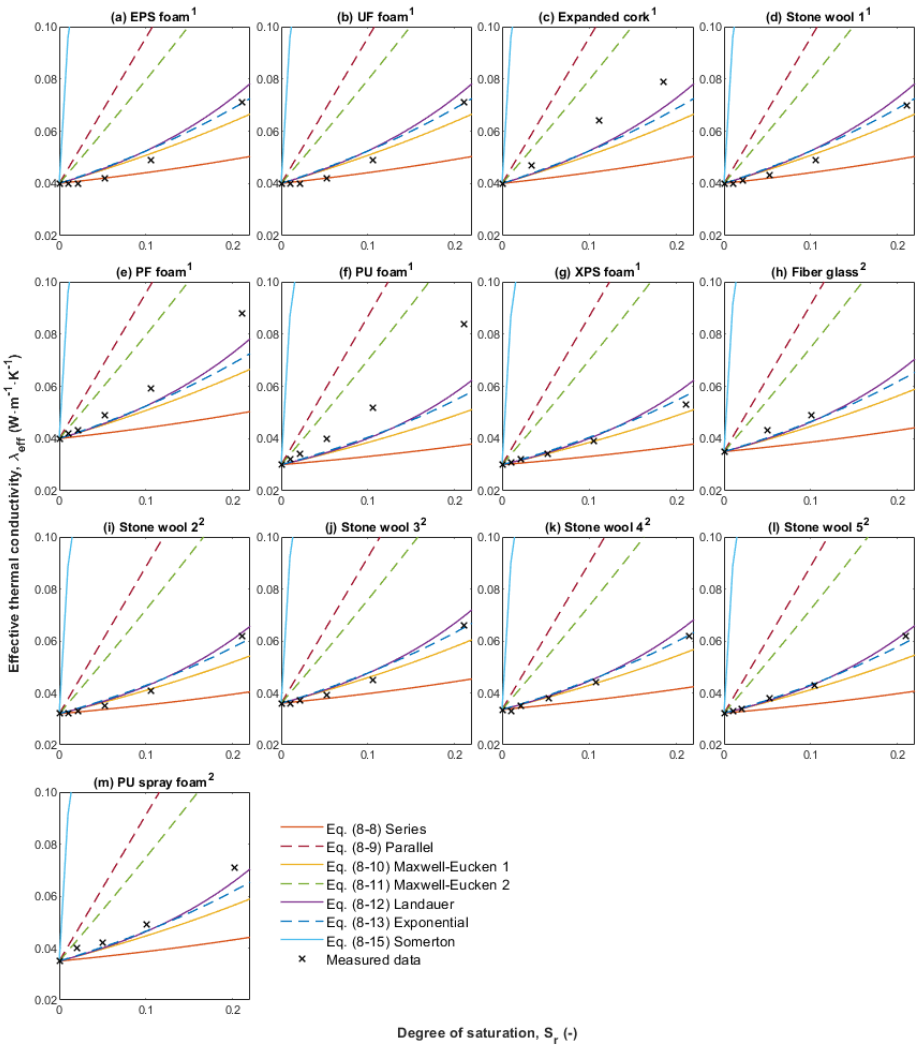

Fig. 8.6 Similar to **Fig. 8.5** but focusing only on lower degrees of saturation.

At lower degrees of saturation (up to 0.2), the insulation materials tend to exhibit effective thermal conductivities closer to the lower bounds. In some instances, they align with the series relation, as illustrated in **Fig. 8.6**. In this lower saturation range, the majority of the measurements follow the trends of Maxwell-Eucken-1's, exponential, and Landauer's relations.

As the moisture content increases further, the effective thermal conductivities demonstrate an exponential trend. Most of the data points fall within a narrower upper bound set by Landauer's relation and a lower bound set by exponential relations, as displayed in **Fig. 8.5**. It should be noted that the measurements do not follow the empirical square root correlation as suggested by Somerton. This could be due to the difference in porosity: Somerton's relation is derived based on material with porosity between 0.3 and 0.5, while the insulation materials investigated in this section are highly porous ($\varphi \geq 0.9$).

Upon overall assessment, the measurement data does not perfectly conform to the derived solutions based on **Eqs. (8-8)** to **(8-15)**. Nevertheless, the trends are notably consistent with an exponential trend. Specifically, the effective thermal conductivity increases gradually at lower moisture content levels and then exponentially approaches the thermal conductivity for a standalone water phase. Therefore, a single linear approximation would either underestimate the effective thermal conductivity at a lower water content range (if approximated using the entire water content range, similar to a parallel relation) or at a higher range (if approximated using only the lower water content range).

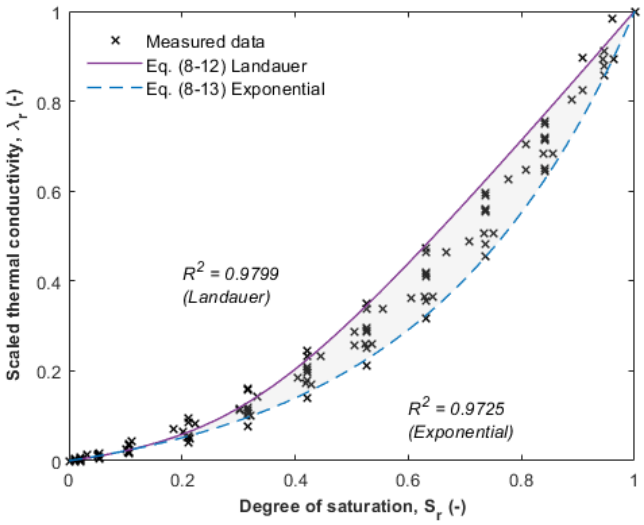

Fig. 8.7 Scaled thermal conductivity (**Eq. (8-16)**) versus degree of saturation (S_r) for **Eqs. (8-12)** and **(8-13)**, plotted against the overall measured data with the corresponding coefficient of determination R^2.

The analysis of the proposed solutions reveals that both Landauer's and exponential relations, represented by **Eqs. (8-12)** and **(8-13)**, provide the best fit for the measured data. The scaled thermal conductivity (λ_r) is defined as follows:

$$\lambda_r(S_r) = \frac{\lambda_{eff}(S_r) - \lambda_{dry}}{\lambda_{sat} - \lambda_{dry}} \tag{8-16}$$

where λ_{dry} is the thermal conductivity for $S_r = 0$, and λ_{sat} is the one for $S_r = 1$. This is plotted against the corresponding S_r in **Fig. 8.7**. Both Landauer's and exponential relations exhibit a high average coefficient of determination (R^2), with values of 0.9799 and 0.9725 respectively. This indicates a strong correlation between the predicted and observed values. Furthermore, **Eq. (8-12)** could serve as the upper bound, while **Eq. (8-13)** could serve as the lower bound for the moisture-dependent thermal conductivity.

8.3.2. Model validation to medium-density materials

Eqs. (8-8) to **(8-15)** are further validated on different medium-density materials. **Fig. 8.8** presents the moisture-dependent thermal conductivity for various concretes, specifically five different wood-clay concrete samples based on Bouguerra [302], and five different wood concrete samples from Taoukil et al. [301]. **Fig. 8.10** shows the moisture-dependent thermal conductivity for ten different peat, soil, and sand samples based on He et al. [300]. The corresponding scaled thermal conductivity for **Fig. 8.8** and **Fig. 8.10** are plotted in **Fig. 8.9** and **Fig. 8.11**, respectively.

The effective thermal conductivity of medium-density materials in **Fig. 8.8** no longer falls within the narrower bounds set by Landauer's and exponential relations. Overall, the data are contained within the wider bounds set by Somerton's and exponential relations, with most of them further falling within narrower bounds set by parallel and Landauer's relation. Instead of an exponential trend exhibited by highly porous materials, the effective thermal conductivity of medium-density moist materials follows a linear trend, corresponding to an average R^2 of 0.9721 for the parallel relation, as shown in **Fig. 8.9**.

In contrast, the effective thermal conductivity of moist sand and soil follows more closely a square root trend, as shown in **Fig. 8.10**. This aligns with the empirical square root correlation suggested by Somerton. Somerton's relation exhibits an average R^2 of 0.9566, while the parallel relation has a lower R^2 of 0.8989. Both Somerton's and parallel relations can serve as upper and lower bounds, respectively, for soil and sand-type materials, as shown in **Fig. 8.11**.

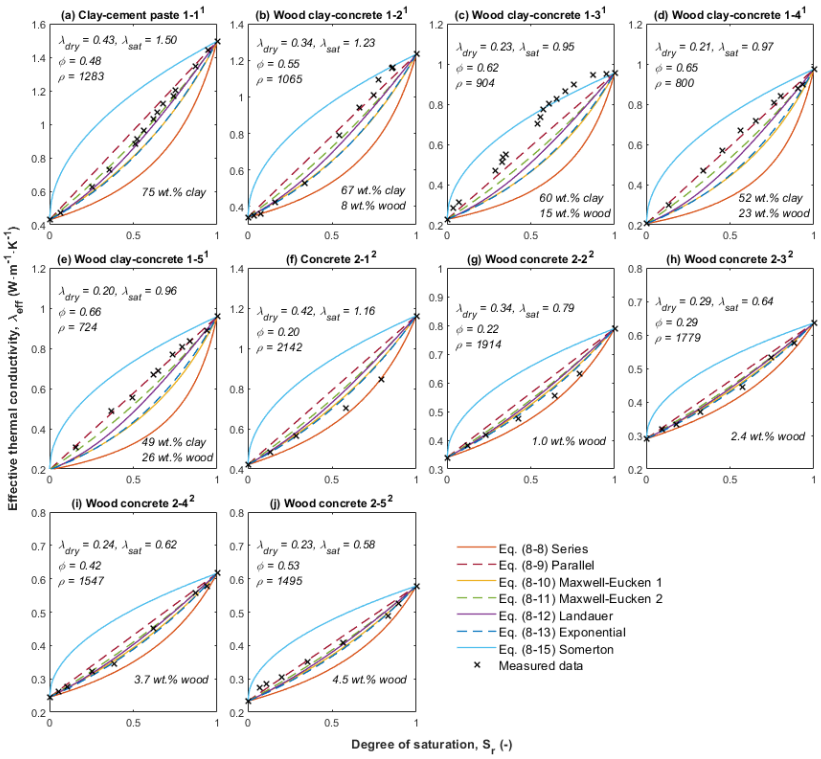

Fig. 8.8 Analytical solutions to approximate moisture-dependent thermal conductivities using **Eqs. (8-8)** to **(8-15)**, in comparison to measurement data of different medium-density materials based on Bouguerra [302] (denoted 1) and Taoukil et al. [301] (denoted 2).

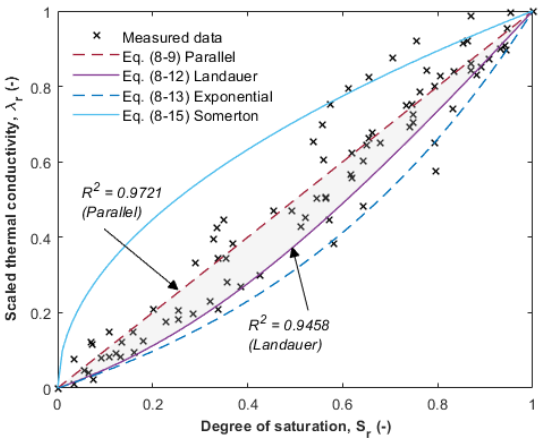

Fig. 8.9 Scaled thermal conductivity (**Eq. (8-17)**) versus degree of saturation (Sr) for **Eqs. (8-9)** and **(8-12)**, plotted against the overall measured data from **Fig. 8.8** with the corresponding coefficient of determination R^2.

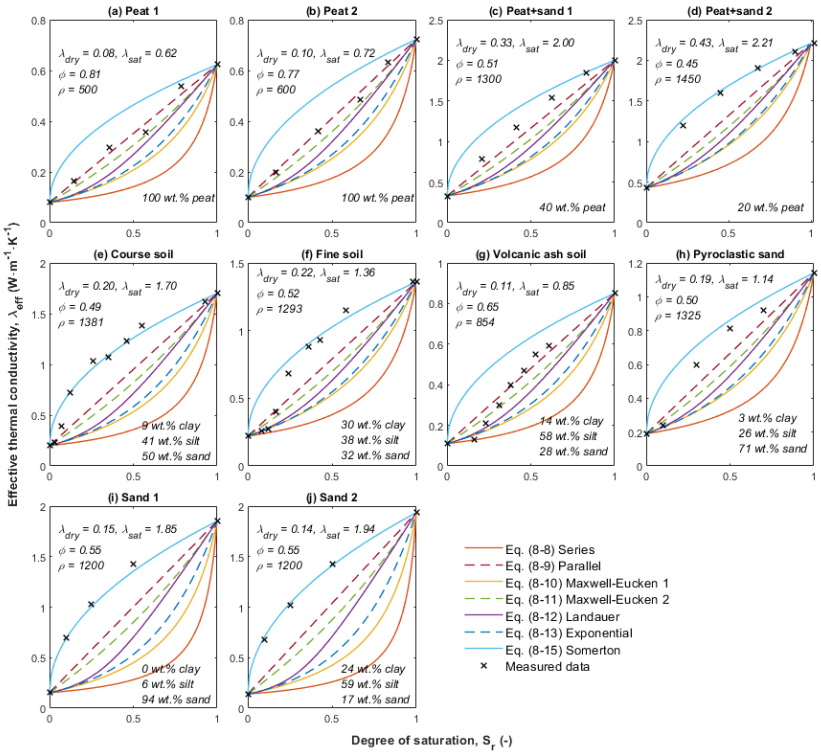

Fig. 8.10 Analytical solutions to approximate moisture-dependent thermal conductivities using **Eqs. (8-8)** to **(8-15)**, in comparison to measurement data of different medium-density materials based on He et al. [300].

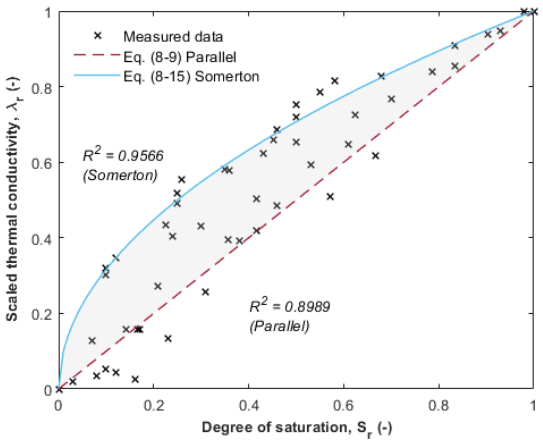

Fig. 8.11 Scaled thermal conductivity (**Eq. (8-17)**) versus degree of saturation (Sr) for **Eqs. (8-9)** and **(8-15)**, plotted against the overall measured data from **Fig. 8.10** with the corresponding coefficient of determination R^2.

8.3.3. Parametric study and discussion

Eqs. (8-8) to **(8-15)** utilize only two main parameters, namely effective dry thermal conductivity (λ_{dry}) and effective saturated thermal conductivity (λ_{sat}), without considering porosity, pore shapes, pore size distribution, or material types. From **Fig. 8.5** to **Fig. 8.11**, a distinct pattern emerges, which is summarized in **Fig. 8.12**. For materials with low λ_{dry} (up to 0.05 $W \cdot m^{-1} \cdot K^{-1}$) and low λ_{sat} (around 0.6 $W \cdot m^{-1} \cdot K^{-1}$), their effective thermal conductivities fall within the narrow and lower boundaries set by exponential and Landauer's relations. For materials with higher λ_{dry} and λ_{sat}, such as medium-density materials, the distribution of their effective thermal conductivity becomes broader. The upper bound shifts higher, limited by the parallel relation, and in the case of soil and sand, by Somerton's relation. Similarly, the lower bound shifts upward, aligning with Landauer's relation, and for soil and sand, with the parallel relation.

When materials are categorized based on their bulk density (ϱ) and porosity (φ), a similar pattern can be observed, as shown in **Fig. 8.13**. For materials with lower bulk densities (below 200 $kg \cdot m^{-3}$) and higher porosity (above 0.9), their thermal conductivities fall within the exponential and Landauer's relations. Additionally, materials with higher bulk densities and lower porosities exhibit effective thermal conductivities that generally follow a linear trend, albeit within a broader range.

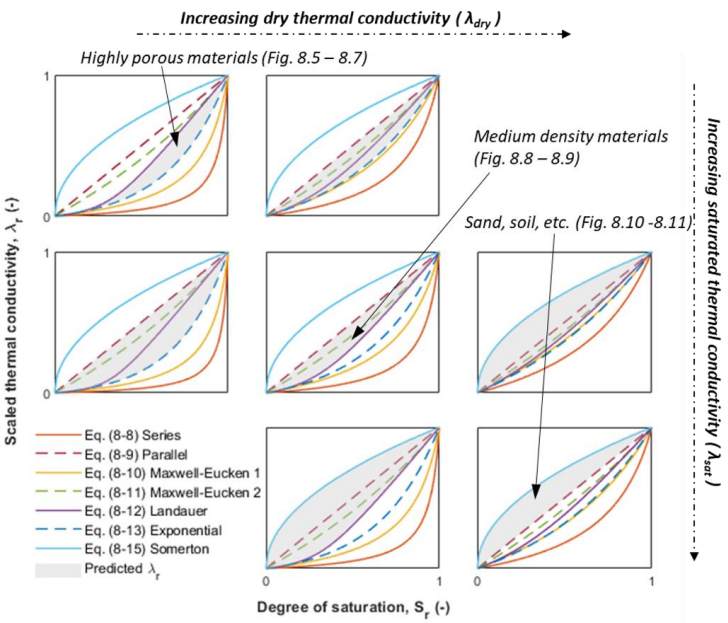

Fig. 8.12 Variations of scaled thermal conductivity with degrees of saturation at different dry thermal conductivity (λ_{dry}) and saturated thermal conductivity (λ_{sat}).

For highly porous materials, the effective thermal conductivities do not show significant variation based on their constituents (organic or inorganic) or form (foam or fibrous mat). The low fraction of the solid phase in these materials diminishes the influence of the solid phase's thermal conductivity on their overall thermal conductivity. Due to their highly porous structure, the water

phase does not form a continuous conduction path at a lower degree of saturation and only increases exponentially at a higher degree of saturation.

Conversely, the thermal conductivity of the solid phase plays a more significant role in the effective thermal conductivity of medium-density materials. It can be observed that sand and soils with higher silica (sand) content align more closely with the upper Somerton's relation, compared to samples with lower silica content, which are closer to a lower parallel relation (**Fig. 8.10**). The granulated form of these materials also contributes significantly. The presence of an additional water layer on granulated materials increases the surface area in contact with neighbouring particles, even at lower degrees of saturation, thereby enhancing the heat conduction paths, as indicated by Somerton's relation.

The broader range of effective thermal conductivity exhibited by the selected medium-density materials can be attributed to the inhomogeneous nature of the material constituents and microstructure, as well as moisture distribution in the moist materials. Additionally, the challenging measurement techniques used can introduce uncertainties to the results. This variability underscores the complexity of accurately predicting thermal conductivity in medium-density materials, highlighting the importance of considering both material composition and microstructural characteristics in thermal conductivity models.

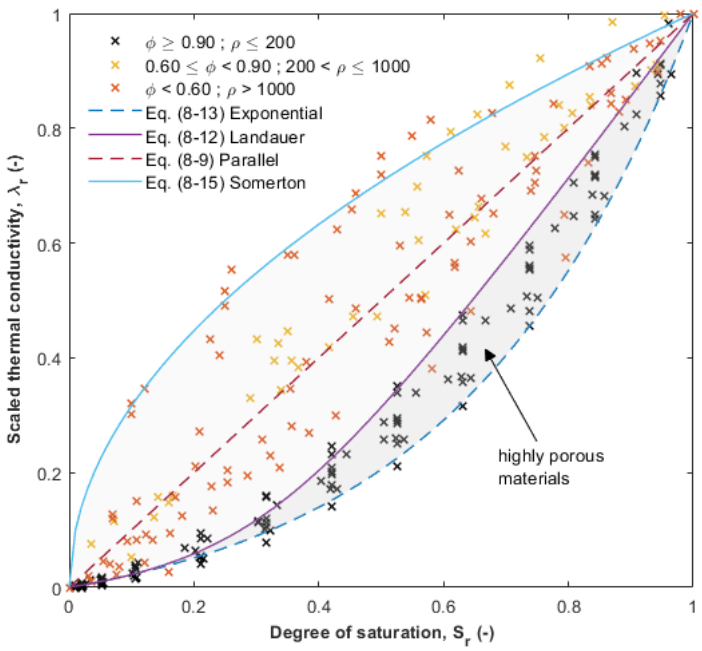

Fig. 8.13 Scaled thermal conductivity (**Eq. (8-17)**) versus degree of saturation (Sr) plotted against the overall measured data from **Fig. 8.5**, **Fig. 8.8** and **Fig. 8.10**. The measured data are categorized based on their porosity (-) and density ($kg \cdot m^{-3}$).

8.4. CONCLUSION

A straightforward and robust two-phase method is proposed to predict moisture-dependent thermal conductivity (λ_{eff}) for porous materials, of medium and high porosity. This approach adapts six analytical solutions from the multiphase model, including series-parallel, Maxwell-Eucken, Landauer's, and exponential relations, for application to moist porous materials. By introducing an arbitrary effective dry phase and a saturated phase, the original tri-phase model, which includes solid, air, and water phases, is simplified into a two-phase model. This reduction streamlines the analysis and facilitates practical implementation.

The proposed method requires only two parameters to predict λ_{eff} under different degrees of saturation (S_r): effective dry thermal conductivity (λ_{dry}, where $S_r = 0$) and effective saturated thermal conductivity (λ_{sat}, where $S_r = 1$). λ_{dry} and λ_{sat} form the lower and upper boundary limits, respectively, of $\lambda_{eff}(S_r)$.

For highly porous materials ($\varphi \geq 0.9$), in the absence of direct λ_{sat} measurement, λ_{sat} can be obtained using the parallel relation. The contribution fraction x_2 is first estimated using **Eq. (8-2)** with λ_{dry}, λ_s, and λ_a as inputs. Then, λ_{sat} is approximated using the same **Eq. (8-2)** with the calculated x_2, λ_s and λ_w. It appears that λ_{sat} is often close to λ_w. Therefore, when λ_s is not known, it is reasonable to equate λ_{sat} to λ_w for highly porous materials. For medium-density materials, λ_{sat} can be obtained using Landauer's relation following the same procedure, though with a lower accuracy.

The validation results indicate that both Landauer's relation, **Eq. (8-12)**, and exponential relation, **Eq. (8-13)**, provide the best fit to the measured data of partially saturated porous media, with average coefficients of determination (R^2) at 0.9799 and 0.9725, respectively. Moreover, Landauer's relation can serve as the upper bound, while the exponential relation can serve as the lower bound for moisture-dependent thermal conductivity.

For medium-density materials, the distribution of their effective thermal conductivity becomes broader. The upper bound aligns with the parallel relation and, in the case of soil and sand, with Somerton's relation. The lower bound aligns with Landauer's relation and, for soil and sand, with the parallel relation.

This proposed approach, grounded in commonly measured parameters, offers a practical method for predicting the thermal conductivity of moist porous insulation material. Its simplicity and reliance on readily available data enhance its feasibility for real-world implementation.

Further assessments for model improvement include combining the study with temperature-dependant thermal conductivity and evaluating the influence of material composition and microstructural characteristics to the models.

9. CONCLUSIONS AND RECOMMENDATIONS

9.1. CONCLUSIONS

This thesis is dedicated to advancing the development of insulation materials for sustainable building performance. It is guided by four research objectives established at the outset, which aim to reduce energy demand, carbon emissions, and material demand in the building and construction sectors. The findings from seven research topics are presented in the preceding chapters, with key conclusions summarized as follows:

In-depth analysis of bio-based insulation composites: Among the four bio-based composites (mycelium, hemp, grass, and cork) investigated, the cork composite exhibits the lowest thermal conductivity, low sorption properties and no risk of mould growth. The hemp, grass and mycelium composites have similar hygric properties and show deterioration under lab-based mould growth tests. The mycelium composite has the highest thermal conductivity and is vulnerable to mould growth in a humid environment. Simulations suggest that a timber frame wall with a fully ventilated cavity is more suitable for low-density bio-based insulation materials compared to a fully ventilated brick wall. The mould growth potential of the studied insulation materials is higher under temperate climates when compared to continental climates.

Wheat and barley straws are investigated as substitutes for conventional insulation materials. Barley straws exhibit lower sorption capacity and thermal conductivity compared to wheat straws. They also show less intense mould growth, attributed to higher wax and lignin contents, lower sorption isotherms, and higher vapour diffusion due to the existence of macropores within stalk structures. These factors suggest that barley straws are more suitable as thermal insulation material than wheat straws. Half of the twenty-two simulated cases, representing different climate types, demonstrate a considerable probability of mould growth within the straw layers. The application of an antifungal surface treatment using boric acid on both wheat and barley straws substantially improves their resistance to mould growth.

Development and evaluation of insulation composites from bio-based, waste-based, and by-products: Geopolymer is demonstrated as a viable alternative to OPC in wood wool geopolymer boards (WWGB) production. The WWGB samples meet both the prescribed minimum compressive strength (20 kPa) and bending strength (1700 kPa) requirements. Mechanical strength is primarily influenced by the Na_2O concentration, followed by the GGBFS percentage and the modulus. The presence of natural fibres impacts the optimal value of Na_2O concentration and modulus for compressive strength. Furthermore, WWGB made from treated wood wool exhibits higher bending strengths. Median thermal conductivities of WWGB fall within the range between 70 and 85 $mW \cdot m^{-1} \cdot K^{-1}$. WWGB show low moisture sorption and water vapour diffusion resistance and is primarily influenced by the fibre component. Bulk densities of WWGB range from 350 to 450 $kg \cdot m^{-3}$, and open porosities range from 70% to 80%.

Further research is conducted on the development of straw geopolymer boards (SGB), where straws serve as alternative fibres for wood wool, and geopolymer functions as a substitute for OPC.

Environmental impact indicators are assessed for SGB and compared to WWGB and wood wool cement boards (WWCB). The investigation focuses on the implications of allocation methods for raw materials. Treating FA, GGBFS and straws as by-products results in significantly increased impact categories. Both SGB and WWGB exhibit higher environmental impacts across more than half of the 19 impact categories compared to WWCB. Overall, binders dominate most indicators, followed by heat curing and drying. Alkali treatment on fibre is another major contributor, especially when characteristic improvement is required for fibre substitution. Transportation plays a minimal role; however, it could become a dominant factor if raw materials are not locally produced. The study indicates the environmental benefits of substituting OPC with geopolymer in terms of global warming potential, however, it is less obvious when considering other impact indicators. However, utilizing straws as a substitute for wood wool reveals disadvantages in overall performance, making it less attractive as a solution.

Alkali-activated lightweight aggregates are produced using stone wool as a precursor. The material characteristics of the fabricated stone wool-based aggregates are influenced by the proportion of milled stone wool and as-is stone wool in their compositions. It has been observed that the fibre morphology of as-is stone wool influences rheology, introducing a greater number of pores or defects, which results in a decrease in mechanical strength. The samples exhibit porosity between 67% to 72%, and dry thermal conductivity ranging from 0.075 to 0.094 $W \cdot m^{-1} \cdot K^{-1}$. However, aggregates with higher porosity demonstrate increased thermal conductivity under humid conditions, attributed to their elevated moisture adsorption and water absorption capacity.

Energy rehabilitation of existing building stocks: A typical Dutch building that has a cavity wall is simulated for its performance when filled in with an advanced aerogel composite. The indoor RH of the reference building is reduced, from an average of 60% RH for the original air cavity wall to 54% RH. The annual heating and cooling demands are significantly reduced, up to a 72% reduction compared to the original construction. The median predicted mean vote (PMV) improves from -1.5 (cool) of the original construction to -0.8 (slightly cool) of rehabilitated walls with aerogel composite, corresponding to the mean predicted percentage dissatisfied (PPD) of 51% and 18% of thermally dissatisfied occupants respectively.

In the hydrothermal simulation involving the utilization of stone wool-based aggregates for crawl space rehabilitation, a notable reduction in water content and an increase in floor surface temperature are observed in the floor assembly of the rehabilitated crawl space partially filled with aggregates, compared to the original construction with an empty crawl space. This decrease in water content within the floor assembly presents potential advantages for maintaining the structural integrity of buildings and mitigating adverse impacts on occupant comfort and health. Furthermore, there is potential for a 5.4% reduction in heating energy consumption after rehabilitation.

Moisture-dependent thermal conductivity: A generalized solution for moisture-dependent thermal conductivity (λ_{eff}) in a highly porous medium is developed, utilizing readily available parameters. By introducing arbitrary dry and saturated phases, the tri-phase model (solid, gas, and water) is simplified into a two-phase model. The proposed method requires only two parameters to predict λ_{eff} under different degrees of saturation (S_r): effective dry thermal conductivity (λ_{dry}) and effective saturated thermal (λ_{sat}). In the absence of direct λ_{sat} measurement, this λ_{sat} can be obtained

using λ_{dry} and the parallel relation for highly porous media and using Landauer's relation for medium-density materials. Validation results indicate that both Landauer's and exponential relations provide the upper bound and lower bounds, respectively, for λ_{eff}. For medium-density materials, the upper bound aligns with the parallel relation and the lower bound aligns with Landauer's relation.

9.2. RESEARCH IMPLICATIONS

The research conducted in this thesis represents an advancement in the development and understanding of sustainable insulation materials, with a particular focus on those derived from bio-based sources, waste, and by-products. This study underscores the potential of these materials and strategies to reduce energy demand, carbon emissions, and material consumption within the building and construction sectors.

The findings reveal that while bio-based insulation materials such as straw, cork, hemp, and grass composites exhibit promising hygrothermal properties, they also face challenges related to moisture susceptibility and mould growth, particularly in humid climates. These issues must be addressed to ensure the long-term durability and performance of these materials. The application of boric acid treatment, as demonstrated with straw-based insulation, offers a promising approach to mitigate these risks, suggesting a viable method to enhance the durability of bio-based insulation materials. Additionally, the study highlights the importance of considering the specific application and climatic conditions when selecting bio-based materials to optimize their performance and durability.

In the development of wood wool geopolymer boards (WWGB) and straw geopolymer boards (SGB), the research confirms the feasibility of substituting conventional ordinary Portland cement (OPC) with alternative binders such as fly ash-based geopolymer. However, the results are less satisfactory when replacing commercial wood wool with agricultural by-product straws, highlighting the challenges associated with using non-conventional bio-based materials. The life cycle assessment (LCA) results further emphasize the necessity of evaluating multiple environmental impact indicators, as material substitution can sometimes result in trade-offs in different aspects of sustainability performance.

The research also illustrates that a one-size-fits-all solution for reducing energy demand, carbon emissions, and material consumption is challenging. For instance, the use of aerogel composites in cavity wall rehabilitation demonstrates a significant reduction in energy demand but also requires careful consideration of the carbon footprint and cost associated with aerogel production. In contrast, recycled stone wool used as insulation aggregates for crawl space rehabilitation offers only moderate improvements but represents an innovative approach to waste management and contributes to the circular economy. Similarly, bio-based insulation composites may offer lower embodied carbon and potential material savings, but their hygrothermal performance generally does not surpass that of conventional insulation materials, such as stone wool or polymer-based options.

Overall, this research underscores the importance of adopting a holistic approach to the development and application of insulation materials within the built environment. The choice of insulation materials should be guided by their intended application, overall building design, and climatic conditions. While bio-based and waste-based materials can contribute to reduced carbon emissions and material consumption, significant energy reductions, especially in space-constrained rehabilitation projects, may necessitate the use of advanced superinsulation materials like aerogel composites.

In conclusion, this thesis highlights the need to balance immediate benefits with long-term implications for building performance, durability, and environmental sustainability. These findings provide valuable insights for future research and industry practices, offering a comprehensive perspective on various insulation solutions and contributing to the advancement of sustainable construction.

9.3. LIMITATIONS AND RECOMMENDATIONS

This thesis presents several limitations, alongside recommendations for future research and development:

Moisture transfer: The research primarily addresses vapour diffusion resistance, without considering the liquid transport coefficient for capillary water conduction. Future studies should comprehensively investigate all major moisture transport mechanisms, including vapour diffusion, capillary conduction, and surface diffusion. Moreover, further analysis of the vapour diffusion resistance factor in bio-based materials is warranted, particularly given the variations observed between wet-cup and dry-cup tests in Chapters 2 and 3.

In-field monitoring and survey: The building performance simulations in Chapters 6 and 7 are based on a typical Dutch building with a cavity wall or narrow crawl space. To validate these simulations, in-field monitoring and survey campaigns are essential. Specifically, tracking indoor humidity, temperature, and energy demand for heating, cooling, and ventilation will help confirm the benefits of energy rehabilitation efforts.

Durability vs sustainability: While natural bio-based insulation materials are biodegradable and reduce end-of-life environmental impacts, this biodegradability can compromise durability compared to conventional materials like mineral wool or polymer-based foams. Applying mould resistance treatments, such as boric acid (as discussed in Chapter 2), may enhance durability but introduce additional environmental burdens, as evidenced by the alkali treatment in Chapter 6. Therefore, comprehensive life cycle assessments of various durability treatments for bio-based materials should be conducted to evaluate the balance between durability and sustainability.

Standardization of bio-based materials: Bio-based materials derived from agricultural by-products or waste are inherently heterogeneous, and influenced by factors such as species type, growth environment, and handling methods. For instance, barley and wheat straws exhibit different material characteristics and durability performances, as shown in Chapter 3. Grouping them under a single category like "straws" can lead to inconsistent performance and reduced confidence in

their application. A systematic study of bio-based materials is necessary to establish standardization based on physical properties or chemical compositions, similar to the cement industry, to provide reliable references for manufacturers, end users, and regulators.

Durability and leaching tests: The geopolymer-based composites developed in Chapters 4, 5, and 7 demonstrate satisfactory insulation and mechanical properties under laboratory conditions. However, durability and leaching tests were not conducted. Given that these composites are cured at 60°C without high-temperature sintering, it is recommended to perform leaching tests to assess potential environmental impacts. Additionally, durability tests should be conducted to evaluate the materials' performance under conditions such as exposure to sunlight, frost, or prolonged water immersion.

Alternative precursors: The use of fly ash and ground granulated blast furnace slag (GGBFS) as precursors for geopolymer binders in Chapters 4 and 5 faces challenges due to the declining availability of these materials as coal power and blast furnace operations are phased out. Alternatives such as fly ash from municipal solid waste incineration or mineral wool waste, as explored in Chapter 7, should be considered. Further research is needed to evaluate these alternatives' effectiveness as binders for natural fibres, their compatibility, and their overall performance.

Sustainable production of alkali activators: The environmental impact of conventional alkali activators, such as sodium hydroxide and sodium silicate solution, is significant in geopolymer production. Future research should focus on developing sustainable methods for producing alkali activators, considering both raw material sourcing and the environmental impact of manufacturing processes.

End-of-life scenarios: The end-of-life scenarios for geopolymer-based composites require further exploration. While incineration is often assumed, alternative treatments such as crushing for reuse in different applications, resource recovery, or other methods aligned with circular economy principles should be thoroughly investigated.

BIBLIOGRAPHY

[1] UNEP, "Global Status Report for Buildings and Construction: Beyond foundations: Mainstreaming sustainable solutions to cut emissions from the buildings sector," Nairobi. doi:10.59117/20.500.11822/45095., 2024.

[2] "Global Resources Outlook 2024: Bend the Trend – Pathways to a liveable planet as resource use spikes.," Nairobi. https://wedocs.unep.org/handle/20.500.11822/44901, 2024.

[3] IEA, "Tracking Clean Energy Progress 2023: Assessing critical energy technologies for global clean energy transitions," Paris. https://www.iea.org/reports/tracking-clean-energy-progress-2023, 2023.

[4] UNEP, "Building Materials and the Climate: Constructing a New Future," Nairobi, 2023.

[5] European Commission, "Circular Economy - Principles for Building Design," https://ec.europa.eu/docsroom/documents/39984, 2020.

[6] WBCSD, "The business case for circular buildings: Exploring the economic, environmental and social value," 2021.

[7] World Green Building Council, "The circular built environment playbook," https://worldgbc.org/article/circular-built-environment-playbook/, 2023.

[8] RVO, "Monitor Energiebesparing Gebouwde Omgeving (Monitor Energy Saving Built Environment)," Rijksdienst voor Ondernemend Nederland, Utrecht, 2021.

[9] RVO, "Lange Termijn Renovatiestrategie: Op weg naar een CO2-arme Gebouwde Omgeving (Long-Term Renovation Strategy: En Route to a low-CO2 Built Environment)," Rijksdienst voor Ondernemend Nederland, Den Haag, 2020.

[10] RVO, "Investeringssubsidie duurzame energie en energiebesparing (ISDE)," 2024. [Online]. Available: https://www.rvo.nl/subsidies-financiering/isde/woningeigenaren/isolatiemaatregelen.

[11] RVO, "Marktinformatie isolatiematerialen, isolatieglas en HR-ketels 2010-2020 (Market information on insulation materials, insulating glass and high-efficiency boilers 2010-2020)," Rijksdienst voor Ondernemend Nederland, Den Haag, 2021.

[12] M. Ganobjak, S. Brunner and J. Wernery, "Aerogel materials for heritage buildings: Materials, properties and case studies," *Journal of Cultural Heritage,* no. 42, pp. 81-98. doi:10.1016/j.culher.2019.09.007, 2020.

[13] IEA, "GlobalABC Roadmap for Buildings and Construction: Towards a zero-emission, efficient and resilient buildings and construction sector," IEA, Paris, 2020.

[14] D. Jones, "1.2 Bio-based building materials and their role in the modern building sector," in *Performance of Bio-based Building Materials*, Woodhead Publishing, 2017, pp. 2-4. doi: 10.1016/B978-0-08-100982-6.00001-X.

[15] C. Brischke, "5.4 Moisture performance," in *Performance of Bio-based Building Materials*, Woodhead Publishing, 2017, pp. 277-285. doi:10.1016/B978-0-08-100982-6.00005-7.

[16] J. V. Acker and S. Palanti, "5.3 Durability," in *Performance of Bio-based Building Materials*, Woodhead Publishing, 2017, pp. 257-277. doi:10.1016/B978-0-08-100982-6.00005-7.

[17] C. C. Pavel and D. T. Blagoeva, "Competitive landscape of the EU's insulation materials industry for energy-efficient buildings," Publications Office of the European Union, Luxembourg, 2018.

[18] Á. Conde, A. B. Sutherland, M. Fraser, G. Roemers, L. Sosa and M. Rohmer, "The Circularity Gap Report: Built Enviroment, the Netherlands," Circle Economy, 2022.

[19] WUFI, "WUFI Pro 6.4 online help, Appendix: Basic: moisture transport in building materials".

[20] WUFI, *WUFI-Bio 40.0 Help: Limitations of the Model.*

[21] WUFI, *WUFI Plus 3.1 manual,* 2018.

[22] UNEP, "2021 Global Status Report for Buildings and Construction: Towards a Zero-emission, Efficient and Resilient Buildings and Construction Sector.," United Nations Environment Programme, Nairobi, 2021.

[23] G. Grazieschi, F. Asdrubal and G. Thomas, "Embodied energy and carbon of building insulating materials: A critical review," *Cleaner Environmental Systems,* vol. 2, p. 100032. doi: 10.1016/j.cesys.2021.100032, 2021.

[24] C. P. Hoang, K. A. Kinney, R. L. Corsi and P. J. Szaniszlo, "Resistance of green building materials to fungal growth," *International Biodeterioration & Biodegradation,* vol. 64, no. 2, pp. 104-113. doi: 10.1016/j.ibiod.2009.11.001, 2010.

[25] A. Brambilla and A. Sangiorgio, "Mould growth in energy efficient buildings: Causes, health implications and strategies to mitigate the risk," *Renewable and Sustainable Energy Reviews,* vol. 132, p. 110093. doi:10.1016/j.rser.2020.110093, 2020.

[26] FAIRM, "FAIRM foam," [Online]. Available: https://www.fairm.nl/material. [Accessed 25 3 2022].

[27] GRAMITHERM, "Gramitherm," [Online]. Available: https://gramitherm.ch/products/?lang=en. [Accessed 25 3 2022].

[28] HEMPFLAX, "HEMPFLAX," [Online]. Available: https://www.hempflax.com/en/applications/construction/. [Accessed 25 3 2022].

[29] "PROSUBER," [Online]. Available: https://www.prosuber.com/geexpandeerde-kurk-productinformatie/. [Accessed 25 3 2022].

[30] D. Kumar, M. Alam, P. X. Zou, J. G. Sanjayan and R. A. Memon, "Comparative analysis of building insulation material properties and performance," *Renewable and Sustainable Energy Reviews,* vol. 131, p. 110038. doi:10.1016/j.rser.2020.110038., 2020.

[31] E. Elsacker, S. Vandelook, J. Brancart, E. Peeters and L. D. Laet, "Mechanical, physical and chemical characterisation of mycelium-based composites with different types of lignocellulosic substrates," *PloS One,* vol. 14, no. 7, p. e0213954. doi:10.1371/journal.pone.0213954, 2019.

[32] N. Simões, R. Fino and A. Tadeu, "Uncoated medium density expanded cork boards for building façades and roofs: Mechanical, hygrothermal and durability characterization," *Construction and Building Materials,* vol. 200, pp. 447-464. doi:10.1016/j.conbuildmat.2018.12.116, 2019.

[33] R. Fino, A. Tadeu and N. Simões, "Influence of a period of wet weather on the heat transfer across a wall covered with uncoated medium density expanded cork," *Energy and Buildings,* vol. 165, pp. 118-131. doi:10.1016/j.enbuild.2018.01.020, 2018.

[34] A. Tadeu, L. Škerget, N. Simões and R. Fino, "Simulation of heat and moisture flow through walls covered with uncoated medium density expanded cork," *Building and Environment,* vol. 142, pp. 195-210. doi:10.1016/j.buildenv.2018.06.009, 2018.

[35] T. Teppand, "3.9 Grass," in *Performance of Bio-based Building Materials*, Woodhead Publishing, 2017, pp. 150-156. doi:10.1016/B978-0-08-100982-6.00003-3.

[36] E. Latif, S. Tucker, M. A. Ciupala, D. C. Wijeyesekera and D. Newport, "Hygric properties of hemp bio-insulations with differing compositions," *Construction and Building Materials,* vol. 66, pp. 702-711. doi: 10.1016/j.conbuildmat.2014.06.021, 2014.

[37] F. Collet, F. Achchaq, K. Djellab, L. Marmoret and H. Beji, "Water vapor properties of two hemp wools manufactured with different treatments," *Construction and Building Materials,* vol. 25, no. 2, pp. 1079-1085. doi: 10.1016/j.conbuildmat.2010.06.069, 2011.

[38] P. P. Dias, L. B. Jayasinghe and D. Waldmann, "Investigation of Mycelium-Miscanthus composites as building insulation material," *Results in Materials,* vol. 10, p. 100189. doi:10.1016/j.rinma.2021.100189, 2021.

[39] Z. Yang, F. Zhang, B. Still and M. White, "Physical and Mechanical Properties of Fungal Mycelium-Based Biofoam," *Journal of Materials in Civil Engineering,* vol. 29, no. 7, pp. 04017030. doi:10.1061/(ASCE)MT.1943-5533.0001866, 2017.

[40] J. M. P. Q. Delgado, E. Barreira, N. M. M. Ramos and V. P. d. Freitas, Hygrothermal Numerical Simulation Tools Applied to Building Physics, SpringerBriefs in Computational Mechanics,, 2013.

[41] ASTM, "ASTM C1498-01 Standard test method for hygroscopic sorption isotherms of building materials".

[42] ASTM, "ASTM E96-00 Standard test methods for water vapour transmission of materials".

[43] SINTEF Community, "Byggdetaljer 523.231 Skallmurvegger," in *Byggforskserien*, SINTEF, 2020.

[44] SINTEF Community, "Byggdetaljer 523.255 Yttervegger av bindingsverk. Varmeisolering og tetting," in *Byggforskserien*, SINTEF, 2020.

[45] Bouwbesluit 2012, "Hoofdstuk 5. Technische bouwvoorschriften uit het oogpunt van energiezuinigheid en milieu. Artikel 5.3. Thermische isolatie".

[46] M. Salonvarra, A. N. Karagiozis, M. Pazera and W. Miller, "Air Cavities Behind Claddings - What Have We Learned?," 1995.

[47] Dru Crawley; Linda Lawrie, "Climate.OneBuilding.Org," [Online]. Available: https://climate.onebuilding.org/default.html. [Accessed 25 3 2022].

[48] ISO, "ISO 13788 Hygrothermal performance of building components and building elements - internal surface temperature to avoid critical surface humidity and interstitial condensation - calculation method," 2012.

[49] EOTA, "EAD 040005-00-1201 Factory-made thermal and/or acoustic insulation products made of vegetable or animal fibres," EOTA, 2015.

[50] ISO, "ISO 846 Plastics - evaluation of the action of microorganisms," 1997.

[51] K. Sedlbauer, M. Krus and K. Breuer, "Mould Growth Prediction with a New Biohygrothermal Method and its Application in Practice," in *Materials Conference*, Lodz, 2003.

[52] H. Pereira and S. Knapic, "2.7 Bark and cork," in *Performance of Bio-based Building Materials*, Woodhead Publishing, 2017, pp. 78-86. doi:10.1016/B978-0-08-100982-6.00002-1.

[53] M. Krus, *Moisture Transport and Storage Coefficients of Porous Mineral Building Materials. Theoretical Principles and New Test Methods,* Fraunhofer IRB Verlag, 1996.

[54] R. H. White and M. A. Dietenberger, "Fire Safety of Wood Construction: Thermal Degradation of Wood," in *Wood Handbook*, Madison, USDA, Forest Service, Forest Products Laboratory, 2010, pp. 18-8.

[55] A. Şen, J. V. d. Bulcke, N. Defoirdt, J. V. Acker and H. Pereira, "Thermal behaviour of cork and cork components," *Thermochimica Acta,* vol. 582, pp. 94-100. doi:10.1016/j.tca.2014.03.007, 2014.

[56] M. Viel, F. Collet, Y. Lecieux, M. L. M. François, V. Colson, C. Lanos, A. Hussain and M. Lawrence, "Resistance to mold development assessment of bio-based building materials," *Composites Part B: Engineering,* vol. 158, pp. 406-418. doi:10.1016/j.compositesb.2018.09.063, 2019.

[57] T. Q. Yuan and R. C. Sun, "1. Introduction," in *Cereal Straw as a Resource for Sustainable Biomaterials and Biofuels*, Elsevier, 2010, pp. 1-7. doi:10.1016/B978-0-444-53234-3.00001-8.

[58] C. H. Koh and D. Kraniotis, "A review of material properties and performance of straw bale as building material," *Construction and Building Materials,* vol. 259, p. 120385. doi:10.1016/j.conbuildmat.2020.120385, 2020.

[59] Food and Agriculture Organization of the United Nations, "FAOSTAT: Crops and livestock products (Europe; Crops Primary; Production Quantity; 2020)," [Online]. Available: https://www.fao.org/faostat/en/#data/QCL. [Accessed 10 2022].

[60] IRC, "Appendix S Strawbale Construction," International Residential Code, 2015.

[61] FASBA, "Strohbaurichtlinie SBR-2019," Fachverband Strohballenbau Deutschland e.V., 2019.

[62] INTERREG, "Cahier technique Paille," INTERREG V-A France-Wallonie-Vlaanderen, 2021.

[63] X. Yin, M. Lawrence, D. Maskell and M. Ansell, "Comparative micro-structure and sorption isotherms of rice straw and wheat straw," *Energy & Buildings,* vol. 173, p. 11–18. doi:10.1016/j.enbuild.2018.04.033, 2018.

[64] M. Bouasker, N. Belayachi, D. Hoxha and M. Al-Mukhtar, "Physical Characterization of Natural Straw Fibers as Aggregates for Construction Materials Applications," *Materials,* vol. 7, no. 4, pp. 3034-3048. doi:10.3390/ma7043034, 2014.

[65] J. Vejeliene, A. Gailius, S. Vejelis, S. Vaitkus and G. Balciunas, "Evaluation of Structure Influence on Thermal Conductivity of Thermal Insulating Materials from Renewable Resources," in *Materials Engineering 2010*, Kaunas, 2011.

[66] A. Laborel-Préneron, C. Magniont and J. Aubert, "Characterization of Barley Straw, Hemp Shiv and Corn Cob as Resources for Bioaggregate Based Building Materials," *Waste Biomass Valor,* 2017.

[67] M. Lawrence, A. Heath and P. Walker, "Determining moisture levels in straw bale construction," *Construction and Building Materials,* vol. 23, p. 2763–2768. doi:10.1016/j.conbuildmat.2009.03.011, 2009.

[68] J. Carfrae, P. Wilde, J. Littlewood, S. Goodhew and P. Walker, "Development of a cost effective probe for the long term monitoring of straw bale buildings," *Building and Environment,* 2010.

[69] R. Bui, M. Labat and J.-E. Aubert, "Comparison of the Saturated Salt Solution and the Dynamic Vapor Sorption techniques based on the measured sorption isotherm of barley straw," *Construction and Building Materials,* vol. 141, p. 140–151. doi:10.1016/j.conbuildmat.2017.03.005, 2017.

[70] C. H. Koh, F. Gauvin, K. Schollbach and H. J. H. Brouwers, "Investigation of material characteristics and hygrothermal performances of different bio-based insulation composites," *Construction and Building Materials,* vol. 346, p. 128440. doi:10.1016/j.conbuildmat.2022.128440, 2022.

[71] O. M. Koskinen, T. M. Husman, T. M. Meklin and A. I. Nevalainen, "The relationship between moisture or mould observations in houses and the state of health of their occupants," *European Respiratory Journal,* vol. 14, no. 6, pp. 1363-1367, 1999.

[72] J. M. Portnoy, K. Kwak, P. Dowling, T. VanOsdol and C. Barnes, "Health effects of indoor fungi," *Annals of Allergy, Asthma & Immunology,* vol. 94, no. 3, pp. 313-320, 2005.

[73] L. Curtis, A. Lieberman, M. Stark, W. Rea and M. Vetter, "Adverse health effects of indoor molds," *Journal of Nutritional & Environmental Medicine,* vol. 14, no. 3, pp. 261-274, 2004.

[74] N. Magan, "Fungal colonization and decomposition of cereal straw," *International Biodeterioration,* vol. 24, no. 4–5, pp. 435-443. doi:10.1016/0265-3036(88)90031-0, 1988.

[75] C. H. Koh and D. Kraniotis, "Hygrothermal performance, energy use and embodied emissions in straw bale buildings," *Energy & Buildings,* vol. 245, p. 111091. doi:10.1016/j.enbuild.2021.111091, 2021.

[76] A. Thomson and P. Walker, "Durability characteristics of straw bales in building envelopes," *Construction and Building Materials,* vol. 68, pp. 135-141. doi:10.1016/j.conbuildmat.2014.06.041, 2014.

[77] B. Marques, A. Tadeu, J. Almeida, J. Antonio and J. Brito, "Characterisation of sustainable building walls made from rice straw bales," *Journal of Building Engineering,* vol. 28, p. 101041. doi:10.1016/j.jobe.2019.101041, 2019.

[78] R. C. Sun and J. Tomkinson, "Appendix 1. Essential Guides for Isolation/Purification of Polysaccharides," in *Encyclopedia of Separation Science*, Academic Press, 2000, pp. 4568-4574. doi:10.1016/B0-12-226770-2/07271-9.

[79] D. Niu, C. Yu, M. Zheng, J. Ren, C. Li and C. Xu, "Effects of ensiling on Irpex lacteus fermentation in wheat straw: Chemical composition, in vitro rumen digestibility, and fungal community," *Animal Feed Science and Technology,* vol. 292, p. 115433. doi:10.1016/j.anifeedsci.2022.115433, 2022.

[80] F. Xu, "2 Structure, Ultrastructure, and Chemical Composition," in *Cereal Straw as a Resource for Sustainable Biomaterials and Biofuels*, Elsevier, 2010, pp. 9-47. doi:10.1016/B978-0-444-53234-3.00002-X.

[81] NPIC, "Boric Acid General Fact Sheet," 2013. [Online]. Available: http://npic.orst.edu/factsheets/boricgen.pdf. [Accessed 08 2022].

[82] E. Estevez-Fregoso, E. D. Farfán-García, I. H. García-Coronel, E. Martínez-Herrera, A. Alatorre, R. I. Scorei and M. A. Soriano-Ursúa, "Effects of boron-containing compounds in the fungal kingdom," *Journal of Trace Elements in Medicine and Biology,* vol. 65, p. 126714. doi:10.1016/j.jtemb.2021.126714, 2021.

[83] E. Baysal, M. K. Yalinkilic, M. Altinok, A. Sonmez, H. Peker and M. Colak, "Some physical, biological, mechanical, and fire properties of wood polymer composite (WPC) pretreated with boric acid and borax mixture," *Construction and Building Materials,* vol. 21, no. 9, pp. 1879-1885. doi:10.1016/j.conbuildmat.2006.05.026, 2007.

[84] B. Lesar and M. Humar, "Re-evaluation of fungicidal properties of boric acid," *European Journal of Wood and Wood Products,* vol. 67, pp. 483–484. doi:10.1007/s00107-009-0342-0, 2009.

[85] M. Palumbo, A. Lacasta, A. Navarro, M. Giraldo and B. Lesar, "Improvement of fire reaction and mould growth resistance of a new bio-based thermal insulation material," *Construction and Building Materials,* vol. 139, pp. 531-539. doi:10.1016/j.conbuildmat.2016.11.020, 2017.

[86] J. L. Fogel and J. D. Lloyd, "Mold performance of some construction products with and without borates," *Forest Products Journal,* vol. 52, no. 2, pp. 38-43, 2002.

[87] M. E. Omodon, C. L. Dillavou and J. Herrera, "The sporocidal and sporostatic effect of sodium polyborate and boron-treated cellulose insulation on common indoor fungal species," *Micología Aplicada International,* vol. 19, no. 2, pp. 35-49, 2007.

[88] Fachverband Strohballenbau Deutschland e.V. (FASBA), "Strohbaurichtlinie SBR-2019," 2019.

[89] European Chemicals Agency (ECHA), "Member state committee draft support document for identification of boric acid as a substance of very high concern because of its CMR properties," 2010.

[90] R. C. Sun and J. Tomkinson, "Comparative study of organic solvent-soluble and water-soluble lipophilic extractives from wheat straw 2: spectroscopic and thermal analysis," *Journal of Wood Science,* vol. 48, p. 222–226. doi:10.1007/BF00771371, 2002.

[91] R. Sun and X.-F. Sun, "Separation and characterization of lipophilic extracts from barley straw," *Separation Science and Technology,,* vol. 36, no. 13, pp. 3027-3048. doi:10.1081/SS-100107644, 2001.

[92] P. Garside and P. Wyeth, "Identification of Cellulosic Fibres by FTIR Spectroscopy: Thread and Single Fibre Analysis by Attenuated Total Reflectance," *Studies in Conservation,* vol. 48, no. 4, pp. 269-275. doi:10.1179/sic.2003.48.4.269, 2003.

[93] Y. Athukorala, G. Mazza and B. D. Oomah, "Extraction, purification and characterization of wax from flax (Linum usitatissimum) straw," *European Journal of Lipid Science and Technology,* vol. 111, no. 7, pp. 705-714. doi:10.1002/ejlt.200800269, 2009.

[94] S. K. Wiśniewska, J. Nalaskowski, E. Witka-Jeżewska, J. Hupka and J. D. Miller, "Surface properties of barley straw," *Colloids and Surfaces B: Biointerfaces,* vol. 29, no. 2-3, pp. 131-142. doi:10.1016/S0927-7765(02)00178-9, 2003.

[95] H. Jiang, Y. Zhang and X. Wang, "Effect of lipases on the surface properties of wheat straw," *Industrial Crops and Products,* vol. 30, no. 2, pp. 304-310. doi:10.1016/j.indcrop.2009.05.009, 2009.

[96] Surface Measurement Systems Limited, *DVS Advanced Analysis Suite User Manual.*

[97] ISO, *ISO 12572 Hygrothermal performance of building materials and products - Determination of water vapour transmission properties - Cup method,* 2016.

[98] Y. A. Çengel and J. M. Cimbala, "2-7 Surface Tension and Capillary Effect," in *Fluid Mechanics Fundamentals and Applications*, McGraw Hill, 2006, pp. 51-54.

[99] C. P. Hedlin, "Sorption isotherms of five types of grain straw at 70 degrees F," *Canadian Agricultural Engineering,* vol. 9, no. 1, pp. 37-39, 1967.

[100] J. Munch-Andersen and B. Andersen, "Halmhuse - Udformning og materialeegenskaber," Statens Byggeforskningsinstitut, 2004.

[101] Deutsches Institut für Bautechnik DIBt, "Thermal insulation made of straw bales," 2017.

[102] M. Reif, J. Zach and J. Hroudová, "Studying the Properties of Particulate Insulating Materials on Natural Basis," in *International Conference on Ecology and new Building materials and products, ICEBMP 2016*, doi: 10.1016/j.proeng.2016.07.390, 2016.

[103] A. Lebed and N. Augaitis, "Research of physical properties of straw for building panels," *International Journal of Engineering Science Invention,* vol. 11, p. 3388; doi:10.3390/su11123388, 2017.

[104] J. P. Costes, A. Evrard, B. Biot, G. Keutgen, A. Daras, S. Dubois, F. Lebeau and L. Courard, "Thermal Conductivity of Straw Bales Full Size Measurements Considering the Direction of the Heat Flow," *Buildings,* vol. 7, no. 1, p. 11. doi:10.3390/buildings7010011, 2017.

[105] A. Shea, K. Wall and P. Walker, "Evaluation of the thermal performance of an innovative prefabricated natural plant fibre building system," *Building services engineering research & technology,* vol. 34, no. 4, pp. 369-380. doi:10.1177/0143624412450023, 2012.

[106] G. J. Langer, J. Bußkamp, E. Terhonen and K. Blumenstein, "Chapter 10 - Fungi inhabiting woody tree tissues," in *Forest Microbiology*, Academic Press, 2021, pp. 175-205. doi:10.1016/B978-0-12-822542-4.00012-7.

[107] K. Kochova, Mechanical and physical properties of fibre-cement composites using alternative natural fibres, PhD Thesis, Technische Universiteit Eindhoven, 2022.

[108] G. v. Elten, "Production of wood wool cement board and wood strand cement board (Eltoboard) on one plant and applications of the products," in *International Inorganic-Bonded Fiber Composites Conference*, São Paulo, 2006.

[109] Editorial, "Concrete needs to lose its colossal carbon footprint," *Nature,* vol. 597, pp. 593-594. doi:10.1038/d41586-021-02612-5, 2021.

[110] R. Feiz, J. Ammenberg, L. Baas, M. Eklund, A. Helgstrand and R. Marshall, "Improving the CO2 performance of cement, part I: utilizing life-cycle assessment and key performance indicators to assess development within the cement industry,," *Journal of Cleaner Production,* vol. 98, pp. 272-281. doi:10.1016/j.jclepro.2014.01.083, 2015.

[111] P. Duxson, J. L. Provis, G. C. Lukey and J. S. v. Deventer, "The role of inorganic polymer technology in the development of 'green concrete'," *Cement and Concrete Research,* vol. 37, no. 12, pp. 1590-1597. doi:j.cemconres.2007.08.018, 2007.

[112] J. L. Provis and S. A. Bernal, "Geopolymers and Related Alkali-Activated Materials," *Annual Review of Materials Research,* vol. 44, pp. 299-327. doi:10.1146/annurev-matsci-070813-113515, 2014.

[113] B. Na, Z. Wang, H. Wang and X. Lu, "Wood-cement compatibility review," *Wood research,* vol. 59, no. 5, pp. 813-826, 2014.

[114] M. Fan, M. K. Ndikontar, X. Zhou and J. N. Ngamveng, "Cement-bonded composites made from tropical woods: Compatibility of wood and cement," *Construction and Building Materials,* vol. 36, pp. 135-140. doi:10.1016/j.conbuildmat.2012.04.089, 2012.

[115] K. Kochova, K. Schollbach, F. Gauvin and H. J. H. Brouwers, "Effect of saccharides on the hydration of ordinary Portland cement," *Construction and Building Materials,* vol. 150, pp. 268-275. doi:10.1016/j.conbuildmat.2017.05.149, 2017.

[116] G. C. H. Doudart de la Grée, Q. Yu and H. J. H. Brouwers, "Assessing the effect of CaSO4 content on the hydration kinetics, microstructure and mechanical properties of cements containing sugars," *Construction and Building Materials,* vol. 43, pp. 48-60. doi:10.1016/j.conbuildmat.2017.03.067, 2017.

[117] J. Tan, W. Lu, Y. Huang, S. Wei, X. Xuan, L. Liu and G. Zheng, "Preliminary study on compatibility of metakaolin-based geopolymer paste with plant fibers," *Construction and Building Materials,* vol. 225, pp. 772-775. doi:10.1016/j.conbuildmat.2019.07.142, 2019.

[118] G. Furtos, L. Molnar, L. Silaghi-Dumitrescu, P. Pascuta and K. Korniejenko, "Mechanical and thermal properties of wood fiber reinforced geopolymer composites," *Journal of Natural Fibers,* vol. 19, no. 13, pp. 6676-6691. doi:10.1080/15440478.2021.1929655, 2021.

[119] G. Furtos, L. Silaghi-Dumitrescu, P. Pascuta, C. Sarosi and K. Korniejenko, "Mechanical Properties of Wood Fiber Reinforced Geopolymer Composites with Sand Addition," *Journal of Natural Fibers,* vol. 18, no. 2, pp. 285-296. doi:10.1080/15440478.2019.1621792, 2019.

[120] H. Ye, B. Asante, G. Schmidt, A. Krause, Y. Zhang and Z. Yu, "Eco-friendly geopolymer-wood building materials: Interactions between geopolymer and wood cell wall," *Journal of Cleaner Production,,* vol. 420, p. 138381. doi:10.1016/j.jclepro.2023.138381, 2023.

[121] A. Kuqo, T. Koddenberg and C. Mai, "Use of dry mixing-spraying process for the production of geopolymer-bonded wood and seagrass fibreboards," *Composites Part B: Engineering,* vol. 248, p. 110387. doi:10.1016/j.compositesb.2022.110387, 2023.

[122] L. Liu, S. Zou, H. Li, L. Deng, C. Bai, X. Zhang, S. Wang and N. Li, "Experimental physical properties of an eco-friendly bio-insulation material based on wheat straw for buildings," *Energy and Buildings,* vol. 201, pp. 19-36. doi:10.1016/j.enbuild.2019.07.037, 2019.

[123] K. Sankar, R. A. S. Ribeiro, M. G. S. Ribeiro and W. M. Kriven, "Potassium-Based Geopolymer Composites Reinforced with Chopped Bamboo Fibers," *Journal of the American Ceramic Society,* vol. 100, no. 1, pp. 49-55. doi:10.1111/jace.14542, 2017.

[124] R. A. S. Ribeiro, M. G. S. Ribeiro, K. Sankar and W. M. Kriven, "Geopolymer-bamboo composite – A novel sustainable construction material," *Construction and Building Materials,* vol. 123, pp. 501-507. doi:10.1016/j.conbuildmat.2016.07.037, 2016.

[125] H. Assaedi, T. Alomayri, F. U. A. Shaikh and I.-M. Low, "Characterisation of mechanical and thermal properties in flax fabric reinforced geopolymer composites," *Journal of Advanced Ceramics,* vol. 4, pp. 272–281. doi:10.1007/s40145-015-0161-1, 2015.

[126] M. Alzeer and K. MacKenzie, "Synthesis and mechanical properties of novel composites of inorganic polymers (geopolymers) with unidirectional natural flax fibres (phormium tenax)," *Applied Clay Science,* vol. 75–76, pp. 148-152. doi:10.1016/j.clay.2013.03.010, 2013.

[127] L. C. d. S. Alves, R. A. d. R. Ferreira, L. B. Machado and L. A. d. C. Motta, "Optimization of metakaolin-based geopolymer reinforced with sisal fibers using response surface methology," *Industrial Crops and Products,* vol. 139, p. 111551. doi:10.1016/j.indcrop.2019.111551, 2019.

[128] R. Chen, S. Ahmari and L. Zhang, "Utilization of sweet sorghum fiber to reinforce fly ash-based geopolymer," *Journal of Materials Science,* vol. 49, pp. 2548–2558. doi:10.1007/s10853-013-7950-0, 2013.

[129] S. Çelikten, "Mechanical and microstructural properties of waste andesite dust-based geopolymer mortars," *Advanced Powder Technology,* vol. 32, no. 1, pp. 1-9. doi:10.1016/j.apt.2020.10.011, 2021.

[130] P. Nath and P. K. Sarker, "Effect of GGBFS on setting, workability and early strength properties of fly ash geopolymer concrete cured in ambient condition," *Construction and Building Materials,* vol. 66, pp. 163-171. doi:10.1016/j.conbuildmat.2014.05.080, 2014.

[131] R. Wimmer, M. Frey, M. Hausmann, T. Keplinger, G. Siqueira and T. Zimmermann, "Plant-Fiber and Wood-Based Functional Materials," in *Springer Handbook of Wood Science and Technology,*, Springer Nature Switzerland AG, 2023, pp. doi:10.1007/978-3-030-81315-4_30.

[132] M. S. Tuğluca, E. Özdoğru, H. İlcan, E. Özçelikci, H. Ulugöl and M. Şahmaran, "Characterization of chemically treated waste wood fiber and its potential application in cementitious composites," *Cement and Concrete Composites,* vol. 137, p. 104938. doi:10.1016/j.cemconcomp.2023.104938, 2023.

[133] R. A. J. Malenab, J. P. S. Ngo and M. A. B. Promentilla, "Chemical Treatment of Waste Abaca for Natural Fiber-Reinforced Geopolymer Composite," *Materials,* vol. 10, no. 6, p. 579. doi:10.3390/ma10060579, 2017.

[134] F. Amalia, N. Akifah, Nurfadilla and Subaer, "Development of Coconut Trunk Fiber Geopolymer Hybrid Composite for Structural Engineering Materials," *IOP Conference Series: Materials Science and Engineering,* vol. 180, pp. doi:10.1088/1757-899X/180/1/012014, 2017.

[135] G. C. H. Doudart de la Grée, V. Caprai, J. v. Dam, H. v. As, H. J. H. Brouwers and Q. Yu, "Ionic interaction and liquid absorption by wood in lignocellulose inorganic mineral binder composites," *Journal of Cleaner Production,* vol. 206, pp. 808-818. doi:10.1016/j.jclepro.2018.09.220, 2019.

[136] MASEA, "Materialdatensammlung für die energetische Altbausanierung: Holzwolle-Leichtbauplatten Lingolith-Platten (Zement) 390/420," 2023. [Online]. Available: https://www.masea-ensan.de/. [Accessed 16 5 2023].

[137] C. Ouellet-Plamondon and G. Habert, "Life cycle assessment (LCA) of alkali-activated cements and concretes," in *Handbook of Alkali-Activated Cements, Mortars and Concretes*, Woodhead Publishing, 2015, pp. 663-686. doi:10.1533/9781782422884.5.663.

[138] S. H. Teh, T. Wiedmann, A. Castel and J. d. Burgh, "Hybrid life cycle assessment of greenhouse gas emissions from cement, concrete and geopolymer concrete in Australia," *Journal of Cleaner Production,* vol. 152, pp. 312-320. doi:10.1016/j.jclepro.2017.03.122, 2017.

[139] L. K. Turner and F. G. Collins, "Carbon dioxide equivalent (CO2-e) emissions: A comparison between geopolymer and OPC cement concrete," *Construction and Building Materials,* vol. 43, pp. 125-130. doi:10.1016/j.conbuildmat.2013.01.023, 2013.

[140] J. Davidovits, "False Values on CO2 Emission For Geopolymer Cement/Concrete published In Scientific Papers, Technical Paper #24, Geopolymer Institute Library, www.geopolymer.org," 2015.

[141] A. Komkova and G. Habert, "Environmental impact assessment of alkali-activated materials: Examining impacts of variability in constituent production processes and transportation," *Construction and Building Materials,* vol. 363, p. 129032. doi:10.1016/j.conbuildmat.2022.129032, 2023.

[142] M. Fawer, M. Concannon and W. Rieber, "Life cycle inventories for the production of sodium silicates," *The International Journal of Life Cycle Assessment,* vol. 4, p. 207–212. doi:10.1007/BF02979498, 1999.

[143] C. Chen, G. Habert, Y. Bouzidi, A. Jullien and A. Ventura, "LCA allocation procedure used as an incitative method for waste recycling: An application to mineral additions in concrete," *Resources, Conservation and Recycling,* vol. 54, no. 12, pp. 1231-1240. doi:10.1016/j.resconrec.2010.04.001, 2010.

[144] D. J. M. Flower and J. G. Sanjayan, "Green house gas emissions due to concrete manufacture," *The International Journal of Life Cycle Assessment,* vol. 12, p. 282–288. doi:10.1065/lca2007.05.327, 2007.

[145] Y. Luo, S. H. Li, K. Klima, H. J. H. Brouwers and Q. Yu, "Degradation mechanism of hybrid fly ash/slag based geopolymers exposed to elevated temperatures," *Cement and Concrete Research,* vol. 151, p. 106649. doi:10.1016/j.cemconres.2021.106649, 2022.

[146] G. Kovalchuk, A. Fernández-Jiménez and A. Palomo, "Alkali-activated fly ash: Effect of thermal curing conditions on mechanical and microstructural development – Part II," *Fuel,* vol. 86, no. 3, pp. 315-322. doi:10.1016/j.fuel.2006.07.010, 2007.

[147] P. Sajan, T. Jiang, C. Lau, G. Tan and K. Ng, "Combined effect of curing temperature, curing period and alkaline concentration on the mechanical properties of fly ash-based geopolymer," *Cleaner Materials,* vol. 1, p. 100002. doi:10.1016/j.clema.2021.100002, 2021.

[148] M. Chandrasekar, M. R. Ishak, S. M. Sapuan, Z. Leman and M. Jawaid, "A review on the characterisation of natural fibres and their composites after alkali treatment and water absorption," *Plastics, Rubber and Composites,* vol. 46, no. 3, pp. 119-136. doi:10.1080/14658011.2017.1298550, 2017.

[149] CEN, *EN 13168 Thermal insulation products for buildings - Factory made wood wool (WW) products - Specification,* 2015.

[150] CEN, *EN 12089 Thermal insulation product for building applications - Determination of bending behaviour,* 2013.

[151] CEN, *EN 826 Thermal insulating products for building applications - Determination of compression behaviour,* 2013.

[152] ISO, *ISO 12571 Hygrothermal performance of building materials and products - Determination of hygroscopic sorption properties,* 2013.

[153] ISO, *ISO 10534-2 Acoustics - Determination of sound absorption coefficient and impedance in impedance tubes - Part 2: Transfer function method,* 1998.

[154] B. Sun, G. Ye and G. d. Schutter, "A review: Reaction mechanism and strength of slag and fly ash-based alkali-activated materials," *Construction and Building Materials,* vol. 326, p. 126843. doi:10.1016/j.conbuildmat.2022.126843, 2022.

[155] Y. Luo, H. J. H. Brouwers and Q. Yu, "Understanding the gel compatibility and thermal behavior of alkali activated Class F fly ash/ladle slag: The underlying role of Ca availability," *Cement and Concrete Research,* vol. 170, p. 107198. doi:10.1016/j.cemconres.2023.107198, 2023.

[156] H. Cheng-Yong, L. Yun-Ming, M. M. A. B. Abdullah, O. Shee-Ween, H. Yong-Jie, N. Hui-Teng, N. Yong-Sing, O. Wan-En, L. Jia-Ni and T. Hoe-Woon, "Durability of natural fiber-reinforced alkali-activated composites," in *Advanced Fiber-Reinforced Alkali-Activated Composites*, Elsevier, 2023, pp. 415-448. doi:10.1016/B978-0-443-15301-3.00015-4.

[157] Y. Huang, J. Tan, X. Xuan, L. Liu, M. Xie, H. Liu, S. Yu and G. Zheng, "Study on untreated and alkali treated rice straw reinforced geopolymer composites," *Materials Chemistry and Physics,* vol. 262, p. 124304. doi:10.1016/j.matchemphys.2021.124304, 2021.

[158] J. L. Stapper, F. Gauvin and H. J. H. Brouwers, "Influence of short-term degradation on coir in natural fibre-cement composites," *Construction and Building Materials,* vol. 306, p. 124906. doi:10.1016/j.conbuildmat.2021.124906, 2021.

[159] M. Zauer, S. Hempel, A. Pfriem, V. Mechtcherine and A. Wagenführ, "Investigations of the pore-size distribution of wood in the dry and wet state by means of mercury intrusion porosimetry," *Wood Science and Technology,* vol. 48, pp. 1229-1440. doi:10.1007/s00226-014-0671-y, 2014.

[160] M. Babaee and A. Castel, "Water vapor sorption isotherms, pore structure, and moisture transport characteristics of alkali-activated and Portland cement-based binders," *Cement and Concrete Research,* vol. 113, pp. 99-120. doi:10.1016/j.cemconres.2018.07.006, 2018.

[161] Y. Luo, Z. Jiang, D. Wang, Y. Lv, C. Gao and G. Xue, "Effects of alkaline activators on pore structure and mechanical properties of ultrafine metakaolin geopolymers cured at room temperature," *Construction and Building Materials,* vol. 361, p. 129678. doi:10.1016/j.conbuildmat.2022.129678, 2022.

[162] B. Botterman, G. C. H. Doudart de la Grée, M. C. J. Hornikx, Q. Yu and H. J. H. Brouwers, "Modelling and optimization of the sound absorption of wood-wool cement boards," *Applied Acoustics,* vol. 129, pp. 144-154. doi:10.1016/j.apacoust.2017.07.017, 2018.

[163] Heraklith, "Heraklith® A2 Decorative Panels," Heraklith, 2023. [Online]. Available: https://www.knaufinsulation.co.uk/products/heraklith-a2-decorative-panel#downloads. [Accessed 2 6 2023].

[164] J. H. Rindel, "Introduction to sound insulation," in *Sound Insulation in Buildings*, CRC Press, 2018, pp. 101-153.

[165] C. V. Nguyen and P. Mangat, "Properties of rice straw reinforced alkali activated cementitious composites," *Construction and Building Materials,* vol. 261, p. 120536. doi:10.1016/j.conbuildmat.2020.120536, 2020.

[166] I. Ismail, S. A. Bernal, J. L. Provis, R. S. Nicolas, S. Hamdan and J. S. v. Deventer, "Modification of phase evolution in alkali-activated blast furnace slag by the incorporation of fly ash," *Cement and Concrete Composites,* vol. 45, pp. 125-135. doi:10.1016/j.cemconcomp.2013.09.006, 2014.

[167] A. Fauzi, M. F. Nuruddin, A. B. Malkawi and M. M. A. B. Abdullah, "Study of Fly Ash Characterization as a Cementitious Material," *Procedia Engineering,* vol. 148, pp. 487-493. doi:10.1016/j.proeng.2016.06.535, 2016.

[168] W. Collier, T. Schultz and V. Kalasinsky, "Infrared Study of Lignin: Reexamination of Aryl-Alkyl Ether C—O Stretching Peak Assignments," *Holzforschung,* vol. 6, pp. 523-528. doi:10.1515/hfsg.1992.46.6.523, 46.

[169] P. Kumar, K. Miller, A. Kermanshahi-pour, S. K. Brar, R. F. Beims and C. C. Xu, "Nanocrystalline cellulose derived from spruce wood: Influence of process parameters," *International Journal of Biological Macromolecules,* vol. 221, pp. 426-434. doi:10.1016/j.ijbiomac.2022.09.017, 2022.

[170] H. Qian, Q. Hou, L. Hong, X. Lu, I. Ziegler-Devin, L. Chrusciel, A. Besserer and N. Brosse, "Effect of highly efficient steam explosion treatment on beech, poplar and spruce solid wood physicochemical and permeable performances," *Industrial Crops and Products,* vol. 182, p. 114901. doi:10.1016/j.indcrop.2022.114901, 2022.

[171] X. Gao, Q. Yu and H. .. H. Brouwers, "Properties of alkali activated slag–fly ash blends with limestone addition," *Cement and Concrete Composites,* vol. 59, pp. 119-128. doi:10.1016/j.cemconcomp.2015.01.007, 2015a.

[172] A. M. Criado, Fernández-Jiménez and A. Palomo, "Alkali activation of fly ash: Effect of the SiO_2/Na_2O ratio: Part I: FTIR study," *Microporous and Mesoporous Materials,* vol. 106, no. 1-3, pp. 180-191. doi:10.1016/j.micromeso.2007.02.055, 2007.

[173] A. Fernández-Jiménez and A. Palomo, "Mid-infrared spectroscopic studies of alkali-activated fly ash structure," *Microporous and Mesoporous Materials,* vol. 86, no. 1-4, pp. 207-214. doi:10.1016/j.micromeso.2005.05.057, 2005.

[174] J. Wang, Z. Hu, Y. Chen, J. Huang, Y. Ma, W. Zhu and J. Liu, "Effect of Ca/Si and Al/Si on micromechanical properties of C(-A)-S-H," *Cement and Concrete Research,* vol. 157, p. 106811. doi:10.1016/j.cemconres.2022.106811, 2022.

[175] S. M. Park, J. G. Jang, N. K. Lee and H. K. Lee, "Physicochemical properties of binder gel in alkali-activated fly ash/slag exposed to high temperatures," *Cement and Concrete Research,* vol. 89, pp. 72-79. doi:10.1016/j.cemconres.2016.08.004, 2016.

[176] S. Zhang, Z. Li, B. Ghiassi, S. Yin and G. Ye, "Fracture properties and microstructure formation of hardened alkali-activated slag/fly ash pastes," *Cement and Concrete Research,* vol. 144, p. 106447. doi:10.1016/j.cemconres.2021.106447, 2021.

[177] X. Gao, Q. Yu and H. J. H. Brouwers, "Reaction kinetics, gel character and strength of ambient temperature cured alkali activated slag–fly ash blends," *Construction and Building Materials,* vol. 80, pp. 105-115. doi:10.1016/j.conbuildmat.2015.01.065, 2015b.

[178] M. G. Grønli, G. Várhegyi and C. D. Blasi, "Thermogravimetric Analysis and Devolatilization Kinetics of Wood," *Industrial & Engineering Chemistry Research,* vol. 41, no. 17, pp. 4201-4208. doi:10.1021/ie0201157, 2002.

[179] C. H. Koh, Y. Luo, F. Gauvin and K. Schollbach, "Utilization of geopolymer in wood wool insulation boards: Design optimization, development and performance characteristics," *Resources, Conservation and Recycling,* vol. 204, p. 107510. doi:10.1016/j.resconrec.2024.107510, 2024.

[180] B. Feng, J. Liu, Z. Lu, M. Zhang and X. Tan, "Study on properties and durability of alkali activated rice straw fibers cement composites," *Journal of Building Engineering,* vol. 63, p. 105515. doi:10.1016/j.jobe.2022.105515, 2023.

[181] M. Weil, K. Dombrowski and A. Buchwald, "Life-cycle analysis of geopolymers," in *Geopolymers*, Woodhead Publishing, 2009, pp. 194-210. doi:10.1533/9781845696382.2.194.

[182] V. Shobeiri, B. Bennett, T. Xie and P. Visintin, "A comprehensive assessment of the global warming potential of geopolymer concrete," *Journal of Cleaner Production,* vol. 297, p. 126669. doi:10.1016/j.jclepro.2021.126669, 2021.

[183] Directive 2008/98/EC, "On waste and repealing certain Directives," European Parliament and Council. http://data.europa.eu/eli/dir/2008/98/2018-07-05.

[184] IenW, *IENM/BSK-2016/55036 Rechtsoordeel bijproduct status poederkoolvliegas (Legal ruling by-product status of pulverized coal fly ash),* Ministerie van Infrastructuur en Waterstaat. https://www.afvalcirculair.nl/afvalstof-of-niet-afvalstof/rechtsoordelen/, 2016.

[185] IenW, *IENM/BSK-2017/215506 Rechtsoordeel LD-Staalslak (legal opinion LD steel slag),* Ministerie van Infrastructuur en Waterstaat. https://www.afvalcirculair.nl/afvalstof-of-niet-afvalstof/rechtsoordelen/, 2017.

[186] *Uitspraak 201102730/1/A4, https://www.raadvanstate.nl/uitspraken/@86437/201102730-1-a4/,* 2012.

[187] CEMBUREAU, "EPD for cement (CEM II)," 2020a. [Online]. Available: https://cembureau.eu/policy-focus/sustainable-construction/sustainability-standards/.

[188] CEMBUREAU, "EPD for cement (CEM III)," 2020b. [Online]. Available: https://cembureau.eu/policy-focus/sustainable-construction/sustainability-standards/.

[189] WBCSD, "The Cement CO_2 and Energy Protocol - CO_2 and Energy Accounting and Reporting Standard for the Cement Industry," 2011. [Online]. Available: https://www.cement-co2-protocol.org/en/index.htm.

[190] PCA, "EPD for Blended Hydraulic cement," 2023. [Online]. Available: https://www.cement.org/sustainability/pcr-epds.

[191] Worldsteel, "Life cycle inventory methodology report for steel products," World Steel Association, 2017.

[192] Eurofer, "A methodology to determine the LCI of steel industry co-products," Eurofer, 2014.

[193] S. González-García, S. Berg, G. Feijoo and M. T. Moreira, "Environmental impacts of forest production and supply of pulpwood: Spanish and Swedish case studies," *The International Journal of Life Cycle Assessment ,* vol. 14, pp. 340–353. doi:10.1007/s11367-009-0089-1, 2009.

[194] M. Lindqvist, U. Palme and J. P. Lindner, "A comparison of two different biodiversity assessment methods in LCA—a case study of Swedish spruce forest," *The International Journal of Life Cycle Assessment ,* vol. 21, pp. 190–201. doi:10.1007/s11367-015-1012-6, 2016.

[195] D. Klein, C. Wolf, C. Schulz and G. Weber-Blaschke, "Environmental impacts of various biomass supply chains for the provision of raw wood in Bavaria, Germany, with focus on climate change," *Science of The Total Environment,* vol. 539, pp. 45-60. doi:10.1016/j.scitotenv.2015.08.087, 2016.

[196] Directive 2018/2001, *On the promotion of the use of energy from renewable sources,* European Parliament and Council. http://data.europa.eu/eli/dir/2018/2001/oj.

[197] Blonk, "Agri-footprint 6 Methodology Report. Part 1: Methodology and basic principles," Blonk, 2022.

[198] C. H. Koh, F. Gauvin, K. Schollbach and H. J. H. Brouwers, "Upcycling wheat and barley straws into sustainable thermal insulation: Assessment and treatment for durability," *Resources, Conservation and Recycling,* vol. 198, p. 107161. doi:10.1016/j.resconrec.2023.107161, 2023.

[199] CEN, "EN 15804+A2 Sustainability of construction works - Environmental product declarations - Core rules for the product category of cnstruction products," CEN, 2019.

[200] CEN, "EN 15804+A1 Sustainability of construction works - Environmental product declarations - Core rules for the product category of cnstruction products," CEN, 2013.

[201] A. Akbarnezhad, M. Huan, S. Mesgari and A. Castel, "Recycling of geopolymer concrete," *Construction and Building Materials,* vol. 101, no. 1, pp. 152-158. doi:10.1016/j.conbuildmat.2015.10.037, 2015.

[202] E. Sanyé Mengual, F. Biganzoli and S. Sala, " User guide for the "Member States - Consumption footprint Tool"," Publications Office of the European Union. doi:10.2760/764257, JRC132621, 2023.

[203] S. Andreasi Bassi, F. Biganzoli, N. Ferrara, A. Amadei, A. Valente, S. Sala and F. Ardente, "Updated characterisation and normalisation factors for the Environmental Footprint 3.1 method," Publications Office of the European Union. doi:10.2760/798894, JRC130796, 2023.

[204] S. Sala, A. K. Cerutti and R. Pant, "Development of a weighting approach for the Environmental Footprint," Publications Office of the European Union. doi:10.2760/945290, 2018.

[205] Kiwa, "Environmental Product Declaration (EPD) EFA-Füller® S-MA by BauMineral," Kiwa-Ecobility Experts, 2023.

[206] MRPI, "1.1.00235.2021 Environmental Product Declaration for Eco2cem GGBS by Ecocem Benelux B.V.," Stichting MRPI, 2021b.

[207] BCS Öko-Garantie, "EPD-Baumineral-018-DE Environmental Product Declaration for EFA-Füller MR3 by BauMineral GmbH," BCS Öko-Garantie GmbH, 2017.

[208] CEN, "EN 16449 Wood and wood-based products - Calculation of the biogenic carbon content of wood and conversion to carbon dioxide," CEN, 2014.

[209] CBS, "Agriculture; Crops, animals and land use by region," 2024a. [Online]. Available: https://www.cbs.nl/nl-nl/economie/landbouw.

[210] Probos, "Sawmills in the Netherlands," 29 1 2024. [Online]. Available: https://rondhoutzagerijen.nl/.

[211] GEM, "Global Coal Plant Tracker," 25 1 2024a. [Online]. Available: https://globalenergymonitor.org/projects/global-coal-plant-tracker/tracker/.

[212] MRPI, "1.1.00095.2020 Environmental Product Declaration for Coal fly ash by Vliegasunie B.V.," Stichting MRPI, 2021a.

[213] GEM, "Global Blast Furnace Tracker," 25 1 2024b. [Online]. Available: https://globalenergymonitor.org/projects/global-blast-furnace-tracker/tracker-map/.

[214] CBS, "Road transport; Key figures per environmental class," 2024b. [Online]. Available: https://opendata.cbs.nl/statline/#/CBS/nl/dataset/83404NED/table?ts=1709039262059.

[215] Y. A. Çengel, "Steady Heat Conduction: Heat Transfer in Common Configurations," in *Heat and Mass Transfer: Fundamentals & Applications*, McGraw Hill, 2020, pp. 170-172.

[216] Rijksoverheid, "Klimaatakkoord (Climate Agreement)," Den Haag, 2019.

[217] Milieucentraal, "Spouwmuurisolatie (cavity wall insulation)," Milieu Centraal, 2022. [Online]. Available: https://www.milieucentraal.nl/energie-besparen/isoleren-en-besparen/spouwmuurisolatie/. [Accessed 31 3 2022].

[218] Bouwbesluit 2012, "Artikel 5.6 Verbouw (Renovation)".

[219] Bouwbesluit 2012, "Artikel 5.3 Thermische isolatie (Thermal insulation)".

[220] M. M. Koebel, J. Wernery and W. J. Malfait, "Energy in buildings - Policy, materials and solutions," *MRS Energy & Sustainability: A Review Journal,* vol. 4, p. e12. doi:10.1557/mre.2017.14, 2017.

[221] I. Rodríguez-Maribona, "Final Report Summary - EFFESUS (ENERGY EFFICIENCY FOR EU HISTORIC DISTRICTS SUSTAINABILITY)," 2017. [Online]. Available: https://cordis.europa.eu/project/id/314678/reporting.

[222] E. Lucchi, F. Roberti and T. Alexandra, "Definition of an experimental procedure with the hot box method for the thermal performance evaluation of inhomogeneous walls," *Energy and Buildings,* vol. 179, pp. 99-111. doi:10.1016/j.enbuild.2018.08.049, 2018.

[223] E. Lucchi, F. Becherini, M. C. Di Tuccio, A. Troi, J. Frick, F. Roberti, C. Hermann, I. Fairnington, G. Mezzasalma, L. Pockelé and A. Bernardi, "Thermal performance evaluation and comfort assessment of advanced aerogel as blown-in insulation for historic buildings," *Building and Environment,* vol. 122, pp. 258-268. doi:10.1016/j.buildenv.2017.06.019, 2017.

[224] NASA, "Sprayable Aerogel Bead Compositions With High Shear Flow Resistance and High Thermal Insulation Value," NASA Tech Briefs, 2022. [Online]. Available: https://ntrs.nasa.gov/citations/20130012683. [Accessed 21 4 2022].

[225] "Silfoam," Active Aerogels, [Online]. Available: https://www.activeaerogels.com/spray-on/. [Accessed 21 4 2022].

[226] E. Cuce, P. M. Cuce, C. J. Wood and S. B. Riffat, "Toward aerogel based thermal superinsulation in buildings: A comprehensive review," *Renewable and Sustainable Energy Reviews,* vol. 34, pp. 273-299. doi:10.1016/j.rser.2014.03.017, 2014.

[227] B. Chal, G. Foray, B. Yrieix, K. Masenelli-Varlot, L. Roiban and J. M. Chenal, "Durability of silica aerogels dedicated to superinsulation measured under hygrothermal conditions," *Microporous and Mesoporous Materials,* vol. 272, pp. 61-69. doi:10.1016/j.micromeso.2018.05.047, 2018.

[228] K. Nocentini, P. Achard and P. Biwole, "Hygro-thermal properties of silica aerogel blankets dried using microwave heating for building thermal insulation," *Energy and Buildings,* vol. 158, pp. 14-22. doi:10.1016/j.enbuild.2017.10.024, 2018.

[229] M. Ibrahim, K. Nocentini, M. Stipetic, S. Dantz, F. G. Caiazzo, H. Sayegh and L. Bianco, "Multi-field and multi-scale characterization of novel super insulating panels/systems based on silica aerogels: Thermal, hydric, mechanical, acoustic, and fire performance," *Building and Environment,* vol. 151, pp. 30-42. doi:10.1016/j.buildenv.2019.01.019, 2019.

[230] H. Guo, S. Cai, K. Li, Z. Liu, L. Xia and J. Xiong, "Simultaneous test and visual identification of heat and moisture transport in several types of thermal insulation," *Energy,* vol. 197, p. 117137. doi:10.1016/j.energy.2020.117137, 2020.

[231] Y. Liu, H. Wu, Y. Zhang, J. Yang and F. He, "Structure characteristics and hygrothermal performance of silica aerogel composites for building thermal insulation in humid areas," *Energy and Buildings,* vol. 228, p. 110452. doi:10.1016/j.enbuild.2020.110452, 2020.

[232] N. R. M. Sakiyama, J. Frick, M. Stipetic, T. Oertel and H. Garrecht, "Hygrothermal performance of a new aerogel-based insulating render through weathering: Impact on building energy efficiency," *Building and Environment,* vol. 202, p. 108004. doi:10.1016/j.buildenv.2021.108004, 2021.

[233] S. Fantucci, E. Fenoglio, G. Grosso, V. Serra, M. Perino, V. Marino and M. Dutto, "Development of an aerogel-based thermal coating for the energy retrofit and the prevention of condensation risk in existing buildings," *Science and Technology for the Built Environment,* vol. 25, no. 9, pp. 1178-1186 . doi:10.1080/23744731.2019.1634931, 2019.

[234] J. Maia, M. Pedroso, N. M. M. Ramos, P. F. Pereira, I. Flores-Colen, M. G. Gomes and L. Silva, "Hygrothermal performance of a new thermal aerogel-based render under distinct climatic conditions," *Energy and Buildings,* vol. 243, p. 111001. doi:10.1016/j.enbuild.2021.111001, 2021.

[235] D. Crawley, L. Lawrie, "Climate.OneBuilding.Org," [Online]. Available: https://climate.onebuilding.org/default.html. [Accessed 25 3 2022].

[236] CBS, "Vier op de tien huishoudens wonen in een rijtjeshuis (Four in ten households live in a terraced house)," [Online]. Available: https://www.cbs.nl/nl-nl/nieuws/2016/14/vier-op-de-tien-huishoudens-wonen-in-een-rijtjeshuis. [Accessed 2 5 2022].

[237] CEN, "EN 16798-1 Energy performance of buildings - Ventilation for buildings - Part 1: Indoor environmental input parameters for design and assessment of energy performance of buildings addressing indoor air quality, thermal environment, lighting and acoustics," 2019.

[238] ISO, "ISO 7730 Ergonomics of the thermal environment - Analytical determination and interpretation of thermal comfort using calculation of the PMV and PPD indices and local thermal comfort criteria," 2005.

[239] WUFI, *WUFI Material Database,* 2022.

[240] P. Moradias, P. D. Silva, J. Castro-Gomes, M. Salazar and L. Pires, "Experimental study on hygrothermal behaviour of retrofit solutions applied to old building walls," *Construction and Building Materials,* vol. 35, pp. 864-873. doi: 10.1016/j.conbuildmat.2012.04.138, 2012.

[241] IenW, "National Circular Economy Programme 2023-2030," IenW, 2023.

[242] O. Väntsi and T. Kärki, "Mineral wool waste in Europe: a review of mineral wool waste quantity, quality, and current recycling methods," *Journal of Material Cycles and Waste Management ,* vol. 16, pp. 62–72. doi:10.1007/s10163-013-0170-5, 2014.

[243] J. Yliniemi, R. Ramaswamy, T. Luukkonen, O. Laitinen, Á. N. d. Sousa, M. Huuhtanen and M. Illikainen, "Characterization of mineral wool waste chemical composition, organic resin content and fiber dimensions: Aspects for valorization," *Waste Management,* vol. 131, pp. 323-330. doi:10.1016/j.wasman.2021.06.022, 2021.

[244] C. P. Ramírez, M. d. R. Merino, C. V. Arrebola, A. V. Barriguete and M. Kosior-Kazberuk, "Analysis of the mechanical behaviour of the cement mortars with additives of mineral wool fibres from recycling of CDW," *Construction and Building Materials,* vol. 210, pp. 56-62. doi:10.1016/j.conbuildmat.2019.03.062, 2019.

[245] A. T. Gebremariam, A. Vahidi, F. D. Maio, J. Moreno-Juez, I. Vegas-Ramiro, A. Łagosz, R. Mróz and P. Rem, "Comprehensive study on the most sustainable concrete design made of recycled concrete, glass and mineral wool from C&D wastes," *Construction and Building Materials,* vol. 273, p. 121697. doi:10.1016/j.conbuildmat.2020.121697, 2021.

[246] A. B. López-García, M. Uceda-Rodríguez, S. León-Gutiérrez, C. J. Cobo-Ceacero and J. M. Moreno-Maroto, "Eco-efficient transformation of mineral wool wastes into lightweight aggregates at low firing temperature and associated environmental assessment," *Construction and Building Materials,* vol. 345, p. 128294. doi:10.1016/j.conbuildmat.2022.128294, 2022.

[247] M. Mastali, A. Zahra, K. Hugo and R. Faraz, "Utilization of mineral wools in production of alkali activated materials," *Construction and Building Materials,* vol. 283, p. 122790. doi:10.1016/j.conbuildmat.2021.122790, 2021.

[248] M. Pavlin, B. Horvat, A. Frankovič and V. Ducman, "Mechanical, microstructural and mineralogical evaluation of alkali-activated waste glass and stone wool," *Ceramics International,* vol. 47, no. 11, pp. 15102-15113. doi:10.1016/j.ceramint.2021.02.068, 2021.

[249] P. Kinnunen, J. Yliniemi, B. Talling and M. Illikainen, "Rockwool waste in fly ash geopolymer composites," *Journal of Material Cycles and Waste Management ,* vol. 19, pp. 1220–1227. doi:10.1007/s10163-016-0514-z, 2016.

[250] K. M. Klima, Y. Luo, H. J. H. Brouwers and Q. Yu, "Effects of mineral wool waste in alkali activated-artificial aggregates for high-temperature applications," *Construction and Building Materials,* vol. 401, p. 132937. doi:10.1016/j.conbuildmat.2023.132937, 2023.

[251] K. G. de Oliveira, K. S. Jokipii-Lukkari and T. Luukkonen, "Assessing alkali activation of waste stone wool from greenhouses combined with direct foaming or granulation to obtain recycled plant substrate," *Open Research Europe,* vol. 4, 2024. doi:10.12688/openreseurope.17101.1.

[252] Milieu Centraal, "Geen of lage kruipruimte, wat nu?," 2024. [Online]. Available: https://www.milieucentraal.nl/energie-besparen/isoleren-en-besparen/vloerisolatie/#geen-of-lage-kruipruimte-wat-nu.

[253] J. Kurnitski, "Crawl space air change, heat and moisture behaviour," *Energy and Buildings,* vol. 32, no. 1, pp. 19-39. doi:10.1016/S0378-7788(99)00021-3, 2000.

[254] P. V. Vijay, K. T. Gadde and H. V. S. GangaRao, "Structural Evaluation and Rehabilitation of Century-Old Masonry and Timber Buildings," *Journal of Architectural Engineering,* vol. 25, no. 2, pp. 05019001. doi:10.1061/(ASCE)AE.1943-5568.0000350, 2019.

[255] E. Nielsen, P. Nørhede, O. Ladefoged and L. Tobiassen, "Evaluation of health hazards by exposure to Mineral wools (glass, stone/slag, HT) and proposal of a health-based quality criterion for ambient air," The Danish Environmental Protection Agency, 2013.

[256] CEN, "EN 1097-3 Test for mechanical and physical properties of aggregates - Part 3: Determination of loose bulk density and voids," 1998.

[257] Y. Hiramatsu, Y. Oka and H. Kiyama, "Rapid Determination of the Tensile Strength of Rocks with Irregular Test Pieces," *Journal of the Mining and Metallurgical Institute of Japan,* vol. 81, no. 932, pp. 1024-1030. doi:10.2473/shigentosozai1953.81.932_1024, 1965.

[258] CEN, *EN 1096-6 Test for mechanical and physical properties of aggregates - Part 6: Determination of particle density and water absoption,* CEN, 2013.

[259] C. H. Koh, K. Schollbach, F. Gauvin and H. J. H. Brouwers, "Aerogel composite for cavity wall rehabilitation in the Netherlands: Material characterization and thermal comfort assessment," *Building and Environment,* vol. 224, p. 109535. doi:10.1016/j.buildenv.2022.109535, 2022.

[260] D. Crawley and L. Lawrie, "Climate.OneBuilding.Org," 2023. [Online]. Available: https://climate.onebuilding.org/default.html. [Accessed 25 3 2022].

[261] WUFI Mateial Database, *POROTON-WDF Perlitefüllung.*

[262] CEN, *EN 13055 Lightweight aggregates,* CEN, 2016.

[263] ISO, *ISO 10456 Building materials and products - hydrothermal properties - tabulated design values and procedures for determining declared and desgin thermal values,* ISO, 2007.

[264] D. Zorić, D. Lazar, O. Rudić, M. Radeka, J. Ranogajec and H. Hiršenberger, "Thermal conductivity of lightweight aggregate based on coal fly ash," *Journal of Thermal Analysis and Calorimetry,* vol. 110, pp. 489–495. doi:10.1007/s10973-012-2339-x, 2012.

[265] A. G. Celik, A. M. Kilic and G. O. Cakal, "Expanded perlite aggregate characterization for use as a lightweight construction raw material," *Physicochemical Problems of Mineral Processing,* vol. 29, no. 2, pp. 689-700. doi:10.5277/ppmp130227, 2013.

[266] Y. Luo and Q. Yu, "Valorization of mineral wool waste in Class F fly ash geopolymer: Geopolymerization, macro properties, and high temperature behavior," *Cement and Concrete Composites,* vol. 145, p. 105318. doi:10.1016/j.cemconcomp.2023.105318, 2024.

[267] C. Chen, X. Wang, Y. Wang, S. Jiu and Y. Chen, "Effect of rock-wool waste on physical, mechanical, and microscopic properties of nonburn solid bricks," *Construction and Building Materials,* vol. 392, p. 131805. doi:10.1016/j.conbuildmat.2023.131805, 2023.

[268] O. Kizinievič, V. Balkevičius, J. Pranckevičienė and V. Kizinievič, "Investigation of the usage of centrifuging waste of mineral wool melt (CMWW), contaminated with phenol and formaldehyde, in manufacturing of ceramic products," *Waste Management,* vol. 34, no. 8, pp. 1488-1494. doi:10.1016/j.wasman.2014.01.010, 2014.

[269] C. Siligardi, P. Miselli, E. Francia and M. L. Gualtieri, "Temperature-induced microstructural changes of fiber-reinforced silica aerogel (FRAB) and rock wool thermal insulation materials: A comparative study," *Energy and Buildings,* vol. 138, pp. 80-87. doi:10.1016/j.enbuild.2016.12.022, 2017.

[270] C. P. Ramírez, E. A. Sánchez, M. d. R. Merino, C. V. Arrebola and A. V. Barriguete, "Feasibility of the use of mineral wool fibres recovered from CDW for the reinforcement of conglomerates by study of their porosity," *Construction and Building Materials,* vol. 191, pp. 460-468.doi:10.1016/j.conbuildmat.2018.10.026, 2018.

[271] Z. Chen, H. Wang, R. Ji, L. Liu, C. Cheeseman and X. Wang, "Reuse of mineral wool waste and recycled glass in ceramic foams," *Ceramics International,* vol. 45, no. 12, pp. 15057-15064. doi:10.1016/j.ceramint.2019.04.242, 2019.

[272] M. Viljanen, J. Bergman, S. Grabko, L. Xiaoshu and R. Yrjoelae, "Ensuring the long service life of unheated buildings. Evaluation methods to avoid moisture damage in unheated buildings," Helsinki Univ. of Technology, 1999.

[273] J. Kurnitski and M. Matilainen, "Moisture conditions of outdoor air-ventilated crawl spaces in apartment buildings in a cold climate," *Energy and Buildings,* vol. 33, no. 1, 2000. doi:10.1016/S0378-7788(00)00061-X.

[274] ISO, "ISO 16957 Measurement of apparent thermal conductivity of wet porous building materials by a periodic method," ISO, 2016.

[275] ISO, "ISO 10051 Thermal insulation - moisture effects on heat transfer - determination of thermal transmissivity of a moist material," ISO, 1996.

[276] T. McFadden, "Thermal Performance Degradation of Wet Insulations in Cold Regions," *Journal of Cold Regions Engineering,* vol. 2, no. 1, 1988. doi:10.1061/(ASCE)0887-381X(1988)2:1(25).

[277] Y. Wang, C. Ma, Y. Liu, D. Wang and J. Liu, "A model for the effective thermal conductivity of moist porous building materials based on fractal theory," *International Journal of Heat and Mass Transfer,* vol. 125, pp. 387-399, 2018. doi:10.1016/j.ijheatmasstransfer.2018.04.063.

[278] X. Qin, J. Cai, P. Xu, S. Dai and Q. Gan, "A fractal model of effective thermal conductivity for porous media with various liquid saturation," *International Journal of Heat and Mass Transfer,* vol. 128, 2019. doi:10.1016/j.ijheatmasstransfer.2018.09.072..

[279] W. Pei, F. Ming, M. Zhang and X. Wan, "A thermal conductivity model for insulation materials considering the effect of moisture in cold regions," *Cold Regions Science and Technology,* vol. 207, p. 103770, 2023. doi:10.1016/j.coldregions.2022.103770.

[280] H. Li, Q. Zeng and S. Xu, "Effect of pore shape on the thermal conductivity of partially saturated cement-based porous composites," *Cement and Concrete Composites,* vol. 81, 2017. doi:10.1016/j.cemconcomp.2017.05.002.

[281] Z. Chu, G. Zhou and R. Li, "Enhanced fractal capillary bundle model for effective thermal conductivity of composite-porous geomaterials," *International Communications in Heat and Mass Transfer,* vol. 113, 2020. doi:10.1016/j.icheatmasstransfer.2020.104527.

[282] Y. Chen, D. Li, X.-Q. Xie, Y. Gao and Y.-L. He, "Theoretical modeling and experimental validation for the effective thermal conductivity of moist silica aerogel," *International Journal of Heat and Mass Transfer,* vol. 147, 2020. doi:10.1016/j.ijheatmasstransfer.2019.118842.

[283] B. Ghanbarian and H. Daigle, "Thermal conductivity in porous media: Percolation-based effective-medium approximation," *Water Resources Research,* vol. 52, no. 1, pp. 295-314, 2015. doi:10.1002/2015WR017236.

[284] J. K. Carson, S. J. Lovatt, D. J. Tanner and A. C. Cleland, "Thermal conductivity bounds for isotropic, porous materials," *International Journal of Heat and Mass Transfer,* vol. 48, no. 11, pp. 2150-2158, 2005. doi:10.1016/j.ijheatmasstransfer.2004.12.032.

[285] D. S. Smith, A. Alzina, J. Bourret, B. Nait-Ali, F. Pennec, N. Tessier-Doyen, K. Otsu, H. Matsubara, P. Elser and U. T. Gonzenbach, "Thermal conductivity of porous materials," *Journal of Materials Research,* vol. 28, p. 2260–2272, 2013. doi:10.1557/jmr.2013.179.

[286] A. Eucken, "Allgemeine Gesetzmäßigkeiten für das Wärmeleitvermögen verschiedener Stoffarten und Aggregatzustände," *Forschung auf dem Gebiet des Ingenieurwesens A,* vol. 11, p. 6–20. doi:, 1940.

[287] Z. Hashin and S. Shtrikman, "A Variational Approach to the Theory of the Effective Magnetic Permeability of Multiphase Materials," *Journal of Applied Physics,* vol. 33, p. 3125–3131. doi:10.1063/1.1728579, 1962.

[288] R. Landauer, "The Electrical Resistance of Binary Metallic Mixtures," *Journal of Applied Physics,* vol. 23, p. 779–784. doi:10.1063/1.1702301, 1952.

[289] G. Tichá, W. Pabst and D. S. Smith, "Predictive model for the thermal conductivity of porous materials with matrix-inclusion type microstructure," *Journal of Materials Science,* vol. 40, pp. 5045–5047. doi:10.1007/s10853-005-1818-x, 2005.

[290] J. Côté and J.-M. Konrad, "A generalized thermal conductivity model for soils and construction materials," *Canadian Geotechnical Journal,* vol. 42, no. 2, pp. 443-458. doi:10.1139/t04-106, 2005.

[291] J. M. Markle, R. A. Schincariol, J. H. Sass and J. W. Molson, "Characterizing the Two-Dimensional Thermal Conductivity Distribution in a Sand and Gravel Aquifer," *Soil Science Society of America,* vol. 70, no. 4, pp. 1281-1294. doi:10.2136/sssaj2005.0293, 2006.

[292] Y. Lin, Z. Shi and P. L. Wildfong, "Thermal conductivity measurements for small molecule organic solid materials using modulated differential scanning calorimetry (MDSC) and data corrections for sample porosity," *Journal of Pharmaceutical and Biomedical Analysis,* vol. 51, no. 4, pp. 979-984. doi:10.1016/j.jpba.2009.10.022, 2010.

[293] Y. A. Çengel and J. M. Cimbala, "Appendix 1 Property tables and charts," in *Fluid Mechanics Fundamentals and Applications*, McGraw Hill, 2006.

[294] Fraunhofer-IBP, "MASEA Datenbank," 2024. [Online]. Available: https://www.masea-ensan.de/.

[295] M. Jiřičková, Z. Pavlík, L. Fiala and R. Černý, "Thermal Conductivity of Mineral Wool Materials Partially Saturated by Water," *International Journal of Thermophysics,* vol. 27, no. 4, pp. 1214–1227. doi:10.1007/s10765-006-0076-8, 2006.

[296] C. Clauser and E. Huenges, "Thermal Conductivity of Rocks and Minerals," in *Rock Physics & Phase Relations: A Handbook of Physical Constants, Volume 3*, 1995, p. doi:10.1029/RF003p0105.

[297] Y. Yang, "Thermal Conductivity," in *Physical Properties of Polymers Handbook*, Springer, 2007, pp. 155-164.

[298] M. Antlauf, N. Boulanger, L. Berglund, K. Oksman and O. Andersson, "Thermal Conductivity of Cellulose Fibers in Different Size Scales and Densities," *Biomacromolecules,* vol. 22, pp. 3800-3809. doi:10.1021/acs.biomac.1c00643, 2021.

[299] W. Pei, F. Ming, M. Zhang and X. Wan, "A thermal conductivity model for insulation materials considering the effect of moisture in cold regions," *Cold Regions Science and Technology,* vol. 207, p. 103770. doi:10.1016/j.coldregions.2022.103770, 2023.

[300] H. He, K. Noborio, Ø. Johansen, M. F. Dyck and J. Lv, "Normalized concept for modelling effective soil thermal conductivity from dryness to saturation," *European Journal of Soil Science,* vol. 71, no. 1, 2019. doi:10.1111/ejss.12820.

[301] D. Taoukil, A. E. bouardi, F. Sick, A. Mimet, H. Ezbakhe and T. Ajzoul, "Moisture content influence on the thermal conductivity and diffusivity of wood–concrete composite," *Construction and Building Materials,* vol. 48, 2013. doi:10.1016/j.conbuildmat.2013.06.067.

[302] A. Bouguerra, "Prediction of effective thermal conductivity of moist wood concrete," *Journal of Physics D: Applied Physics,* vol. 32, 1999. doi:10.1088/0022-3727/32/12/318.

[303] Y. Çengel and J. Cimbala, "Appendix 1 Property tables and charts," in *Fluid Mechanics Fundamentals and Applications*, McGraw Hill, 2006.

[304] H. He, M. Li, M. Dyck, B. Si, J. Wang and J. Lv, "Modelling of soil solid thermal conductivity," *International Communications in Heat and Mass Transfer,* vol. 116, p. 104602, 2020. doi:10.1016/j.icheatmasstransfer.2020.104602.

[305] W. H. Somerton, J. A. Keese and S. L. Chu, "Thermal Behaviour of Unconsolidated Oil Sands," *SPEJ,* pp. 513-521, 1974.

[306] K. Udell and J. S. Fitch, "Heat and Mass Transfer in Capillary Porous Media Considering Evaporation, Condensation and Non-Condensible Gas Effects," *23rd ASME/AIChE national heat transfer conference,* pp. 103-110, 1985.

[307] WUFI, *WUFI Material (North America and Fraunhofer-IBP databases),* WUFI, 2024.

APPENDIX A ADDITIONAL MATERIAL PROPERTIES

Table A.1 Material properties for other components used in simulation [239].

	Solid brick	Wood fibreboard	Gypsum board	Wood cladding	Cellulose (reference)
Bulk Density ϱ_{bulk}, dried (kg·m^{-3})	1900	300	732	400	55
Porosity (%)	0.24	0.8	0.72	0.9	0.93
Specific Heat Capacity C_p (J·kg^{-1}·K^{-1})	850	1400	1384	1880	2544
Thermal Conductivity λ (W·m^{-1}·K^{-1})	0.6	0.05	0.1925	0.086	0.0357
Vapour Diffusion Resistance Factor μ (dimensionless)	10	12.5	6.8	552	2
Free Water Saturation w_{sat} (%)	10	50	48	845	898

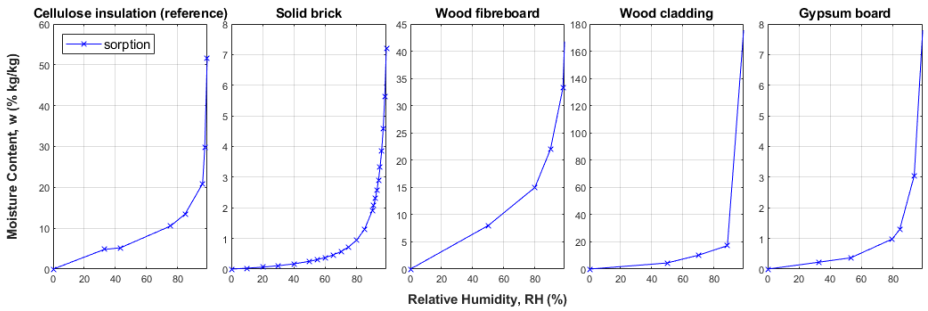

Fig. A.1 Sorption curve for other components used in simulation [239]. Moisture content w after 99% RH is excluded from the plot for clarity, refer to w_{sat} for 100% relative humidity in **Table A.1**.

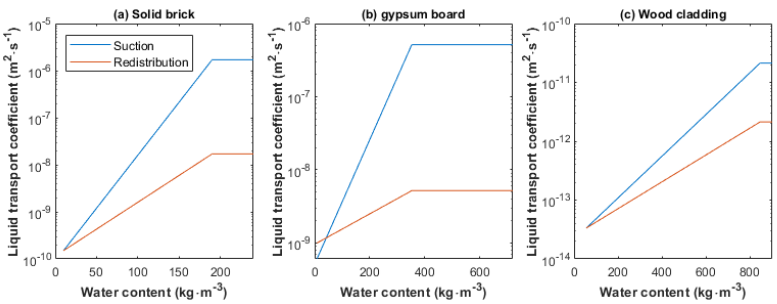

Fig. A.2 Liquid transport coefficient for other components used in simulation [239].

Table A.2 Main material properties for simulation.

	Barley Straws	Wheat Straws	Barley Straws (treated)	Wheat Straws (treated)	Lime Plaster
Bulk Density ϱ_{bulk}, dried (kg·m^{-3})	100	100	100	100	1600
Porosity (%)	0.89 *	0.90 *	0.88 *	0.90 *	0.4
Specific Heat Capacity C_p (J·kg^{-1}·K^{-1})	1645 *	1735 *	1692 *	1745 *	850
Thermal Conductivity λ (W·m^{-1}·K^{-1})	0.052 *	0.061 *	0.054 *	0.059 *	0.7
Vapour Diffusion Resistance Factor μ (-)	5 *#	5 *#	5 *#	5 *#	7
Moisture Content at RH=80% (%)	0.13 *	0.14 *	0.14 *	0.15 *	0.02

*Note * The values are obtained from the experiments in this study.*
Note # A single μ-values of 5 was applied to all samples, averaged from the measurement results. Although the cup measurement results (wet-cup value higher than dry-cup value) are assumed to be due to swelling phenomena as discussed earlier, there is insufficient literature to support this assumption conclusively. Therefore, it was decided that an average value is more appropriate for all four samples since their individual values do not vary significantly from one another.

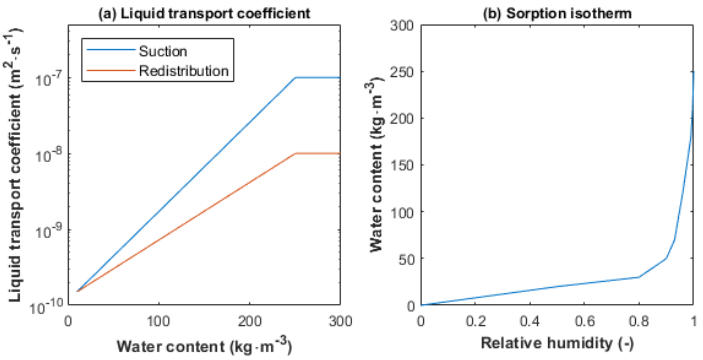

Fig. A.3 Liquid transport coefficient and sorption isotherm for lime plaster.

Table A.3 Material properties for solid brick, glass wool, stone wool and PU foam for simulation [239].

	Solid Brick	Glass wool	PU Foam	Stone Wool
Bulk density ϱ_{bulk}, dried (kg·m^{-3})	1900	36	39	60
Porosity (%)	0.24	0.986	0.99	0.95
Specific heat capacity C_p (J·kg^{-1}·K^{-1})	850	850	1470	850
Thermal conductivity λ (W·m^{-1}·K^{-1})	0.6	0.0343	0.025	0.04
Vapour diffusion resistance factor μ (-)	10	1.3	88.93	1.3
Free water saturation w_{sat} (%)	10	1017	72	75

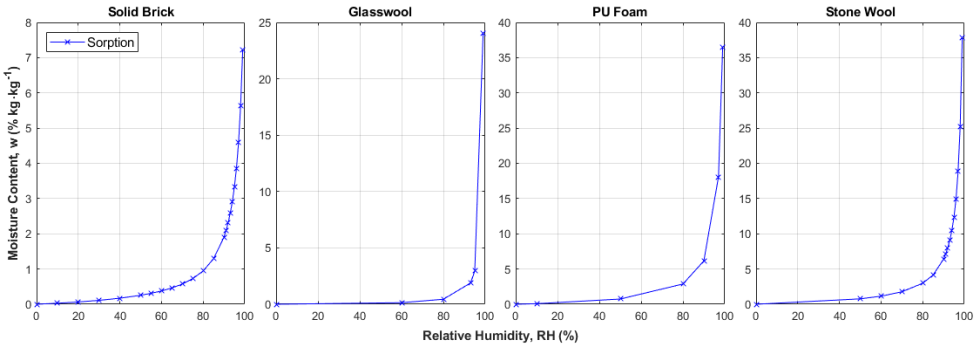

Fig. A.4 Sorption curve for solid brick, glass wool, stone wool and PU foam for simulation [239]. Moisture content after 99% RH is excluded from the plot for clarity, refer to w_{sat} for 100% relative humidity in **Table A.3**.

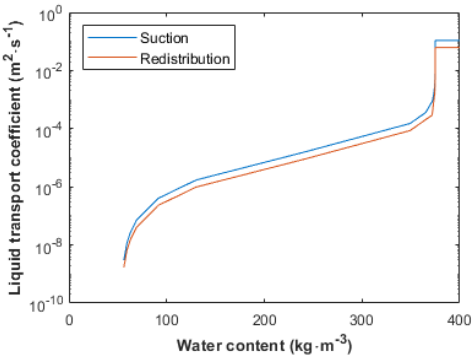

Fig. A.5 Liquid transport coefficient modelled for M86 aggregates.

APPENDIX B BOUNDARY CONDITIONS

Table B.1 Summary of weather profile for simulated exterior climates.

Climate profile (Köppen climate classification)	**Cfa**	**Cfb**	**Cfc**	**Dfa**	**Dfb**	**Dfc**
Location	Milan ITA	Eindhoven NLD	Tórshav FRO	Kherson UKR	Oslo NOR	Sodankylä FIN
Altitude (m)	103	22	61	54	96	183
Temperature, mean (°C)	14.6	10.9	7.1	11.5	7.2	1.3
Relative Humidity, mean (%)	72.6	79.5	82.7	73.4	72.8	79.4
Wind Speed, mean ($m \cdot s^{-1}$)	1.8	3.8	6.6	2.9	2.7	2.6
Normal Rain ($mm \cdot a^{-1}$)	754.5	733.7	1419.8	625.2	658.4	567.3
Counter Radiation ($kWh \cdot m^{-2} \cdot a^{-1}$)	2978.9	2883.8	2715.3	2868.2	2661.8	2454.7
Driving Rain Direction (-)	NE	SW	West	NW	NE	SE

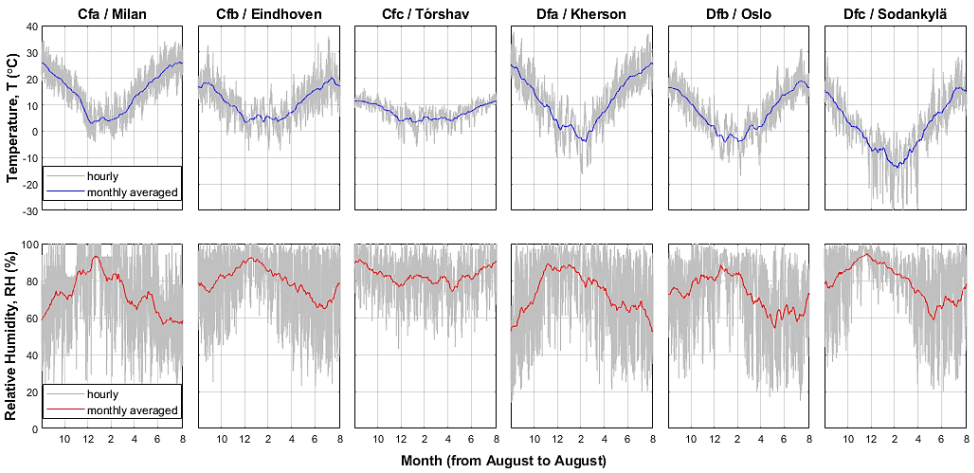

Fig. B.1 Simulated climates with temperature and relative humidity profiles plotted against Months. Note Köppen climate classification description: C – temperate, D – continental, f – no dry season, a – hot summer, b – warm summer, c – cold summer.

Table B.2 Summary of boundary and initial conditions.

Exterior boundary conditions	
Climate	Refer to **Table B.1** and **Fig. B.1**
Heat resistance ($m^2 \cdot K \cdot W^{-1}$)	0.0588
Short wave radiation absorptivity (-)	-
Long wave radiation emissivity (-)	-
Adhering fraction of rain (-)	0.7
Interior boundary conditions	
Climate	EN 13788 humidity class 3, temperature 20°C
Heat resistance ($m^2 \cdot K \cdot W^{-1}$)	0.125
Initial conditions	
Relative humidity (-)	0.8
Temperature in components (°C)	20

Table B.3 Simulated cases.

Climate Type [1]	***Represented Location*** [2]	***Temp (°C)***	***RH (%)***	***Rain ($mm \cdot a^{-1}$)***	***Simulated Orient*** [3]	***Wheat yield ($hg \cdot ha^{-1}$)*** [4]	***Barley yield ($hg \cdot ha^{-1}$)*** [4]
BSk	Baku, AZE	15.6	76.1	243.9	N	31,555	28,884
BSh	Coimbatore, IND	26.8	68.9	997.3	SW	35,334	28,372
BWk	Damascus, SYR	18.0	51.4	80.7	SW	22,927	20,617
BWh	Cairo, EGY	23.3	55.5	35.2	W	65,003	37,406
Cfa	Houston, USA	20.5	73.3	88.2	E	34,746	41,785
Cfb	Amsterdam, NLD	11.0	79.7	838.6	SW	93,781	72,588
Cfc	Auckland, NZL	15.7	80.7	1280.3	N	88,522	69,180
Cwa	Islamabad, PAK	22.3	60.0	904.1	E	28,059	9,682
Cwb	Addis Ababa, ETH	17.1	61.4	1633.5	S	29,705	25,012
Cwc	La Paz, BOL	7.8	59.7	975.8	E	11,993	8,943
Csa	Perth, AUS	18.6	61.4	577.1	W	16,917	19,878
Csb	Nakuru, KEN	18.6	67.9	1427.9	N	26,287	35,721
Csc	Chile Chico, CHL	8.2	65.3	706.0	NW	62,860	73,725
Dfa	Almaty, KAZ	10.0	63.0	716.1	SW	10,137	12,866
Dfb	Kyiv, UKR	9.7	71.8	659.3	NW	41,566	34,174
Dfc	Yellowknife, CAN	-3.1	67.1	313.6	NE	33,834	38,066
Dwa	Pyongyang, PRK	9.4	73.7	1303.9	S	12,207	11,662

Climate Type [1]	*Represented Location* [2]	*Temp (°C)*	*RH (%)*	*Rain (mm·a^{-1})*	*Simulated Orient* [3]	*Wheat yield (hg·ha^{-1})* [4]	*Barley yield (hg·ha^{-1})* [4]
Dwb	Vladivostok, RUS	5.5	72.1	637.4	SE	27,016	24,001
Dwc	Mohe, CHN	-3.2	65.2	426.8	NE	56,298	39,354
Dsa	Bishkek, KGZ	12.3	55.0	921.8	W	25,093	22,717
Dsb	Sivas, TUR	9.7	62.3	410.8	SE	27,811	26,565
Dsc	Soldotna, USA	3.2	71.1	187.7	E	34,746	41,785

[1] Climate type is as per Köppen climate classification: B = dry, C = temperate, D = continental, W = arid desert, S = semi-Arid, w = dry winter, f = no dry season, s = dry summer, a = hot summer, b = warm summer, c = cold summer.
[2] ISO 3166-1 alpha-3 codes (three-letter country codes) are used to represent the countries.
[3] Simulated wall orientation is facing the driving rain direction: N = north, S = south, W = west, E = east.
[4] Quantity is based on the annual wheat and barley yield (hectogram/hectare) in the whole country in the year 2019.

Table B.4 Summary of boundary and initial conditions.

Exterior boundary conditions	
Climate	Refer to **Table B.3**
Heat resistance (m^2·K·W^{-1})	0.0588
Short wave radiation absorptivity (-)	-
Long wave radiation emissivity (-)	-
Adhering fraction of rain (-)	0.7
Interior boundary conditions	
Climate	EN 13788 humidity class 3, temperature 20°C
Heat resistance (m^2·K·W^{-1})	0.125
Initial conditions	
Relative humidity (-)	0.8
Temperature in components (°C)	20

Table B.5 Summary of weather profile for simulated exterior climate.

Climate profile (Köppen climate classification)	Cfb
Location	Eindhoven, NLD
Altitude (m)	22
Temperature, mean (°C)	10.9
Relative humidity, mean (%)	79.5
Wind speed, mean ($m \cdot s^{-1}$)	3.8
Normal rain, sum ($mm \cdot a^{-1}$)	733.7
Counter radiation, sum ($kWh \cdot m^{-2} \cdot a^{-1}$)	2883.8

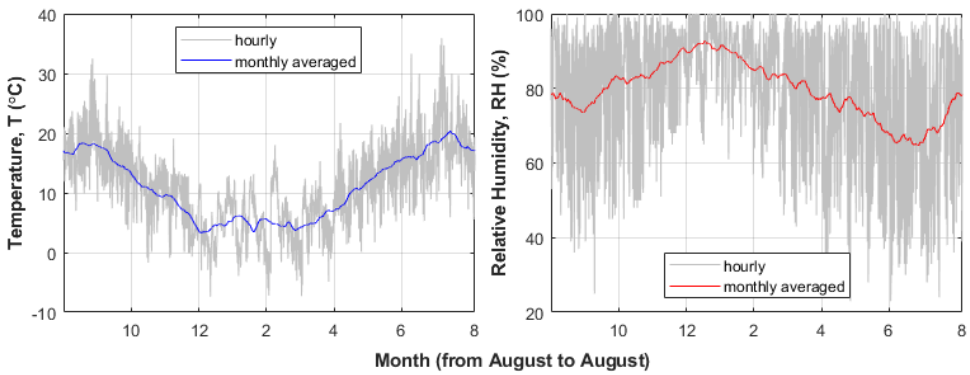

Fig. B.2 Simulated climate with temperature and relative humidity profiles plotted against months.

Table B.6 Summary of boundary and initial conditions.

Exterior boundary conditions	
Climate	Refer to **Table B.5** and **Fig. B.2**
Heat resistance ($m^2 \cdot K \cdot W^{-1}$)	0.0588
Short wave radiation absorptivity (-)	-
Long wave radiation emissivity (-)	-
Adhering fraction of rain (-)	0.7
Interior boundary conditions	
Climate	EN 13788 humidity class 3, temperature 20°C
Heat resistance ($m^2 \cdot K \cdot W^{-1}$)	0.125
Initial conditions	
Relative humidity (-)	0.8
Temperature in components (°C)	20

Table B.7 Summary of boundary and initial conditions.

Exterior boundary conditions	
Climate	Refer to **Table B.5** and **Fig. B.2**
Climate (ground)	Represented by sine curve (mean 11°C, amplitude 7°C)
Heat resistance ($m^2 \cdot K \cdot W^{-1}$)	0.04 (wall, window), 0 (floor), 0.1 (ceiling)
Short wave radiation absorptivity (-)	0.4
Long wave radiation emissivity (-)	0.9
Shading	no
Linearized thermal bridge ($W \cdot m^{-1} \cdot K^{-1}$)	0.68
Interior boundary conditions	
Heat resistance ($m^2 \cdot K \cdot W^{-1}$)	0.13 (wall, window), 0.17 (floor), 0.1 (ceiling)
Solar gain, inner distribution (-)	0.289 (wall), 0.028 (window), 0.131 (floor, ceiling)
Daily heat gain, internal load (W)	8485
Clothing, for PMW/PPD (clo)	0.7
Air velocity, for PMV/PPD ($m \cdot s^{-1}$)	0.1
Initial conditions	
Relative humidity in components (-)	0.8
Temperature in components (°C)	20
Relative humidity in room (-)	0.55
Temperature in room (°C)	20
CO_2 concentration (ppmw)	400

LIST OF NOTATIONS

ABBREVIATIONS

ADP	abiotic depletion potential
AP	acidification potential
ATR	attenuated total reflection
BFS	blast furnace slag
CDW	construction and demolition waste
DSC	differential scanning calorimetry
DSV	dynamic vapour sorption
DTG	derivative thermogravimetry
EF	environmental footprint
EP	eutrophication potential
EPD	environmental product declaration
EPA	expanded perlite aggregates
EPS	expanded polystyrene
ETP	eco-toxicity potential
FA	fly ash
FT-IR	Fourier transform-infrared
GHG	greenhouse gas
GGBFS	ground granulated blast furnace slag
GWP	global warming potential
HAM	heat, air and moisture transport
HTP	human toxicity potential
IEQ	indoor environmental quality
IRP	ionizing radiation potential
LCA	life cycle assessment
LOI	loss on ignition
luluc	land use and land use change
LWA	lightweight aggregates
micro-CT	micro-computed tomography
ODP	depletion potential of the stratospheric ozone layer
OPC	ordinary Portland cement
PET	polyethylene terephthalate
PF	phenol formaldehyde / phenolic
PM	particulate matter emissions
PMV	predicted mean vote
POCP	formation potential of tropospheric ozone
PPD	predicted percentage dissatisfied
PU / PUR	polyurethane
RH	relative humidity
SEM	scanning electron microscope
SGB	straw geopolymer board
SQP	soil quality potential
SSS	saturated salt solutions
SWS	single-weighted scope
TGA	thermogravimetric analysis

UF	urea-formaldehyde
XPS	extruded polystyrene
XRD	X-ray diffraction
XRF	X-ray fluorescence spectrometry
WW	wood wool
WWCB	wood wool cement board
WWGB	wood wool geopolymer board
WDP	water deprivation potential

NOMENCLATURES - LATIN:

A (m^2)	area
C_p ($J \cdot kg^{-1} \cdot °C^{-1}$)	specific heat capacity
d (m)	thickness
D_w ($m^2 \cdot s^{-1}$)	liquid transport coefficient
g ($kg \cdot m^{-2} \cdot s^{-1}$)	water vapour transmission rate
E (kWh)	energy consumption
H ($J \cdot m^{-3}$)	enthalpy
h_v ($J \cdot kg^{-1}$)	evaporation enthalpy of water
I_x (%)	transmittance intensity at wavenumber x
H (J)	enthalpy of the air in the simulated zone,
m (kg)	mass
m_{dry} (kg)	dry mass
p (Pa)	water vapour partial pressure
P (kW)	power
Q (W)	heat flow
R-value ($m^2 \cdot K \cdot W^{-1}$)	thermal resistance
R^2 (dimensionless)	coefficients of determination
U-value ($W \cdot m^{-2} \cdot K^{-1}$)	thermal transmittance
v ($m^3 \cdot m^{-3}$)	volume fraction
w ($kg \cdot kg^{-1}$)	moisture or water content
w_{sat} ($kg \cdot kg^{-1}$)	free water saturation
$\dot{W}$ ($kg \cdot s^{-1}$)	moisture flow
t (s)	time
T (°C)	temperature
TL (dB)	sound transmission loss

NOMENCLATURES - GREEK:

α (dimensionless)	sound absorption coefficient
λ ($W \cdot m^{-1} \cdot K^{-1}$)	effective thermal conductivity
λ_{dry} ($W \cdot m^{-1} \cdot K^{-1}$)	effective dry thermal conductivity
λ_{sat} ($W \cdot m^{-1} \cdot K^{-1}$)	effective saturated thermal conductivity
σ_{10} (MPa)	compression stress at a strain of 10%
σ_b (MPa)	bending strength
δ ($kg \cdot m^{-1} \cdot s^{-1} \cdot Pa^{-1}$)	water vapour diffusion coefficient in air
δ_{air} ($kg \cdot m^{-1} \cdot s^{-1} \cdot Pa^{-1}$)	water vapour permeability of air
ϱ_{bulk} ($kg \cdot m^{-3}$)	bulk density
$\varrho_{particle}$ ($kg \cdot m^{-3}$)	skeletal density
φ (dimensionless)	porosity
μ (dimensionless)	water vapour diffusion resistance factor

LIST OF PUBLICATIONS

PEER-REVIEWED JOURNAL PAPERS

[1] **C.H. Koh** and H.J.H. Brouwers, "A simple two-phase approach to predict moisture-dependent thermal conductivity for porous insulation materials," International Journal of Heat and Mass Transfer 234, 126138 (2024).

[2] **C.H. Koh**, Y. Luo, F. Gauvin, K. Schollbach and H.J.H. Brouwers, "A Circular Approach to Stone Wool: Alkali-Activated Lightweight Aggregates," Developments in the Built Environment 19, 100506 (2024).

[3] **C.H. Koh**, Y. Luo, F. Gauvin, and K. Schollbach, "Utilization of geopolymer in wood wool insulation boards: Design optimization, development and performance characteristics," Resources, Conservation and Recycling 204, 107510 (2024).

[4] **C.H. Koh**, F. Gauvin, K. Schollbach and H.J.H. Brouwers, "Upcycling wheat and barley straws into sustainable thermal insulation: Assessment and treatment for durability," Resources, Conservation and Recycling 198, 107161 (2023).

[5] Y. Luo, **C.H. Koh**, S.H. Li, H.J.H. Brouwers, Qingliang Yu, "Understanding the thermal behaviour of geopolymeric composites designed by packing model," Cement and Concrete Composites 143, 105265 (2023).

[6] **C.H. Koh**, F. Gauvin, K. Schollbach and H.J.H. Brouwers, "Investigation of material characteristics and hygrothermal performances of different bio-based insulation composites," Construction and Building Materials 346, 128440 (2022).

[7] **C.H. Koh**, K. Schollbach, F. Gauvin, and H.J.H. Brouwers, "Aerogel composite for cavity wall rehabilitation in the Netherlands: Material characterization and thermal comfort assessment," Building and Environment 224, 109535 (2022).

[8] K.M. Klima, **C.H. Koh**, H.J.H. Brouwers, Q. Yu, "Synergistic effect of surfactants in porous geopolymer: Tailoring pore size and pore connectivity," Cement and Concrete Composites 124, 104774 (2022).

[9] **C.H. Koh**, F. Gauvin, K. Schollbach and H.J.H. Brouwers, "Evaluating environmental impacts of geopolymer and straw-based wood wool cement boards," submitted.

[10] K.M. Klima, **C.H. Koh**, J.C.O. Zepper, Q. Yu, "Geopolymer composites exposed to high temperatures: the role of pore connectivity and pore size distribution," submitted.

[11] H. Song, **C.H. Koh**, S. Pantaléo, F. Berger, W. Chen, F. Gauvin and H.J.H. Brouwers, "Durability assessment of alkyl ketene dimer hydrophobic treatment of bio-based thermal insulation materials," submitted.

[12] Y. Luo, **C.H. Koh**, H.J.H. Brouwers, "High-temperature performance of geopolymer mortar: An experimental and numerical modelling study," in preparation.

[13] D. Liu, J.C.O. Zepper, **C.H. Koh**, Y. Chen, Q. Yu, "NOx abatement properties of autoclaved BOF slag-based photocatalytic mortars," in preparation.

CONFERENCE PROCEEDINGS

[1] **C.H. Koh**, F. Gauvin, K. Schollbach and H.J.H. Brouwers, "Straw wool geopolymer board: straw-geopolymer compatibility and its insulation performance", The 3rd International Conference of Sustainable Building Materials, 25-27 September 2023, Wuhan, China. Poster.

[2] **C.H. Koh**, F. Gauvin, K. Schollbach and H.J.H. Brouwers, "Development of wood wool geopolymer board: a greener alternative to wood wool cement board", The 7th International Conference: Non-traditional Cement and Concrete (NTCC 2023), 25-28 June 2023, Brno, Czech Republic. Poster.

[3] **C.H. Koh**, F. Gauvin, K. Schollbach and H.J.H. Brouwers, "Loose straw and its composites as building insulation materials", The 4th International Conference on the Chemistry of Construction Materials, 26-28 September 2022, Karlsruhe, Germany. Oral presentation.

CURRICULUM VITAE

Koh Chuen Hon, also known as **Alex Koh**, was born on March 22, 1984, in Kuantan, Malaysia. He earned his Bachelor's degree in Mechanical Engineering from Universiti Teknologi Malaysia (UTM) in 2007, with his undergraduate project focusing on the design and development of a dexterous robotic hand. Following his undergraduate studies, he accumulated twelve years of experience in the offshore construction industry. His work spanned various regions and included pipe spool fabrication in Norway, offshore pipeline, cable, and umbilical installation in the North Sea, marine base and on-site construction projects in the Middle East, and fabrication and offshore constructions in Southeast Asia. In 2021, he obtained a Master's degree in Structural Engineering and Building Technology from OsloMet in Norway. His master's project involved a two-way coupled fluid-structure interaction method for the aerodynamic analysis of tall timber buildings.

In 2021, he started a PhD in the Building Materials Group in the Department of the Built Environment at the Eindhoven University of Technology. He is part of the MOOI project "Bright Renovation Insulation for building envelope through (Advanced) Materials and Methods (BRIMM)", which is funded by the Netherlands Enterprise Agency (RVO). Under the supervision of prof. dr. ir. H.J.H. Brouwers, dr. Dipl.-Min. K. Schollbach and dr. F. Gauvin, his research is focused on the development of building insulation materials for sustainable building performance. The results of this research are documented in this dissertation.

Bouwstenen is een publicatiereeks
van de Faculteit Bouwkunde,
Technische Universiteit Eindhoven.
Zij presenteert resultaten van
onderzoek en andere activiteiten op
het vakgebied der Bouwkunde,
uitgevoerd in het kader van deze
Faculteit.

Bouwstenen en andere proefschriften van de
TU/e zijn online beschikbaar via:
https://research.tue.nl/

Reeds verschenen in de serie
Bouwstenen

nr 1
Elan: A Computer Model for Building Energy Design: Theory and Validation
Martin H. de Wit
H.H. Driessen
R.M.M. van der Velden

nr 2
Kwaliteit, Keuzevrijheid en Kosten: Evaluatie van Experiment Klarendal, Arnhem
J. Smeets
C. le Nobel
M. Broos
J. Frenken
A. v.d. Sanden

nr 3
Crooswijk: Van 'Bijzonder' naar 'Gewoon'
Vincent Smit
Kees Noort

nr 4
Staal in de Woningbouw
Edwin J.F. Delsing

nr 5
Mathematical Theory of Stressed Skin Action in Profiled Sheeting with Various Edge Conditions
Andre W.A.M.J. van den Bogaard

nr 6
Hoe Berekenbaar en Betrouwbaar is de Coëfficiënt k in x-ksigma en x-ks?
K.B. Lub
A.J. Bosch

nr 7
Het Typologisch Gereedschap: Een Verkennende Studie Omtrent Typologie en Omtrent de Aanpak van Typologisch Onderzoek
J.H. Luiten

nr 8
Informatievoorziening en Beheerprocessen
A. Nauta
Jos Smeets (red.)
Helga Fassbinder (projectleider)
Adrie Proveniers
J. v.d. Moosdijk

nr 9
Strukturering en Verwerking van Tijdgegevens voor de Uitvoering van Bouwwerken
ir. W.F. Schaefer
P.A. Erkelens

nr 10
Stedebouw en de Vorming van een Speciale Wetenschap
K. Doevendans

nr 11
Informatica en Ondersteuning van Ruimtelijke Besluitvorming
G.G. van der Meulen

nr 12
Staal in de Woningbouw, Korrosie-Bescherming van de Begane Grondvloer
Edwin J.F. Delsing

nr 13
Een Thermisch Model voor de Berekening van Staalplaatbetonvloeren onder Brandomstandigheden
A.F. Hamerlinck

nr 14
De Wijkgedachte in Nederland: Gemeenschapsstreven in een Stedebouwkundige Context
K. Doevendans
R. Stolzenburg

nr 15
Diaphragm Effect of Trapezoidally Profiled Steel Sheets: Experimental Research into the Influence of Force Application
Andre W.A.M.J. van den Bogaard

nr 16
Versterken met Spuit-Ferrocement: Het Mechanische Gedrag van met Spuit-Ferrocement Versterkte Gewapend Betonbalken
K.B. Lubir
M.C.G. van Wanroy

nr 17
De Tractaten van Jean Nicolas Louis Durand
G. van Zeyl

nr 18
Wonen onder een Plat Dak: Drie Opstellen over Enkele Vooronderstellingen van de Stedebouw
K. Doevendans

nr 19
Supporting Decision Making Processes: A Graphical and Interactive Analysis of Multivariate Data
W. Adams

nr 20
Self-Help Building Productivity: A Method for Improving House Building by Low-Income Groups Applied to Kenya 1990-2000
P. A. Erkelens

nr 21
De Verdeling van Woningen: Een Kwestie van Onderhandelen
Vincent Smit

nr 22
Flexibiliteit en Kosten in het Ontwerpproces: Een Besluitvormingondersteunend Model
M. Prins

nr 23
Spontane Nederzettingen Begeleid: Voorwaarden en Criteria in Sri Lanka
Po Hin Thung

nr 24
Fundamentals of the Design of Bamboo Structures
Oscar Arce-Villalobos

nr 25
Concepten van de Bouwkunde
M.F.Th. Bax (red.)
H.M.G.J. Trum (red.)

nr 26
Meaning of the Site
Xiaodong Li

nr 27
Het Woonmilieu op Begrip Gebracht: Een Speurtocht naar de Betekenis van het Begrip 'Woonmilieu'
Jaap Ketelaar

nr 28
Urban Environment in Developing Countries
editors: Peter A. Erkelens
George G. van der Meulen (red.)

nr 29
Stategische Plannen voor de Stad: Onderzoek en Planning in Drie Steden
prof.dr. H. Fassbinder (red.)
H. Rikhof (red.)

nr 30
Stedebouwkunde en Stadsbestuur
Piet Beekman

nr 31
De Architectuur van Djenné: Een Onderzoek naar de Historische Stad
P.C.M. Maas

nr 32
Conjoint Experiments and Retail Planning
Harmen Oppewal

nr 33
Strukturformen Indonesischer Bautechnik: Entwicklung Methodischer Grundlagen für eine 'Konstruktive Pattern Language' in Indonesien
Heinz Frick arch. SIA

nr 34
Styles of Architectural Designing: Empirical Research on Working Styles and Personality Dispositions
Anton P.M. van Bakel

nr 35
Conjoint Choice Models for Urban Tourism Planning and Marketing
Benedict Dellaert

nr 36
Stedelijke Planvorming als Co-Produktie
Helga Fassbinder (red.)

nr 37
Design Research in the Netherlands
editors: R.M. Oxman
M.F.Th. Bax
H.H. Achten

nr 38
Communication in the Building Industry
Bauke de Vries

nr 39
Optimaal Dimensioneren van Gelaste Plaatliggers
J.B.W. Stark
F. van Pelt
L.F.M. van Gorp
B.W.E.M. van Hove

nr 40
Huisvesting en Overwinning van Armoede
P.H. Thung
P. Beekman (red.)

nr 41
Urban Habitat: The Environment of Tomorrow
George G. van der Meulen
Peter A. Erkelens

nr 42
A Typology of Joints
John C.M. Olie

nr 43
Modeling Constraints-Based Choices for Leisure Mobility Planning
Marcus P. Stemerding

nr 44
Activity-Based Travel Demand Modeling
Dick Ettema

nr 45
Wind-Induced Pressure Fluctuations on Building Facades
Chris Geurts

nr 46
Generic Representations
Henri Achten

nr 47
Johann Santini Aichel: Architectuur en Ambiguiteit
Dirk De Meyer

nr 48
Concrete Behaviour in Multiaxial Compression
Erik van Geel

nr 49
Modelling Site Selection
Frank Witlox

nr 50
Ecolemma Model
Ferdinand Beetstra

nr 51
Conjoint Approaches to Developing Activity-Based Models
Donggen Wang

nr 52
On the Effectiveness of Ventilation
Ad Roos

nr 53
Conjoint Modeling Approaches for Residential Group preferences
Eric Molin

nr 54
Modelling Architectural Design Information by Features
Jos van Leeuwen

nr 55
A Spatial Decision Support System for the Planning of Retail and Service Facilities
Theo Arentze

nr 56
Integrated Lighting System Assistant
Ellie de Groot

nr 57
Ontwerpend Leren, Leren Ontwerpen
J.T. Boekholt

nr 58
Temporal Aspects of Theme Park Choice Behavior
Astrid Kemperman

nr 59
Ontwerp van een Geïndustrialiseerde Funderingswijze
Faas Moonen

nr 60
Merlin: A Decision Support System for Outdoor Leisure Planning
Manon van Middelkoop

nr 61
The Aura of Modernity
Jos Bosman

nr 62
Urban Form and Activity-Travel Patterns
Daniëlle Snellen

nr 63
Design Research in the Netherlands 2000
Henri Achten

nr 64
Computer Aided Dimensional Control in Building Construction
Rui Wu

nr 65
Beyond Sustainable Building
editors: Peter A. Erkelens
Sander de Jonge
August A.M. van Vliet
co-editor: Ruth J.G. Verhagen

nr 66
Das Globalrecyclingfähige Haus
Hans Löfflad

nr 67
Cool Schools for Hot Suburbs
René J. Dierkx

nr 68
A Bamboo Building Design Decision Support Tool
Fitri Mardjono

nr 69
Driving Rain on Building Envelopes
Fabien van Mook

nr 70
Heating Monumental Churches
Henk Schellen

nr 71
Van Woningverhuurder naar Aanbieder van Woongenot
Patrick Dogge

nr 72
Moisture Transfer Properties of Coated Gypsum
Emile Goossens

nr 73
Plybamboo Wall-Panels for Housing
Guillermo E. González-Beltrán

nr 74
The Future Site-Proceedings
Ger Maas
Frans van Gassel

nr 75
Radon transport in Autoclaved Aerated Concrete
Michel van der Pal

nr 76
The Reliability and Validity of Interactive Virtual Reality Computer Experiments
Amy Tan

nr 77
Measuring Housing Preferences Using Virtual Reality and Belief Networks
Maciej A. Orzechowski

nr 78
Computational Representations of Words and Associations in Architectural Design
Nicole Segers

nr 79
Measuring and Predicting Adaptation in Multidimensional Activity-Travel Patterns
Chang-Hyeon Joh

nr 80
Strategic Briefing
Fayez Al Hassan

nr 81
Well Being in Hospitals
Simona Di Cicco

nr 82
Solares Bauen: Implementierungs- und Umsetzungs-Aspekte in der Hochschulausbildung in Österreich
Gerhard Schuster

nr 83
Supporting Strategic Design of Workplace Environments with Case-Based Reasoning
Shauna Mallory-Hill

nr 84
ACCEL: A Tool for Supporting Concept Generation in the Early Design Phase
Maxim Ivashkov

nr 85
Brick-Mortar Interaction in Masonry under Compression
Ad Vermeltfoort

nr 86
Zelfredzaam Wonen
Guus van Vliet

nr 87
Een Ensemble met Grootstedelijke Allure
Jos Bosman
Hans Schippers

nr 88
On the Computation of Well-Structured Graphic Representations in Architectural Design
Henri Achten

nr 89
De Evolutie van een West-Afrikaanse Vernaculaire Architectuur
Wolf Schijns

nr 90
ROMBO Tactiek
Christoph Maria Ravesloot

nr 91
External Coupling between Building Energy Simulation and Computational Fluid Dynamics
Ery Djunaedy

nr 92
Design Research in the Netherlands 2005
editors: Henri Achten
Kees Dorst
Pieter Jan Stappers
Bauke de Vries

nr 93
Ein Modell zur Baulichen Transformation
Jalil H. Saber Zaimian

nr 94
Human Lighting Demands: Healthy Lighting in an Office Environment
Myriam Aries

nr 95
A Spatial Decision Support System for the Provision and Monitoring of Urban Greenspace
Claudia Pelizaro

nr 96
Leren Creëren
Adri Proveniers

nr 97
Simlandscape
Rob de Waard

nr 98
Design Team Communication
Ad den Otter

nr 99
Humaan-Ecologisch Georiënteerde Woningbouw
Juri Czabanowski

nr 100
Hambase
Martin de Wit

nr 101
Sound Transmission through Pipe Systems and into Building Structures
Susanne Bron-van der Jagt

nr 102
Het Bouwkundig Contrapunt
Jan Francis Boelen

nr 103
A Framework for a Multi-Agent Planning Support System
Dick Saarloos

nr 104
Bracing Steel Frames with Calcium Silicate Element Walls
Bright Mweene Ng'andu

nr 105
Naar een Nieuwe Houtskeletbouw
F.N.G. De Medts

nr 106 and 107
Niet gepubliceerd

nr 108
Geborgenheid
T.E.L. van Pinxteren

nr 109
Modelling Strategic Behaviour in Anticipation of Congestion
Qi Han

nr 110
Reflecties op het Woondomein
Fred Sanders

nr 111
On Assessment of Wind Comfort by Sand Erosion
Gábor Dezsö

nr 112
Bench Heating in Monumental Churches
Dionne Limpens-Neilen

nr 113
RE. Architecture
Ana Pereira Roders

nr 114
Toward Applicable Green Architecture
Usama El Fiky

nr 115
Knowledge Representation under Inherent Uncertainty in a Multi-Agent System for Land Use Planning
Liying Ma

nr 116
Integrated Heat Air and Moisture Modeling and Simulation
Jos van Schijndel

nr 117
Concrete Behaviour in Multiaxial Compression
J.P.W. Bongers

nr 118
The Image of the Urban Landscape
Ana Moya Pellitero

nr 119
The Self-Organizing City in Vietnam
Stephanie Geertman

nr 120
A Multi-Agent Planning Support System for Assessing Externalities of Urban Form Scenarios
Rachel Katoshevski-Cavari

nr 121
Den Schulbau Neu Denken, Fühlen und Wollen
Urs Christian Maurer-Dietrich

nr 122
Peter Eisenman Theories and Practices
Bernhard Kormoss

nr 123
User Simulation of Space Utilisation
Vincent Tabak

nr 125
In Search of a Complex System Model
Oswald Devisch

nr 126
Lighting at Work: Environmental Study of Direct Effects of Lighting Level and Spectrum on Psycho-Physiological Variables
Grazyna Górnicka

nr 127
Flanking Sound Transmission through Lightweight Framed Double Leaf Walls
Stefan Schoenwald

nr 128
Bounded Rationality and Spatio-Temporal Pedestrian Shopping Behavior
Wei Zhu

nr 129
Travel Information: Impact on Activity Travel Pattern
Zhongwei Sun

nr 130
Co-Simulation for Performance Prediction of Innovative Integrated Mechanical Energy Systems in Buildings
Marija Trčka

nr 131
Niet gepubliceerd

nr 132
Architectural Cue Model in Evacuation Simulation for Underground Space Design
Chengyu Sun

nr 133
Uncertainty and Sensitivity Analysis in Building Performance Simulation for Decision Support and Design Optimization
Christina Hopfe

nr 134
Facilitating Distributed Collaboration in the AEC/FM Sector Using Semantic Web Technologies
Jacob Beetz

nr 135
Circumferentially Adhesive Bonded Glass Panes for Bracing Steel Frame in Façades
Edwin Huveners

nr 136
Influence of Temperature on Concrete Beams Strengthened in Flexure with CFRP
Ernst-Lucas Klamer

nr 137
Sturen op Klantwaarde
Jos Smeets

nr 139
Lateral Behavior of Steel Frames with Discretely Connected Precast Concrete Infill Panels
Paul Teewen

nr 140
Integral Design Method in the Context of Sustainable Building Design
Perica Savanović

nr 141
Household Activity-Travel Behavior: Implementation of Within-Household Interactions
Renni Anggraini

nr 142
Design Research in the Netherlands 2010
Henri Achten

nr 143
Modelling Life Trajectories and Transport Mode Choice Using Bayesian Belief Networks
Marloes Verhoeven

nr 144
Assessing Construction Project Performance in Ghana
William Gyadu-Asiedu

nr 145
Empowering Seniors through Domotic Homes
Masi Mohammadi

nr 146
An Integral Design Concept for Ecological Self-Compacting Concrete
Martin Hunger

nr 147
Governing Multi-Actor Decision Processes in Dutch Industrial Area Redevelopment
Erik Blokhuis

nr 148
A Multifunctional Design Approach for Sustainable Concrete
Götz Hüsken

nr 149
Quality Monitoring in Infrastructural Design-Build Projects
Ruben Favié

nr 150
Assessment Matrix for Conservation of Valuable Timber Structures
Michael Abels

nr 151
Co-simulation of Building Energy Simulation and Computational Fluid Dynamics for Whole-Building Heat, Air and Moisture Engineering
Mohammad Mirsadeghi

nr 152
External Coupling of Building Energy Simulation and Building Element Heat, Air and Moisture Simulation
Daniel Cóstola

nr 153
Adaptive Decision Making In Multi-Stakeholder Retail Planning
Ingrid Janssen

nr 154
Landscape Generator
Kymo Slager

nr 155
Constraint Specification in Architecture
Remco Niemeijer

nr 156
A Need-Based Approach to Dynamic Activity Generation
Linda Nijland

nr 157
Modeling Office Firm Dynamics in an Agent-Based Micro Simulation Framework
Gustavo Garcia Manzato

nr 158
Lightweight Floor System for Vibration Comfort
Sander Zegers

nr 159
Aanpasbaarheid van de Draagstructuur
Roel Gijsbers

nr 160
'Village in the City' in Guangzhou, China
Yanliu Lin

nr 161
Climate Risk Assessment in Museums
Marco Martens

nr 162
Social Activity-Travel Patterns
Pauline van den Berg

nr 163
Sound Concentration Caused by Curved Surfaces
Martijn Vercammen

nr 164
Design of Environmentally Friendly Calcium Sulfate-Based Building Materials: Towards an Improved Indoor Air Quality
Qingliang Yu

nr 165
Beyond Uniform Thermal Comfort on the Effects of Non-Uniformity and Individual Physiology
Lisje Schellen

nr 166
Sustainable Residential Districts
Gaby Abdalla

nr 167
Towards a Performance Assessment Methodology using Computational Simulation for Air Distribution System Designs in Operating Rooms
Mônica do Amaral Melhado

nr 168
Strategic Decision Modeling in Brownfield Redevelopment
Brano Glumac

nr 169
Pamela: A Parking Analysis Model for Predicting Effects in Local Areas
Peter van der Waerden

nr 170
A Vision Driven Wayfinding Simulation-System Based on the Architectural Features Perceived in the Office Environment
Qunli Chen

nr 171
Measuring Mental Representations Underlying Activity-Travel Choices
Oliver Horeni

nr 172
Modelling the Effects of Social Networks on Activity and Travel Behaviour
Nicole Ronald

nr 173
Uncertainty Propagation and Sensitivity Analysis Techniques in Building Performance Simulation to Support Conceptual Building and System Design
Christian Struck

nr 174
Numerical Modeling of Micro-Scale Wind-Induced Pollutant Dispersion in the Built Environment
Pierre Gousseau

nr 175
Modeling Recreation Choices over the Family Lifecycle
Anna Beatriz Grigolon

nr 176
Experimental and Numerical Analysis of Mixing Ventilation at Laminar, Transitional and Turbulent Slot Reynolds Numbers
Twan van Hooff

nr 177
Collaborative Design Support: Workshops to Stimulate Interaction and Knowledge Exchange Between Practitioners
Emile M.C.J. Quanjel

nr 178
Future-Proof Platforms for Aging-in-Place
Michiel Brink

nr 179
Motivate: A Context-Aware Mobile Application for Physical Activity Promotion
Yuzhong Lin

nr 180
Experience the City: Analysis of Space-Time Behaviour and Spatial Learning
Anastasia Moiseeva

nr 181
Unbonded Post-Tensioned Shear Walls of Calcium Silicate Element Masonry
Lex van der Meer

nr 182
Construction and Demolition Waste Recycling into Innovative Building Materials for Sustainable Construction in Tanzania
Mwita M. Sabai

nr 183
Durability of Concrete with Emphasis on Chloride Migration
Przemysław Spiesz

nr 184
Computational Modeling of Urban Wind Flow and Natural Ventilation Potential of Buildings
Rubina Ramponi

nr 185
A Distributed Dynamic Simulation Mechanism for Buildings Automation and Control Systems
Azzedine Yahiaoui

nr 186
Modeling Cognitive Learning of Urban Networks in Daily Activity-Travel Behavior
Şehnaz Cenani Durmazoğlu

nr 187
Functionality and Adaptability of Design Solutions for Public Apartment Buildings in Ghana
Stephen Agyefi-Mensah

nr 188
A Construction Waste Generation Model for Developing Countries
Lilliana Abarca-Guerrero

nr 189
Synchronizing Networks: The Modeling of Supernetworks for Activity-Travel Behavior
Feixiong Liao

nr 190
Time and Money Allocation Decisions in Out-of-Home Leisure Activity Choices
Gamze Zeynep Dane

nr 191
How to Measure Added Value of CRE and Building Design
Rianne Appel-Meulenbroek

nr 192
Secondary Materials in Cement-Based Products: Treatment, Modeling and Environmental Interaction
Miruna Florea

nr 193
Concepts for the Robustness Improvement of Self-Compacting Concrete: Effects of Admixtures and Mixture Components on the Rheology and Early Hydration at Varying Temperatures
Wolfram Schmidt

nr 194
Modelling and Simulation of Virtual Natural Lighting Solutions in Buildings
Rizki A. Mangkuto

nr 195
Nano-Silica Production at Low Temperatures from the Dissolution of Olivine - Synthesis, Tailoring and Modelling
Alberto Lazaro Garcia

nr 196
Building Energy Simulation Based Assessment of Industrial Halls for Design Support
Bruno Lee

nr 197
Computational Performance Prediction of the Potential of Hybrid Adaptable Thermal Storage Concepts for Lightweight Low-Energy Houses
Pieter-Jan Hoes

nr 198
Application of Nano-Silica in Concrete
George Quercia Bianchi

nr 199
Dynamics of Social Networks and Activity Travel Behaviour
Fariya Sharmeen

nr 200
Building Structural Design Generation and Optimisation including Spatial Modification
Juan Manuel Davila Delgado

nr 201
Hydration and Thermal Decomposition of Cement/Calcium-Sulphate Based Materials
Ariën de Korte

nr 202
Republiek van Beelden:
De Politieke Werkingen van het Ontwerp in Regionale Planvorming
Bart de Zwart

nr 203
Effects of Energy Price Increases on Individual Activity-Travel Repertoires and Energy Consumption
Dujuan Yang

nr 204
Geometry and Ventilation:
Evaluation of the Leeward Sawtooth Roof Potential in the Natural Ventilation of Buildings
Jorge Isaac Perén Montero

nr 205
Computational Modelling of Evaporative Cooling as a Climate Change Adaptation Measure at the Spatial Scale of Buildings and Streets
Hamid Montazeri

nr 206
Local Buckling of Aluminium Beams in Fire Conditions
Ronald van der Meulen

nr 207
Historic Urban Landscapes:
Framing the Integration of Urban and Heritage Planning in Multilevel Governance
Loes Veldpaus

nr 208
Sustainable Transformation of the Cities:
Urban Design Pragmatics to Achieve a Sustainable City
Ernesto Antonio Zumelzu Scheel

nr 209
Development of Sustainable Protective Ultra-High Performance Fibre Reinforced Concrete (UHPFRC):
Design, Assessment and Modeling
Rui Yu

nr 210
Uncertainty in Modeling Activity-Travel Demand in Complex Uban Systems
Soora Rasouli

nr 211
Simulation-based Performance Assessment of Climate Adaptive Greenhouse Shells
Chul-sung Lee

nr 212
Green Cities:
Modelling the Spatial Transformation of the Urban Environment using Renewable Energy Technologies
Saleh Mohammadi

nr 213
A Bounded Rationality Model of Short and Long-Term Dynamics of Activity-Travel Behavior
Ifigeneia Psarra

nr 214
Effects of Pricing Strategies on Dynamic Repertoires of Activity-Travel Behaviour
Elaheh Khademi

nr 215
Handstorm Principles for Creative and Collaborative Working
Frans van Gassel

nr 216
Light Conditions in Nursing Homes: Visual Comfort and Visual Functioning of Residents
Marianne M. Sinoo

nr 217
Woonsporen: De Sociale en Ruimtelijke Biografie van een Stedelijk Bouwblok in de Amsterdamse Transvaalbuurt
Hüseyin Hüsnü Yegenoglu

nr 218
Studies on User Control in Ambient Intelligent Systems
Berent Willem Meerbeek

nr 219
Daily Livings in a Smart Home: Users' Living Preference Modeling of Smart Homes
Erfaneh Allameh

nr 220
Smart Home Design: Spatial Preference Modeling of Smart Homes
Mohammadali Heidari Jozam

nr 221
Wonen: Discoursen, Praktijken, Perspectieven
Jos Smeets

nr 222
Personal Control over Indoor Climate in Offices: Impact on Comfort, Health and Productivity
Atze Christiaan Boerstra

nr 223
Personalized Route Finding in Multimodal Transportation Networks
Jianwe Zhang

nr 224
The Design of an Adaptive Healing Room for Stroke Patients
Elke Daemen

nr 225
Experimental and Numerical Analysis of Climate Change Induced Risks to Historic Buildings and Collections
Zara Huijbregts

nr 226
Wind Flow Modeling in Urban Areas Through Experimental and Numerical Techniques
Alessio Ricci

nr 227
Clever Climate Control for Culture: Energy Efficient Indoor Climate Control Strategies for Museums Respecting Collection Preservation and Thermal Comfort of Visitors
Rick Kramer

nr 228
Fatigue Life Estimation of Metal Structures Based on Damage Modeling
Sarmediran Silitonga

nr 229
A multi-agents and occupancy based strategy for energy management and process control on the room-level
Timilehin Moses Labeodan

nr 230
Environmental assessment of Building Integrated Photovoltaics: Numerical and Experimental Carrying Capacity Based Approach
Michiel Ritzen

nr 231
Performance of Admixture and Secondary Minerals in Alkali Activated Concrete: Sustaining a Concrete Future
Arno Keulen

nr 232
World Heritage Cities and Sustainable Urban Development:
Bridging Global and Local Levels in Monitoring the Sustainable Urban Development of World Heritage Cities
Paloma C. Guzman Molina

nr 233
Stage Acoustics and Sound Exposure in Performance and Rehearsal Spaces for Orchestras:
Methods for Physical Measurements
Remy Wenmaekers

nr 234
Municipal Solid Waste Incineration (MSWI) Bottom Ash:
From Waste to Value Characterization, Treatments and Application
Pei Tang

nr 235
Large Eddy Simulations Applied to Wind Loading and Pollutant Dispersion
Mattia Ricci

nr 236
Alkali Activated Slag-Fly Ash Binders: Design, Modeling and Application
Xu Gao

nr 237
Sodium Carbonate Activated Slag: Reaction Analysis, Microstructural Modification & Engineering Application
Bo Yuan

nr 238
Shopping Behavior in Malls
Widiyani

nr 239
Smart Grid-Building Energy Interactions: Demand Side Power Flexibility in Office Buildings
Kennedy Otieno Aduda

nr 240
Modeling Taxis Dynamic Behavior in Uncertain Urban Environments
Zheng Zhong

nr 241
Gap-Theoretical Analyses of Residential Satisfaction and Intention to Move
Wen Jiang

nr 242
Travel Satisfaction and Subjective Well-Being: A Behavioral Modeling Perspective
Yanan Gao

nr 243
Building Energy Modelling to Support the Commissioning of Holistic Data Centre Operation
Vojtech Zavrel

nr 244
Regret-Based Travel Behavior Modeling: An Extended Framework
Sunghoon Jang

nr 245
Towards Robust Low-Energy Houses: A Computational Approach for Performance Robustness Assessment using Scenario Analysis
Rajesh Reddy Kotireddy

nr 246
Development of sustainable and functionalized inorganic binder-biofiber composites
Guillaume Doudart de la Grée

nr 247
A Multiscale Analysis of the Urban Heat Island Effect: From City Averaged Temperatures to the Energy Demand of Individual Buildings
Yasin Toparlar

nr 248
Design Method for Adaptive Daylight Systems for buildings covered by large (span) roofs
Florian Heinzelmann

nr 249
Hardening, high-temperature resistance and acid resistance of one-part geopolymers
Patrick Sturm

nr 250
Effects of the built environment on dynamic repertoires of activity-travel behaviour
Aida Pontes de Aquino

nr 251
Modeling for auralization of urban environments: Incorporation of directivity in sound propagation and analysis of a framework for auralizing a car pass-by
Fotis Georgiou

nr 252
Wind Loads on Heliostats and Photovoltaic Trackers
Andreas Pfahl

nr 253
Approaches for computational performance optimization of innovative adaptive façade concepts
Roel Loonen

nr 254
Multi-scale FEM-DEM Model for Granular Materials: Micro-scale boundary conditions, Statics, and Dynamics
Jiadun Liu

nr 255
Bending Moment - Shear Force Interaction of Rolled I-Shaped Steel Sections
Rianne Willie Adriana Dekker

nr 256
Paralympic tandem cycling and handcycling: Computational and wind tunnel analysis of aerodynamic performance
Paul Fionn Mannion

nr 257
Experimental characterization and numerical modelling of 3D printed concrete: Controlling structural behaviour in the fresh and hardened state
Robert Johannes Maria Wolfs

nr 258
Requirement checking in the building industry: Enabling modularized and extensible requirement checking systems based on semantic web technologies
Chi Zhang

nr 259
A Sustainable Industrial Site Redevelopment Planning Support System
Tong Wang

nr 260
Efficient storage and retrieval of detailed building models: Multi-disciplinary and long-term use of geometric and semantic construction information
Thomas Ferdinand Krijnen

nr 261
The users' value of business center concepts for knowledge sharing and networking behavior within and between organizations
Minou Weijs-Perrée

nr 262
Characterization and improvement of aerodynamic performance of vertical axis wind turbines using computational fluid dynamics (CFD)
Abdolrahim Rezaeiha

nr 263
In-situ characterization of the acoustic impedance of vegetated roofs
Chang Liu

nr 264
Occupancy-based lighting control: Developing an energy saving strategy that ensures office workers' comfort
Christel de Bakker

nr 265
Stakeholders-Oriented Spatial Decision Support System
Cahyono Susetyo

nr 266
Climate-induced damage in oak museum objects
Rianne Aleida Luimes

nr 267
Towards individual thermal comfort: Model predictive personalized control of heating systems
Katarina Katic

nr 268
Modelling and Measuring Quality of Urban Life: Housing, Neighborhood, Transport and Job
Lida Aminian

nr 269
Optimization of an aquifer thermal energy storage system through integrated modelling of aquifer, HVAC systems and building
Basar Bozkaya

nr 270
Numerical modeling for urban sound propagation: developments in wave-based and energy-based methods
Raúl Pagán Muñoz

nr 271
Lighting in multi-user office environments: improving employee wellbeing through personal control
Sanae van der Vleuten-Chraibi

nr 272
A strategy for fit-for-purpose occupant behavior modelling in building energy and comfort performance simulation
Isabella I. Gaetani dell'Aquila d'Aragona

nr 273
Een architectuurhistorische waardestelling van naoorlogse woonwijken in Nederland: Het voorbeeld van de Westelijke Tuinsteden in Amsterdam
Eleonore Henriette Marie Mens

nr 274
Job-Housing Co-Dependent Mobility Decisions in Life Trajectories
Jia Guo

nr 275
A user-oriented focus to create healthcare facilities: decision making on strategic values
Emilia Rosalia Catharina Maria Huisman

nr 276
Dynamics of plane impinging jets at moderate Reynolds numbers – with applications to air curtains
Adelya Khayrullina

nr 277
Valorization of Municipal Solid Waste Incineration Bottom Ash - Chemical Nature, Leachability and Treatments of Hazardous Elements
Qadeer Alam

nr 278
Treatments and valorization of MSWI bottom ash - application in cement-based materials
Veronica Caprai

nr 279
Personal lighting conditions of office workers - input for intelligent systems to optimize subjective alertness
Juliëtte van Duijnhoven

nr 280
Social influence effects in tourism travel: air trip itinerary and destination choices
Xiaofeng Pan

nr 281
Advancing Post-War Housing: Integrating Heritage Impact, Environmental Impact, Hygrothermal Risk and Costs in Renovation Design Decisions
Lisanne Claartje Havinga

nr 282
Impact resistant ultra-high performance fibre reinforced concrete: materials, components and properties
Peipeng Li

nr 283
Demand-driven Science Parks: The Perceived Benefits and Trade-offs of Tenant Firms with regard to Science Park Attributes
Wei Keat Benny Ng

nr 284
Raise the lantern; how light can help to maintain a healthy and safe hospital environment focusing on nurses
Maria Petronella Johanna Aarts

nr 285
Modelling Learning and Dynamic Route and Parking Choice Behaviour under Uncertainty
Elaine Cristina Schneider de Carvalho

nr 286
Identifying indoor local microclimates for safekeeping of cultural heritage
Karin Kompatscher

nr 287
Probabilistic modeling of fatigue resistance for welded and riveted bridge details. Resistance models and estimation of uncertainty.
Davide Leonetti

nr 288
Performance of Layered UHPFRC under Static and Dynamic Loads: Effects of steel fibers, coarse aggregates and layered structures
Yangyueye Cao

nr 289
Photocatalytic abatement of the nitrogen oxide pollution: synthesis, application and long-term evaluation of titania-silica composites
Yuri Hendrix

nr 290
Assessing knowledge adoption in post-disaster reconstruction: Understanding the impact of hazard-resistant construction knowledge on reconstruction processes of self-recovering communities in Nepal and the Philippines
Eefje Hendriks

nr 291
Locating electric vehicle charging stations: A multi-agent based dynamic simulation
Seheon Kim

nr 292
De invloed van Lean Management op de beheersing van het bouwproces
Wim van den Bouwhuijsen

nr 293
Neighborhood Environment and Physical Activity of Older Adults
Zhengying Liu

nr 294
Practical and continuous luminance distribution measurements for lighting quality
Thijs Willem Kruisselbrink

nr 295
Auditory Distraction in Open-Plan Study Environments in Higher Education
Pieternella Elizabeth Braat-Eggen

nr 296
Exploring the effect of the sound environment on nurses' task performance: an applied approach focusing on prospective memory
Jikke Reinten

nr 297
Design and performance of water resistant cementitious materials– Mechanisms, evaluation and applications
Zhengyao Qu

nr 298
Design Optimization of Seasonal Thermal Energy Storage Integrated District Heating and Cooling System: A Modeling and Simulation Approach
Luyi Xu

nr 299
Land use and transport: Integrated approaches for planning and management
Zhongqi Wang

nr 300
Multi-disciplinary optimization of building spatial designs: co-evolutionary design process simulations, evolutionary algorithms, hybrid approaches
Sjonnie Boonstra

nr 301
Modeling the spatial and temporal relation between urban land use, temperature, and energy demand
Hung-Chu Chen

nr 302
Seismic retrofitting of masonry walls with flexible deep mounted CFRP strips
Ömer Serhat Türkmen

nr 303
Coupled Aerostructural Shape and Topology Optimization of Horizontal-Axis Wind Turbine Rotor Blades
Zhijun Wang

nr 304
Valorization of Recycled Waste Glass and Converter Steel Slag as Ingredients for Building Materials: Hydration and Carbonation Studies
Gang Liu

nr 305
Low-Carbon City Development based on Land Use Planning
Gengzhe Wang

nr 306
Sustainable energy transition scenario analysis for buildings and neighborhoods - Data driven optimization
Shalika Saubhagya Wickramarachchi Walker

nr 307
In-between living and manufactured: an exploratory study on biobuilding components for building design
Berrak Kirbas Akyurek

nr 308
Development of alternative cementitious binders and functionalized materials: design, performance and durability
Anna Monika Kaja

nr 309
Development a morphological approach for interactive kinetic façade design: Improving multiple occupants' visual comfort
Seyed Morteza Hosseini

nr 310
PV in urban context: modeling and simulation strategies for analyzing the performance of shaded PV systems
Ádám Bognár

nr 311
Life Trajectory, Household Car Ownership Dynamics and Home Renewable Energy Equipment Adoption
Gaofeng Gu

nr 312
Impact of Street-Scale Built Environment on Walking/Cycling around Metro Stations
Yanan Liu

nr 313
Advances in Urban Traffic Network Equilibrium Models and Algorithms
Dong Wang

nr 314
Development of an uncertainty analysis framework for model-based consequential life cycle assessment: application to activity-based modelling and life cycle assessment of multimodal mobility
Paul Martin Baustert

nr 315
Variable stiffness and damping structural joints for semi-active vibration control
Qinyu Wang

nr 316
Understanding Carsharing-Facilitating Neighborhood Preferences
Juan Wang

nr 317
Dynamic alignment of Corporate Real Estate to business strategies: An empirical analysis using historical data and in-depth modelling of decision making
Howard Cooke

nr 318
Local People Matter: Towards participatory governance of cultural heritage in China
Ji Li

nr 319
Walkability and Walkable Healthy Neighborhoods
Bojing Liao

nr 320
Light directionality in design of healthy offices: exploration of two methods
Parisa Khademagha

nr 321
Room acoustic modeling with the time-domain discontinuous Galerkin method
Huiqing Wang

nr 322
Sustainable insulating lightweight materials for enhancing indoor building performance: miscanthus, aerogel and nano-silica
Yuxuan Chen

nr 323
Computational analysis of the impact of façade geometrical details on wind flow and pollutant dispersion
Xing Zheng

nr 324
Analysis of urban wind energy potential around high-rise buildings in close proximity using computational fluid dynamics
Yu-Hsuan Jang

nr 325
A new approach to automated energy performance and fault detection and diagnosis of HVAC systems: Development of the 4S3F method
Arie Taal

nr 326
Innovative Admixtures for Modifying Viscosity and Volume Change of Cement Composites
Hossein Karimi

nr 327
Towards houses with low grid dependency: A simulation-based design optimization approach
Zahra Mohammadi

nr 328
Activation of demand flexibility for heating systems in buildings: Real-life demonstration of optimal control for power-to-heat and thermal energy storage
Christian Finck

nr 329
A computational framework for analysis and optimisation of automated solar shading systems
Samuel B. de Vries

nr 330
Challenges and potential solutions for cultural heritage adaptive reuse: a comparative study employing the Historic Urban Landscape approach
Nadia Pintossi

nr 331
Shared control in office lighting systems
Tatiana Aleksandrovna Lashina

nr 332
Comfort in Urban Public Spaces
You Peng

nr 333
Numerical modelling of metal soap formation in historical oil paintings
Gerardus Johannes Anna Maria Eumelen

nr 334
A transdisciplinary decision-making approach to food-water-energy nexus: A guide towards sustainable development
Maryam Ghodsvali

nr 335
Numerical modelling of transient low-frequency sound propagation and vibration in buildings
Indra Sihar

nr 336
Characterization of impact sound from lightweight joist floors
Yi Qin

nr 337
Cities for Children: Supporting Children and Caregivers in Participatory Urban Planning
Özlemnur Ataol

nr 338
Engaging the unengaged: Exploring citizen participation in nature-based solutions in China
Li Dai

nr 339
Municipal Solid Waste Incineration Residues: analysis, treatments, and applications
Ekaterina Loginova

nr 340
Enhancing the Uptake of Nature-Based Solutions in Urban Settings: An Information Systems Approach
Shahryar Ershad Sarabi

nr 341
Work Schedule Arrangements in Two-Adult Households with Children
Bilin Han

nr 342
Increasing awareness of urban cultural heritage using digital technologies: empirical design and analysis of a new multi-media web platform
Benshuo Wang

nr 343
Mechanical and physical properties of fibre-cement composites using alternative natural fibres
Katerina Kochova

nr 344
Numerical and experimental investigation of urban microclimate in a real compact heterogeneous urban area
Nestoras Antoniou

nr 345
Examining in-class activities to facilitate academic achievement in higher education: A framework for optimal indoor environmental conditions
Henk W. Brink

nr 346
High-temperature resistant geopolymers: composition, microstructure and performance
Kinga Malgorzata Klima

nr 347
Individual and household decision-making in shared parking
Qianqian Yan

nr 348
In-situ formation of LDHs in Alkali activated binders
Tao Liu

nr 349
Condition assessment of concrete sewer pipes through an integrated experimental-numerical approach
Irene C. Scheperboer

nr 350
In situ PU-based characterization of sound absorbing materials for room acoustic modeling purposes
Baltazar Briere de La Hosseraye

nr 351
Uncertainty analysis and management in building energy data mining: A bottom-up approach considering the temporal and spatial aspect of data
Waqas Khan

nr 352
Personalized Heating Control Systems to improve thermal comfort and reduce energy consumption
Michal Veselý

nr 353
Restorative value of the urban greenscape: Urban residential streets as restorative environments
Robert P. van Dongen

nr 354
Urban ventilation and the compact Mediterranean city: numerical investigations of the dynamic relationships between density, morphology and wind flow
Olga Palusci

nr 355
Data science for buildings: a multi-scale approach bridging occupants to smart-city energy planning
Julien Leprince

nr 356
Class Association Rule Models for Predicting Transportation Mode Choice
Jiajia Zhang

nr 357
Acceptance and use of autonomous vehicles
Zhihui Tian

nr 358
Consumer Acceptance of Crowdshipping Services
Chenyu Wang

nr 359
Determinants of habitual participation in leisure-time physical activity and active travel in life trajectories
Xiaoyue Chen

nr 360
Analysis of Citizens' Motivation and Intention Using Modern Information Technology in Urban Planning Public Participation
Wenshu Li

nr 361
Linking smart and physical port cities. Port-city interface areas: from obsolete/isolated to smart environments.
Mercè de Miguel Capdevila

nr 362
Assessment and improvement of indoor thermal comfort and energy demand of Chinese heritage apartment buildings under climate change
Muxi Lei

nr 363
Indoor airflow and heat transfer in a cross-ventilated generic building: wind tunnel experiments and computational fluid dynamics analyses
Katarina Kosutova

nr 364
A Robotic Construction Simulation Platform for Light-weight Prefabricated Structures. Lifetime prediction of vertical-axis wind turbines based on CFD simulations and high-cycle fatigue modeling
Aiyu Zhu

nr 365
Lifetime prediction of vertical-axis wind turbines based on CFD simulations and high-cycle fatigue modeling
Feiyu Geng

nr 366
Computational modeling of convective heat transfer at building surfaces
Samy Iousef

nr 367
Numerical simulation of the atmospheric boundary layer with application to natural ventilation
Raffaele Vasaturo

nr 368
Bouwen zonder scrupules. De Nederlandse bouwnijverheid tijdens de bezetting en de eerste jaren van wederopbouw (1940-1950)
Geert-Jan Mellink

nr 369
Factors Promoting a Positive Experienced Neighborhood Public Space--A Virtual Environment-based analysis.
Yuwen Zhao

nr 370
Place quality making in high-speed railway station areas: Devising place quality indicators for urban design, beyond the transport-land use divide
Jinglun Du

nr 371
Sustainable Bio-based Adsorptive Concrete for Phosphorus Removal
Fan Wu

nr 372
The physical workplace as a resource for mental health: A salutogenic approach to a mentally healthy workplace design at home and at the office
Lisanne Bergefurt

nr 373
High-end application of basic oxygen furnace steel slag as sustainable building materials
Muhammad Jawad Ahmed

nr 374
Energy-Efficient Urban Rail Transit Operations: Models, Algorithms, and Applications
Kang Huang

nr 375
Household Energy Efficiency Adoption: Influencing Factors and Diffusion Interventions
Hua Du

nr 376
High-temperature resistant geopolymer-based materials out of industrial residuals.
Yan Luo

nr 377
A Simulation Approach Exploring the Impacts of Land Use Variables on Travel Behavior.
Xiaoming Lyu

nr 378
Understanding and modelling individual preferences for Mobility as a Service
Valeria Caiati

nr 379
Linking the physical and digital built environment - Enabling occupant-centric decision-making using cross-domain semantic digital twins
Alex Donkers

nr 380
Indoor Air Quality in Daycare Centers: Assessing and Mitigating Indoor Exposure on Young Children
Hailin Zheng

nr 381
A Data-Driven Approach to Understanding Visitors' Behavior to Reduce the Negative Effects of Tourism in Historical Cities
Sezi Karayazi

nr 382
Wind effects on internal depressurization for asbestos abatement
Anjali Radhakrishnan Jayakumari

nr 383
Spatiotemporal Graph Convolutional Neural Network for Robust and Accurate Traffic Flow Prediction
Yutian Liu

nr 384
Photo-responsive functional aluminosilicate cementitious materials - Design, Performance and Durability
Daoru Liu

nr 385
High-end applications of basic oxygen furnace slag as a cementitious binder. Phase Assemblage, Mechanical & Chemical Activation, Composites Application
Winnie Franco Santos

nr 386
Towards improved performance modelling of distributed PV systems in the built environment
Bin Meng

This thesis explores the development of insulation materials with the aim of enhancing sustainable building performance by reducing energy consumption, carbon emissions, and material usage in the construction industry. The research is structured around four key areas. The first area focuses on bio-based insulation composites, examining the durability and hygrothermal performance of materials such as straws, hemp, grass, cork, and mycelium. The findings emphasize the potential of these materials as effective insulation solutions, while also identifying their limitations in various environmental conditions. The second area of research involves the development and evaluation of insulation composites made from bio-based materials, industrial waste, and by-products. This section highlights innovative approaches such as substituting ordinary Portland cement with fly ash-based geopolymer, replacing wood wool with straw, and recycling stone wool to create alkali-activated lightweight aggregates. The third focus is on the energy rehabilitation of existing buildings, particularly through the use of advanced insulation strategies. The research investigates the application of aerogel composites in cavity walls and alkali-activated lightweight aggregates made from recycled stone wool as ground cover insulation in crawl spaces. Finally, the thesis proposes a simplified method for predicting moisture-dependent thermal conductivity of porous materials. In summary, this thesis underscores the potential of bio-based and waste-based insulation materials to contribute significantly to sustainable building practices. It also addresses the challenges of balancing performance, durability, and environmental impact in the development of these innovative materials.

DEPARTMENT OF THE BUILT ENVIRONMENT

TU/e EINDHOVEN UNIVERSITY OF TECHNOLOGY